TUDelft

Iv-Infra

Fatigue Assessment of Complex Riveted Connections

A study on old steel bridges using Advanced Finite Element Analysis

Rico Reijers
MSc Thesis

Delft University of Technology
January 29th, 2024

Fatigue Assessment of Complex Riveted Connections

A study on old steel bridges using Advanced Finite Element Analysis

by

Rico Reijers

to obtain the degree of Master of Science at
the Delft University of Technology, in Civil
Engineering.

Cover: Aerial view of several of the spans of the John S. Thompsonbridge.
          Source: © Studio Retouched, Rijkswaterstaat

An electronic version of this thesis is available at http://repository.tudelft.nl/.

Preface

The thesis before you represents my final delivery to obtain the degree of Master of Science in Civil Engineering, and was performed in cooperation with Delft University of Technology, at the Faculty of Civil Engineering and Geosciences, and Iv-Infra.

Without the people at Iv-Infra, who have provided me with the subject of this report and the inspiration to investigate it, and in particular my daily supervisor, Walter Langedijk, this research could not have come about, and I would like to express my sincere gratitude to both him and everyone else at Iv-Infra for the opportunity to intern at their company.

A special thank you goes out to Anis Mohabeddine, my daily supervisor at TU Delft, for his intensive and enthusiastic guidance throughout this project, his availability and openness for my questions, and his eternal patience when I struggled to fully grasp both complex issues as well as the simplest of concepts.

Thirdly, I would like to thank Milan Veljkovic, the chair of my assessment committee, as well as the final people of whom the committee is composed: Henk den Besten, for his detailed, invaluable feedback on my report, and Trayana Tankova, for her time.

Finally, I would like to express my appreciation for my friends, family, and anyone else who has shown an interest in my work, who have been able to provide my with the support and motivation to keep going and conclude this thesis.

Rico Reijers

Haarlem, January 2024

Summary

As the traffic volume increases, the infrastructure must adapt accordingly. To this end, numerous traffic bridges have been constructed over the last 150 years. During this time, many bridges have ended up abandoned, replaced or demolished. However, many still stand and function to this day. Because bridges are commonly built based on an expected lifetime of 75 to 100 years, a large quantity of bridges are reaching the end of their design lifetime, or even are far overdue. To ensure these bridges are remain operational without experiencing catastrophic failures, they have to be recalculated, and if need be, repaired, strengthened or replaced. A common method of construction of steel bridges in the early-to-mid 1900s was through a process called hot riveting. Unfortunately, these riveted bridges regularly display incredibly complex geometries, combined with the fact that riveting is a largely obsolete building method nowadays, means that reassessment of these bridges often proves to be difficult, as a limited number of options is available in official guidelines to tackle these problems. Furthermore, several bridges across the globe had experienced failure due to fatigue, a phenomenon that was commonly unaccounted for in the design, and for particularly old bridges even unknown altogether.

While fatigue phenomena have been extensively investigated throughout the years, studies pertaining to the fatigue of riveted connections are relatively limited. The Eurocode on fatigue, EN-1993-1-9 (2012) includes only two detail categories. Additional guidelines, like RBK Steel (2017) expand upon these detail categories, but focus primarily on built-up beam cross-sections in riveted structures, rather than riveted connections. In order to attempt to more accurately assess the complex joints present in ancient steel bridges, this thesis attempts to answer the following question:

What would be a suitable approach to model complex riveted joints and assess their fatigue life considering a balance between the level of complexity and applicability in design practice?

To answer this question, a literature review has been performed, in which the different factors that affect the resistance of a riveted connection to static or fatigue loading have been investigated, showing important factors to be the material properties, presence of clamping stresses on the rivets, stress ranges, stress ratios and level of multiaxiality in the joint. Furthermore, a detailed overview of the fatigue calculation methods based on standard guidelines, as well as alternative approaches, such as the local strain-life approach, are presented.

The reassessment of the static resistance of the John S. Thompsonbridge performed by Iv-Infra is investigated, zooming in on some of the issues of complex riveted joints that needed to be worked around.

Detailed Finite Element (FE) models of the bridge joint observed in Iv-Infra's recalculation have been constructed with shell elements, based on the experimental and numerical studies on riveted joints from the literature. The FE models presume only axial loading on the beams of the joint, based on the truss-like structure of the bridge. Models with and without prestressing applied to the rivets have been considered separately. Critical sections within the models have been identified, and re-modelled using sub-models with solid elements. The results on one such critical sections are highlighted.

With the results from these sub-models, a fatigue life estimation is made through strain-life and stress-life estimation methods. The strain-life (ε-N) and stress-life (S-N) curves for the considered critical section are presented. The effects of mean stress effects (through the Smith-Watson-Topper (SWT) adaptation) and multiaxial loading (through the maximum shear strain criterion (MSSC)) are

investigated. Through the establishment of empirical formulae, a relationship between the applied axial force to the joint and the local stresses and strains is described. These empirical formulae, which represent the transfer functions, the calculation of the fatigue life of the observed critical location can be significantly simplified. A simple example of the estimation of the fatigue life until failure is provided using the transfer function, based on a single load range (and the resulting local stress- and strain range). The simple example shows that a stress concentration factor-based (SCF) method as prescribed by the Eurocodes is not preferable to estimate the fatigue life, resulting in very conservative estimations. The gap in estimated fatigue life between the SWT-approach and the MSSC-approach suggests that mean stress effects have a significantly larger influence on the remaining fatigue life than the level of multiaxiality in this joint. This is further backed by the expected inherent working of the truss beams, where local mean stresses in a critical location will almost always be non-zero, due to the beams generally being either in tension of compression, without switching. On top of the fact that the axial loads from the diagonal and horizontal beams will remain proportional to each other, limiting the degree of multiaxiality, MSSC does not account for these non-zero mean stresses.

Prestressing shows no effect on the S-N or ε-N curves, but incorporation of prestressing into the models does show a significant benefit to the fatigue life estimation of the joint, as lower overall stress- and strain ranges are observed following from the same applied load as non-preloaded models. Applying a small clamping stress of 40 MPa on the rivets improves the estimated fatigue life by two to three times its original estimation. This suggests that clamping stresses on the rivets should likely be considered in the fatigue assessment of a riveted structure.

Applying the different methods in practice is most easily done through the SCF-method. It requires a slightly simpler model than the other two methods, has no need for transfer functions, and utilizes a very simple formula requiring no additional material data. However, because the models for SWT and MSSC are only slightly more complex, and model building is a substantial part of the assessment, the advantages of using SCF do not weigh up to the expected increase in accuracy and decrease in conservativity that is found with either of the other methods. Given that mean stress effects are generally more prevalent in joints, SWT is the preferred method to perform a fatigue assessment, over the SCF- and MSSC-approaches.

Recommendations for future research include an experimental analysis of a full-scale joint to complement the findings of this thesis and to corroborate the proposed estimation methods and the use of transfer functions to estimate fatigue lives. Additionally, a complete fatigue estimation for a full-scale joint, considering multiple critical sections and their individual fatigue responses, can be performed.

Table of Contents

1. Introduction

Over the course of the last century and a half, both national and international infrastructure has had to adapt to a growing volume in traffic. Between the start of the nineteenth century and the end of the twentieth century, numerous bridges have been built across the globe to facilitate this increase. While many of these bridges have since been demolished, replaced or abandoned, most are still in operation. The majority of bridges are designed for a service lifetime of 75 to 100 years. Given that a large quantity of the bridges that still perform their function today are built in a period between the 1880s and 1960s, a lot of them are approaching the end of their design lifetime. Therefore, it is important to know how much longer these ancient bridges can remain operational in order to avoid catastrophic failures. Through remedial works, which often include maintenance, repair and strengthening interventions, their lifetime can be extended. In the majority of instances, this necessitates extensive calculation and complex analyses. Such analyses, which aim to capture both the global behaviour of the structure, and the localized behaviour within the structural connections, are often significantly more advanced than is commonly practiced in design offices and engineering firms.

The most common way to fabricate structural metallic connections before the 1950s, was through a process called hot riveting. However, the rise of bolting and welding has relegated the riveting method to obscurity. Only a limited number of construction companies are still able to perform this technique, and only for remedial works. This means that, while a significant amount of research has been done on riveted connections and structures, many theoretical and practical issues remain either unanswered, or answered unsatisfactorily. Many research studies limit themselves to simple connections; connections that are applied in practice only to a limited degree, and often as part of a bigger element. As a result, when assessing the remaining structural integrity of these older bridges, an engineer is regularly limited to simple hand calculations, which require a lot of assumptions on for example the force distributions within a joint, resulting in fairly conservative calculations. Moreover, the recalculation of bridges often raises concerns pertaining to fatigue, as it is a phenomenon that was unknown at the time of construction. Similar to structural investigations, most fatigue-related studies of riveted connections focus on simple connections, meaning they are limited in their applicability to practical challenges. Overall, a more complete overview of the static and fatigue strength of riveted connections is required.

As the issue of remaining life of ancient bridges is being tackled in the Netherlands, the lack of information and normative guidelines has become more apparent. An example of this is Iv-Infra's recalculation of the John S. Thompsonbridge, which is located near Grave. While the static resistance of the bridge was assessed, many simplifications were used to estimate the behaviour of the joints, resulting in very conservative calculations. Furthermore, given the complexity of the joints, which commonly consist of tens of individual plates and hundreds of rivets, Iv-Infra has left the assessment of the remaining fatigue life of the joints out of the scope entirely.

1.1.   Current state of research and research gap

Although riveting has become largely obsolete and is no longer being used as a construction technique, considerable research has been done on the strength and fatigue resistance of rivets. In particular, Colette's (2014) historical analysis on the riveting process stands out as an excellent source of general information. Many individual factors related to the strength of riveted connections have been researched and described in this work. Studies on material properties and geometric parameters, such as rivet dimensions and joining typology, have shown to be crucial to the strength of connections (Schenker, Salmon, & Johnston, 1954) (Sire, Gallegos Mayorga, & Plu, 2015). While

the individual effects of these factors have been studied fairly extensively, studies concerned with a multitude of factors, assessing possible interaction between different factors, are limited. Furthermore, given the manual labour involved in constructing ancient metallic bridges, they are prone to imperfections. Both of these issues are particularly relevant in reassessments of steel bridges, which often contain incredibly complex joints and tend to result in a large amount of uncertainty during (re)calculation.

Beyond the static strength properties of riveted connections, fatigue is a relatively newly discovered issue that many bridges face. Given its recency, designs that account for fatigue have not been considered until after riveting had become a largely obsolete method of construction. Several studies have looked at the fatigue resistance of rivets and riveted connections (Brühweiler, Smith, & Hirt, 1990) (Bertolesi, Buitrago, Adam, & Calderón, 2021) (de Jesus A. M., et al., 2011), but they face the same problem that studies looking at static strength of riveted connections face: practical examples of riveted connections are often far more complex and encompass significantly more issues than can reasonably be represented by a single study. The result is that modern day standards for the reassessment of riveted bridges, such as EN 1993-1-9 (2012) and RBK Steel (2017), primarily provide solutions for fatigue problems in riveted connections for standard cases, which cannot be easily adapted to more complex connections. Furthermore, the few detail categories provided by these standards, with which fatigue assessments are performed, focus primarily on built-up riveted cross-sections, rather than the often far more complex riveted joints. Despite the efforts of several researchers to expand on the current standards (e.g. Taras & Greiner (2010), Pedrosa et al. (2019) or Gallegos Mayorga et al. (2016)), a major gap in the knowledge on how riveted structures behave under cyclic loading remains.

1.2.   Problem definition

It is problematic that, even though a lot of traffic bridges are reaching the end of their design lifetime, there is no definitive method to investigate the remaining fatigue life of complex riveted joints in such ancient bridges. While general cases can be investigated, it is imperative to find a more overarching method that with which a multitude of influential factors can be assessed. Regular, hand calculation methods often fail to incorporate a complete set of factors, or at the very least, a set as complete as possible, resulting in calculations that either may not be representative for complex connections or may lead to overly conservative assessments. Better and more complete methods of ascertaining the fatigue life of riveted joints need to be provided, in order to potentially cut down significantly on both the conservativeness of calculations and time required for reassessments while still ensuring both accurate and safe results. Furthermore, these methods should be applicable by non-research driven institutes, like engineering firms, so they can be applied in practice.

1.3.   Research objectives

The aim of this study is to develop a strategy that can be applied to complex riveted connections with which the fatigue assessment can be performed. Through the literature review, the different factors that may influence the resistance of riveted connections to static and cyclic loads can be investigated. Furthermore, the available methods used to assess the fatigue of structural riveted connections need to be outlined, both conventional approaches prescribed by standards as well as more advanced approaches. To apply the different approaches, a detailed Finite Element model of a riveted joint needs to be developed. Finally, the different methods have to be compared.

To complete the research objectives, the following research question has been devised:

What would be a suitable approach to model complex riveted joints and assess their fatigue life considering a balance between the level of complexity and applicability in design practice?

The following sub-questions will be raised to facilitate answering this question:

1) What factors can be determined to influence the structural and fatigue resistance of riveted joints?
    a. What factors should be considered in the (re)calculation of riveted metallic bridges
2) What methods are currently available to determine the structural and fatigue resistance of riveted connections?
    a. What methods are prescribed by the standards to be used in practical examples of (re)calculations?
    b. What non-standard, advanced methods are available for the fatigue assessment of riveted joint?
3) What design choices and modelling techniques need to be employed to ensure the results from a detailed riveted joint Finite Element model are valid?
4) How do the methods prescribed by the standards compare to the advanced assessment methods?
5) What are the advantages and disadvantages of the different methods considered, both in terms of accuracy and complexity of use?

1.4. Report outline
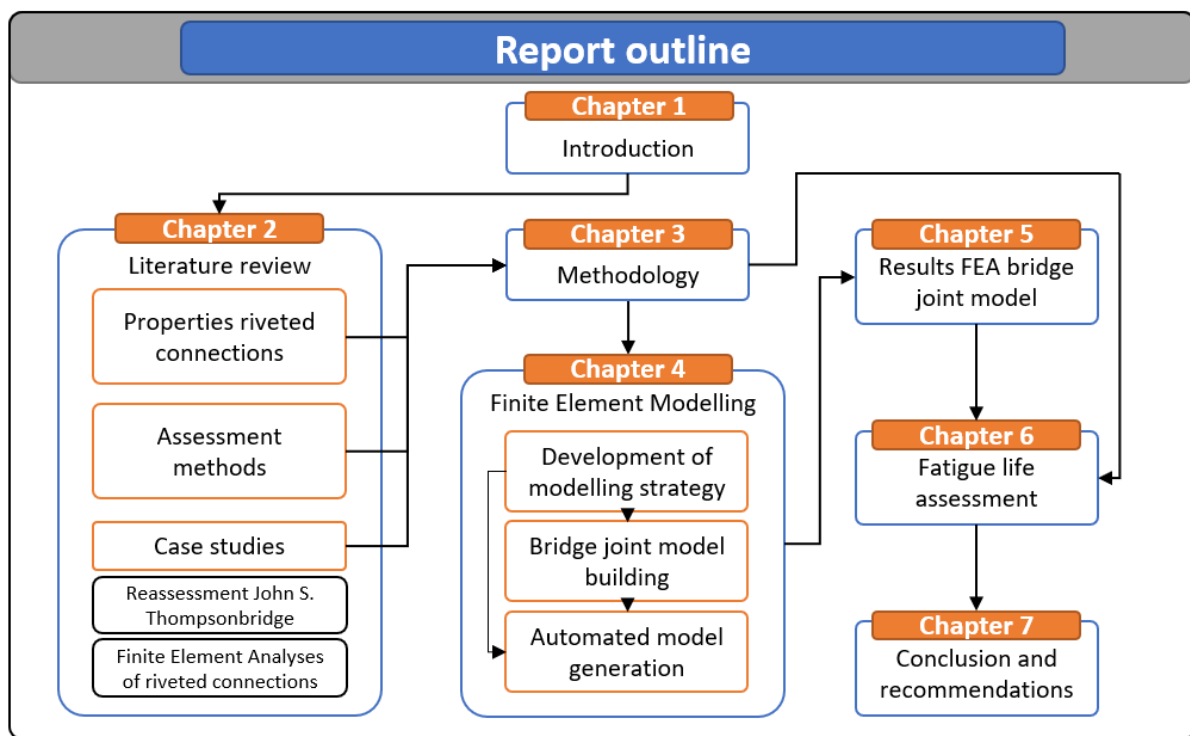
Figure 1: Structure of the report

The following chapter presents the literature review, which attempts to offer relevant background information and showcase previous studies performed on the topics relevant to this report. It covers the properties of rivets individually and riveted connections as a whole. It also highlights available assessment methods for the investigation of the structural and fatigue behaviour of riveted connections. Furthermore, several case studies are presented. The first case study covers the recalculation on strength of the John S. Thompsonbridge performed by Iv-Infra. It elaborates on the steps taken to evaluate the joint and illustrates some of the issues encountered when reassessing

old bridges. Finally, the other two cases relate to the assessment of riveted connections using Finite Element Analysis.

The third chapter describes the methodology used to answer the research questions posed in this report. Several reference models based on the case studies are constructed with ABAQUS. Through the adaptation of the findings in these reference models, an advanced Finite Element model of one of the complex riveted joints from the John S. Thompsonbridge is created. Different methods to perform fatigue assessment as described in the literature are applied, utilizing results from the bridge joint model. Their results are compared through a simple fatigue life calculation. It also states limitations of the adopted methodology.

Chapter four introduces the Finite Element modelling. Some background information of modelling in ABAQUS is provided. It presents the reference models made to replicate the case studies and investigates the assumptions and modelling decisions that need to be made to derive accurate results from a detailed Finite Element model. The parameters and inputs required to generate the bridge joint model are described. Finally, it elaborates on the process of automatic model generation, which is adopted in the generation of the bridge joint model.

Chapter five presents the results gathered from the bridge joint model. It highlights important locations in the model, and provides inside in the forces, stresses and strains acting on the models. Furthermore, a simple validation of the output forces is made based on hand-calculations and the results from the existing Finite Element model by Iv-Infra.

The sixth chapter applies the different fatigue life assessments methods presented in chapter two to the bridge joint model, based on the results gathered in chapter five. It compares standardized methods to non-standard advanced methods. A simple fatigue life calculation is performed with each of the investigated methods, and their results and ease of use are discussed.

The concluding chapter answers the research questions based on the research performed in previous chapters. Additionally, it offers recommendations for future studies on the topic.

2. Literature review

2.1. Riveting process

While in the current day and age welded and bolted connections are the most prevalent means of construction of steel structures, this has not always been the case. Starting in the 1860s, and all the way up to the 1950s, almost one hundred years later, riveting was the most common way of connecting structural steel elements. Before the 1860s the application of rivets was limited due to the brittleness of cast iron, which was vulnerable to the repeated hammering of rivets, but as the techniques of production improved and quality increased, culminating into the creation and application of wrought iron and eventually steel, so did the possibility of applying rivets. Where in the 1860s structural rivets were only used in small bridges, by the time the 1890s came around, structural rivets were being applied almost everywhere, both in large steel bridges as well as in high-rise buildings (Vermes, 2007) (Leslie, 2010). This remained the case until the 1950s and 60s, when bolts and welds started to make their advance, for their increased strength and ease of application.

Before any conclusive statements can be done on the structural behaviour of rivets and riveted connections, one needs to understand the riveting process and the effects it has on rivet behaviour.

Structural rivets, in their uninstalled (undriven) form, are formed from a solid cylindrical iron or steel bar, the rivet shank, with one end usually crushed into a spherical head, commonly referred to as the shop head. The crushing of the shop head is usually done by the manufacturer, within a factory. The opposing end of the rivet, the field head, similarly to the shop head, is made through crushing of the shank. However, this is not done until the plates that need to be joined, also referred to as plies, have holes drilled or punched into them, to fit the rivets. Once these holes are present, the rivet is stuck in, and the field head is formed. This can be done either on site, or again, within a factory in the case of predesigned elements. Figure 2 displays the geometrical parameters of a rivet, with:

- d as the shank diameter;
- D as the head diameter;
- h as the head height;
- R as the radius of curvature of the head;
- e as the thickness of a plate;
- g as the grip length, the combined total thickness of the plates through which the rivet is driven;
- p as the rivet pitch, the distance between rivets;
- l as the rivet lap, the longitudinal distance between the rivet and the end of a plate;
- v as the edge distance, the transversal distance between the rivet and the end of a plate.
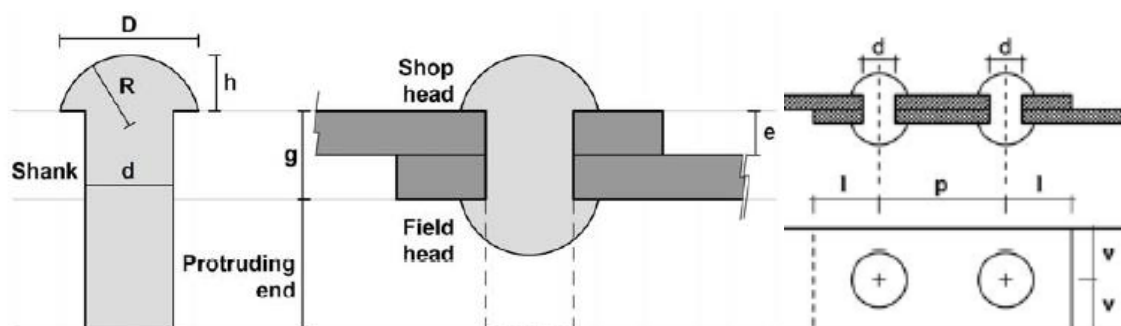

Figure 2: Geometrical parameters of a rivet (Colette, 2014)

The riveting process can be done through hot- or cold-forming. This thesis focuses on hot-forming, as cold-riveting was generally unsuitable for structural application. Construction of a riveted connection through hot forming, either on site or in a factory, requires an entire team of riveters. The first step in this process is already mentioned and requires the plates to be fastened to have holes punched or drilled to the appropriate size. Once the rivet hole is completed, the rivet stoker proceeds to heat up the rivet to between 950°C and 1100°C, which on site, without proper measuring equipment, related to a cherry-red to white-hot colour of the rivet. Subsequently, the rivet passer tosses the rivet to the rivet catcher, who, equipped with tongs, places the rivet in its designated hole. The holder-on then keeps the rivet in place, while the riveter repeatedly hammers the protruding rivet shank to form the field head. This hammering was initially done manually, but as time progressed, this would be taken over by a riveting machine, which could be powered by steam, hydraulic or pneumatic energy. The complete group of riveters responsible for the riveting process would be called a rivet gang (Colette, 2014).

2.2. Properties of a riveted connection

2.2.1. Structural behaviour

There are two ways to consider the structural behaviour of a riveted connection (Figure 3). Due to the fact the rivet is heated as it gets placed in the plates, and the subsequent cooling down, the shank of the rivet shrinks longitudinally. As a result, the rivet heads exert a transversal force onto the plates, the clamping force, squeezing them together. As long as the tensile forces on the plates do not exceed the frictional resistance of the connection as a result of these clamping forces, the connection performs as a friction-type fastener. This means the rivets act similarly to prestressed high-strength bolts, preventing the connection from slipping.
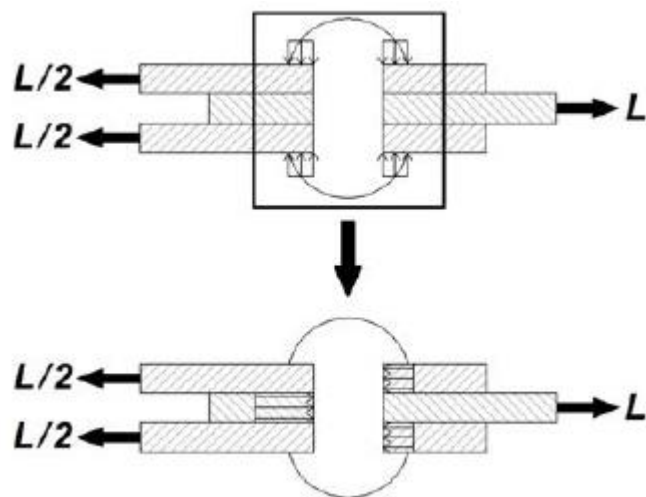
Figure 3: Transition of loading of plies from friction- (top) to bearing-type (bottom) fastener (Åkesson, 2010)
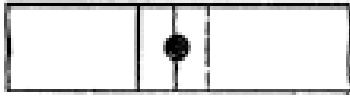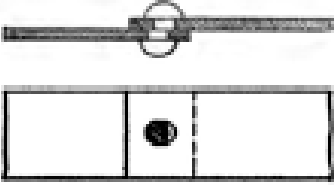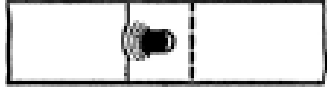
Once the frictional strength is exceeded by the loads acting on the plates, the connection starts to slip. As soon as this happens, the connection turns into a bearing-type fastener, where the shear loads are transferred through the shank of the rivet onto the plates.

The fact that riveted connections act as a bearing-type fastener is observed through the different failure modes that are commonly observed in such connections. There are four main failure mechanisms in riveted joints subjected to shear loads, none of which are defined through the frictional resistance of a joint. The first failure mode though, grip crushing, is related to the clamping force. Grip crushing occurs when the clamping force applied by the rivet exceeds the yield strength of the plies, resulting in the deformation of plies in transversal direction. It often occurs when the ratio between the thickness of rivet shank (d) and plate (e) is too excessive. Grip crushing can easily be avoided by taking an appropriate d/e-ratio in the design of a joint, and thus has conditioned the design of all riveted connections, regardless of the used design method (Colette, 2014).

The three other failure modes are affected by the design of the connection and occur due to shear loading. Plate tensile failure is defined through the rivet pitch and the edge distance, as well as the

ultimate tensile strength of the plate. Exceeding the plate tensile resistance results in the tearing of the plate along the line of rivets. Rivet shear failure is dependent on the ultimate shear resistance of the rivets, as well as the shear planes defined through the thickness of the shank. If this failure mode occurs, the rivet shears due to the tensile forces exerted on it by the plates. Finally, plate bearing is characterized by the ultimate bearing resistance of the plate, on top of both the rivet lap and the d/e-ratio, similar to grip crushing. If it occurs, the rim of the rivet holes gets crushed by the pressure imposed on the plate by the rivets and vice versa. Table 1 illustrates these three failure modes.

Table 1: Failure modes riveted connection (Twelvetrees, 1900)

Plate tensile failure	Rivet shear failure	Plate bearing failure

While the overall structural behaviour of a riveted connection is affected by both its frictional and its shear- and bearing resistance (Sire, Gallegos Mayorga, & Plu, 2015), in modern day calculations the connection is only considered to be a bearing-type fastener. There are two main reasons why this is the case. As mentioned, it is a known phenomenon that the frictional strength is not a governing factor for the ultimate structural behaviour, even though the shear behaviour improves slightly when the frictional strength increases (Twelvetrees, 1900). Secondly, the frictional strength is, aside from being a complex and not entirely understood mechanic, also incredibly variable. A large number of variables affect the frictional strength, and the precise effect of these variables is often tough to quantify (Colette, 2014). In some cases, even the variables themselves are tough to quantify, let alone their impact.

Some of the factors affecting the frictional strength and ultimate strength of riveted joints are highlighted below (Colette, 2014):

- Mechanical properties of the rivet bar.
  The most straightforward factor is the properties of the rivet itself. In general, usage of steel and high-strength steel results in higher ultimate tensile strength, ultimate bearing strength and clamping forces than usage of (wrought and/or puddle) iron does. Even within iron rivet bars, there is a large variability of mechanical properties, due to non-conformity of manufacturing processes or wildly different chemical compositions.
- Shank diameter.
  Tensile tests on wrought iron and steel bars (O'Sullivan & Swailes, 2009) (Cox & Munse, 1952) have shown that a decrease in shank diameter yields an increase in ultimate tensile strength, albeit a small increase. O'Sullivan and Swailes suggest the reason for this, at the very least in wrought iron, may be due to an increased number of hot workings on the bars.
- Rivet heads.
  Rivet can have a more round head (round snap head, higher h/D-ratio) compared to the standard shop head, or a flatter head (button head, lower h/D-ratio). Too small h/D-ratios may lead to a decrease in ultimate tensile strength. This means that failure of the rivet head could be used to define the ultimate tensile strength of a rivet. Applying standardized h/D-ratios will prevent the failure of the head under normal circumstances. That said, both

manufacturing and driving errors that result in a misformed rivet head could affect both the ultimate tensile strength and the clamping force of the rivet.

- Heating temperature.

The temperature at which rivets are driven has a positive effect on the yield and ultimate tensile strength of rivets, as well as the ductility. Overheating however, for example to increase the ease of driving, will reduce the ductility and increase brittleness.

- Soaking time.

Cox & Munse (1952) state that the time rivets are soaked affects their properties, with a small decrease in ultimate tensile strength at increased soaking times.

- Driving technique.

D'Aniello et al. (2011) have found that the hot-riveting process increases the ultimate tensile strength of a rivet by up to 20%. Additionally, the upgrade from hand-riveting to machine-riveting, aside from its positive effect on time consumption, also has a positive influence on the frictional and ultimate shear strength (Schenker, Salmon, & Johnston, 1954). Furthermore, there is an increase in ultimate tensile strength when using a hydraulic hammer compared to a pneumatic hammer, and when using a pneumatic hammer compared to a manually operated hammer.

- Joining typology.

The typology used to create a connection has an effect on the shear behaviour of said connection. The most common means of connecting are either lap- or butt spliced connections, in which lap splices connect two members directly to each other, whereas butt splices apply one or two cover plates to connect the members. Application of lap joints subject the joint to eccentrically applied loads, introducing additional bending moments. In the same manner, the asymmetry of single lap-and butt joints introduces additional bending moments. In general, achieving symmetric loading through the application of double butt splices yields the best results

It was also common practice to apply filler plates to joints where the splices did not line up properly. While, as far as the author can tell, no research has been conducted on the effect of filler plates on riveted connections, there are studies on high-strength bolted connections that suggest filler plates may have a negative effect on the capacity of a connection (Dusicka & Lewis, 2010) (Moriyama, Takai, Yamaguchi, & Kozai, 2020).

- Rivet pattern and spacing.

Obviously, multiple rivet lines and rows affect the load distribution within a connection, where multiple riveted splice connections generally perform better than single riveted splice connections. Additionally, applying rivets in lines as opposed to rows allows for a more optimal use of the net section of the plates, increasing the ultimate strength of the joint.

Figure 4: Common rivet patterns (Colette, 2014)

In addition to individual spacing between rivets and edges, two commonly adopted rivet patterns can be distinguished: chain- and zigzag patterns (see Figure 4). In general, chain patterns perform better than zigzag patterns, as per De Jonge (1945). In particular the convergent zigzag patterns perform poorly, despite being universally accepted in the civil engineering industry in the early 1900s. While the outer rows of convergent joints do
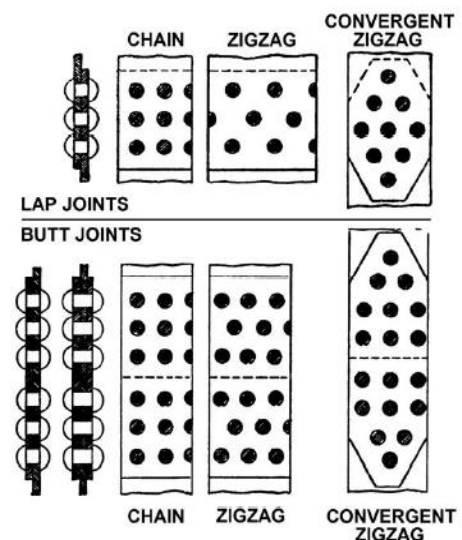
maximize the net section of the plates, a significantly larger amount of shear load is concentrated in relatively fewer rivets, possibly resulting in the failure of the outer rivets before the maximized net section even comes into play (Davis, Woodruff, & Davis, 1940). This failure of outer rivets before the inner rivets reach their full shear capacity, called unbuttoning, can happen in all multiple riveted joints, but is significantly more prevalent in convergent joint configurations.

- G/d-ratio.
It is possible to design a plate such that it can be divided over several strips of equal width, each of which has a hole in the centre. The width of these strips is referred to as the gage (G). The efficiency of a joint is defined as the ultimate strength (either in bearing, tension or shear, dependent on the governing failure mode) of a perforated plate as a percentage of the ultimate tensile strength of an unperforated plate. According to Schenker, Salmon & Johnston (1954), a relation between the efficiency and the G/d-ratio of a joint can be noted. It has even been shown that, for small values of G/d, it is possible to exceed an efficiency of 100%, creating a situation in which ultimate tensile strength of net section of the perforated plate is larger than the ultimate tensile strength of an unperforated plate.

- Shank upset.
The upset of a rivet, or the degree to which the shank is deformed to fill the rivet hole, is the upset. Improper upset means the shank is not properly in contact with the plies, leading to smaller contact areas and thus higher shearing and bearing concentrations in the shank. The three main factors affecting the shank upset are the grip length, the driving technique and the driving temperature. In general, clearances between shank and plies are more likely to occur at the centre of the shank and near the shop head. A larger grip length often results in more areas with clearance (Figure 5).
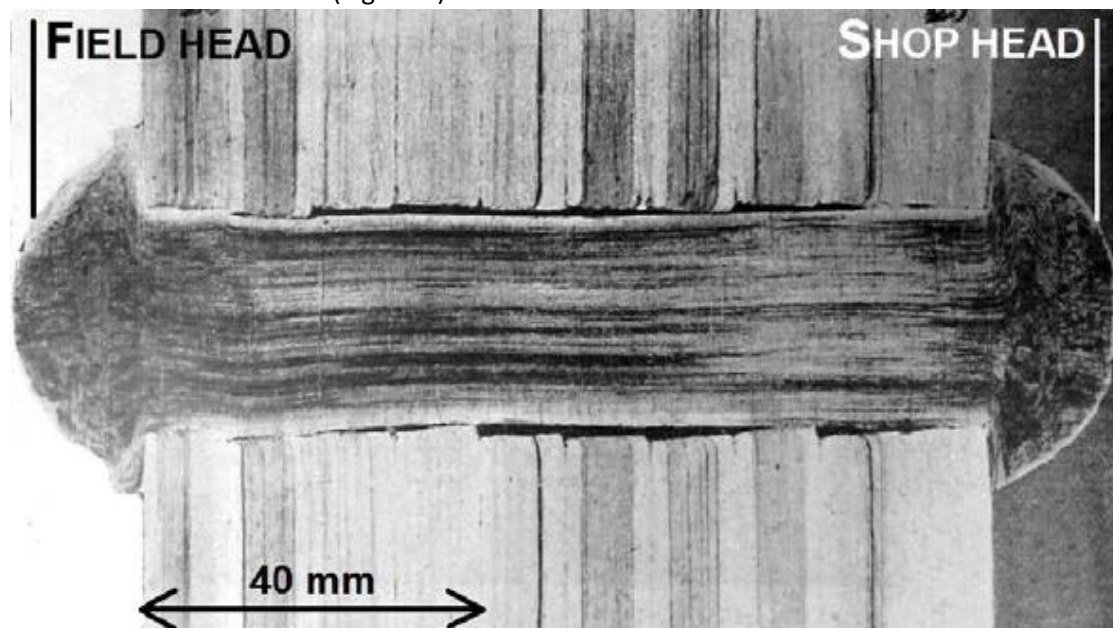
Figure 5: Superior upset near the field head in a long-gripped rivet (Frémont, 1906)

Additionally, machine riveting positively influences the upset of the shank when compared to hand riveting, by the ability to compensate for installation errors such as insufficiently tightened plates and misaligned rivet holes. Similarly, driving rivets at the appropriate temperature positively affects the shank upset, whereas too low temperatures result in improper filling of the rivet holes.

- Grip length.

 As mentioned, the grip length affects the upset of the shank, which in turn affects the shearing and bearing capacity of a riveted connections, with better performances for shorter grip lengths. On the opposite end of the spectrum, grip length is one of the most influential aspects of the onset of the clamping forces, but they have been found to increase for larger grip lengths, reaching the level of yield stresses at grip lengths exceeding 100 mm (Wilson & Thomas, 1938). Additionally, larger grip lengths have a positive effect on the scatter of actual clamping forces (Leonetti, Maljaars, Pasquarelli, & Brando, 2020).
- Protective layers.

 Protective layers such as certain paints may affect the friction coefficient between the plates.

Unfortunately, the precise quantifications of these factors are often unknown, especially without detailed (chemical) analyses and (destructive) testing of the rivets. Additionally, even if theoretically the exact background details of the rivets were known, inconsistencies and human error always remain as an unknown.

2.2.1.1. Strength assessment of riveted connections

Initial design of riveted structures was largely based on empirical methods, stemming from the original use of rivets: boiler work. As time went on, more analytical methods were devised as well, rooted in mathematical models (Colette, 2014). However, a complete picture, involving the complete understanding of most, if not all, factors was never reached.

As a result of the uncertainty of some of these factors, the modern-day standards for calculations on the static structural behaviour of riveted connections are based on several assumptions. These assumptions are as follows (EN 1993-1-8:2007, 2007):

- The rivet shank completely fills the rivet hole after driving;
- The contribution of frictional strength can be neglected;
- Riveted connections behave in pure shear/bending;
- Applied loads are uniformly distributed within the rivets of a given joint.

Given these assumptions, the design calculations on riveted connections largely follow the same principles as bolted connections. Partial safety factors are the same as those for regular bolts. The design shear, bearing and tensile strength of rivets are defined according to Table 2. The presence of combined shear and tension is assessed the same way one would assess it for bolts.

Table 2: Design resistances bolts

Failure mode	Shear	Bearing	Tension
Formula	$F_{v,Rd} = \dfrac{0,6 * f_{ur} * A_0}{\gamma_{M2}}$	$F_{b,Rd} = \dfrac{k_1 * \alpha_b * f_u * d * t}{\gamma_{M2}}$	$F_{t,Rd} = \dfrac{0,6 * f_{ur} * A_0}{\gamma_{M2}}$
Variables	f_{ur} = tensile strength rivet A_0 = rivet hole area	k_1 and α_b follow the same definitions as for bolts and are dependent on the rivet spacing f_u = tensile strength plate d = rivet diameter t = thickness plate	See shear failure

In certain cases, additional reduction factors may need to be adopted. As mentioned in the previous section, the presences of filler plates may have a negative effect on the design strength of the connection. With limited research on the effect of filler plates on riveted connections, the same formula for bolts can be adapted to rivets. Therefore, if the thickness of the filler plate(t_p) exceeds one third of the rivet diameter (d), the following safety factor is adopted:

$$\beta_p = \frac{9d}{8d + 3t_p} \leq 1 \qquad \qquad Eq.\ 1$$

Similarly, both bolted and riveted connections require an additional safety when exceptionally long connections are applied (see Figure 6). Given the fact that it is not uncommon for riveted connections to consist of large rows, this factor often needs to be taken into consideration. If L_j exceeds fifteen times the rivet diameter, safety factor β_{Lf} is adopted:

$$\beta_{Lf} = 1 - \frac{L_j - 15 * d}{200 * d}\ and\ 0,75 \leq \beta_{Lf} \leq 1,0 \qquad Eq.\ 2$$
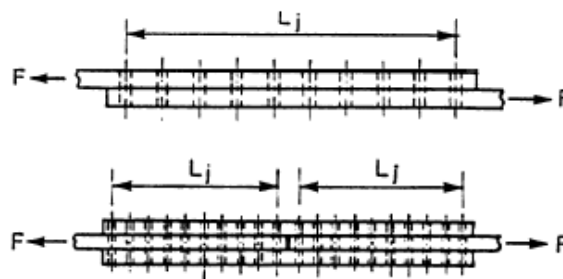
Figure 6: L_j in long lap- or butt joints

In addition to this, EN 1993-1-8 and the Dutch National Annex state some minimum requirements on newly built riveted connections. New rivets must be constructed of S235 steel. When applying S235 steel, the value f_{ur} can be taken as 400 MPa. Furthermore, to limit poor shank upset, the grip length must be limited to 4,5d or 6,5d for hammered and pressed rivets respectively.

However, it should be noted that the application of new riveted connections in constructions is largely obsolete. Most calculations on riveted connections are related to reassessments of structures, rather than new structures. This means that, as addendum to EN 1993-1-8, in the Netherlands, it is not uncommon to take RBK Steel (Richtlijnen Beoordeling Kunstwerken) into consideration. This document is to function as the basis for NEN 8703, which is a guideline to be added to the NEN 8700-series on reassessment of existing (steel) structures. RBK Steel, rather than taking S235 as base material, provides an overview of historic guidelines and their assumed f_y, f_u and f_{ur} for iron and steel types that are no longer applied. Another requirement imposed by RBK Steel states that, when reassessing rivets, they cannot be taken as loadbearing when a shift of the rivet can be observed, or when severe corrosion damage is present. Finally, RBK provides the spring model, a model that can be used to derive the load distribution in multiple riveted connections.

2.2.2. Fatigue behaviour
Fatigue failure of steel members is a phenomenon that has only relatively recently been more widely discussed and understood, with some of the earlier studies dating to well within the 20th century. This means that many bridges, and in particular the older bridges originating from before and around the 1900-mark, have not been designed with fatigue resistance in mind. Therefore, when reassessing a bridge, the remaining fatigue life needs to be taken into consideration.

Despite the fact that riveted connections generally perform well under cyclic loads, fatigue failure accounts for a major part of the failure of metallic bridges, because riveted bridges are often somewhat overdesigned for the (static) design loads, especially for the degree of loading at the time of construction, while at the same time not being designed for fatigue. Part of the reason that riveted connections perform well under cyclic loading is due to the clamping stresses on the plates imposed by the rivets. Higher clamping forces in the connection allow for more of the applied force to be transferred through friction, reducing the bearing forces on the rivet and thereby the stress concentrations at the notches (Leonetti, Maljaars, Pasquarelli, & Brando, 2020) (Riedel, Sieber, & Flederer, 2021), as well as the resulting stress ranges. As mentioned in Chapter 2.2.1, clamping forces are wildly variable, and dependent on a lot of variables. Zhou (1994) has found average values for the clamping stress to be around 84 MPa, but with a standard deviation of almost half of that value (± 41 MPa). Similar values have been found by Leonetti et al. (2020), who've based their research on rivets with a grip length/diameter ratio of close to unity, ranging from 60 MPa to 100 MPa for 3 and 2 plates respectively. However, as illustrated by the large standard deviation, even within the same structure, large discrepancies can be observed. Aside from the clamping forces, while it is a dominant feature of fatigue resistance, there are several other factors affecting the fatigue resistance of a riveted connection (Taras & Greiner, 2010):

- Material properties.
  Similar to the static behaviour of rivets, material properties affect the response to cyclic loads. It is generally accepted that older iron- and steel types perform worse than newer materials do.
- Stress Range.
  The effect of stress range is fairly self-explanatory, rooted in the basis of fatigue calculations. In general, under larger stress ranges, specimens fail after fewer cycles.
- Stress Ratio.
  The stress ratio is defined as the ratio between the minimum and the maximum stress acting on an element, usually ranging from -1 to 1. As the value of the stress ratio decreases, the number of cycles that can be withstood increases (Kumar & Singh, 1995) (Maddox, Gurney, Mummery, & Booth, 1978). This stress ratio, although still influential, has less of an impact on welded connections, due to their large tensile residual stresses, which are not present in riveted connections. It should be noted, however, that while the relation established by Taras & Greiner is generally accepted, it appears that it cannot be correlated directly to all riveted assemblies and may require further research (Sire, Caiza, Espion, & Ragueneau, 2020).

- Degree of bearing pressure.
  This factor is more of an extension to the effect of clamping force, rather than an influence by itself. Reducing the bearing pressure in rivet holes, decreases the stress concentrations in- and around them. Therefore, when little to no

Figure 7: Fatigue cracking on either side of a rivet (Vermes, 2007)

shear forces are transferred by the rivet shank onto the walls of the rivet hole, the specimens are less prone to fatigue than when larger shear forces are transferred, which require transfer through the rivet shank.
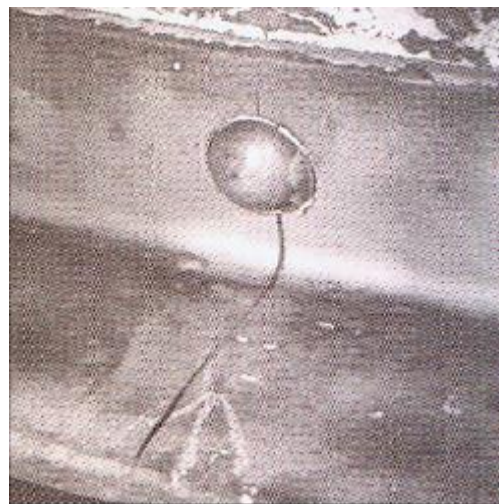
- Imperfect driving.

  Wyly and Scott (1956) have found that improper punching or drilling of rivet holes during erection may result in initial nicks or cracks, which can subsequently lead to fatigue failure. Similarly, eccentric bearing of a rivet can result in premature fatigue failure.

In testing, fatigue failure can be defined as the complete severing of a cross-sectional component of an element by a fatigue crack and another crack has appeared in a secondary element (DiBattista, Adamson, & Kulak, 1998) (Baker & Kulak, 1985). By the time this complete severing has occurred, it is not uncommon for an additional crack to have formed on the opposite end of the element (see Figure 7).
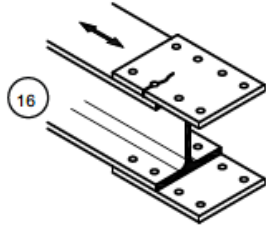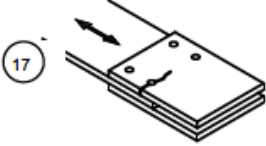
In addition to the general factors mentioned above, it should be noted that there are different forms of fatigue failure, as the failure can occur in either the connecting or the connected elements, these being the rivets and plates respectively. In the overwhelming majority of cases, the first cracks in the case of fatigue failure will occur in (cover) plates, with cracks originating from the rivet holes. However, it is possible for the rivets to fail themselves, often resulting in the popping off of the rivet head, which in the calculation of connections is assumed to result in a complete loss of function of the rivet (RBK Staal, 2017).

2.2.2.1.   Fatigue assessment of riveted connections

Detail categories in standards

As mentioned, fatigue is a relatively new aspect of structural design. This, in combination with the fact that riveted designs are, in general, no longer being applied in practice and have not been for several decades, the actual standards on the fatigue of riveted connections are somewhat limited. EN1993-1-9 (2012) and the Dutch National Annex define just two fatigue classes that can be used in a nominal fatigue approach (see Table 3).

Table 3: Riveted fatigue classes as defined in EN 1993-1-9

Detail category	Detail	Description
70		Riveted connection with single-sided gusset plates.
90		Riveted connection with double-sided gusset plates.

Similar to the structural strength of rivets though, RBK Steel provides additional information on riveted connections in the case they need to be reassessed for their fatigue resistance. RBK Steel redefines the two detail categories from EN 1993-1-9, and expands on them, resulting in a total of seventeen separate detail categories. These are shown in Annex A. The S-N curve of each of the detail categories follows the same shape as the fatigue curve for shear stress intervals as taken from EN 1993-1-9 (see Figure 8), with m = 5 and the detail category at location 1, although for rivets it is

applied to normal stress intervals rather than shear stress intervals. The corresponding formula is given by Eq. 3, where $\Delta\sigma_c^m$ is described by the relevant detail category. It is quite evident that these detail categories are largely based on the aforementioned work by Taras & Greiner (2010).

$$\Delta\sigma_R^m N_R = \Delta\sigma_c^m * 2 * 10\text{\textasciicircum}6 \quad \text{for } N \leq 10^8 \qquad \textit{Eq. 3}$$
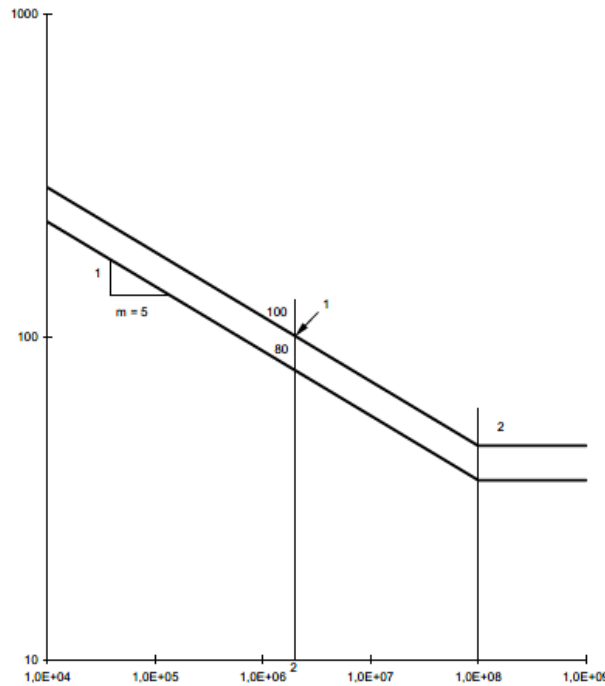
Figure 8: Fatigue curve for shear stress intervals

Additionally proposed detail categories

On top of these detail categories, recent studies by several researchers on ancient French and Portuguese bridges have suggested that the detail categories proposed by Taras & Greiner and subsequent adoption of them by RBK Steel may not be sufficient in providing a proper representation of the actual S-N curves for said bridges, in particular in the high-cycle fatigue domain (Gallegos Mayorga, et al., 2016) (Pedrosa, et al., 2019). Additionally, these studies provide suggestions for S-N curves and the resulting detail categories that may more accurately represent connections from such ancient bridges. It should be noted though that their work is not perfect (as acknowledged in their reports), and as opposed to the different detail categories defined by Taras & Greiner and RBK Steel, multiple loading situations and joining typologies are combined into the same S-N curves.

Gallegos Mayorga et al. (2016) have looked at several specimens of puddle iron connections as taken from ancient railway bridges. In particular, single riveted lap joints, single riveted butt joints and double riveted butt joints have been observed. Following the tests conducted on these specimens, they have compared the results to the known detail categories. It has been concluded that the detail categories adopted by the Eurocodes may not provide an adequate lower boundary. Taras & Greiner have provided a better S-N curve, but high-cycle fatigue remains inadequately represented. The lower boundary (95% confidence interval) S-N curve proposed by Gallegos Mayorga et al. assumes $\Delta\sigma_C$ = 51,7 MPa and m = 3,9 (Figure 10), and more accurately represents the fatigue data of riveted connections.
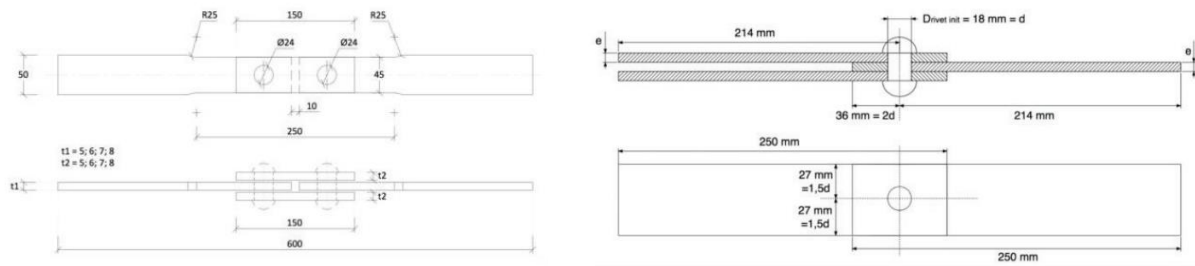
Figure 9: Geometries of single riveted double lap and butt joints observed by Gallegos Mayorga et al. (2016)
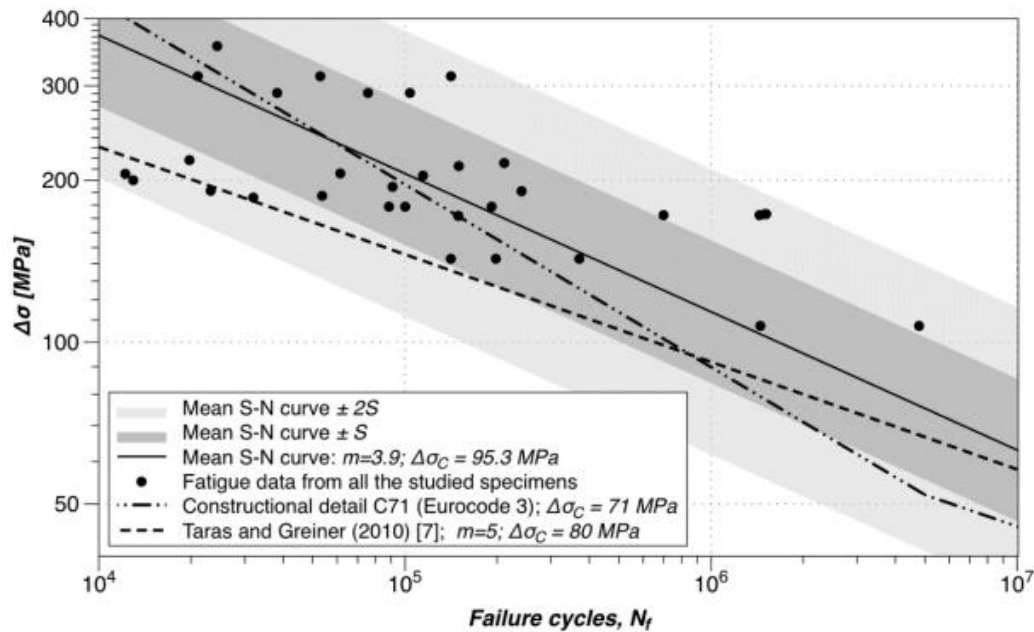
Figure 10: Fatigue data and possible S-N curves (Gallegos Mayorga, et al., 2016)

Pedrosa et al. (2019) have conducted a similar study, taking samples of riveted connections from ancient railway bridges and subjecting them to fatigue tests. Similar to Gallegos Mayorga et al. (2016), single riveted lap joints, single riveted butt joints and double riveted butt joints have been observed. While Pedrosa et al. have made a distinction between lap- and butt- connections, no difference has been established between cracking in the middle plate or the cover plate (for butt joints) in the S-N curves. Additionally, only transversal cracks have been observed, meaning additional research on longitudinal crack may need to be performed. The suggested S-N curve for lap joints follows $\Delta\sigma_C$ = 55 MPa and m = 6, while the S-N curve for butt joints assumes $\Delta\sigma_C$ = 107 MPa and m = 10. S-N curves are shown in Figure 12 and Figure 13.

Figure 11: Example geometries of the single riveted lap and butt joint observed by Pedrosa et al. (2019)

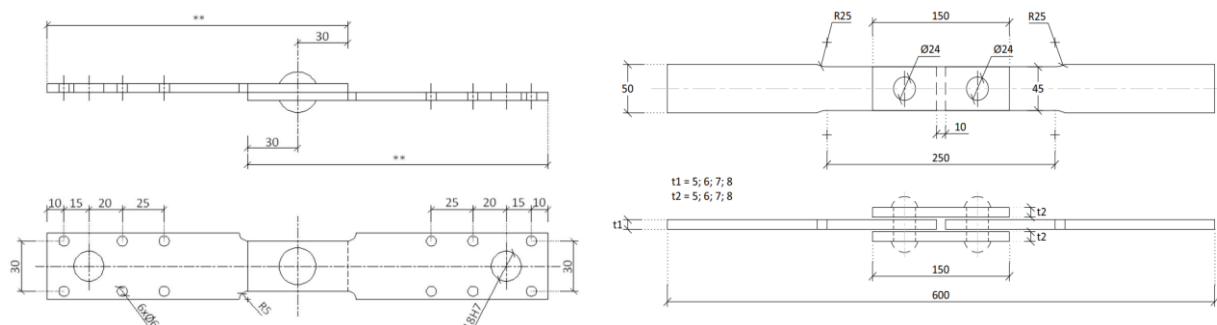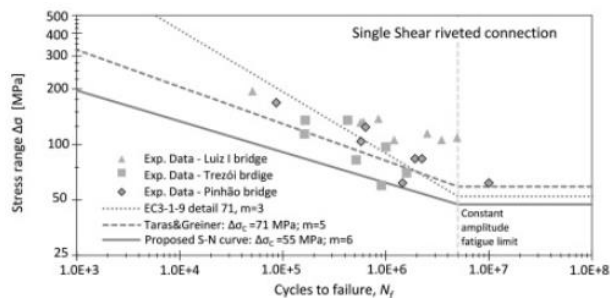Figure 12: S-N curve lap joints (Pedrosa, et al., 2019) Figure 13: S-N curve butt joints (Pedrosa, et al., 2019)
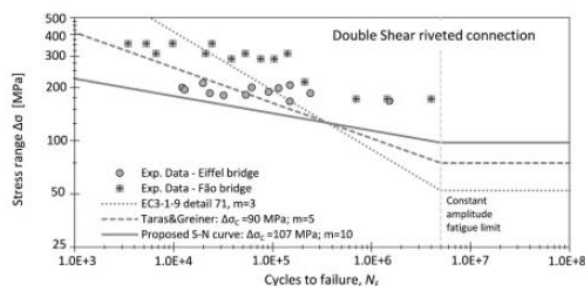
Damage calculation

The purpose of finding the detail category of a certain bridge component, section or connection, is to assess the remaining fatigue life. There are two general ways to determine the remaining fatigue life of riveted structures, both of which largely follow the same procedure as for regular steel structures. EN 1993-1-9 (2007) adopts the damage accumulation method using Palmgren-Miner's Rule. This method requires knowledge on the (representative) stress history of a given detail. Using this history, all stress ranges can be found. Finding the total number of times a certain stress range occurs, and the maximum number of times this can occur without failure (based on the S-N curves), yields all data required to implement into Palmgren-Miner's formula (Eq. 4).

$$D = \sum_{i}^{n} \frac{n_i}{N_i}$$ *Eq. 4*

In this formula, D represents the cumulative damage number, n is the number of different observed stress ranges throughout the stress history, n_i is the times a given stress range *i* occurs within the stress history, and N_i is the number of times the given stress range *i* can occur until failure occurs, according to the detail category. Once $D \geq 1,0$, the observed structure is considered to have failed under fatigue loads. It should be noted that RBK Steel assumes an additional condition on riveted connections consisting of materials used from before 1965. This condition, $D \leq D_{lim}$, is dependent on the applied steel type, and the acting tensile stresses in the observed plate in ultimate limit state (σ_{Sd}^{+}). Table 4 represents the value D_{lim}, where intermediate values for σ_{Sd}^{+}/f_y may be interpolated. If the initial condition $D \leq 1,0$ is abided, but D exceeds D_{lim}, additional material tests need to be performed. These material tests may allow for the additional condition of D_{lim} to be neglected.

Table 4: Value for D_{lim}

f_y = 235 N/mm²		f_y = 355 N/mm²	
σ_{Sd}^{+}/f_y	D_{lim}	σ_{Sd}^{+}/f_y	D_{lim}
0	1	0	1
0,2	0,95	0,2	0,95
0,4	0,90	0,4	0,90
0,6	0,85	0,6	0,85
0,8	0,80	0,8	0,70
1,0	0,65	1,0	0,50

2.2.2.2. Alternative approaches and considerations for fatigue assessment

Local strain-life approach

Rather than using the stress-life curves to assess the fatigue life of a structure, which is limited in applicability, other methods can be applied to model the crack initiation phase. One such method is

through Local Approaches to fatigue. This method focuses on local or notch stresses or strains in an element. One of the biggest advantages of this method is that plastic strain as a result from elevated stress concentrations (e.g., near notches), which lead to crack initiation, can be taken into consideration, resulting in a more accurate representation of the response to cyclic loading and the remaining fatigue life.

Strain-life methods are based on the true stresses and strains. When a specimen is loaded in tension, it increases in length. However, as the volume remains unchanged, the area must decrease. The difference between engineering stress/strain and true stress/strain lies within this fact. Engineering stress and strain are based on the original dimensions of a specimen, whereas true stress and strain account for this change in dimensions. This means that engineering stress is calculated using the original area of a specimen, while true stress is calculated using the actual area. The result is a difference in stress-strain relationship (see Figure 14). Engineering stresses (and strains) usually decrease once necking of a specimen occurs. True strains are measured using a strain gauge, and true stress will increase until failure occurs (at fracture stress and strain, σ_f and ε_f respectively) (Fatigue Theory Reference Manual, 2002). A characteristic of a true stress/strain curve is that it should not have a negative slope, something the engineering stress/strain curve does have.
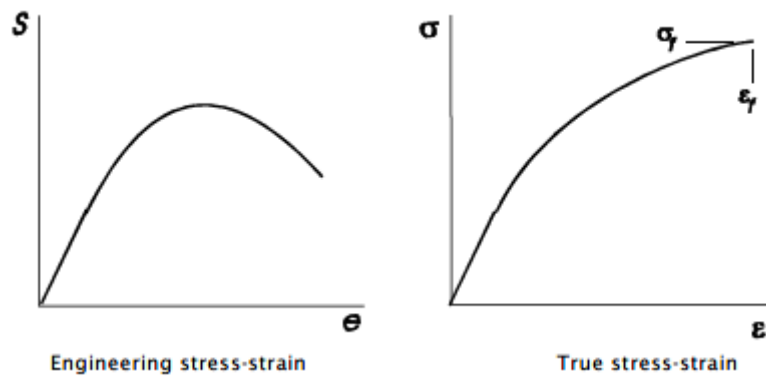
Figure 14: Conventional tensile test displaying the difference between engineering and true stress-strain relations (Fatigue Theory Reference Manual, 2002)

True strains act logarithmically, while engineering strains behave linearly. In the elastic region of materials, at low strains, the curves are nearly identical, while at larger strains they diverge significantly. Converting engineering strains and stresses to true strains and stresses is fairly straightforward. The following analytical formulae are generally accepted to represent this conversion, in which the t- and e-subscripts represent true- and engineering stresses/strains respectively:

$$\sigma_t = \sigma_e * (1 + \varepsilon_e)$$

<div align="right">*Eq. 5*</div>

$$\varepsilon_t = ln\,(1 + \varepsilon_e)$$

<div align="right">*Eq. 6*</div>

In order to properly represent both the elastic and plastic response of a material, a definition of the total strain is required. Ramberg and Osgood (1943) have proposed the following relation for the total strain, consisting of an elastic and a plastic component, in which E represents the Young's modulus and K and n are the strain hardening coefficient and exponent respectively:

$$\varepsilon = \varepsilon_e + \varepsilon_p = \frac{\sigma}{E} + \left(\frac{\sigma}{K}\right)^{\frac{1}{n}} \qquad \text{Eq. 7}$$

This formula only describes a monotonic curve though, a true strain curve as a result of a single load application. Fatigue is related to the cyclic loading of elements. If yielding occurs at each of these load applications, a stress-strain hysteresis loop is formed as the material response. According to Masing's hypothesis, this hysteresis loop can be described with the following equation:

$$\Delta\varepsilon = \frac{\Delta\sigma}{E} + 2\left(\frac{\Delta\sigma}{2K'}\right)^{\frac{1}{n'}} \qquad \text{Eq. 8}$$

This hysteresis loop may (initially) be unstable, as a result from hardening/softening of the material, resulting in increasing or decreasing stress-responses respectively. In general, after a certain number of cycles, an equilibrium will be reached, stabilizing the hysteresis loop.
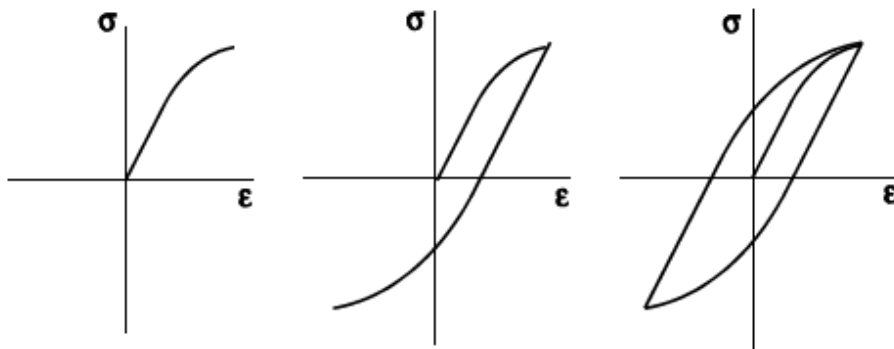
Figure 15: Hysteresis loop showing the cyclic behaviour as plotted in a stress-strain graph (Fatigue Theory Reference Manual, 2002)
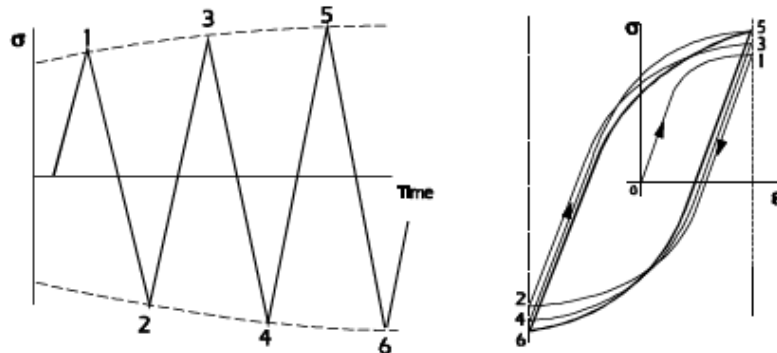
Figure 16: Cyclic hardening until stability

While different strain amplitudes may produce a differently sized hysteresis loop, the tips of each loop should correspond with a point along the cyclic stress-strain curve (Figure 17).
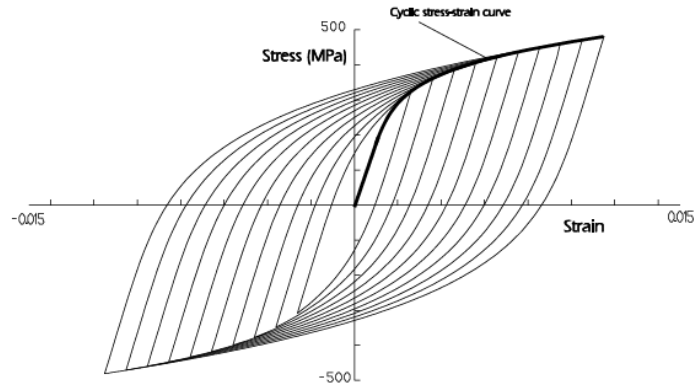
Figure 17: Tips of hysteresis loops going through the cyclic stress-strain curve

The relationship between true elastic stress amplitude and endurance (which is expressed in half-cycles or reversals, denoted as $2N_f$) has been first proposed by Basquin (1910) and can be plotted as a linear relation on $\log_{10}$-$\log_{10}$ axes (Eq. 9). Similarly, Manson and Coffin (1954) have found a linear relation between the true plastic strain amplitude and the endurance on $\log_{10}$ axes (Eq. 10). Adapting Basquin's equation to strain and taking the superposition of both equations, the strain-life relationship can be constructed (Eq. 11). The resulting strain-life relationship is shown in Figure 18. Note that in each of these equations, the stress- and strain amplitudes are given, rather than the stress and strain themselves.

$$\frac{\Delta\sigma_e}{2} = \sigma_f'\big(2N_f\big)^b \qquad\qquad \text{Eq. 9}$$

$$\frac{\Delta\varepsilon_p}{2} = \varepsilon_f'\big(2N_f\big)^c \qquad\qquad \text{Eq. 10}$$

$$\frac{\Delta\varepsilon}{2} = \frac{\sigma_f'}{E}\big(2N_f\big)^b + \varepsilon_f'\big(2N_f\big)^c \qquad\qquad \text{Eq. 11}$$

The constants in these equations are all material parameters, and defined as follows:

- σ_f' as the fatigue strength coefficient;
- b as the fatigue strength exponent (Basquin's exponent);
- ε_f' as the fatigue ductility coefficient;
- c as the fatigue ductility exponent (Coffin-Manson exponent);
- E as the Young's modulus.
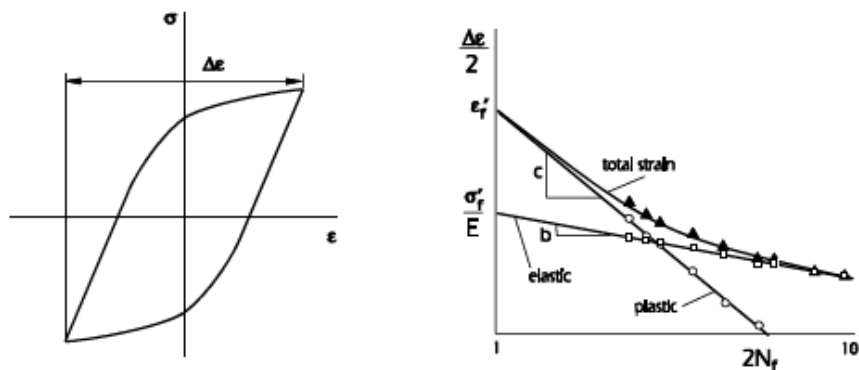
Figure 18: Strain-life relation (Fatigue Theory Reference Manual, 2002)

It should be noted that the strain amplitude is not the only factor affecting the fatigue strength. It is a known phenomenon that specimens under a zero mean stress perform better in fatigue tests than the same specimens under a non-zero mean stress. One of the earlier adaptations of the strain-life equation that incorporates this fact was proposed by Morrow (1968). This equation (Eq. 12) incorporates the mean stress in the elastic term. However, while this equation provides acceptable results, it is theoretically incorrect. Modifying the elastic term by the mean stress without adjusting the plastic term suggests that the relation between the elastic and plastic strain is affected by mean stress. This would mean the hysteresis loop changes with the mean stress, but experimental studies show this is not the case.

$$\frac{\Delta\varepsilon}{2} = \frac{\sigma_f' - \sigma_{mean}}{E}(2N_f)^b + \varepsilon_f'(2N_f)^c \qquad\qquad \textit{Eq. 12}$$

The most common adaptation of Eq. 11 that does account for the mean stress effect is proposed by Smith, Watson & Topper (1970), and assumes that rather than only strain amplitude, the fatigue life is a function of the product of the strain amplitude and the maximum stress (Eq. 13). This formula is obtained through the fact that, at zero mean stress, $\sigma_{max} = \Delta\sigma/2$. Taking this fact, and subsequently implementing Eq. 9 on the right hand side, Eq. 13 is obtained. The one prerequisite for the Smith-Watson-Topper equation is that it becomes undefined for compressive maximum stresses. While this may seem quite consequential, compressive cycles are often considered to be inconsequential for fatigue damage, and usually do not need to be considered.

$$\frac{\Delta\varepsilon}{2}\sigma_{max} = \frac{(\sigma_f')^2}{E}(2N_f)^{2b} + \sigma_f'\varepsilon_f'(2N_f)^{b+c} \qquad\qquad \textit{Eq. 13}$$

Actual values for each of the variables should be obtained experimentally. This is particularly the case for cast and wrought iron, which have non-uniform properties and may differ wildly from structure to structure. As a result, their hysteresis loops have an asymmetrical shape and require additional information to construct an appropriate fatigue response. For more modern and standardized steel- or aluminium-types, values for each of the variables should be obtained through experiments as well, although, if available, previous studies can be consulted. Several methods to approach these variables have been assessed, and the general consensus is that most methods are able to give a general prediction, but still have a significant discrepancy between the predicted and actual values (Troschenko & Khamaza, 2010). The most accurate methods appear to be the averaged parameters method, the Roessle-Fatemi hardness method and the Muralidharan-Manson modified universal slopes method. A slightly older study by Park and Song (1995) also acknowledges Bäumel & Seegers Uniform Material Law as an adequate approach. Their definitions of parameters for steels are given in Table 5. The reason their accuracy is limited is largely due to the fact that b and c are considered to be constant, which does not accurately represent the actual experimental data, though for the current approximation methods, it still provides the best overall results (Niederwanger, Ladinek, Lang, Timmers, & Lener, 2019).

Table 5: Strain-life parameters for different approximation methods. HB is the Brinell hardness

	σ'_f	ε'_f	b	c
Averaged parameters	$1,5\sigma_u$	$0,45$	$-0,09$	$-0,59$
Roessle-Fatemi	$4,25HB + 225$	$\dfrac{0,32HB^2 - 487HB + 191000}{E}$	$-0,09$	$-0,56$
Muralidharan-Manson	$0,623E\left(\dfrac{\sigma_u}{E}\right)^{0,832}$	$0,0196\varepsilon_f^{0,1555}\left(\dfrac{\sigma_u}{E}\right)^{-0,53}$	$-0,09$	$-0,56$
Uniform Materials Law	$1,5\sigma_u$	$0,59\alpha$ With: $\begin{cases} \alpha = 1 & for\ \dfrac{\sigma_u}{E} \leq 0.003 \\ \alpha = 0,812 - \dfrac{74\sigma_u}{E} & for\ \dfrac{\sigma_u}{E} \geq 0,003 \end{cases}$	$-0,087$	$-0,58$

Similitude concept

Once the strain-life relation has been appropriately established, actual fatigue damage calculation follows the same principles as application of the S-N curves, using Palmgren-Miner's rule (Eq. 4). However, it is not always feasible to establish the appropriate strain-life relation, because stress concentrations at the critical location may be unable to be measured in practice, e.g., due to physical constraints. It is possible though, to extrapolate the strains of a nearby point unaffected by stress concentrations, the nominal strains, to the critical point. This local strain-life approach is based on the assumption that if the strain history in a local notch tip is the same as the strain history in a test specimen of the same material, the fatigue response in both the local notch tip and in the test specimen will be the same, and can be described by the same material strain-life (ε-N) curve, also referred to as the Similitude Concept (Glinka, 2010). There are several methods to apply this concept. Most commonly accepted is Neuber's Rule. Using the elastic stress concentration factor K_t, the local stress and strain can be determined (Eq. 14). The other parameters refer to nominal stress and strain (S and e) and the true local stress and strain (σ and ε).

$$\Delta\sigma\Delta\varepsilon = K_t\Delta S * K_t\Delta e$$

<div align="right">Eq. 14</div>

The right-hand side of the formula represents an initial estimate of the local stress and strain, which results in the local stress-strain product of an infinitely elastic material. Neuber suggests that this product must be constant, so the product for an infinitely elastic material would yield the same results as the product of the true stress-strain of an elastic-plastic material (Figure 19).
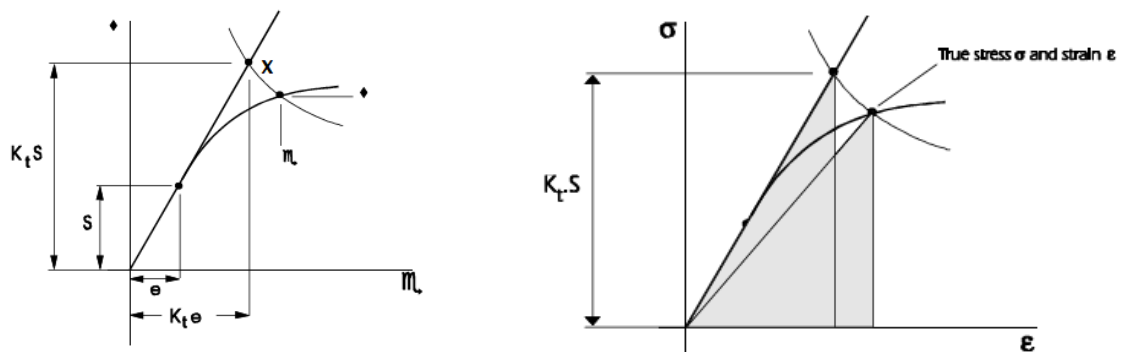

Figure 19: Neuber's rule for calculating local stress-strain

There are other methods to extrapolate nominal stresses and strains to local ones. A brief summary of some of these methods are as follows. Glinka's method is similar to Neuber's Rule, in the sense that both assume an approximately equal area under the 'infinitely elastic' and cyclic stress-strain curve. While Neuber approximates these based on selected local stresses and strains, Glinka proposes to incorporate the stress-strain curve to more accurately equalize the two areas. It is shown though, that Glinka's method often underestimates the local stresses and strains. For cases which involve the general yielding of a material, rather than only a local area, Neuber and Glinka are insufficient. In this case the Seeger-Heuler method can be used, which introduces a different stress concentration factor based on the yielding strength of the material and relates the nominal stresses to local stresses using that factor. However, it is uncommon for nominal stresses to approach the yield stress in notched components, so the Seeger-Heuler method is rarely used (Fatigue Theory Reference Manual, 2002).

When assessing the remaining fatigue life of structures using the strain-life method, only a critical component needs to be found. Because of the ability to extrapolate nominal stresses and strains it allows for this method to be more suitable for structures with complex geometries, which often experience stress concentrations that are tough to assess, as opposed to the use of the S-N curves, which are only applicable to a limited set of details.

Multiaxial fatigue

Another issue that should be considered is that most S-N curves, but also the strain-life approach proposed above, are only applicable to uniaxial loading conditions. While this may be an acceptable assumption for built-up riveted beams and columns, joints (and in particular the complex joints applied in riveted bridges) are often subjected to multiaxial loading. There is a number of methods to assess the fatigue life of joints under multiaxial loads, with a varying degree of complexity in implementation. These methods can be subdivided in five categories (You & Lee, 1996):

- Empirical formulas and modifications of the Coffin-Manson equations (Eq. 11);
- Application of stress/strain invariants;
- Use of space averages of stress or strain;
- Critical plane approaches;
- Accumulation of energy on materials.

Garud (1981) and You & Lee (1996) have performed surveys on the various methods suggested for multiaxial fatigue analysis. Garud (1981) expresses a preference for energy-based approaches, stating that many of the stress- and strain based approaches fail to adequately consider the multiaxial stress-strain response of the material, which is a crucial element of the fatigue process. Furthermore, no distinction is made between the crack initiation and the crack propagation phase. Regardless, several methods are still deemed appropriately accurate in either the low- or high-cycle fatigue domain. You & Lee (1996) do not share the same bias towards energy-based methods, as they are unable to incorporate the effect of the loading path. Additionally, the interaction between out-of-phase stress and strain components cannot be considered, although this is an issue many of the regular stress-/strain-based methods suffer from too. Many of the methods they have covered, require extensive knowledge of the materials, introduce a multitude of variables and define complicated formulas. This results in difficult implementation in practical examples.

The most common and relatively simple formulas for multiaxial fatigue assessment are the principal strain criterion and the maximum shear strain criterion. The principal strain criterion suggests fatigue cracks initiate in the plane that experiences the most extreme strain amplitude, resulting in Eq. 15. For uniaxial fatigue problems, this equation reduces to Eq. 11, as the principal strain direction

is the same as the direction under which the specimen is loaded. The principal strain criterion is primarily applied to the analysis of brittle materials. Applying it to ductile materials tends to result in unsafe life estimates.

$$\frac{\Delta\varepsilon_1}{2} = \frac{\sigma_f'}{E}\left(2N_f\right)^b + \varepsilon_f'\left(2N_f\right)^c$$

<div align="right">*Eq. 15*</div>

Rather than suggesting fatigue cracks occur most commonly in principal strain directions, the maximum shear strain criterion proposes that cracks occur in planes that undergo the largest shear strain amplitude. Using Mohr's strain circle (with $\varepsilon_1 > \varepsilon_2 > \varepsilon_3$), the maximum shear strain can be obtained using Eq. 16. The formula for the maximum shear strain criterion then becomes as in Eq. 17. Finally, by applying uniaxial material properties, C1 and C2 can be evaluated based on elastic- and plastic strain Poisson's ratios, which are approximately 0,3 and 0,5 respectively (Eq. 18). As opposed to the principal strain criterion, this method has a tendency to give conservative life estimates for ductile materials but may not give safe life estimates for brittle materials.

$$\frac{\gamma_{max}}{2} = \frac{(\varepsilon_1 - \varepsilon_3)}{2}$$

<div align="right">*Eq. 16*</div>

$$\frac{\Delta\gamma_{max}}{2} = C1\frac{\sigma_f'}{E}\left(2N_f\right)^b + C2\,\varepsilon_f'\left(2N_f\right)^c$$

<div align="right">*Eq. 17*</div>

$$\frac{\Delta\gamma_{max}}{2} = (1+v_e)\frac{\sigma_f'}{E}\left(2N_f\right)^b + (1+v_p)\varepsilon_f'\left(2N_f\right)^c = 1,3\frac{\sigma_f'}{E}\left(2N_f\right)^b + 1,5\varepsilon_f'\left(2N_f\right)^c$$

<div align="right">*Eq. 18*</div>

One of the methods that may turn out to be more universally applicable is Brown-Miller's method (Brown & Miller, 1973). Their theory, like the maximum shear strain criterion, suggests that the maximum fatigue damage occurs on the plane with the largest maximum shear strain amplitude. However, in this method the damage becomes a function of both the maximum shear strain amplitude and the strain amplitude normal to the plane on which the maximum shear strain acts. Using Mohr's strain circle, the maximum shear strain and the strain normal to this shear strain can be related to the principal strains. Though their initial research produced an expression only suitable for low-cycle fatigue and did not specify the functional relationship (Eq. 19), later adaptations can be applied to the complete fatigue life of a material. Kandil, Brown & Miller (1982) have rewritten the conventional strain-life equation from Eq. 11 to incorporate Brown-Miller's equation (Eq. 20). Constants C_1 and C_2 are taken to be 1,65 and 1,75 respectively, based on the assumption that cracks initiate from the plane on which the maximum shear strain acts. More complex variable amplitude loading may result in a different plane on which the crack initiates, which also results in slight variations in C_1 and C_2, though 1,65 and 1,75 are universally accepted. Eq. 20 is also recommended by the Fatigue Theory Reference Manual (2002) to be used for ductile materials, as it gives the most realistic life estimates for these types of materials. For brittle materials, non-conservative life estimates can still be found though.

$$(\varepsilon_1 - \varepsilon_3)/2 = f((\varepsilon_1 - \varepsilon_3)/2)$$

<div align="right">*Eq. 19*</div>

$$\frac{\Delta\gamma_{max}}{2} + \frac{\Delta\varepsilon_n}{2} = C_1\frac{\sigma_f'}{E}\left(2N_f\right)^b + C_2\varepsilon_f'\left(2N_f\right)^c$$

<div align="right">*Eq. 20*</div>

Fracture mechanics

In the case the crack initiation phase is not relevant, e.g., when fatigue cracking has already occurred in the detail, or $D \geq 1,0$, an alternative method can be applied to find the remaining fatigue life. While this crack growth analysis, based on linear elastic fracture mechanics, is not implemented into the Eurocodes, the British Standard (2015) and RBK Steel both allow for application of this method. In its essence, the fatigue crack growth method relies on the power law established by Paris and Erdogan (1963), which is used to establish a relation between the fatigue crack growth (FCG) rate da/dN and the stress intensity factor ΔK (Eq. 21). C and m are constants relating to the material properties.

$$\frac{da}{dN} = C * (\Delta K)^m \qquad \qquad \textit{Eq. 21}$$

There are three crack growth regimes (Figure 20) that can be used to describe the relation between da/dN and ΔK, plotted on a bi-logarithmic scale. The first domain is bounded by ΔK_{th}, which is the threshold value for ΔK below which no macro crack growth will occur. The upper boundary, in the third domain, is K_C, which represents the maximum value for ΔK. Exceeding K_C results in the complete failure of a specimen. The middle domain is the linear relation between the two extremes and is described by Paris and Erdogan's power law. The three regions can be denominated as the threshold region, the Paris region and the unstable tearing crack growth region (Correia, et al., 2017).
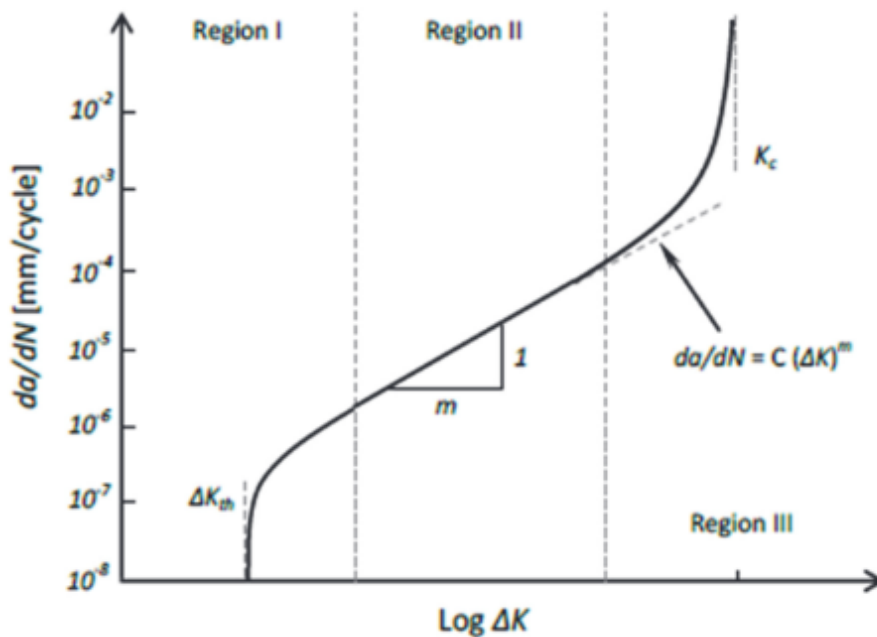
Figure 20: Crack growth regimes (Correia, et al., 2017)

In order to apply the power law, Eq. 21 needs to be integrated from a_i (initial crack size) to a_f (final crack size), resulting in the total number of cycles until failure (Eq. 22). There is a multitude of ways to find each of these parameters. Constants C and m, as mentioned, are dependent on material factors, and can be estimated through the analysis of experimental data. Additionally, recommended values for commonly used materials under standard conditions can be taken from the British Standard (2015), or from previously performed analyses of older, no longer applied materials. Such analyses on wrought iron and mild steel, which are commonly used materials in riveted structures have been performed by for example Correia et al. (2017), de Jesus et al. (2011) or Raposo et al.

(2017). The stress intensity factor can be found through the use of Eq. 23, or through the use of Finite Element modelling (see for example Chapter 2.3.2.1). Additionally, a_i and a_f can be found by implementing ΔK_{th} and K_C respectively into Eq. 23. Finally, Y is a factor dependent on the geometry of the observed detail.

$$N_f = \int_{a_i}^{a_f} \frac{1}{C * (\Delta K)^m} \, da \qquad \text{Eq. 22}$$

$$\Delta K = Y(\Delta \sigma)\sqrt{\pi a} \qquad \text{Eq. 23}$$

In the case ΔK_{th} is unknown, the initial crack size can also be found through simple observation of the specimen. There are several methods of obtaining the actual size of this crack, outlined in Annex T of the British Standard. If no crack can be observed, and a fatigue assessment through crack growth analysis needs to be performed based on a damage number exceeding 1,0, RBK Steel states that it is allowed to assume a crack of a size equal to a defect that can be reliably detected using a given inspection technique, the detection limit, as taken from Annex T of the British Standard. Several inspection techniques are available. The detection limit ranges from a crack size of 1,5 x 10 mm (effective crack depth x total crack width) for e.g., focused phased array inspection to a crack size of 3 x 15 mm for e.g., conventional ultrasonic testing.

2.2.3. Corrosion

As most other metallic structures, old, riveted bridges are subject to the onset of corrosion. As a matter of fact, one of the bigger challenges related to old steel bridges, is this onset of corrosion. Several studies have been performed to assess the effect corrosion has on rivets and riveted connections. This chapter intends to summarize the findings of these studies.

Before any conclusions on corrosion damage can be drawn, the corrosion types need to be identified. Firstly, classification based on the general appearance and form can be done. This is most commonly done through visual inspection, either by the naked eye, or using magnification tools. There are several means to classify corrosion. The following types of corrosion can be classified (Cinitha, Umesha, & Nagesh, 2014) (Landolfo, Cascini, & Portioli, 2010) (Liang, 2021):

- General (uniform) corrosion
  As the most common type of corrosion, it is also usually seen as the most serious type of corrosion of steel bridges. This type occurs when a chemical reaction affects the entire exposed surface of a metal element. The chemical reaction may be due to exposure to open atmospheres, such as air, water and soil. The resulting corrosion happens homogenously across the metal, having a thinning effect. As a result, this type of corrosion is fairly predictable, and is used as a basis for most predictive corrosion models. In general, this type of corrosion can be presented as a loss of weight or a decrease in thickness.
- Pitting corrosion
  Pitting corrosion is a localized form of corrosion, resulting in pits or holes in a small area of the affected material that penetrate inwards. The onset of pitting corrosion can be both chemical or mechanical in nature, e.g., through contact with aeriated water or an impact that results in the destruction of a possible protective layer respectively. This type of corrosion can be detrimental to metal elements, but is tough to identify and predict.
- Crevice corrosion
  Similar to pitting corrosion, this type of corrosion is a localized form of corrosion. Crevice corrosion occurs at or near the metal surface that is shielded by another material, resulting

in an inhomogeneous oxygen flow. This in turn causes a difference in ion concentration, which is the root cause of the corrosion process.

- Galvanic corrosion
Galvanic corrosion is the result of the application of two different types of metals, one of which more noble than the other. Electric contact between the two results in one of the metals acting as an anode, whereas the other acts as a cathode. The anode-metal will start to experience an increased rate of corrosion.

- Erosion corrosion
This corrosion is the result of a corrosive fluid flowing past the metal at rapid speeds. Abrasive action of the metal causes it to experience an accelerated loss of material.

- Cavitation
Turbulence in fluids cause the creation of bubbles and vacuums. These may suddenly collapse due to changes in pressure near the surface. This implosion produces small pressure waves, which impact on the (metal) surface, eroding any protective layers and causing pitting in the material.

- Stress corrosion
Specific corrosive environments may occur, which by themselves have little to no effect on a material, but once (tensile) stresses are applied, result in the brittle failure of the element. This phenomenon is known as stress corrosion.

- Fatigue corrosion
Following the same principle as stress corrosion, fatigue corrosion may occur in specific environments, failing without notice as the result of the combined effect of the corrosive environment and cyclic loading.
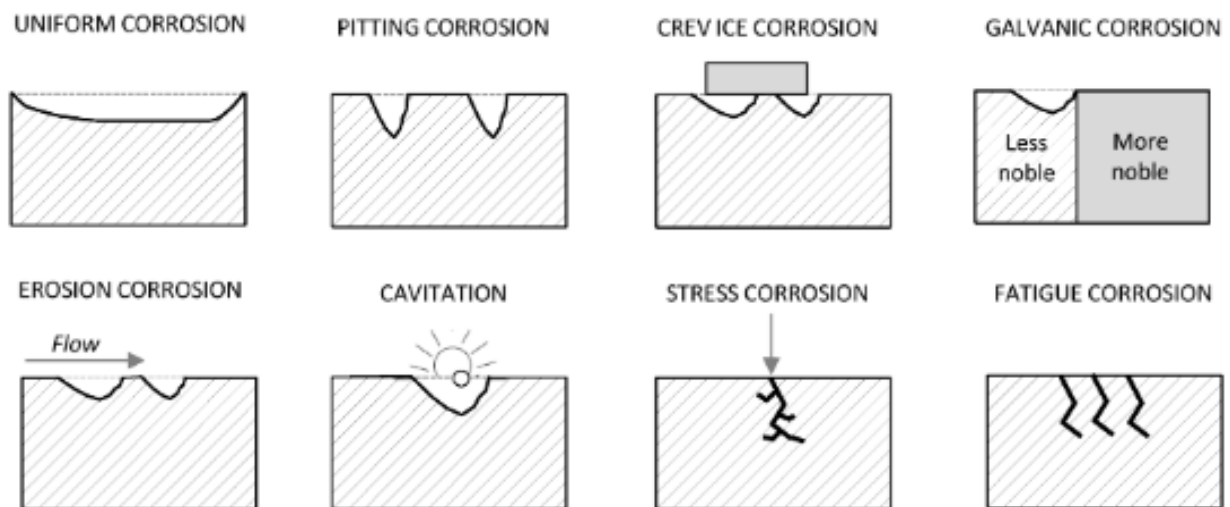
Figure 21: Different types of corrosion (Landolfo, Cascini, & Portioli, 2010)

Another method is classifying through the reaction that takes place on the surface of the metal. Examples are of such classes are chemical, mechanical or electrochemical corrosion.

Finally, degradation mechanisms can be classified based on the corrosive environment:

- Microbial and bacterial corrosion
This type of corrosion is based on the presence of micro-organisms and bacteria and around the metal surface. It usually occurs in soils or fresh- or sea water

- Gaseous corrosion

When the main corrosive agent is a dry gas, without the presence of a liquid on the metal surface, one speaks of gaseous corrosion.

- Marine corrosion

  Splash zones or the immersion of a (part of) a structure near seas and/or oceans may result in marine corrosion, where seawater is the main acting corrosive agent.

- Underground corrosion

  When materials are surrounded by soils, but the corrosive agent is not microbial or bacterial in nature, corrosion can be considered to be underground corrosion.

- Atmospheric corrosion

  Three types of atmospheric corrosion types can be deduced: dry, damp and wet corrosion. Damp and wet corrosion may occur either in- or outdoors and is the result of wet and dry cycles due to condensation or rainfall. The root cause of damp corrosion is the formation of a thin film of electrolytes on the metal surface, as a result of the adsorption of water molecules when the metal reaches a critical humidity (Roberge, 2019). Wet corrosion is a consequence of the eroding effect of flowing water. Finally, dry corrosion is the result of oxidation of the metal due to oxygen in the air, without the presence of any liquids. This type of corrosion is highly sensitive to changes in temperature, and it is usually the least severe of the three types of atmospheric corrosion.

Furthermore, it should be noted that different degrees of corrosion may be present. It is standard practice to label steel specimens as uncorroded, mildly corroded, moderately corroded or severely corroded, each of which has an increasingly negative effect on the properties on the respective element. One of the ways to measure degree of corrosion, for example for uniform degradation, is through loss of thickness. A thickness loss of less than 25% compared to the original thickness is seen as mild corrosion, whereas losses of over 50% are quantified as severe corrosion. This way of measuring is not appropriate in all cases, since not all corrosion is uniform. Sometimes it may be adequate to take an average loss of thickness, rather than actual or maximum loss of thickness along a cross-section. Even more unequal corrosion, such as pitting, can best be quantified by degree of pitting intensity. Regardless of manner of quantification, what still holds is that several studies have shown that mildly corroded elements experience very little decrease in structural properties such as ultimate yield and tensile strength, while severe corrosion can significantly reduce these properties (Nakai, Matsuhita, & Yamamoto, 2006) (Fisher, Yen, & Wang, 1991) (Cinitha, Umesha, & Nagesh, 2014) (Macho, Ryjáček, & Campos e Matos, 2019).

On top of a change in structural properties, and the resulting decrease in static strength due to these changes, as well as a general decrease in cross-section, corrosion has a significant effect on the fatigue behaviour of steel members. Several studies have shown that as the degree of corrosion increases, the fatigue life decreases, though it should be noted that this mostly holds in situations where the notch effect of corrosion exceeds the notch effects already present due to e.g., rivet holes or changes in cross-section. Additional notch effects as a result of changing cross-sections may be introduced due to ununiform corrosion though (Zhang, Li, Liang, & Akid, 2013) (Macho, Ryjáček, & Campos e Matos, 2019) (Zahrai, 2003) (Fisher, Yen, & Wang, 1991).

Most of these studies are related to steel plates or beam elements. The fatigue resistance of rivets is also affected by corrosion, since material reductions due to corrosion can lead to a decrease in the clamping force imposed by the rivet heads. Tests by Heinemeyer and Feldmann (2011) have shown that a volume loss of the rivet head of 22% due to corrosion coincides with a reduction of the prestressing stresses of 10%. Once this volume loss is exceeded, severe reductions in prestressing can be expected.

2.3.   Case studies from the literature

In this chapter several case studies are consulted and discussed. The first section of this chapter covers a study performed by Iv-Infra, involving the recalculation of the John S. Thompsonbridge on its remaining static strength. While large parts of the bridge were subject to recalculation, this case study focuses mostly on a specific joint rather than the complete bridge. The purpose of this chapter is to present some of the issues involved with the conventional recalculation of joints, how these issues are tackled, and to discuss any limitations that may remain. The recalculation is performed in accordance with the Eurocodes and RBK Steel, as well as some additional (or in some cases conflicting) specifications by Rijkswaterstaat (RWS). Furthermore, the joint discussed in this section will be further investigated in Chapter 5-8, in which Finite Element Software will be used to investigate the fatigue behaviour of this joint.

As the John S. Thompsonbridge is only assessed on its static strength, and not its fatigue strength, an additional case study is shown in Annex B, in which the recalculation of the fatigue strength of the Konninginnebridge is discussed. Since this bridge is not a riveted bridge, it is mainly included for illustrative purposes, and to identify possible differences between riveted and non-riveted joints.

The second subchapter delves into the experimental and numerical assessments of a riveted joint of two ancient metallic bridges. The purpose of these investigations is to shed light on the local behaviour of riveted connections and their static and fatigue response. De Jesus, da Silva & Correia have studied the fatigue behaviour of a riveted connection originating from an ancient bridge in Portugal ((2015), (2014)), utilizing both experimental and numerical approaches. Similarly, D'Aniello et al. (2011) have performed an experimental study on the shear behaviour of riveted connections under static loading, utilizing specimens extracted from an ancient bridge in Italy. Building upon D'Aniello, et al.'s work, Lundkvist et al. (2023) have created a modelling framework which can be used to design and predict the response of riveted connections to static loading, including different failure modes. These studies are the subject of the final part of this chapter.

2.3.1.   Static analysis of the John S. Thompsonbridge

2.3.1.1.   Background

The John S. Thompsonbridge, constructed between 1927 and 1929, sometimes referred to as Grave Bridge, is a riveted truss bridge crossing the Meuse near Grave, and is part of the N324, connecting Nijmegen to Den Bosch. It consists of nine spans, spanning a total of 515,17m. Each of the spans acts as their own independent bridge section. Furthermore, two of the spans are also part of a weir complex (Span II and III). As commissioned by RWS, all nine spans need to be reassessed in terms of static strength and stability, with an intended remaining lifespan of 30 years under normal use. This reassessment is particularly related to the main structural system, which means the main truss beams, the crossbeams and the stringers, as well as several fundamental connections. As previously mentioned, this case study will focus mainly on one such joints.
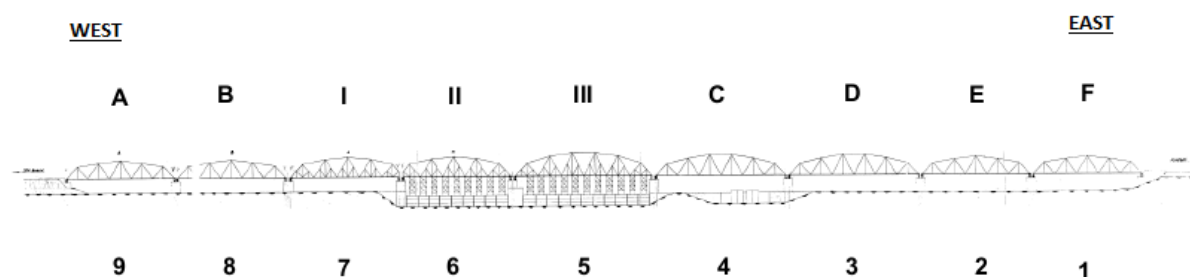

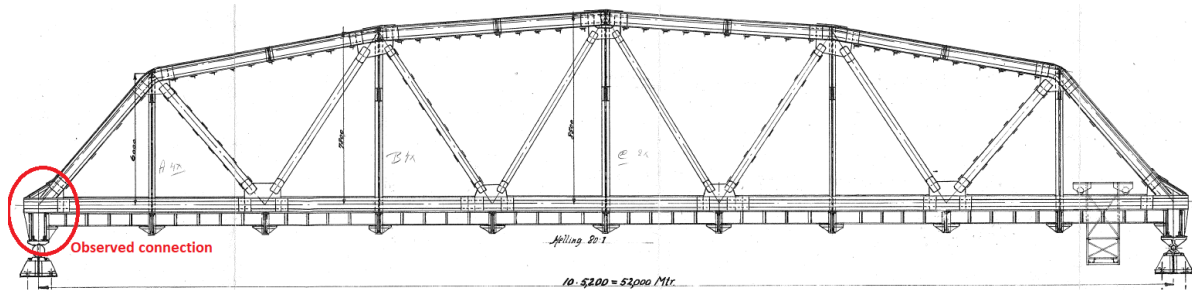*Figure 22: Numbering of spans John S. Thompsonbridge*

Figure 23: Relevant joint in span A/B/E/F.

Spans A, B, E and F are deemed to be identical for the purpose of this recalculation. The joint this case study focuses on, is located at the bottom west corner of one of the spans A, B, E or F, and forms the connection between the truss system and the support, transferring the forces on the bridge to its substructure.

Given the age of the bridges, the used materials are not representative of current day materials. Without the appropriate knowledge on the strength of the materials, a material assessment has been performed. This assessment has concluded that the steel used in the bridge is "Siemens-Martin steel" (which will from this point onward be referred to as mild steel). As per RBK Steel, this type of steel is equivalent to standard S235 steel and in calculations is assumed to have the same material properties. The same material is used for the rivets. All rivets have a diameter of 24 mm. Their grip length depends on the location and number and size of plates they bind together. It should be noted that the calculations were done using standard partial factors (γ_{M0} = 1,00, γ_{M1} = 1,00, γ_{M2} = 1,25), as opposed to the partial factors that are normally required for recalculations. This has been done in as per RWS's specifications, but no additional reasoning has been provided.

Loads have been defined using the Eurocodes. Loads that are considered are self-weight, traffic loads (LM1, LM4, crowd loads, braking- and acceleration loads and the uniformly distributed cycling- and pedestrian loads), wind loads and thermal loads. Traffic load case LM3, as well as concentrated cycling/pedestrian loads are not within the scope of this project. Similarly, impact, seismic and crane loads are not within the scope of the project. Finally, LM2 and snow loads had been considered, but have shown to result in significantly lower loads than other load combinations due to e.g., LM1 or crowd loads. As such, they are not governing and not considered in the overall calculations. The ψ-factors for each of the load cases are shown in Table 6. Permanent loads have a ψ-factor of 1,0. Both ULS and SLS have the same combinations and factors, except for the partial factors, which in SLS are all equal to 1,0.

Table 6: ψ-factors for the considered load combinations

	LM1	Horizontal loads	Pedestrian lanes	Crowd loads	Wind loads	Thermal loads
Combination 1	1,0	0,8	0,4	0,0	1,0	0,3
Combination 2	0,8	1,0	0,4	0,0	1,0	0,3
Combination 3	0,0	0,0	1,0	1,0	0,0	0,3

2.3.1.2. Bridge model

In order to verify the bridge, a model has been constructed in SCIA Engineer. Each of the beams, stringers and crossbeams have been modelled using beam elements, with appropriate cross-sections (Figure 24 and Figure 25). The built-up cross-sections present in the riveted bridge are modelled as a single a cross-section, with each of the different plates that build up the beams acting as one beam. See Figure 26 for an example.
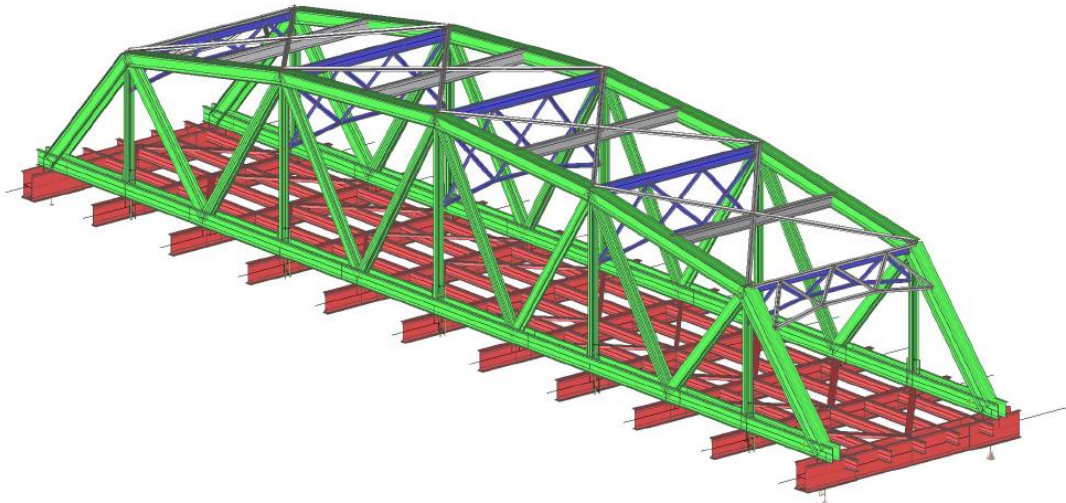
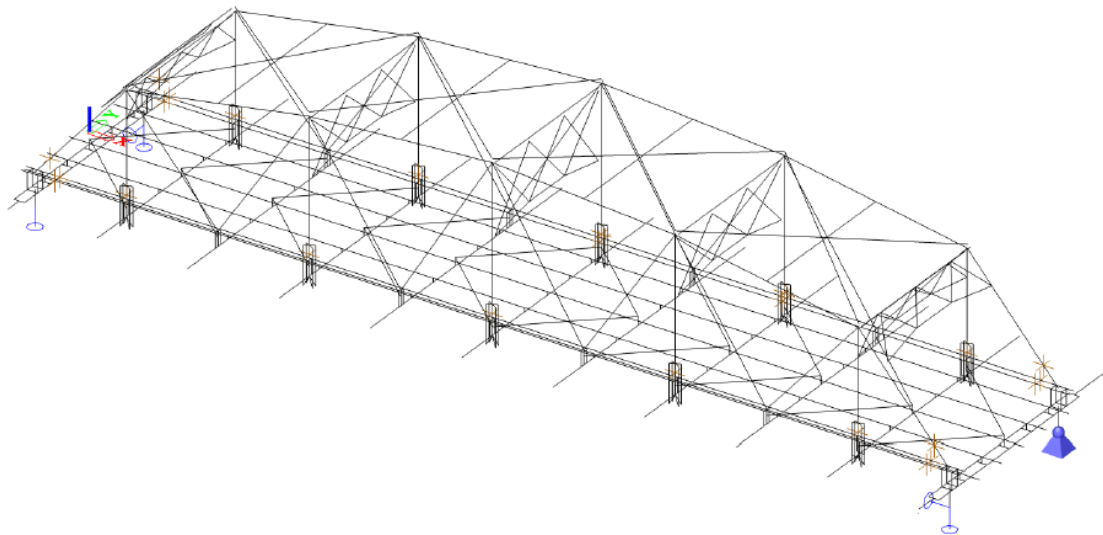*Figure 24: Model John S. Thompsonbridge as rendered in SCIA Engineer*

Figure 25: Unrendered beam model John S. Thompsonbridge

Figure 26: Example of a built-up cross-section and its properties in SCIA

Each of the corners of the bridge has four vertical supports. In longitudinal direction (x-axis), at the end of the bridge both joints are supported horizontally. In transversal direction (y-axis), two horizontal supports are applied on either end of the bridge. The result is a statically determined system in longitudinal direction, but statically indetermined in transversal direction. The result is some additional transversal forces, dependent on the joint stiffness. However, these transversal forces are not considered in the assessment of the joints. Additionally, it should be noted that, while the supports are modelled as a point support, in reality they have a width, which means the actual stress distributions may differ slightly from the modelled behaviour. Each of the joints withing the main structural system of the bridge is assumed to act rigidly.

Buckling of the beams can be assessed by SCIA. For riveted connections, buckling curve c is used. Buckling length factors are found through an iterative process, with the found values inserted into SCIA Engineer as fixed values.

Almost all beams are connected through rigid links. In situations where the centrelines of beams are connected eccentrically, rigid 'dummy' beams are used to connect them.

Using this model, the internal forces and stresses in the bridge are calculated, and the individual beams are verified based on the Eurocodes. Figure 27 shows the maximum unity check on each of the beams in the bridge.
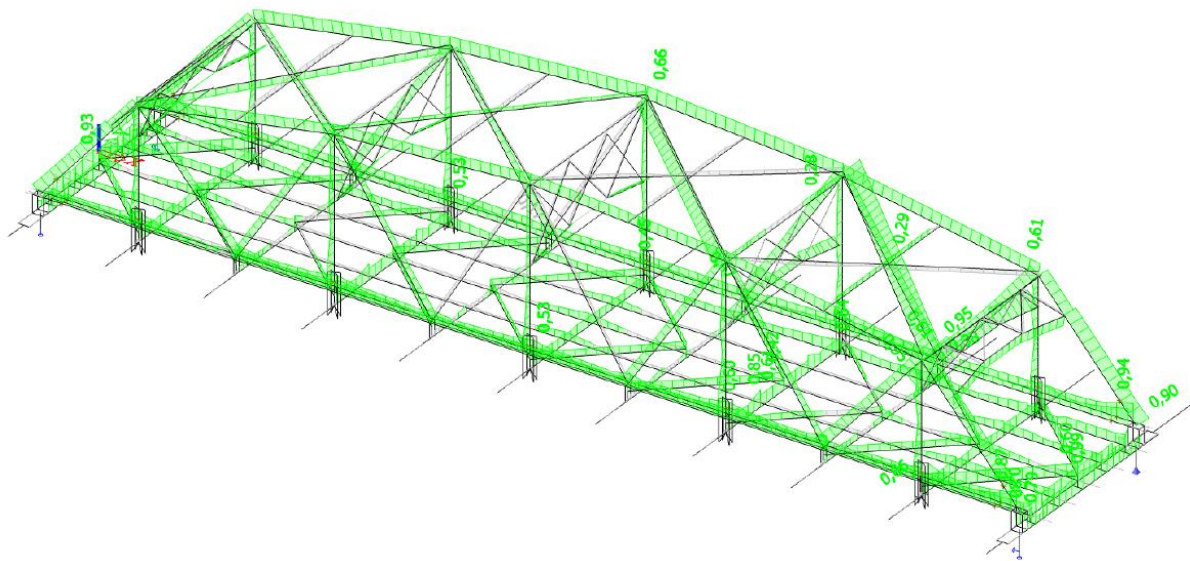
Figure 27: Unity checks on each of the beams

2.3.1.3.   Joint verification

This model is unable to calculate the detailed stresses within the joints due to their complexity (see Figure 28, Annex C and Annex D) and the assumptions made when modelling. In order to be able to assess these connections, additional hand calculations are performed.
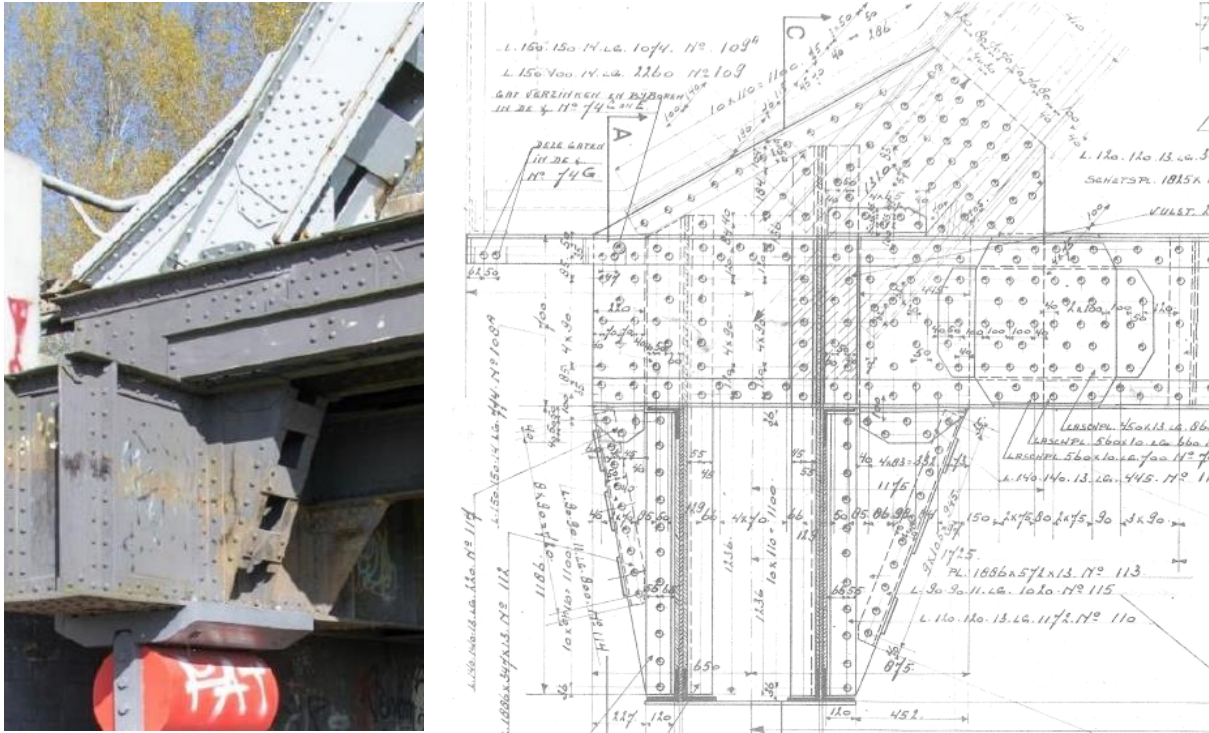
Figure 28: Example of a complex joint and its structural drawing

To find the forces acting on a joint, several cuts have been made within the beams of the bridge model, near the location of the joints. In Figure 25 these locations are represented by small, brown marks. By isolating the joint and comparing the strength of the individual elements at this cut to the strength and resulting unity check at the same location within the model, a verification of the joint can be performed. Alternatively, by applying the (internal) forces on the beams at the location of the cuts, as taken from the model, and applying them manually to the isolated joint, the resistance of the joint can be assessed directly, in the case no comparable value of the unity check in the model is available as a result of the assumptions made to construct it. By assuming several cuts within the joint, several subsections of the joint can be assessed. However, one can easily realize that, because the actual force distribution within the joint is unknown, the maximum stresses that occur in the joint may not occur precisely on the assumed cuts. Therefore, there is no one hundred percent guarantee that the joint will not fail. In Iv-Infra's report, it is deemed that enough situations are considered that the verification is sufficient to draw conclusions from.

The original report checks each of the four joints illustrated in Figure 29, but for the purpose of this thesis, only the verification of joint K1 is reviewed. Calculations are performed based on the Eurocodes (or chapter 2.2.1).

Figure 29: Assessed joints

Four different cuts are considered for the evaluation of K1. Cut I-I is a vertical cut located at the end of the main longitudinal beam of the bridge, where the webs of the beam merge into gusset plates, which can be considered to be the main part of the joint. The L-plates that form the flanges along the main longitudinal beam remain uninterrupted. Cut II-II is a horizontal cut, cutting across the gusset plate, parallel to the main longitudinal beam. It is situated right above the top of the main longitudinal beam and is used to determine the resistance of the gusset plate to any loads introduced by t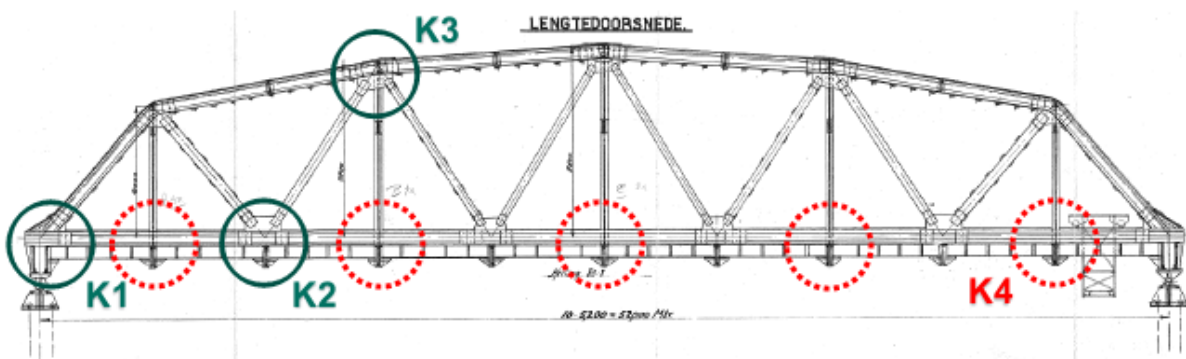he diagonal beam. The third cut, cut III-III, is similar to the first, though it is located at the point where the webs of the diagonal beam merge into the gusset plate. Again, the flanges (both on the in- and outside of the beam) remain uninterrupted. In addition to the axial forces introduced by the diagonal, this cut is

Figure 30: Considered cuts for structural assessment of the joint

also used to assert the kinked plate and the kinked flange at the top of the diagonal, which connect the diagonal to the gusset plate as well. Cut IV-IV is situated at the very bottom of the joint, at the location where the joint is connected to the supports and assess the capacity of the joint based on the support forces. Finally, cut V-V also relates the capacity of the joint to the load distribution resulting from the support forces. It assumes the bottom section of the joint to be representable by a portal consisting of tensile and compressive beams and transfers the support forces through them to the bottom of the main longitudinal beam.

Cut I-I

Several structural components along cut I-I can be identified, namely the L-plates that function as flanges of the main beam, the web of the main longitudinal beam and an internal and external cover plate. Additionally, there is a filler plate present that covers the gap between the external cover plate and the web of the beam. However, this filler plate is not considered to contribute to the resistance of the joint. Within SCIA Engineer, the presence of rivets has not been considered, meaning only the resistance of the gross cross-section of the beam is used to verify the overall resistance at the location of the cut. This means that the net cross-section of the L-plates and beam web need to be verified manually. Additionally, the rivet strength and the capacity of the cover plates need to be considered. Capacity of cover plates is combined into one calculation, as they work in parallel. They have approximately the same dimensions.
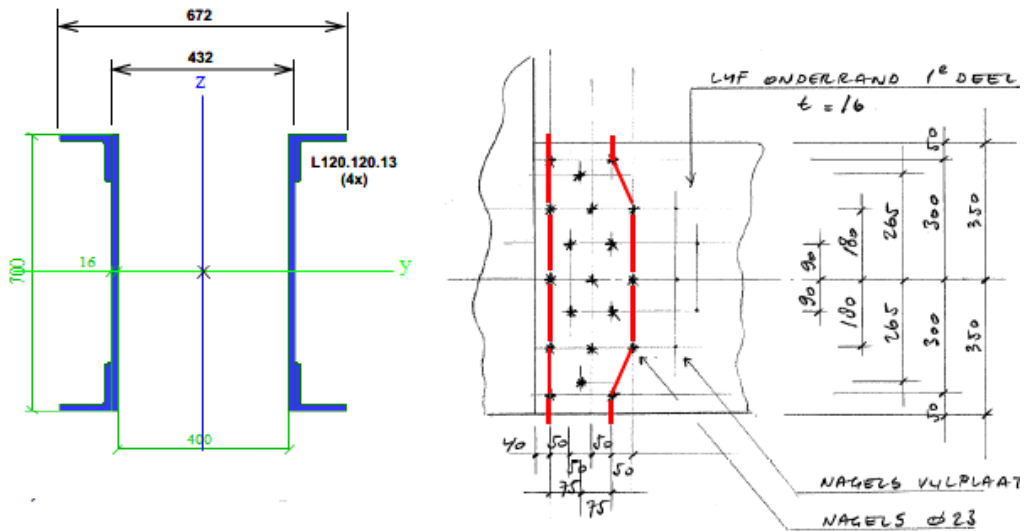
Figure 31: Considered cross-section longitudinal beam at cut I-I, with net cross-section marked in red

Table 7: Capacity of the beam at cut I-I

	L-plates	Rivets	Beam web	Cover plates	Rivets
Gross cross-sectional capacity	698 kN	-	2632 kN	3102 kN	-
Net cross-sectional capacity	689 kN	-	2405 kN	2799 kN	-
Shear capacity	-	1503 kN	-	-	3237 kN
Bearing capacity	-	2717 kN	-	-	2888 kN
Increase in U.C.	1,01	-	1,09	-	-

As can be seen in Table 7, the net cross-sectional capacity of the beam web is governing over the capacity of the cover plate and the rivets. The result is an increase of 1,09 in unity check compared to the value calculated by SCIA. This increase in unity check is governing over the increase in unity check at the L-plates, where the net cross-sectional capacity is governing over the rivets, and the unity check is only increased by a factor of 1,01. The final unity check becomes $1,09 * 0,67 = 0,73$, where 0,67 is the original unity check calculated by SCIA (Figure 32). This means the capacity of the joint at cut I-I is sufficient.
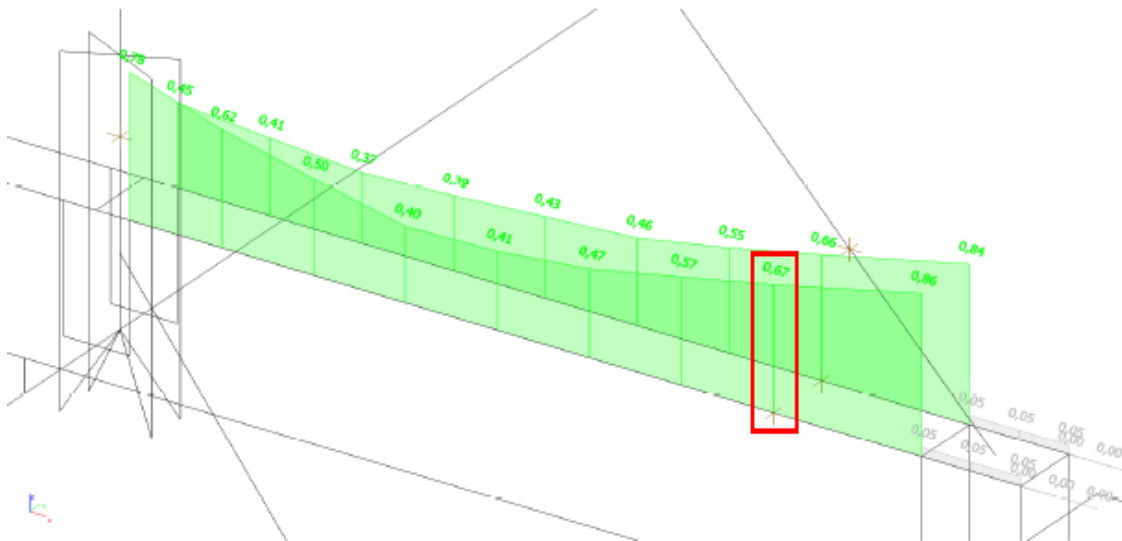
Figure 32: Unity checks longitudinal beam as calculated by SCIA Engineer

Cut II-II

Because the gusset plate is not modelled within SCIA, comparing unity checks of manual and computed calculations, the method used to assess cut I-I, is not applicable to this situation. Instead, the capacity of the gusset plate along this cut is calculated and verified based on the governing loads introduced by the diagonal beam. The minimal and maximal forces acting on the plate can be taken directly from SCIA (Table 8), by finding the maximal and minimal internal forces in the diagonal. In the calculation V_y, V_z and M_x are neglected, because their influence on the capacity is negligible. Normal forces in the gusset plate are calculated using both the acting normal force, and the normal force resulting from the eccentricity between the location to which M_z is applied and the location of the gusset plate. Additionally, the forces have been adjusted to account for the fact that the the diagonal beam is not situated parallel to cut II-II.

Figure 33: Cross-section diagonal beam

Table 8: Internal forces diagonal beam

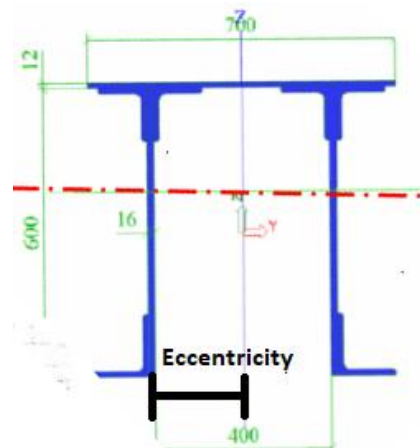| Staaf	css	dx [mm]	BG	N [kN]	Vy [kN]	Vz [kN]	Mx [kNm]	My [kNm]	Mz [kNm]
B50	CS2 - 0-A - Bovenrand 1e deel	7939,8	N1042/23	**-3985,99**	21,45	-1,54	-1,89	80,22	64,57
B21	CS2 - 0-A - Bovenrand 1e deel	0,0	N2037/49	**-1601,64**	5,60	17,00	3,93	-50,86	-41,27
B21	CS2 - 0-A - Bovenrand 1e deel	7939,8	Z1031/73	-2513,40	**-94,01**	-51,19	2,57	-267,83	**-481,67**
B50	CS2 - 0-A - Bovenrand 1e deel	7939,8	N1031/15	-3121,75	**83,17**	-68,94	-2,71	-383,36	**423,61**
B50	CS2 - 0-A - Bovenrand 1e deel	7939,8	N2031/43	-2953,73	74,61	**-72,68**	-2,48	**-408,97**	374,59
B21	CS2 - 0-A - Bovenrand 1e deel	0,0	N2042/51	-2313,15	15,32	**97,50**	4,34	-156,23	-63,41
B21	CS2 - 0-A - Bovenrand 1e deel	0,0	Z1031/73	-2463,43	-44,69	-25,92	**-5,42**	38,80	132,32
B50	CS2 - 0-A - Bovenrand 1e deel	0,0	N1031/15	-3069,54	33,85	-42,18	**6,14**	57,01	-111,77
B21	CS2 - 0-A - Bovenrand 1e deel	7939,8	N2042/51	-2335,56	51,94	64,67	-1,59	**483,23**	245,59

The unity checks resulting from both the semi-enveloping and the enveloping forces are shown in Table 9. The semi-enveloping verification functions as a lower limit of the unity check, whereas the enveloping verification is an upper limit. Both situations result in unity checks lower than 1,0, so the capacity at cut II-II is sufficient.

Table 9: Forces and unity checks along cut II-II

N [kN]	M_Y [kNm]	M_Z [kNm]	N_{plate} [kN]	$M_{y,plate}$ [kNm]	N_{II-II} [kN]	$M_{y,II-II}$ [kNm]	V_{II-II} [kN]	$\sigma_{n,Ed}$ [MPa]	$\sigma_{b,Ed}$ [MPa]	τ_{Ed} [MPa]	$\sigma_{c,Ed}$ [MPa]	UC
Semi-enveloping verification												
3986	80	65	2149	40	1624	40	1408	58	5	50	107	0,48
1602	51	41	900	26	680	26	589	24	3	21	46	0,19
2513	268	**482**	2415	134	1825	134	1582	65	16	56	127	0,54
3122	383	**424**	2580	192	1950	192	1690	70	23	60	140	0,60
2954	**409**	375	2378	205	1797	205	1558	64	25	56	131	0,56
2313	156	63	1308	78	988	78	657	35	10	31	69	0,30
2463	39	132	1549	20	1170	20	1014	42	2	36	77	0,33
3070	58	112	1804	29	1363	29	1182	49	4	42	90	0,38
2336	**483**	246	1759	242	1330	242	1152	47	30	41	105	0,45
Enveloping verification												
3986	483	482	3152	252	2382	242	2064	85	30	74	172	0,73

Cut III-III

Cut III-III can be assessed using the same principle as cut I-I. Gross cross-section is shown in Figure 33. Similar to the longitudinal beam, there are internal and external cover plates present, as well as an external filler plate. In addition to the outer L-plates at the top and bottom, there are internal L-plates present as well at the top. All L-plates continue beyond the cut. The inner L-plate is kinked and continues along the gusset plate and parallel to the kinked cover plate at the top of the diagonal beam. The lower and upper L-plates have different dimensions, and therefore are assessed separately. Furthermore, in addition to the beam itself, the kinked plate and kinked

Figure 34: Distinction between L-plates, cover plates and filler plates. Internal cover plate is marked in purple, filler plate in yellow, external cover plate in green and L-plates in blue

internal L-plate at the top of the diagonal have a function to transfer forces from the beam to the joint, and thus needs to be considered as well. Within the table, the upper, internal L-plate and the kinked cover plate are combined into one verification.

Table 10: Capacity of the beam at cut III-III

	Lower L-plates	Rivets	Upper external L-plates	Rivets	Beam web	Cover plates	Rivets	Upper internal L-plates and kinked cover plate	Rivets
Gross capacity [kN]	705	-	590	-	2256	2421	-	3154	-
Net capacity [kN]	703	-	576	-	1991	2060	-	2881	-
Shear capacity [kN]	-	685	-	801	-	-	3792	-	3166
Bearing capacity [kN]	-	912	-	760	-	-	3021	-	3020
Increase in U.C. [-]	1,03	-	1,02	-	1,13	-	-	1,09	-

Given the unity checks in Figure 35, one can find that the unity check of the diagonal at the location of cut III-III becomes $1,13 * 0,75 = 0,85$, with the net cross-sectional capacity of the web of the diagonal being the governing element.
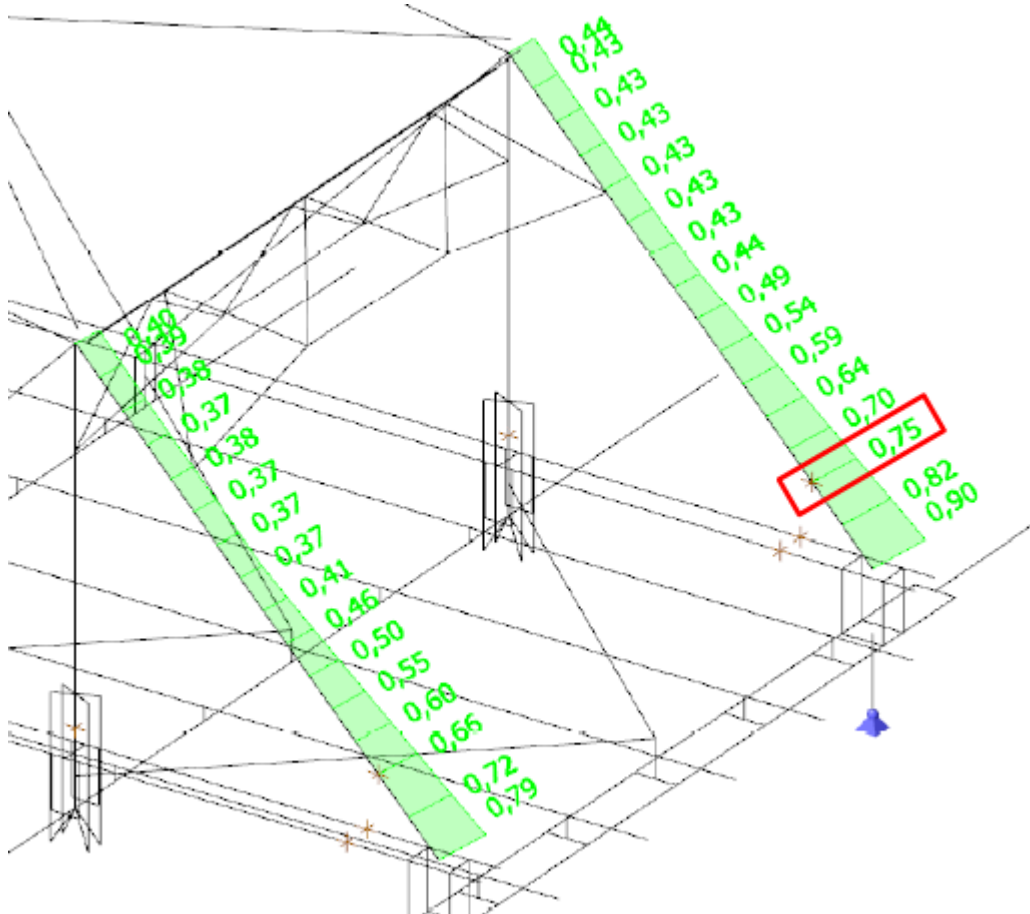
Figure 35: Unity checks diagonal as calculated by SCIA Engineer

The end diagonal is part of the main structural system of the bridge and therefore needs to abide by certain stability constraints. An additional analysis shows that the stability system acts as a sway frame, for which a 1st order analysis will suffice. The additional safety factor resulting from this analysis is 1,06. The final unity check then becomes $1,06 * 0,85 = 0,90$, which is still sufficient.

Cut IV-IV

The assessment of the joint in cut IV-IV is made based on the forces in the support as found in SCIA. Because the precise distribution of forces through the two webs is unknown, the effective area is taken as the area of all relevant elements the cut goes through. This includes:

1) Web 1 and 2;
2) Effective area of the combined filler plates and flanges of the L-plates on the outside of the webs;
3) Effective area of the combined filler plates and flanges of the L-plates on the inside of the webs;
4) Eight L-plates on the outside of the webs;
5) Four L-plates on the inside of the webs;
6) Four plates perpendicular to webs 1 and 2.

Dividing the total effective area of these elements by two results in the effective area of each of the two webs, with which the capacity can be calculated.
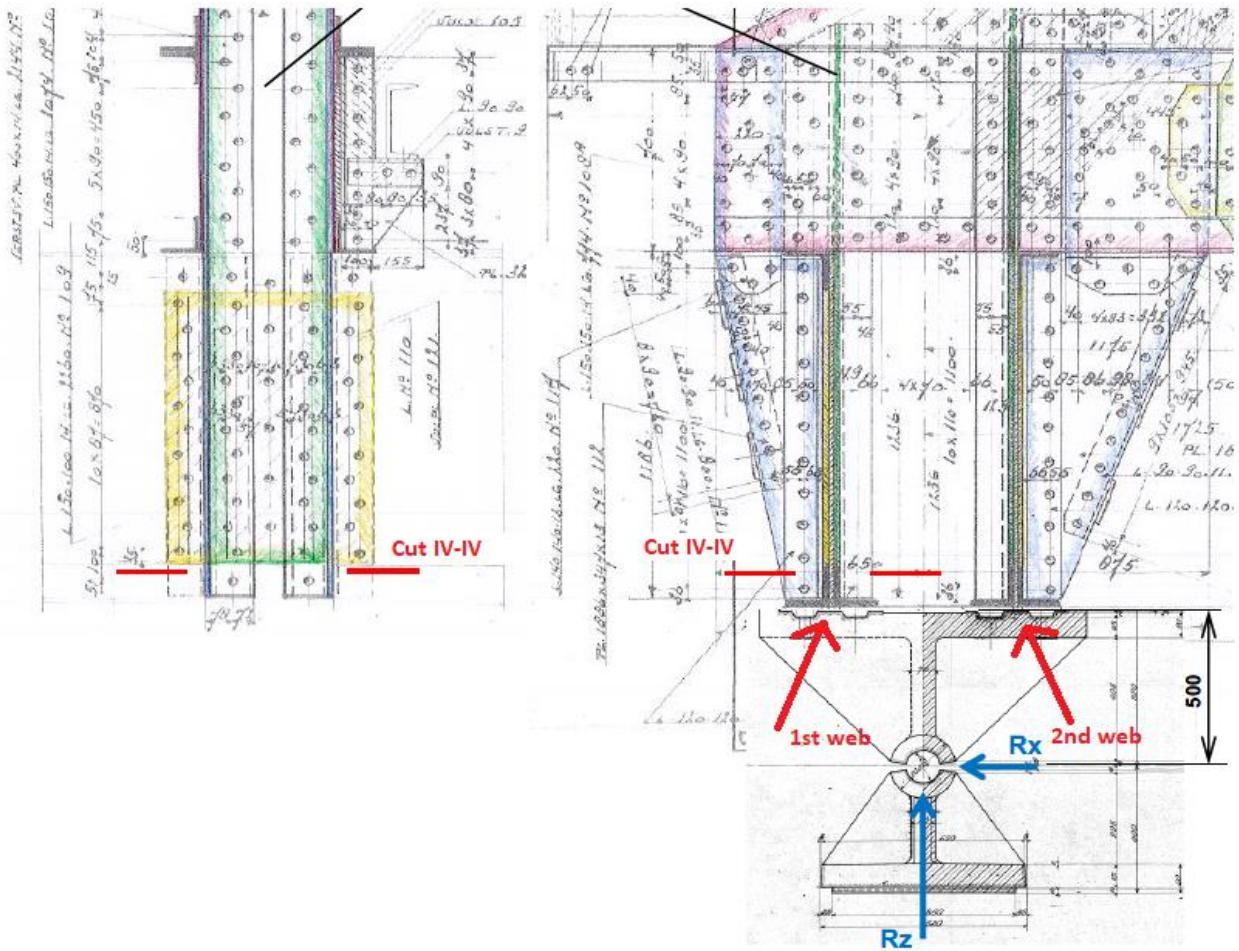
Figure 36: Cut IV-IV and its relevant webs

Support forces act as displayed in Figure 36, which in turn act on the effective areas of web 1 and web 2. The corresponding support forces are displayed in Table 11. Despite the fact that there is a small opening between the L-plates and the support, in cooperation with RWS it has been assumed that these elements do contribute to the transfer of forces, given the small size of the gap. Had this not been the case, the cross-section at cut IV-IV would not be close to being sufficient. Additionally, the flanges of the L-plates from 4) and 5) parallel to webs 1 and 2 are not considered, as they already contribute to the effective area of 2) and 3).

Table 11: Minimum and maximum support forces

Steunpunt	BG	Rx [kN]	Ry [kN]	Rz [kN]
SPT1/N372	N2031/5	**-774,15**	-329,45	3470,68
SPT3/N370	N2041/7	**755,33**	0,00	1754,57
SPT1/N372	N2041/7	45,23	**-347,05**	3439,56
SPT1/N372	Z2043/8	560,05	**333,68**	1873,79
SPT3/N370	N2047/9	726,70	0,00	**1337,26**
SPT1/N372	N1031/4	-727,77	-335,81	**3729,23**

Figure 37: Support force distribution on the joint

It should be noted that R_x can be both positive and negative, meaning the resulting forces $F_{v,Ed,L}$ and $F_{v,Ed,R}$ acting on the webs may be swapped. The governing normal force acting on one of the webs,

accounting for the eccentricity of R_x, becomes 2568 kN. With a capacity of $N_{Rd,web}$ = 6856 kN per web, the unity check becomes 0,37. Therefore, the joint is sufficient at cut IV-IV as well.

Cut V-V

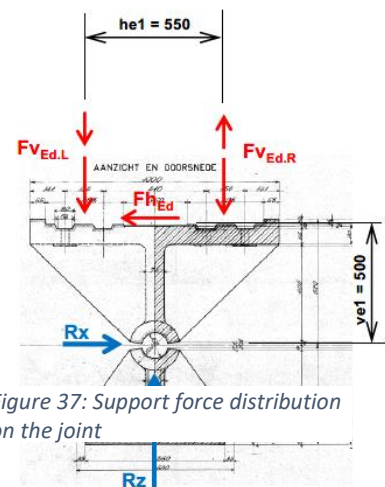For cut V-V, the distribution of forces through the joint is investigated. Using a very basic schematic, based on a portal created by tensile- and compressive beams, this distribution is approached. In accordance with RWS, an additional model was constructed in SCIA Engineer, to assess whether this force distribution appears to be appropriate.
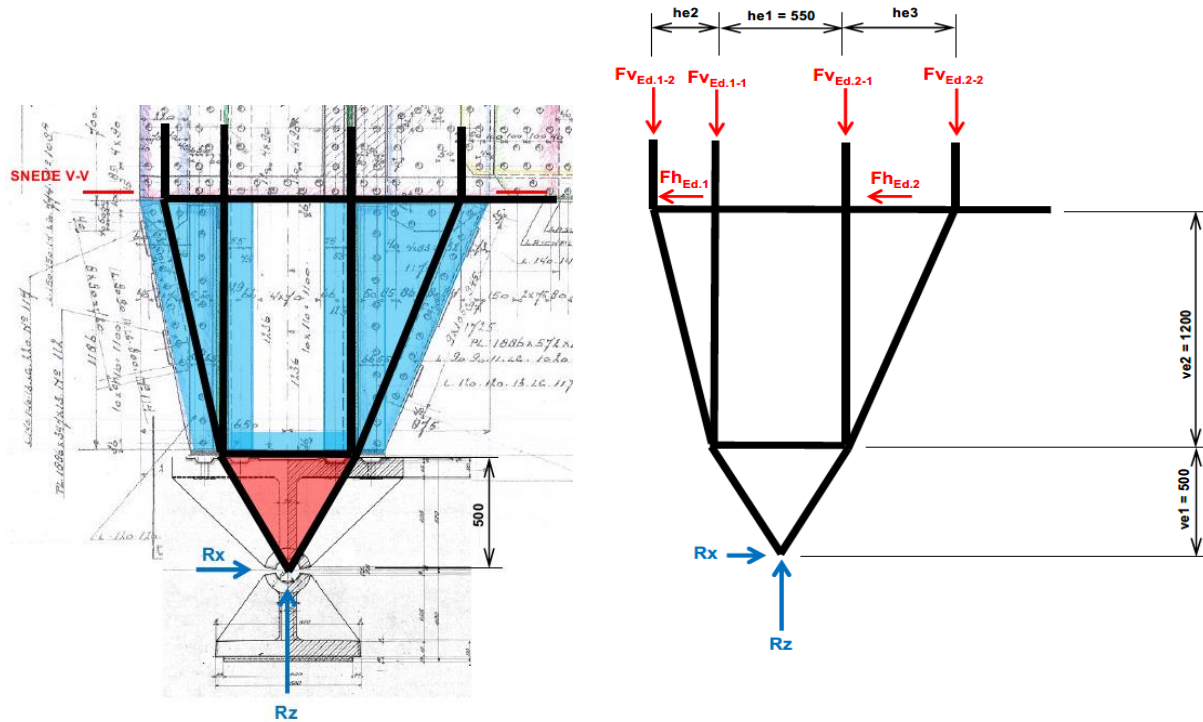
Figure 38: Schematic representation of bottom section joint

Using the support forces taken from Table 11 and the known dimensions of the joint, the values for h_{e2} and h_{e3} can be found. Subsequently, each of the internal forces defined in Figure 38 can be determined. The largest vertical force can be found in $F_{V,Ed,2-1}$ when R_x is negative, resulting in $F_{V,Ed,2-1}$ = 2662 kN. The largest horizontal force will be in $F_{h,Ed,2}$ (587 kN), and can be either positive or negative, matching the sign of R_x. $F_{V,Ed,1-1}$ and $F_{V,Ed,2-1}$ are taken up entirely by the built-up connecting beams in the middle, which consist of the internal filler plates (shown in green in Figure 36) and internal L-plates. $F_{V,Ed,1-2}$ and $F_{V,Ed,2-2}$ are taken up by the triangular sections. These triangular sections extend slightly in the vertical direction, where they are connected to the gusset plate, to which the forces are transferred through rivets. Horizontal forces $F_{h,Ed,1}$ and $F_{h,Ed,2}$ are transferred through small L-plates connected to the uninterrupted L-plates mentioned at cut I-I. The unity checks for each of these sections are displayed in Table 12. It shows that the rough assumptions made to calculate the joint manually result in an insufficiently strong joint.

Table 12: Capacity of the joint at cut V-V, manual simplification

	$F_{V,x-1}$ through built-up connecting beam	Rivets	$F_{V,x-2}$ through triangular sections	Rivets	F_H through L-plates	Rivets
Gross capacity [kN]	2876	-	1601	-	-	-
Net capacity [kN]	2650	-	1442	-	-	-
Shear capacity [kN]	-	2888	-	2769	-	911
Bearing capacity [kN]	-	4522	-	3952	-	1235
Increase in U.C. [-]	1,09	-	1,11	-	-	-
Maximum F_{Ed} [kN]	2662	-	1501	-	587	-
Actual U.C.	1,00	-	1,04	-	0,64	-

In order to further assess this cut, a simple model has been made in SCIA, to attempt to more accurately define the acting forces. The triangular section at the bottom consists of very stiff dummy beams, and simulates the support of the bridge. The beams at the top of the model are also very stiff dummy beams, used to assess the assess the forces at the location the bottom of the joint is connected to the gusset plate. Supports are chosen such that the forces are directly available and the distances between them match up with h_{e1}, h_{e2} and h_{e3} as defined in Figure 38. Using the maximum forces on the support at the bottom (taken from Table 11), the resulting forces and stresses at the 'supports' at the top and internal stresses are calculated. Results are shown in Figure 39 and Figure 40. Finally, the unity checks relating to the SCIA model are found in Table 13.
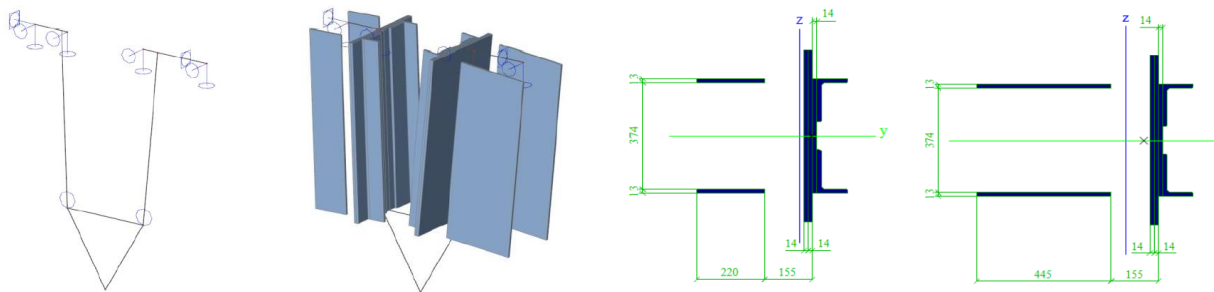

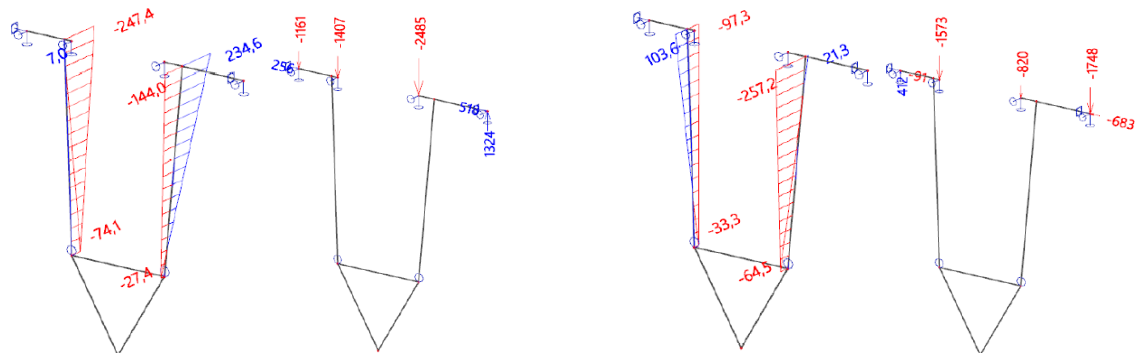Figure 41: SCIA model to assess force distribution cut V-V, including assumed cross-sections

Figure 39: Normal stresses and reaction force for negative R_x

Figure 40: Normal stresses and reaction forces for positive R_x

Table 13: Capacity of the joint at cut V-V, SCIA simplification

	Stress in plates from SCIA [MPa]	$F_{V,x-1}$ through built-up connecting beam [kN]	$F_{V,x-2}$ through triangular sections [kN]	F_H through L-plates [kN]
Governing capacity	235	2650	1442	911
Maximum calculated force	257,2	2485	1748	683
U.C.	1,09	0,94	1,21	0,75

While the results from the manual assessment and the modelled assessment of cut V-V vary slightly, the results are similar enough that it can be assumed they represent an acceptable indication of the actual force distribution within the joint. There are various assumptions that can be done to influence the result. Should the beams that represent the triangular portal be modelled vertically rather than under a slight angle, different values would be found. Similarly, different assumptions on which cross-sections do and which do not contribute to the resistance of the joint significantly affect their capacity. Additionally, adjusting the distance h_{e3} to the centre of the group of rivets will positively influence the forces on the right triangular section, but negatively influence the left triangular section. The overall result remains the same though, in which the joint is not sufficiently strong.

Some additional consideration that may be of note:

- Part of the force R_x may be neglected, as they are additionally applied forces resulting from the static indeterminacy of the system;
- Applying the spring stiffness of the joint to the complete bridge model will affect the force distribution throughout the bridge;
- The out-of-plane force R_y is not considered;
- Additional transversal forces coming from the main truss system are not considered;
- The friction and rolling resistance of the rolling support are not considered.

2.3.1.4.   Limitations

The issues that follow from the method described in this chapter can be divided in three main categories. Some of the factors involved in two of these categories have already been discussed. The categories are:

1) Unknown force/stress distribution;
2) Unknown capacity contribution within joint;
3) Non-universality.

Both category 1 and category 2 result in the fact that the precise distribution of forces throughout a joint is unknown. Therefore, the location of governing stresses is unknown as well. The issue with this is demonstrated by the methods adopted for these joint. Had only cut I-I through IV-IV been adopted, the joint would be considered safe, with no structural adaptations necessary. Only when cut V-V was assessed, the joint turned out to be unsafe. General knowledge on the behaviour of stresses and joints may be able to off-set this issue slightly, allowing for the constructor to assess possible critical locations, but unfortunately there is no guarantee all critical locations are being considered.

Unknown force and stress distribution in its basis stems from the fact that SCIA Engineer has been used to model the bridge. SCIA is not inherently designed for the design and calculation of joints.

While this is not necessarily a major issue, as other software packages are available to model joints. However, the precise properties of a joint do affect the distribution of forces throughout the system as a whole, and in its current state, only generic assumptions have been made on the stiffness behaviour of the joints (they are assumed to be rigid), without the required information to back these claims up. That does not mean it is a poor assumption, just an unproven one. Furthermore, within the bridge model, the supports are not modelled correctly when compared to the real situation. Rolling supports have a width, as well as a rolling and frictional resistance, all of which affect its stress distribution, but are not considered. Additionally, many of the forces acting on the joint are unknown or unspecified. Transversal forces originating from the main structural system are not considered, and the static indeterminacy of the bridge result in additional forces applied to bridge, while in reality these may not need to be considered.

Unknown contribution to capacity lies within the complexity of the joint itself. Riveted bridges are naturally complex, with many different elements under many different stress distributions, and therefore, many different elements have many different contributions to the overall strength capacity of the joint. It will always be tough to define the which elements contribute to which degree of loading. In order to simplify the definition, several assumptions have been made to assess the joint. Assuming an effective width that contributes to the resistance of specific loads allows for the (manual) calculation of the joint resistance, but may not be entirely accurate. Additionally, filler plates are generally considered to not have an effect on the load capacity, but it seems unlikely they have no effect whatsoever. As a matter of fact, as mentioned in Chapter 2.2.1, the presence of filler plates may have a negative effect on the overall capacity of the joint. Finally, simplifying a (section of a) joint may allow for easier calculation, but does not guarantee an accurate distribution, as illustrated by the fact that even small adjustments of the model may result in different stress distributions.

Finally, non-universality is an issue. It does not directly affect the calculation of the joint, but it does pose a threat to the verifiability of the adopted methods. The methods used for assessing this joint are incredibly specific, and cannot easily be adapted to and compared with other (types of) joints. Even within the joint, several assessment methods were used. It is impossible to know if, had the same methods been available for the different cuts, the result would match up. Therefore, a more widely applicable and verified approach would be preferable.

On a final note, this report did not assess the remaining fatigue strength of the joint, for the simple reason that there is no general method that can accurately predict the strength for such complex issues, as well as a lack of knowledge on the (effect of) relevant traffic data.

2.3.2. Local behaviour of riveted joints

2.3.2.1. Local behaviour with De Jesus et al.

De Jesus, et al. (2015) and (2014) have investigated the fatigue of riveted and bolted joints originating from the Fão bridge, an ancient riveted bridge in Portugal. The first study takes an experimental approach, performing material tests on the model, with as aim to identify material properties of the joint material, as well as their fatigue behaviour and crack propagation data. The second study takes the data gathered in the experimental study and applies it to a numerical model in ANSYS, utilizing its capabilities to get detailed information on the stress- and strain distribution within a joint. Furthermore, it compares the standard S-N curve used for riveted joints (Eurocode 3, detail category 71) to the S-N curves derived both from the experimental set-up and the numerical models, for different degrees of clamping stress. The studies have found that the numerical models are able to generate an S-N curve very similar to the one found in experiments (Figure 42). The slope

of the curve proposed in Eurocode 3 (m = 3) does not accurately represent the experimental data, where a slope with m = 5 appears to be more suitable. However, it should be noted that a limited number of experimental data points was available, reducing the confidence in this statement.
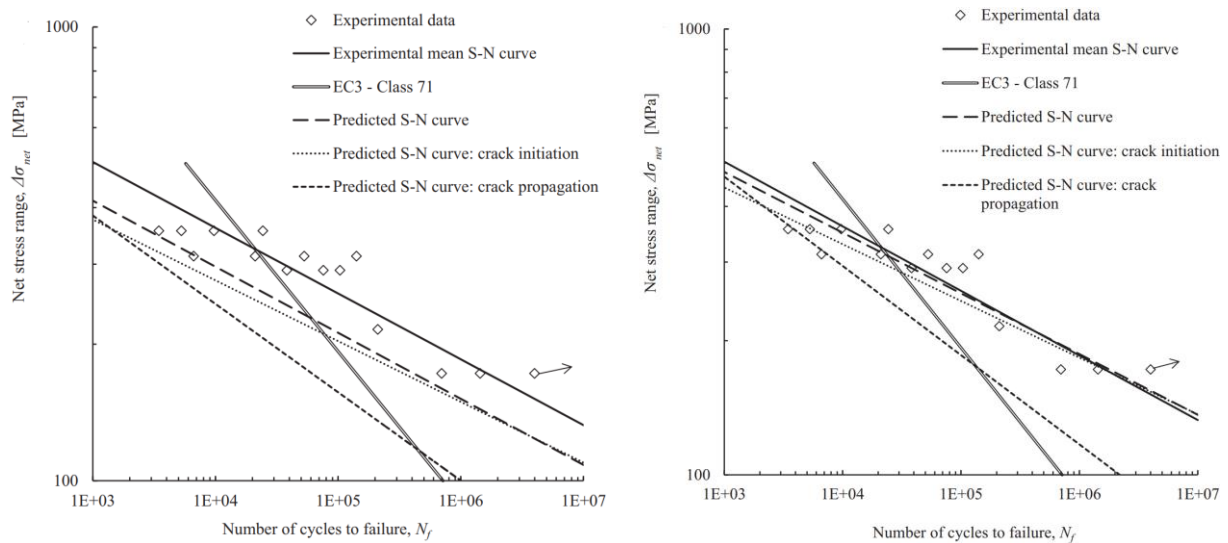
Figure 42: Standard, experimental and numerical S-N curves for riveted joints under 0,63 MPa (left) and 22,78 MPa (right) clamping stress (de Jesus, da Silva, & Correia, 2014)

Model specifications

De Jesus, et al. (2014) have constructed their model using ANSYS, following its design guidelines and utilizing its Parametric Design Language.

The material properties used are derived directly from the experimental study De Jesus et al. have performed: the Young's modulus is found to be 198,70 GPa, and the material has a Poisson's ratio of 0.26. The density of the material was not specified in De Jesus' work. The geometry of the model is similarly taken directly from the experimental study and is displayed in Figure 43. In order to reduce the calculation time of the model, De Jesus et al. have utilized the three planes of symmetry present in the specimen. Finally, contrary to bolts, the rivets have been modelled to completely fill up the rivet hole, using a solid, cylindrical part, leaving no clearance.

Figure 43: Experimental set-up of the reference model

The model utilizes two types of load definitions. The first definition accounts for the clamping stresses imposed on the plates by the rivets. Similar to real world situations, these clamping stresses are applied through the assumed axial shrinkage of the rivet shank as a result of a decrease in te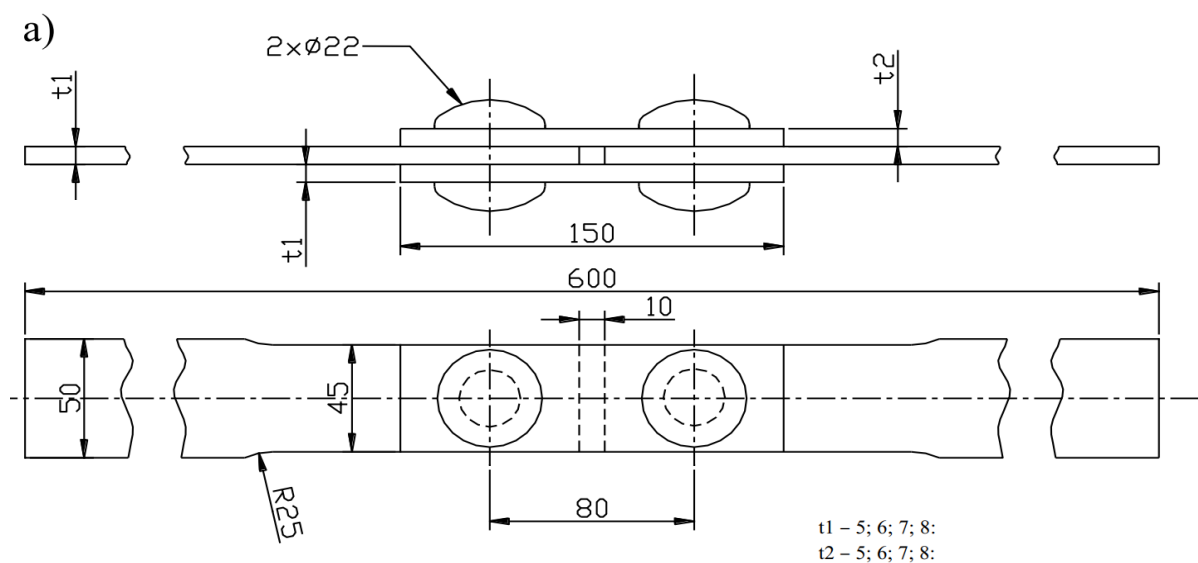mperature. The thermal expansion coefficient in axial direction is taken to be $\alpha_x = 10^{-5}$ °C^{-1}. The transverse directions are assumed to have null expansion coefficients. While this method is comparable to the real riveting process, it has been chosen primarily for convenience, as for explicit models it is often the simplest method of application. The second load definition is the applied load, for which a uniform displacement of 0,1 mm at the end of the specimen has been taken.

Contact is modelled using the Augmented Lagrange algorithm provided by ANSYS. This method requires the definition of the normal contact stiffness, which in turn is responsible for the degree to which a contact and target surfaces can penetrate. The relationship between contact and target surface is established through an imaginary elastic spring between the two surfaces. Within this spring, the contact force is a product of the contact stiffness (κ) and the penetration (δ). This contact force is responsible for "pulling back" the contact surface such that the penetration reaches an acceptable level. The contact stiffness is dependent on the relative stiffness of the two bodies, and can be scaled through the normal penalty stiffness factor (FKN factor). The acceptable level of penetration, or tolerance, is the product of the mesh size (which is responsible for the thickness of the respective element) and the normal tolerance penetration factor (FTOLN). As long as ANSYS identifies penetrations above the penetration tolerance, the model is considered to be unconverged. De Jesus et al. have modelled several situations, with varying FKN and FTOLN factors, though for the purpose of this report, only a factor of 1,0 and 0,1 for the FKN- and FTOLN-factors respectively are considered.

De Jesus et al. have made no specifications on the mesh size, though a picture is provided. This picture is displayed in Figure 44. As specified, this displays only 1/8th of the experimental model. Nodes at a symmetry plane have been restrained to have null displacement along the normal direction of those planes. For the mesh, 20-noded hexahedra isoparametric elements with full integration were used. Contact pairs were modelled using surface-to-surface contact finite elements. Contacts considered were plate-to-plate, rivet head-to-plate and rivet shank-to-plate.
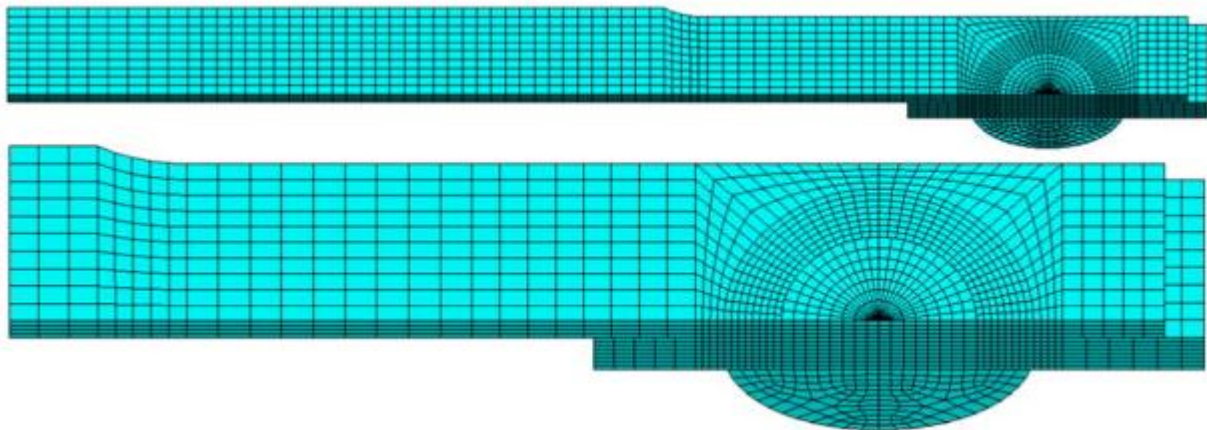
Figure 44: Mesh of riveted connection by De Jesus et al. (2014)

Model results

Both the crack initiation phase and the crack propagation phase have been considered by De Jesus et al. (2014). As this report focuses primarily on the crack initiation phase, only the results relevant to this phase will be discussed. Two types of results have been provided. Firstly, the elastic stress field along the direction of loading in four different situations have been shown. The situations

considered involve variations in amount of friction (either null friction, μ = 0, or high friction, μ = 0,6) and the presence of prestressing on the rivets (either 0 MPa or 22,78 MPa). The precise reasoning behind this specific value of clamping stress remains unspecified, though based on Figure 42 it can be assumed that this value is taken as it most closely represents experimental results. All the stress fields have been gathered based on the standard values for FKN and FTOLN. The stress fields can be found in Figure 45.

The stress fields can give a general overview of the type of stress distributions that can be expected in the plates. It is clear that in general, stress concentrations occur around the hole in the middle plate, in the side perpendicular to the loading direction. Models without friction generally experience larger compressive stress concentrations and smaller tensile stress concentrations. The prestressing of rivets appears to have a positive influence on stress concentrations, in particular in the models with friction.
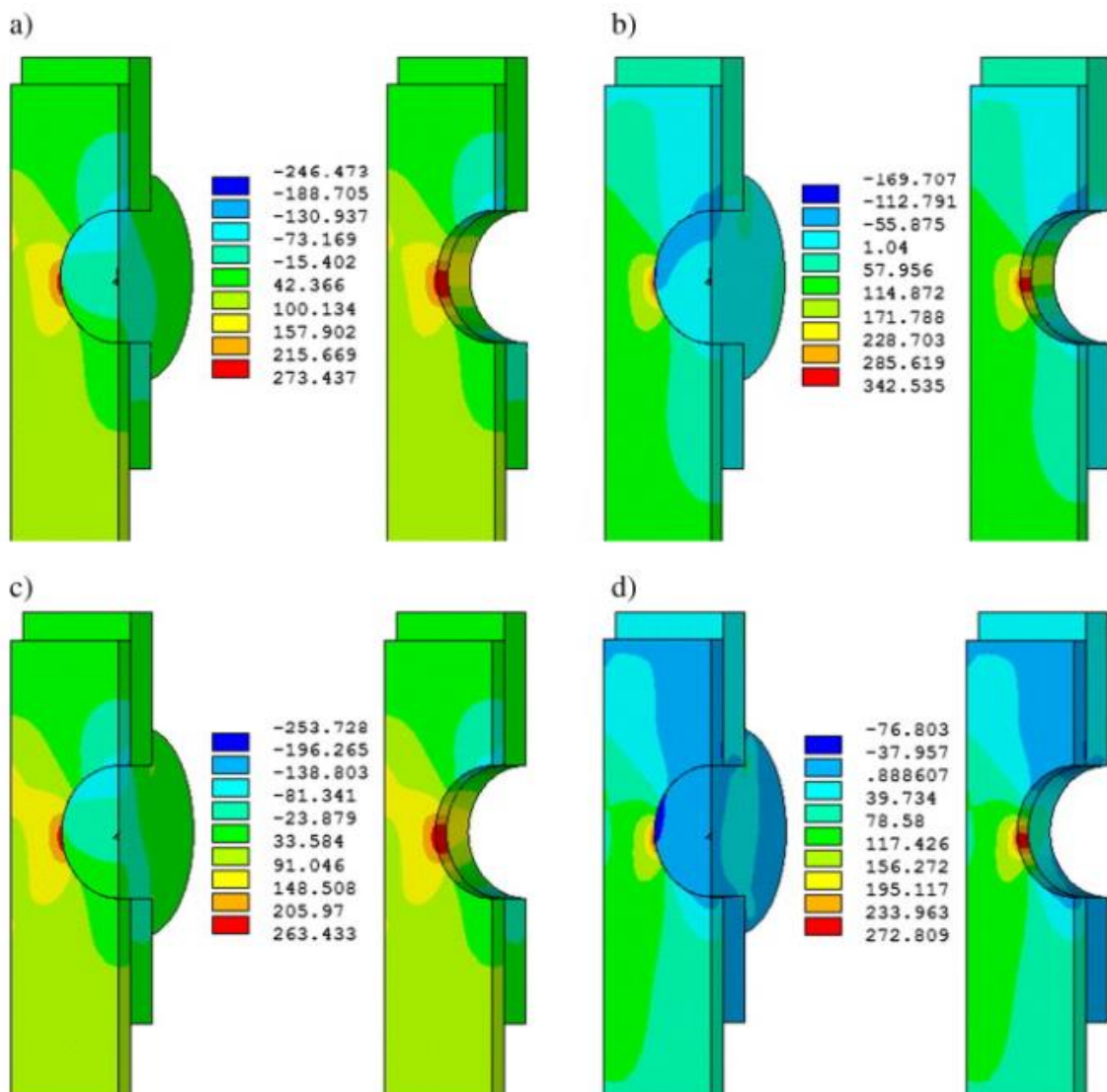

Figure 45: Elastic normal stress fields for different configurations: a) null friction, null clamping; b) friction of 0,6, null clamping; c) null friction, clamping of 22,78 MPa; d) friction of 0,6, clamping of 22,78 MPa (de Jesus, da Silva, & Correia, 2014)

In addition to gathering the stress concentrations from these figures, De Jesus et al. (2014) have denoted the force acting at the end of the model, resulting from the imposed displacement. With these forces, in combination with the stress concentrations and the known geometry of the model, the stress concentration factors can be derived, using Eq. 24.

$$K_t = \frac{\sigma_{max}}{\sigma_{net}} = \frac{\sigma_{max}}{\dfrac{F}{A_{net}}} = \frac{\sigma_{max} * (b - d)t}{F} \qquad \text{Eq. 24}$$

While precise stresses in a model may be tough to replicate, as they are heavily reliant on material factors like the material properties, but also on design choices such as mesh size. However, stress concentrations should remain consistent throughout different models, despite different design choices. As such they are suitable factors with which different models can be compared. They can be used to clearly establish the effect of, in this case, the effect of friction and prestressing on the stress concentrations near a rivet hole.

Table 14: Stress concentration factors for different models

	No Friction / No Prestress	Friction / No Prestress	No Friction / Prestress	Friction / Prestress
σ_{max} [MPa]	273,44	342,54	263,43	272,81
F [kN]	21,24	22,84	20,96	27,64
K_t [-]	2,16	2,52	2,11	1,66

Table 14 displays the stress concentrations found for the four models displayed in Figure 45. The force (F) provided by De Jesus et al. (2014) is representative only for the models that use symmetry planes, resulting in an effective area of 1/4th the actual area of the specimen. As a result, the calculated net stresses are four times lower than would be the case for the actual specimen. The values provided in Table 14 are adjusted for this area, and represent the forces that would act on the actual specimen.
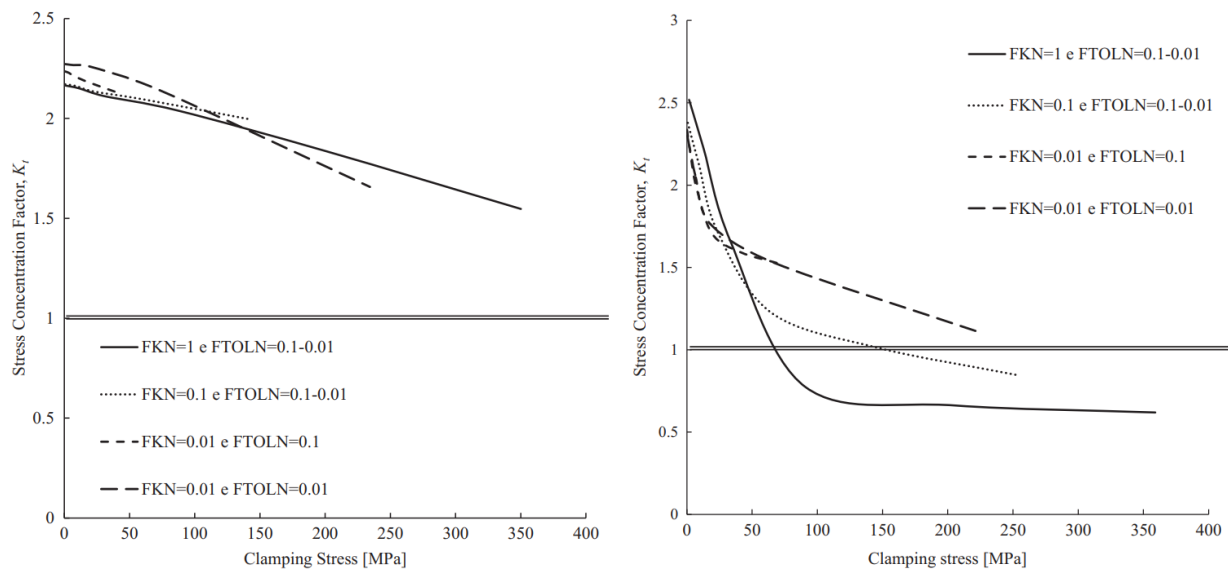
Figure 46: Stress concentration factors related to clamping stresses for null friction (left) and a friction of μ = 0,6 (right) (de Jesus, da Silva, & Correia, 2014)

On top of the stress concentrations related to the four models referenced earlier, De Jesus et al. (2014) have generated a curve for stress concentration factors related to clamping stresses, for different FKN- and FTOLN factors and different degrees of friction. In Figure 46, these curves are displayed for models with null friction and with a friction of μ = 0,6. Additionally, the locations for

clamping stresses of 22,78 MPa have been marked. Only the values for FKN = 1 and FTOLN = 0,1 are relevant for this report. It can be seen that the stress concentrations factors found in the initial four models (Table 14) line up perfectly with the generated stress concentration factor curves below.

2.3.2.2.   Local behaviour with D'Aniello et al. and Lundkvist et al.

D'Aniello et al. experimental specifications

D'Aniello et al. (2011) have performed some experimental research on the shear strength of riveted connections. For this research, aged plates and rivets originating from an unspecified old railway bridge in Italy have been retrieved. With these plates and rivets, a total of twenty-two different specimens have been constructed (Figure 47). In order to investigate the effect of different factors, a multitude of different typologies have been applied. The specimens aim to illustrate the effects of load eccentricity (through asymmetric joints), net area (through the use of larger rivets and thicker plates), plate width, joint length and rivet clamping force on the mechanical response of riveted joints. Labels of the specimens denote respectively the splice configuration (symmetric (S) or unsymmetric (U)), rivet diameter, steel plate thickness and number of rivets. Additionally, U-19-10-2 and U-19-10-4 have two different typologies, to consider different plate widths. Specimens with an unspecified plate width have a width of either 70 mm (for specimens with a rivet diameter of 16 mm and 22 mm) or 90 mm (for specimens with a rivet diameter of 19 mm).

Furthermore, D'Aniello et al.'s (2011) attempt to assess the adequacy of the formulae adopted by the Eurocodes (see also Chapter 2.2.1.1) to predict the theoretical resistance of the joint configurations, as well as propose new formulae that may indicate more accurately the resistance and failure modes of these riveted specimens.

For this report, in particular the stress-strain diagrams obtained by D'Aniello et al. are of relevance, though a full overview of their work is provided.

Figure 47: Rivet typologies investigated by D'Aniello et al. (2011)

D'Aniello et al. have conducted tensile coupon tests, Brinnel hardness tests, chemical analyses and Charpy-V notch tests. The results indicate that the plate material is consistent with modern day steel grade S275, with an average yield stress of 291 MPa (standard deviation SD = 5,63 MPa, coefficient of variation CV = 0,02) and average ultimate stress of 433 MPa (SD = 5,48, CV = 0,01). No modern-day equivalent for the rivet material has been found. The average yield stress of 315 MPa (SD = 26,03 MPa and CV = 0,08) and average ultimate stress of 412 MPa (SD = 17,85 and CV = 0,04) however do appear to be consistent with steel produced through the Martin-Siemens process, not dissimilar to the materials utilized in the John S. Thompsonbridge.

In particular the test set-up for the tensile tests is relevant for this thesis, as these are the experiments that have been replicated by Lundkvist et al. (2023). The tests were carried out with a Zwick/Roell testing machine and loaded in tension through displacement of the specimen ends until failure. The in-plane displacement is measured through a pair of Linear Variable Differential Transformers (LVDTs) on either end of the specimen, positioned at 30 mm from the nearest plate discontinuity (see Figure 48). For each test, the maximum load and the type of failure mode have been recorded.
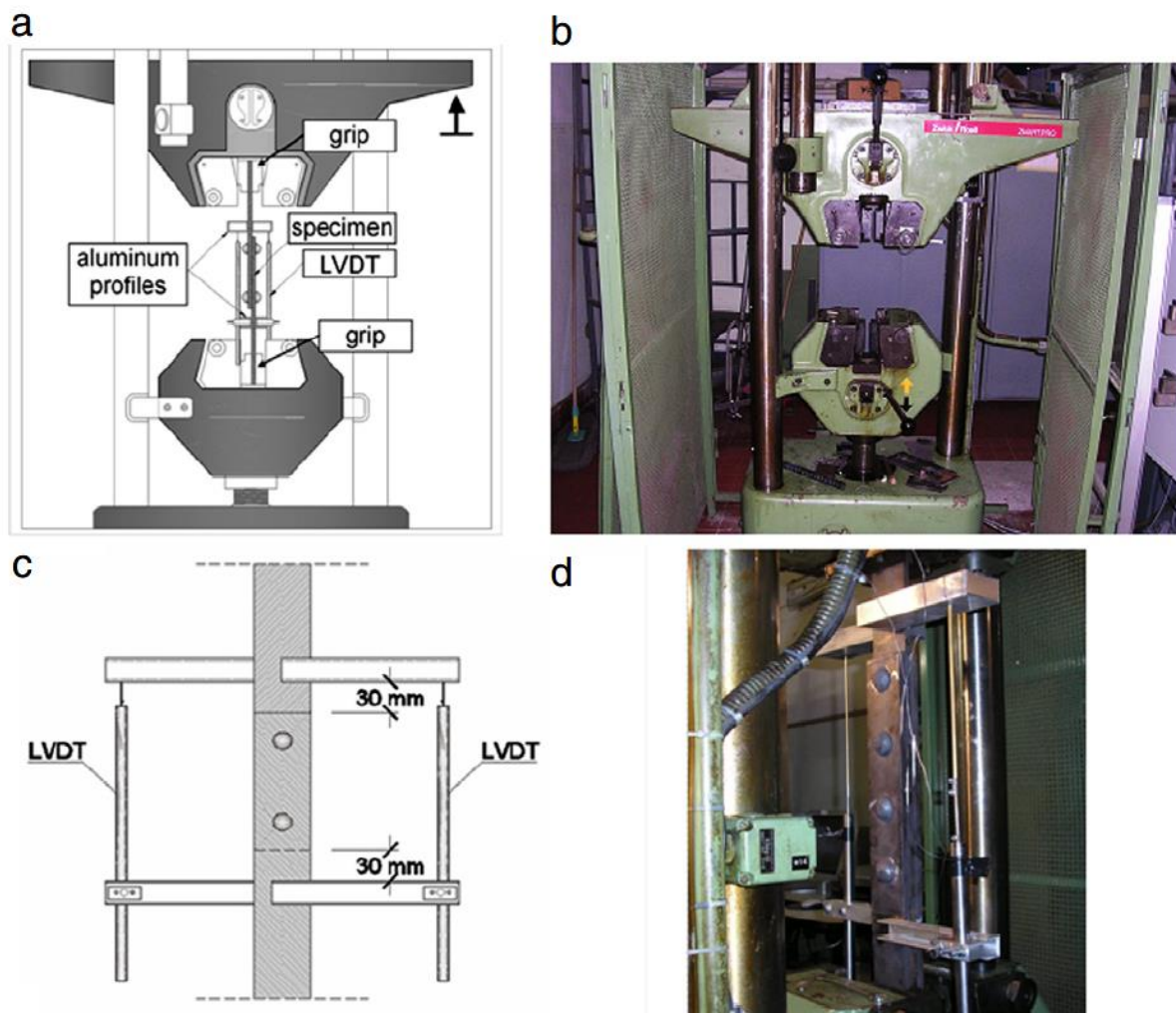

Figure 48: Tensile test set-up adopted by D'Aniello et al. (2011)

In short, the experiments show the following results for the different investigated parameters:

- Load eccentricity has a negative effect on the ultimate strength of the connections. This behaviour is particularly pronounced in singly-riveted specimens. As the joint length increases, the negative influence of bending on the shear strength of the connections decreases.
- A smaller ratio between net- and gross area of the specimen results in higher ultimate tensile strengths than their larger counterparts. This phenomenon is commonly referred to as 'net efficiency', and is observed in other studies as well (Schenker, Salmon, & Johnston, 1954), (Cox & Munse, 1952).
- Varying the plate width yields the same effects on the net efficiency as one might expect from varying the net-to-gross-area ratio. Interesting to note is that changes in plate width incidentally change the observed failure mechanism as well. D'Aniello et al. also observe that, despite the fact that in some specimens the distance between rivet hole and plate edge is smaller than the minimum prescribed by the Eurocode, a significant reserve of strength is left over when compared to the theoretical strength calculated in accordance with the Eurocodes.
- The joint length has a significant effect on the shear behaviour of the connections. Despite the fact that for the tested specimens the minimum ratio between plate end and rivet hole (e_1/d) exceeds the minimum ratio prescribed by the Eurocodes, failure in pure bearing still occurred in some instances. Increasing number of rivets alongside the rivet length did not linearly increase the average strength, as failure modes shifted from rivet failure to other failure modes.
- Differences in slip, where some specimens experienced a gradual slip, while for other specimens a sudden slip occurred, is attributed to varying degrees of prestressing. However, the precise levels of prestressing are unknown. The experiments indicate however that the slip is so small that they do not have an appreciable effect on the shape of the force-displacement curve, nor will they be significant on real structures. This confirms that the connections behave as bearing-type connections.

To illustrate the relation between experimental strength and the predicted strength and failure modes by the Eurocodes (calculated according to the formulae described in Chapter 2.2.1.1, based on the experimentally found average strengths and safety factor γ_{M2} equal to unity), D'Aniello et al. have provided Figure 49. It shows, on average, that the experimental ultimate strengths are a factor 1,40 larger than those calculated by the Eurocodes. Furthermore, the Eurocode formulae have predicted the wrong failure mode in the cases denoted by a 'V'.
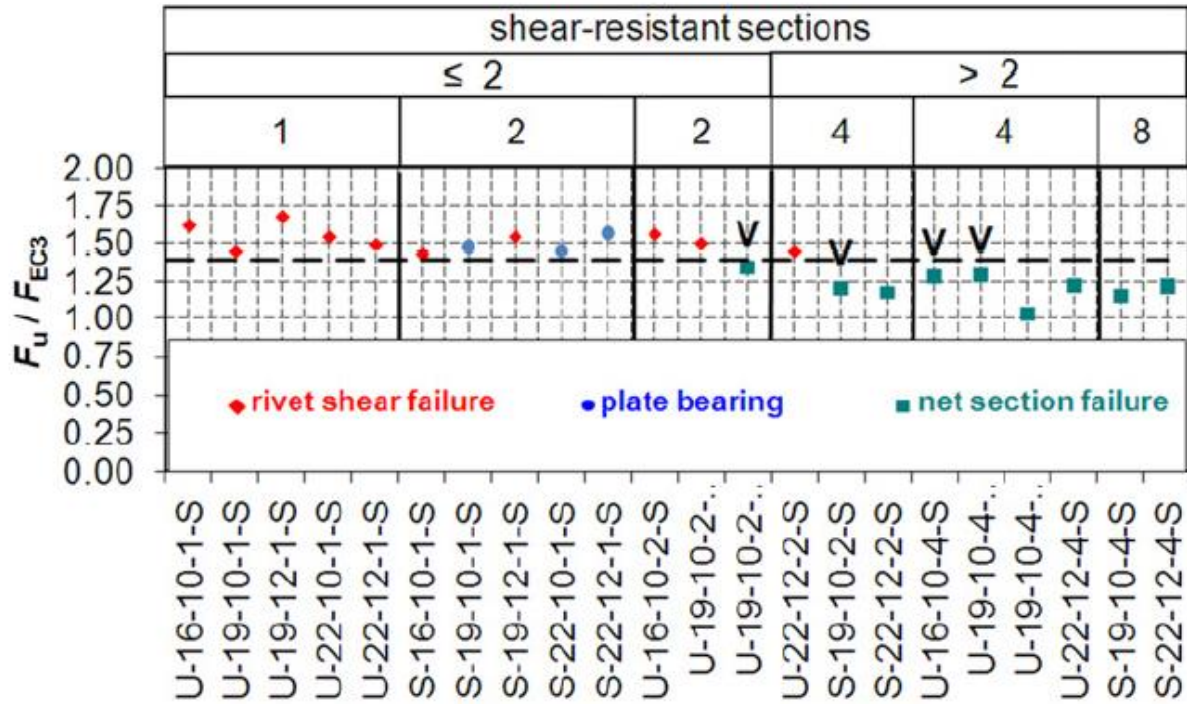
Figure 49: Relation between experimental and theoretical ultimate strength based on the Eurocodes (D'Aniello, Portioli, Fiorino, & Landolfo, 2011)

D'Aniello et al. state that the differences between experimental and theoretical strengths can partly be explained by the driving process. Hot-driven rivets generally experience an increase in ultimate strength of up to 20%, an effect that the Eurocodes do not take into effect. The remaining overstrength found by D'Aniello et al. is attributed to an underestimation of the ultimate rivet shear strength by the Eurocodes. While the Eurocodes assume a rivet shear to tensile strength ratio $f_{ur,v}/f_{ur} = 0,6$, a ratio of 0,75 appears to be more in line with experimental results. Therefore, D'Aniello et al. propose for the rivet shear strength to be calculated as follows, as opposed to the formula displayed in Table 2:

$$F_{v,Rd} = \frac{\Omega_1 * \Omega_2 * f_{ur} * A_0}{\gamma_{M2}}$$

Eq. 25

The overstrength of specimens failing in bearing likely corresponds to the present clamping forces, but as D'Aniello et al. have not quantified these, no modifications to the formula describing the bearing failure mode have been proposed. Finally, the overstrength in tensile failure modes is attributed to the net efficiency, which do Eurocodes do not incorporate. D'Aniello et al. propose that the reduction factor adopted by the Eurocode may be neglected for more accurate results, resulting in Eq. 26:

$$N_{u,Rd} = \frac{A_{net} * f_u}{\gamma_{M2}}$$

Eq. 26

With these proposals, the experimental-to-theoretical ultimate strength ratio approaches unity (denoted by the dashed line in Figure 50). Furthermore, the predicted failure modes line up perfectly with those observed in the experiments.
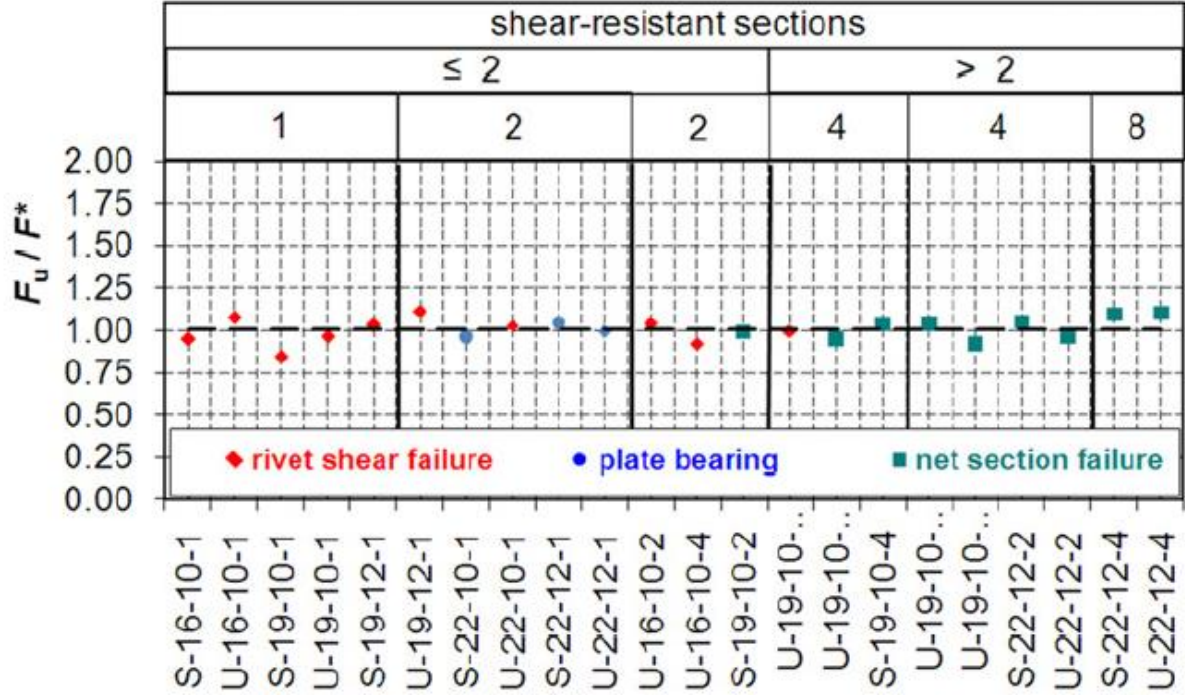
Figure 50: Relation between experimental and theoretical ultimate strength based on D'Aniello et al.'s modifications of the formulae from the Eurocode (D'Aniello, Portioli, Fiorino, & Landolfo, 2011)

Lundkvist et al. model specifications

Lundkvist et al. (2023) have created a modelling framework able to predict the strength, as well as the failure modes of riveted joints, built upon D'Aniello et al.'s experimental work. The purpose of this framework is to be able to accurately predict the static behaviour of a riveted joint, without the need to perform extensive experimentation on the materials. The model created by Lundkvist et al. is built in ABAQUS/Explicit

In order to adequately model riveted joints, Lundkvist et al. (2023) adopt an isotropic elasto-plasticity model to represent the true stress-strain curves of a given material. This model is given by Eq. 27. Within this model, $\sigma_0, N, \varepsilon_0, \varepsilon_N$ and ε_s represent respectively, the initial yield stress, the hardening exponent, the initial yield strain, a normalizing strain and an offset strain.

$$\sigma = \begin{cases} E\varepsilon & \varepsilon < \varepsilon_0 \\ \sigma_0 & \varepsilon_0 < \varepsilon < \varepsilon_s + \varepsilon_N \\ \sigma_0 * \left(\dfrac{\varepsilon - \varepsilon_s}{\varepsilon_N}\right)^N & \varepsilon > \varepsilon_s + \varepsilon_N \end{cases}$$

Eq. 27

The strain region $\varepsilon_0 < \varepsilon < \varepsilon_s + \varepsilon_N$ represents a Lüder Plateau, which has been observed in some of the rivets and plates tested by D'Aniello et al. (2011). In the case a Lüder Plateau is absent, the normalizing strain is set to be equal to the initial yield strain, while the offset strain can be set to zero.

Lundkvist et al. (2023) further adopt a ductile damage model, which, when combined with the above elasto-plasticity model, results in a model that is very agreeable with the experimental force-displacement curves found by D'Aniello et al. (2011), examples of which can be seen in Figure 54 to Figure 55. However, this thesis largely focuses on the fatigue response of riveted connections, as opposed to the static loading investigated by Lundkvist et al. and D'Aniello et al. It is therefore assumed that the ultimate strength of the materials is not reached and damage as a result from

static loading will not occur. As such, the damage model remains outside the scope of this thesis. From Figure 54 and Figure 55 it can be seen that, even without this ductile damage model, the model produces very agreeable results with the experimental results, as long as the ultimate stress is not yet reached and the onset of necking is yet to occur. This is the case for all of the models shown in Lundkvist et al.'s report.

Material properties adopted by Lundkvist et al. are primarily based on the properties derived by D'Aniello et al. Through tensile coupon tests, the stress-strain response of the plates and rivets of the specimens have been characterized. The experimental results show that the material properties of the plates correspond to what is now known as S275. The rivets however show a large variability in their properties (average yield strength and ultimate strength of 315 MPa and 412 MPa respectively, with a standard deviation of ±26 MPa and ±18 MPa respectively), likely due to a non-uniform manufacturing- and driving process. With these properties, no modern-day equivalent steel representative for these rivets can be determined. The experimental stress-strain response has been converted into a true stress-strain response (see Figure 51). This response directly serves as the input of the elasto-plastic behaviour of the materials in the three dimensional, non-linear FEA model that Lundkvist et al. have constructed, and can be expressed through Eq. 27.
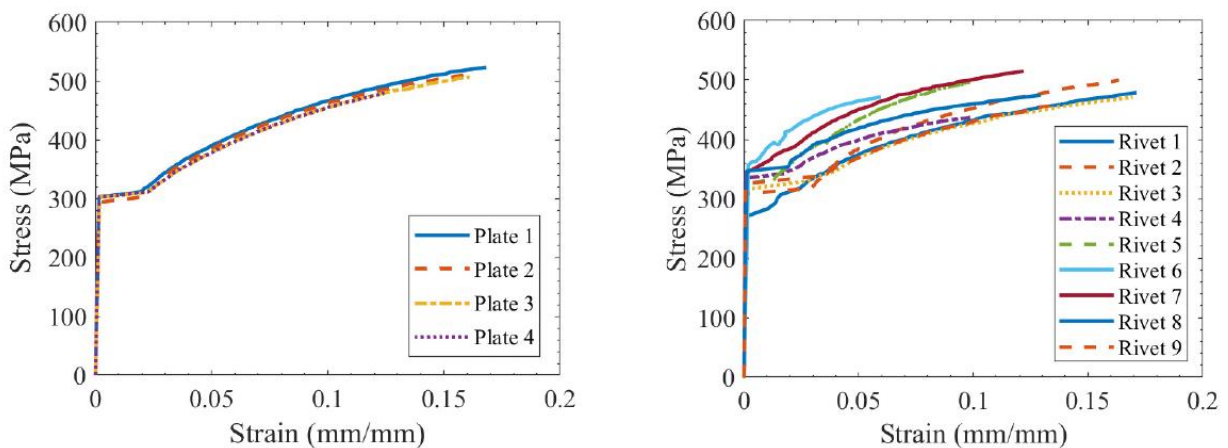
Figure 51: True stress-strain response of the plates and rivets by Lundkvist et al. (2023)

Contact interaction in the model is defined through ABAQUS general contact method, which automatically detects elements from different parts (either the plates or the rivets) that are close enough to be considered in contact, and models their interaction accordingly. With this method, contact between different plates or between plate and rivet can be identified. The friction coefficient (μ) used for the contact interaction for both the rivets and the plates is set to 0,2.

General lay-out of the models considered is displayed in Figure 52. Within this figure, d represents the diameter of the rivet shank (which fully fills the rivet hole; no clearance is present) and is equal to 16 mm, t is the thickness of the plates (10 mm), w is the width of the plates (70 mm), and r is the shortest distance from the centre of the rivet to the edge of the plate, which is the same both to the long edge as well as the nearest short edge of the specimen: 35 mm. Finally, e represents the distance from the centre of the rivet to the furthest edge of the plates. This distance corresponds to the location of the LVDT used in the

Figure 52: Lay-out of symmetric and asymmetric models

experimental set up, at a 30 mm distance from the nearest plate discontinuity. This means e is equal to 65 mm. D'Aniello et al. have performed experiments on a total of twenty-two different typologies for rivet connections, varying between number of rivets, rivet size, number of plates, plate size and rivet distance. Of these twenty-two specimens, Lundkvist et al. have taken nine specimens to model and compare numerical results to the experimental ones.
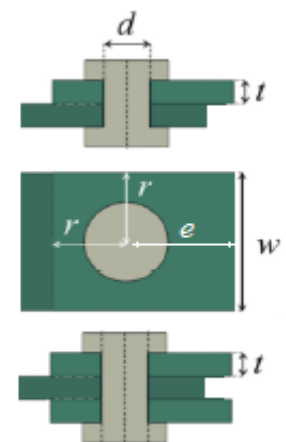
The models of Lundkvist et al. adopt a fixed boundary condition on one end of the specimen, while a quasi-static load is applied on the opposing end of the specimen. This load is defined as a result of the displacement (δ) of the specimen. The displacement, which propagates from 0 up to 12 mm, mimics the experiments performed by D'Aniello et al.

In addition to loading resulting from this imposed displacement, the model adopts a prestress on the rivet. While D'Aniello et al. have noted that some prestressing is present in the rivets, no precise values are determined. Based on the axial shrinkage of mild steel rivets due to thermal changes, the prestress is expected to lie within the range of 20 to 200 MPa, with an average of 100 MPa. Lundkvist et al. have not specified the precise degree of prestressing for each of the models, though it is assumed that they have adopted this same prestress of 100 MPa. The prestress is applied as a pressure, situated directly on top of the rivet heads (see Figure 53). This application of prestress generally results in a uniform axial stress distribution in the rivet shank, and an increase in the pre-load shows a slight increase in the joint strength, matching the findings of other studies (Sire, Gallegos Mayorga & Plu, (2015), Al-Bahkali (2011)). As such, this method of pre-load application is deemed adequate.
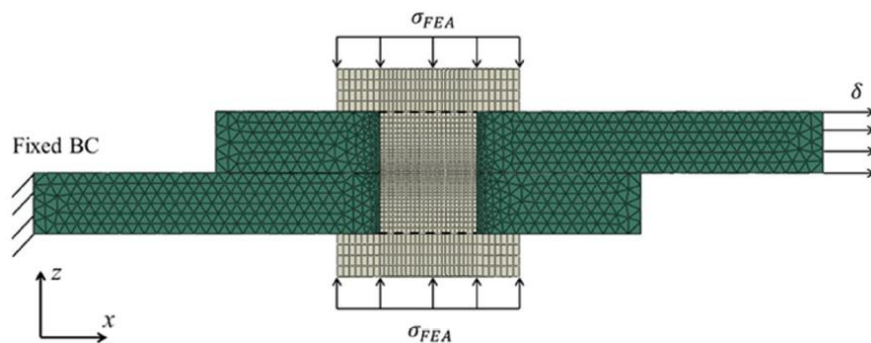
Figure 53: Loads and boundary conditions on the model by Lundkvist et al. (2023)

The global element size of all of Lundkvist et al.'s models is set to 2 mm for both the plates and the rivets, though refinements down to 0,3 mm are adopted in critical regions. Linear hexahedron and tetrahedral elements have been used for the models.

The models Lundkvist et al. consider are several singly riveted specimens similar to the one displayed in Figure 52 and Figure 53, as well as two doubly riveted specimens, and a final one with four rivets. Singly riveted specimens are varied by shank diameter, plate thickness, number of plates (either two for asymmetric loading or three for symmetric loading) and plate width. The doubly riveted specimens are primarily present to investigate symmetric versus asymmetric loading on multiple rivets. The results of two of Lundkvist et al.'s models are displayed in Figure 54 and Figure 55, and can be considered to be representative for all models. It is quite evident that Lundkvist et al.'s models quite accurately predict the damage that occurs on riveted specimens. In particular before necking occurs, the models show a very large conformity with the experiments.

Figure 54: The experimental force-displacement curves found by D'Aniello et al. (2011) compared to two FEA models constructed by Lundkvist et al. (2023) for a singly riveted, symmetrically loaded specimen

Figure 55: The experimental force-displacement curves found by D'Aniello et al. (2011) compared to two FEA models constructed by Lundkvist et al. (2023) for a singly riveted, unsymmetrically loaded specimen

3. Methodology

This chapter will cover the methodology adopted to investigate the research problems and questions presented in Chapter 1.

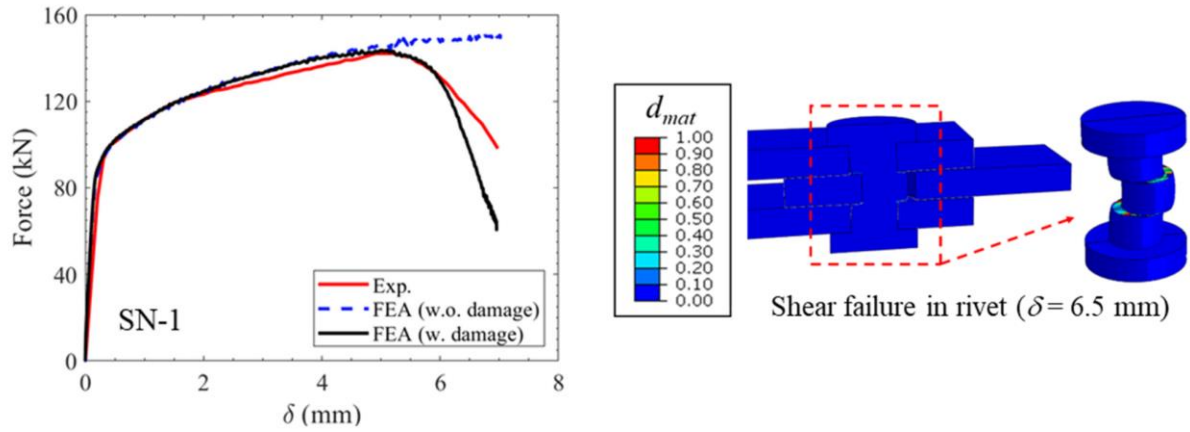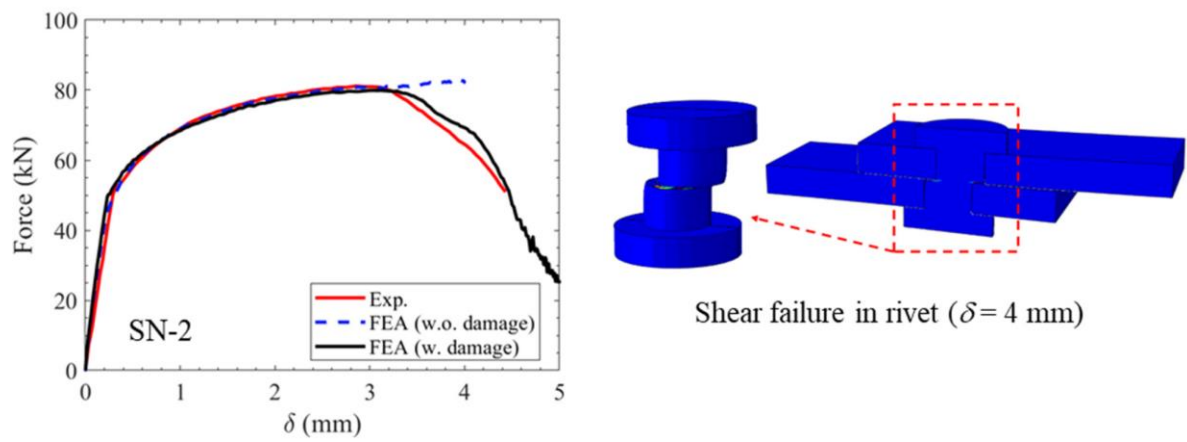The literature review has shown a significant number factors that may be of influence on the fatigue behaviour of a riveted connection. Taras & Greiner (2010) have outlined a number of factors that may affect the crack initiation phase of fatigue behaviour in their research. They cite material properties, stress ratios, stress ranges and rivet prestressing as important aspects. However, they note that modern-day standards are inadequate in providing enough detail categories for the fatigue assessment of riveted connections, and have created their own addendum to the detail categories provided by the Eurocode guidelines. This is further backed by an alternative approach to estimate the crack initiation phase, the strain-life approach. Several adaptations of the base strain-life equation attempt to incorporate the influential aspects into the strain-life approach.

This report attempts to investigate the application of these strain-life equations to a complex riveted connection. The base material ε-N curve (Eq. 11) is compared to different adaptations, such as the incorporation of mean stress effects (which is directly related to the stress ratio outlined by Taras & Greiner), through application of the Smith-Watson-Topper equation. Moreover, as the Eurocodes are only applicable to specimens subject to simple loading situations, this report will attempt to investigate the effect of multiaxial loading by using the maximum shear strain criterion. Furthermore, the Eurocode makes no distinction between prestressed and non-prestressed rivets. However, prestressing is a crucial aspect of the fatigue resistance of a riveted connection, and given the non-uniformity of clamping stresses on rivets throughout a structure, the fatigue response throughout a riveted joint may vary wildly. The presence of clamping forces and its influence on the overall fatigue response of riveted connections will be illustrated.

To compare the different methods of fatigue life estimation, a detailed Finite Element model is constructed in ABAQUS, based on the complex, full-scale joint investigated by Iv-Infra. Before an adequate model can be created, a clear overview of the model assumptions and design choices needed to build an accurate model need to be provided. To this end, several reference models are constructed, which attempt to replicate the results observed in the case studies by De Jesus et al. (2014), as well as D'Aniello et al. (2011) and Lundkvist et al. (2023). The purpose of these reference models is to identify different modelling methodologies and ascertain what methods would be appropriate to apply in the bridge joint model. An overview of the findings in these reference models, and what resulting design choices, such as modelling of contacts and mesh type and size, are adopted to the bridge joint model, are presented. To facilitate the construction of the bridge joint model, given that it will be run a multitude of times to investigate different aspects of the fatigue behaviour of the joint, a script to automatically generate the structure is set up, utilizing ABAQUS' Python-based scripting language. An insight in the steps taken to create this automatic model generations, as well as a number of the inputs required for the script, is provided.

Based on the truss-like structure of the bridge, the investigated loading situation on the bridge joint is assumed to be limited to axial force on the beams only. General stress distribution throughout the bridge joint model as a result from these axial forces is assessed through an investigation of the expected output forces on the beams of the joint. Axial forces acting on the main horizontal beam of the bridge joint as a result of axial forces on the diagonal beam from the ABAQUS model are compared to a simple hand calculation based on force equilibrium, as well as the results gathered from the SCIA models built by Iv-Infra. Detailed investigation of the results of this bridge joint model is performed through the identification of critical sections within the model. Critical sections are

locations in the model which experience high stress concentrations. This report limits itself to a single critical section. The initial bridge joint model with which a critical section is identified, is built upon shell elements. To more accurately capture the internal stresses and strains around the critical location, a sub-model is incorporated into the model, replacing the shell elements with solid mesh elements. Results in this critical section from the sub-model will be gathered and will be used to apply the different fatigue life estimation methods. Differences in results between different models (e.g., shell- versus solid-based critical section or prestressed versus non-prestressed model) are illustrated.

With the results from the bridge joint model, the strain-life equations are applied and the resulting strain-life curves are compared. Furthermore, empirical formulae (referred to as transfer functions) are drawn up to relate the applied external axial force to the resulting local stress- and strain concentrations. The purpose of these empirical formulae is to simplify the fatigue life estimation of complex riveted joints, decreasing the number of times an advanced Finite Element model needs to be run. An example using a theoretical load situation is used to illustrate the use of these empirical formulae. Furthermore, this example is used to calculate the expected fatigue life of the investigated critical section of the bridge joint until failure for a single load case, using the various methods described before. A simplification of the assumptions on the bridge joint model is made to include a fatigue life estimation of the section using the stress concentration factor, a stress-based estimation method, which is the method commonly adopted in the Eurocodes. This simplification is normally not applicable, but is performed to illustrate differences and similarities between the different approaches. With this inclusion, a comparison can be made between standard fatigue life estimation methods prescribed in the Eurocodes, and the alternative strain-based fatigue life estimation methods.

Finally, a short assessment of the different methods and their applicability to a practical example is discussed, and a recommendation on which approach would be most useful in practice is made.

4. Finite Element Modelling in ABAQUS

In order to be able to gather information on the fatigue response of the joint from the John S. Thompsonbridge, an in-depth Finite Element Analysis (FEA) may be made. To perform this analysis, a multitude of software packages are available. For this report, ABAQUS is used to gather detailed results on the joint, such as the stress- and strain distribution. The method used to define an accurate model of the bridge joint is described by Figure 56.

This chapter includes a short introduction into ABAQUS and the two separate methods ABAQUS can adopt to perform a FEA. Both methods have been used to construct the model of the bridge joint. However, given a lack of experimental data on the bridge joint, in order to develop an experimentally validated Finite Element (FE) model, both case studies pertaining to the local behaviour of rivets described in Chapter 2.3.2 have been consulted. In this chapter, the respective experiments have been recreated with reference models in ABAQUS, and the experimental results are compared to the results gathered from the Finite Element models. Once the reference model results are confirmed to align with the experimental results, the assumptions from the reference models form the basis for the design choices of the complete model of the bridge joint, ensuring the results from the bridge joint model are rooted in reality.

The assumptions governed by the case study results, in addition to general, prerequisite information needed to create an accurate model, such as the geometry, material properties and boundary conditions of the bridge joint, are laid out.

With as purpose to simplify the development of the model and to be able to easily adjust any parameters without having to rebuild the model from scratch, the bridge joint model is built up using ABAQUS' Python-based scripting language and Excel. Chapter 4.2.3 will provide some context to the steps taken in this process. To facilitate this, several snippets of code will be included, so a basic understanding of Python may be required.

Figure 56: Development of modelling strategy

4.1. Introduction to ABAQUS modelling

ABAQUS is used to create both the reference models and the bridge joint model. The behaviour of the models is heavily influenced by contact between elements and elasto-plastic behaviour of the material at stress concentrations. Therefore, non-linear dynamic analyses need to be performed. ABAQUS offers two methods for performing such dynamic analyses. ABAQUS/Standard, an implicit method, utilizes the Hilber-Hughes-Taylor operator (Hilber, Hughes, & Taylor, 1978). This operator not only solves for the dynamic quantities of a model at a time $t + \Delta t$ based on values at a time t, but also on the quantities found at the time $t + \Delta t$ (in which Δt is the observed time increment). For each time increment, this iterative calculation is done by inverting the integration operator matrix and solving a set of nonlinear equations. However, as is evident from the technical drawings (see Annex C and Annex D) and the IDEA Statica model (see Annex E), the modelled joint consists of an incredibly large number of plates and rivets. As such, an exceptionally large number of contact surfaces is present within the model. The excessive number of contact interactions that need to be considered results in an increased number of iterations and causes severe convergence issues that
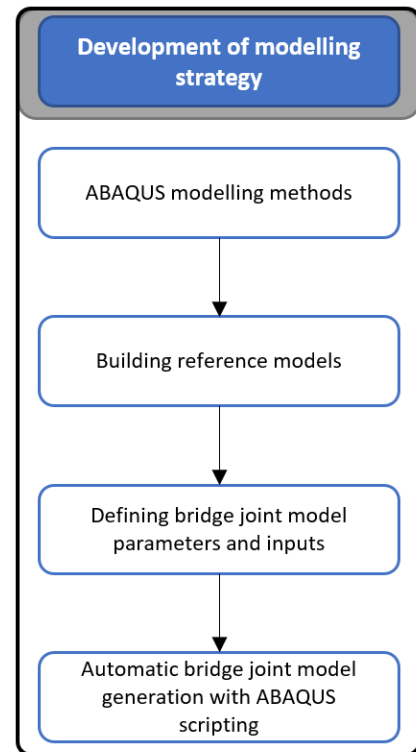
cannot be solved using this method. Rather than using this implicit solver, ABAQUS/Explicit, an explicit dynamic analysis, can be used. This procedure performs a large amount of small time increments to minimise the dynamic force to almost zero, and subsequently finds the dynamic quantities at $t + \Delta t$ solely based on the known values at t. For this, it utilizes an explicit central-difference time integration rule in order to solve the equations of motion of the body (see Eq. 28 and Eq. 29), in which u^N is a degree of freedom.

$$\dot{u}^N_{i+\frac{1}{2}} = \dot{u}^N_{i-\frac{1}{2}} + \frac{\Delta t_{i+1} + \Delta t_i}{2} \ddot{u}^N_i \qquad \text{Eq. 28}$$

$$u^N_{i+1} = u^N_i + \Delta t_{i+1} \dot{u}^N_{i+\frac{1}{2}} \qquad \text{Eq. 29}$$

Furthermore, by using diagonal element mass matrices to define the acceleration at the start of the increment (see Eq. 30), calculating inverse matrices is inherently simplified and requires only n operations, for which n is the number of degrees of freedom in the model. In Eq. 30, M^{NJ} is used to describe the mass matrix, P^J is the applied load vector and I^J denotes the internal force vector.

$$\ddot{u}^N_i = (M^{NJ})^{-1}\left(P^J_i - I^J_i\right) \qquad \text{Eq. 30}$$

Because this explicit method is based on such small time increments, and the following step is extrapolated from the current, known values with simple formulae, convergence will not be an issue and each increment takes very little time to compute. However, because there is an elevated number of increments and the model itself is fairly large, using the explicit procedure does result in a time-intensive calculation process.

4.2.   Development of modelling strategy

With the different modelling methods in ABAQUS discussed, one can look into modelling the bridge joint. However, in order to justify gathering results from the model of the joint, the results need to be validated. The John S. Thompsonbridge has no experimental data available, so the model cannot be validated directly. Therefore, experimental studies on old, riveted bridges from the literature have been consulted, and their results have been compared to reference models, in order to develop a strategy with which the bridge joint model can be constructed. The consulted studies are by De Jesus et al. ((2014) and (2015)), where a riveted connection originating from an ancient steel bridge has been observed both through experimental and numerical approaches, and a combination of D'Aniello et al.'s (2011) experimental research on the shear strength of riveted connections, and the subsequent modelling framework designed by Lundkvist et al. (2023), built upon D'Aniello et al.'s work, which can be used to design and predict the response of riveted connections to static loading, including different failure modes. These experimental studies on which the reference models are based have been described in detail in Chapter 2.3.2. In particular, the ability to model the local behaviour of a riveted joint is assessed through the comparative assessment of these experimental studies.

Upon completion of the reference models, an overview will be provided of the necessities required to construct the bridge model, where they have been gathered from, and how they have been implemented.

4.2.1. Reference model building

4.2.1.1. *Reference model De Jesus et al.*

In order to assess whether the results of De Jesus et al. (2014) could be appropriately incorporated in the bridge joint model, reference models have been constructed. Their purpose is to reproduce De Jesus' results, while maintaining a model of which the design choices can be incorporated into the construction of the bridge joint model, such that the results from the joint model can be considered valid. Initial models were made using ABAQUS/Standard, which was adopted before the realization was made that ABAQUS/Explicit was preferred to model complex joints like the bridge joint.

A few considerations need to be made before this model can be constructed. Firstly, the models made in this report are created utilizing ABAQUS, while De Jesus et al. (2014) have made their models with ANSYS. As such, the models will inherently differ. The aim is not to perfectly reproduce the original results, but to produce results that are comparable to the original. Secondly, De Jesus' model is a highly detailed model, with solid elements and a very fine mesh. Because the bridge joint model is incredibly large, it is not feasible to adopt this same level of detail for the complete detail as is used in the models in De Jesus' study. While the bridge joint model may consist of solid elements at some locations, it is primarily constructed utilizing shell elements. Therefore, solid element models will initially be used to identify whether the models by De Jesus et al. and the reference model provide comparable results, but shell element models and models utilizing both shell- and solid elements are subsequently constructed and assessed whether they too provide acceptable results. Thirdly, De Jesus et al. (2014) have not specified the size of the rivet head, which means its precise measurement is unknown and its size has been chosen in accordance with the rivets from the bridge joint model. Two types of rivet heads have been adopted. The first uses the standard spherical rivet heads, and are applied in the ABAQUS/Standard analyses, while the other, rather than the spherical shape that is standard for rivet heads in real-life applications, have a cylindrical shape, which allows for easier application of clamping stresses in ABAQUS/Explicit. Their height and diameter still match the most common rivet head dimensions described by Colette (2014). This difference in shape may slightly affect the distribution of prestress through the joint. However, as the contact surface between the rivet head and plates remain consistent between the different head shaped, its effect will be negligible. Finally, De Jesus' study focuses primarily on the elastic stress concentrations of the specimen, which is why it only considers very small displacements. As such, the specimen will likely experience negligible plasticity, and its plastic behaviour is therefore not considered.

For the reference models constructed, both in ABAQUS/Standard and ABAQUS/Explicit, the material properties and dimensions are taken directly from the model by De Jesus et al. (2014). In the original paper, the density of the material used is omitted. Therefore, the material is assumed to be representable by standard mild steel, and is modelled with a density of 7850 kg/m^3.

Contact is modelled using the general contact method provided by ABAQUS, where ABAQUS automatically identifies elements from different parts that are in contact with each other and models their interaction accordingly. The first notable difference between ABAQUS/Standard and ABAQUS/Explicit is the application of prestress, when present. ABAQUS/Standard allows for the definition of bolt forces, which represent any prestressing forces that may be applied to the bolt. ABAQUS/Explicit has no such function to inherently inscribe preloads onto bolts, which means they need to be applied manually to the rivet heads on either side of the rivet. This is done by applying an axial pressure onto the spherical rivet heads. Prestressing forces are ensured to have fully established before the additional displacements are enforced. The displacement of 0,1 mm is

applied to reference points, which are directly connected to the cross-section on either end of the specimen.

The mesh used remains largely consistent throughout the different models. All models are constructed with hex-dominated mesh elements. Rivets are modelled as solids, using solid elements at all times, while the plates are modelled with either solid- or shell elements. Both the rivets and the outer plates of the specimen have a global mesh element size of 3 mm. The mesh of the rivets is achieved through partitioning of the rivet along its internal planes, and subsequently utilizing a sweeping pattern to assign the mesh. The middle plates have a global mesh element size of 5 mm, though a refinement of the mesh is applied near the rivet hole, where a mesh element size of 1,5 mm was utilized, in order to more accurately assess the stress concentrations.
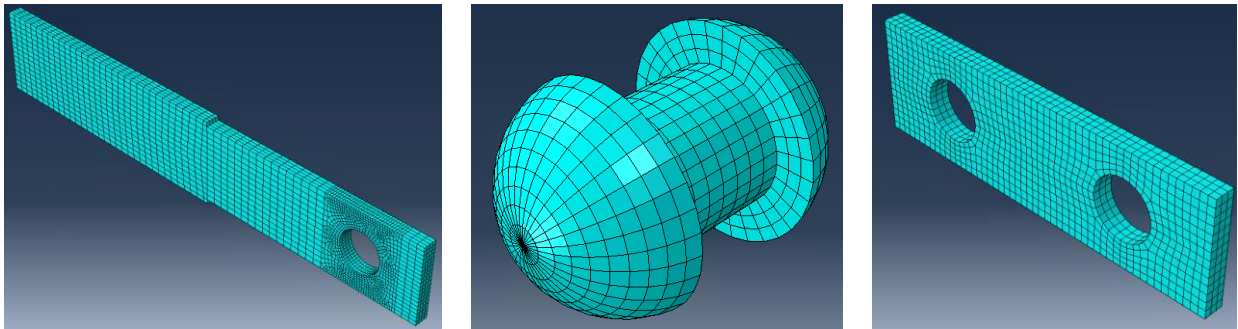

Figure 57: Mesh of inner plate, rivet and outer plate of reference model (solid elements)
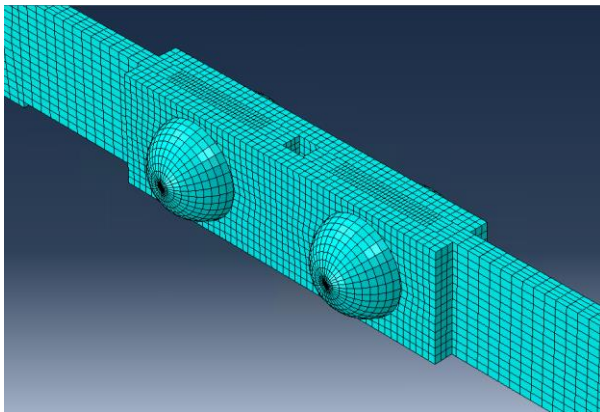

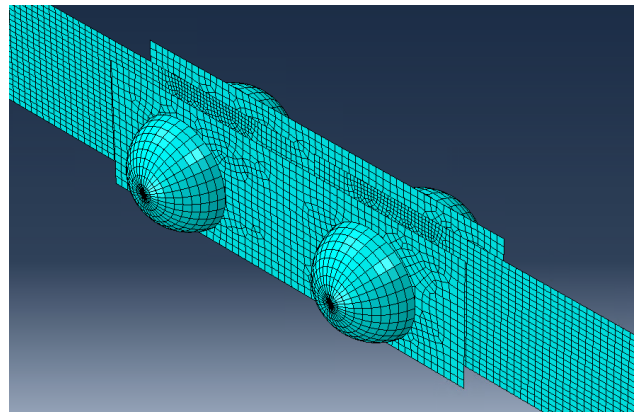*Figure 58: Mesh of reference model, solid elements*

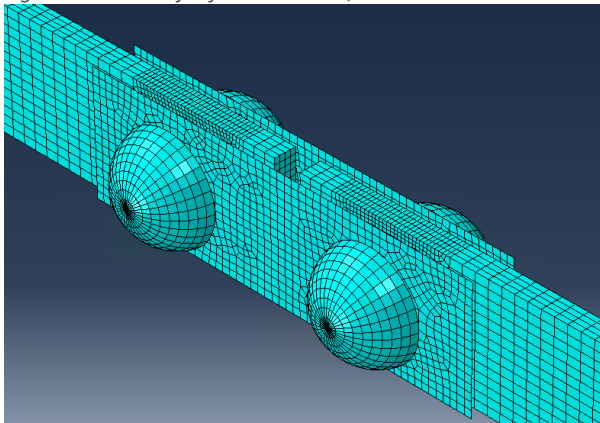*Figure 59: Mesh of reference model, shell elements*

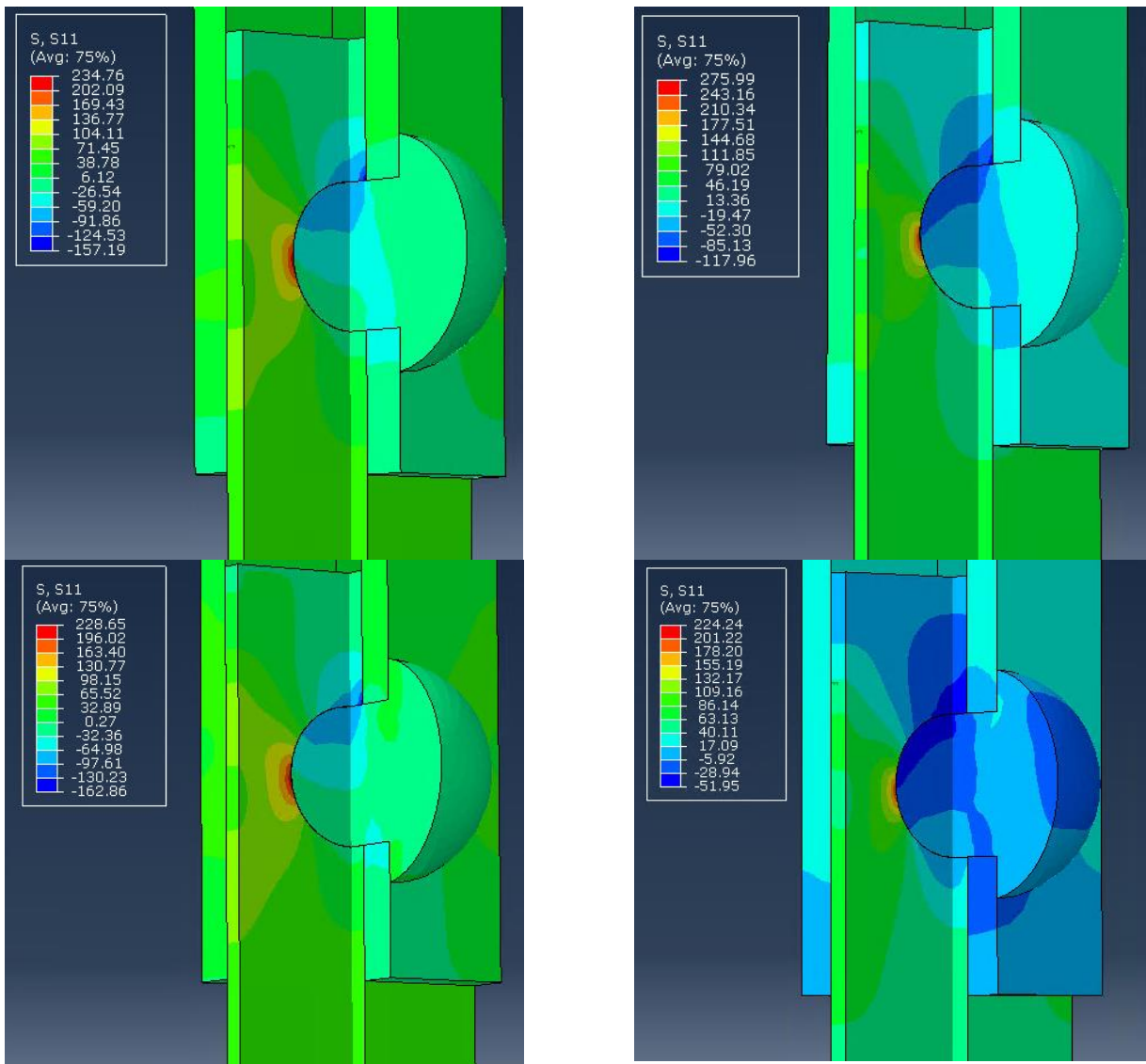*Figure 60: Mesh of reference model, shell- and solid elements*

Figure 61: Stress distribution in ABAQUS/Standard. Situations with, from left to right, top to bottom, 1) no friction and no prestress, 2) friction and no prestress, 3) prestress and no friction and 4) friction and prestress

Initial models in ABAQUS/Standard constructed with 8-noded (linear[1]) solid mesh elements generally show comparable trends in stress concentrations for the four different considered situations, though their actual values stray relatively far from the expected values found in the work by De Jesus et al (see Table 15). Applying 20-noded (quadratic[1]) solid mesh elements show much better results (Table 16). While the stress concentrations and resulting forces still differ slightly, the distribution of stresses throughout the specimen (Figure 61), as well as the stress concentration factor, are very comparable to De Jesus' model, suggesting that this model can be used to relatively accurately predict the stress concentration factors. A similar trend is found for models using shell elements (Table 17 and Table 18). However, shell element-based models do underestimate the stress concentrations and forces by a larger margin than solid element-based models. By applying a combination of shell elements and solid elements in the most critical plates, which in this case are the central plates, similar results are found to a model utilizing solely solid elements (Table *19* and Table 20). This means such a combined model can be utilized to relatively accurately predict the stress concentrations factors. Combining both elements utilizes both the accuracy of solid elements and the lower computational time of shell elements, making it suitable for modelling large joints.

---

[1] Linear and quadratic mesh elements refer to the shape functions used to approximate the displacement between nodes.

Table 15: Stress concentrations, forces and stress concentration factor for solid 8-noded (linear) mesh elements in ABAQUS/Standard

	No Friction / No Prestress	Friction / No Prestress	No Friction / Prestress	Friction / Prestress
σ_{max} [MPa]	200,4	216,6	197,6	177,0
F [kN]	18,2	18,9	19,0	21,3
K_t	1,85	1,93	1,85	1,39
Difference between reference model and De Jesus:				
σ_{max}	26,71%	36,77%	24,99%	35,12%
F	14,55%	17,29%	14,17%	22,79%
K_t	14,23%	23,54%	12,61%	15,97%

Table 16: Stress concentrations, forces and stress concentration factor for solid 20-noded (quadratic) mesh elements in ABAQUS/Standard

	No Friction / No Prestress	Friction / No Prestress	No Friction / Prestress	Friction / Prestress
σ_{max} [MPa]	234,8	276	228,6	225,0
F [kN]	18,2	18,9	18,0	21,3
K_t	2,17	2,45	2,13	1,77
Difference between reference model and De Jesus:				
σ_{max}	14,13%	19,43%	13,22%	17,53%
F	14,45%	17,25%	14,07%	22,83%
K_t	-0,38%	2,63%	-0,99%	-6,87%

Table 17: Stress concentrations, forces and stress concentration factor for shell 4-noded (linear) mesh elements in ABAQUS/Standard

	No Friction / No Prestress	Friction / No Prestress	No Friction / Prestress	Friction / Prestress
σ_{max} [MPa]	167,6	197,7	167,2	179,5
F [kN]	15,2	16,5	15,1	20,3
K_t	1,85	2,01	1,86	1,49
Difference between reference model and De Jesus:				
σ_{max}	38,71%	42,28%	36,53%	34,20%
F	28,39%	27,58%	27,91%	26,74%
K_t	14,41%	20,30%	11,96%	10,19%

Table 18: Stress concentrations, forces and stress concentration factor for shell 8-noded (quadratic) mesh elements in ABAQUS/Standard

	No Friction / No Prestress	Friction / No Prestress	No Friction / Prestress	Friction / Prestress
σ_{max} [MPa]	194,6	235,6	194,4	208,6
F [kN]	15,2	16,5	15,1	20,3
K_t	2,16	2,39	2,16	1,73
Difference between reference model and De Jesus:				
σ_{max}	28,83%	31,22%	26,20%	23,54%
F	28,63%	27,58%	27,91%	26,70%
K_t	0,29%	5,02%	-2,37%	-4,32%

Table 19: Stress concentrations, forces and stress concentration factor for shell 4-noded and solid 8-noded (linear) mesh elements in ABAQUS/Standard

	No Friction / No Prestress	Friction / No Prestress	No Friction / Prestress	Friction / Prestress
σ_{max} [MPa]	194,3	212,0	190,2	182,0
F [kN]	17,7	18,5	17,5	21,3
K_t	1,85	1,92	1,82	1,44
	Difference between reference model and De Jesus:			
σ_{max}	28,94%	38,11%	27,80%	33,29%
F	16,85%	18,87%	16,36%	23,05%
K_t	14,54%	23,71%	13,67%	13,31%

Table 20: Stress concentrations, forces and stress concentration factor for shell 8-noded and solid 20-noded (quadratic) mesh elements in ABAQUS/Standard

	No Friction / No Prestress	Friction / No Prestress	No Friction / Prestress	Friction / Prestress
σ_{max} [MPa]	228,2	272,8	219,4	235,4
F [kN]	17,7	18,5	17,6	21,3
K_t	2,17	2,47	2,10	1,86
	Difference between reference model and De Jesus:			
σ_{max}	16,54%	20,36%	16,71%	13,71%
F	16,81%	18,83%	16,27%	23,12%
K_t	-0,32%	1,89%	0,53%	-12,23%

Upon further investigation, as previously mentioned, it has been concluded that ABAQUS/Standard is not a method usable to model large joints, as it is unable to model the enormous number of contact interactions present in the bridge joint model. Therefore, the results described above are no longer suitable, and a re-evaluation is required using ABAQUS/Explicit. In its core principles, the model remains the same, with the same properties, dimensions and interactions, as well as similar mesh sizes as the ABAQUS/Standard model. As discussed, the application of prestress needs to be approached slightly differently, though it is only a minor adjustment. In addition to the application of prestresses, ABAQUS/Explicit uses different mesh elements compared to ABAQUS/Standard. More importantly, ABAQUS/Explicit does not support the use of quadratic mesh elements, which were essential in formulating accurate results in ABAQUS/Standard. Only models with linear mesh elements can be constructed.

Table 21: Stress concentrations, forces and stress concentration factor for solid 8-noded (linear) mesh elements in ABAQUS/Explicit

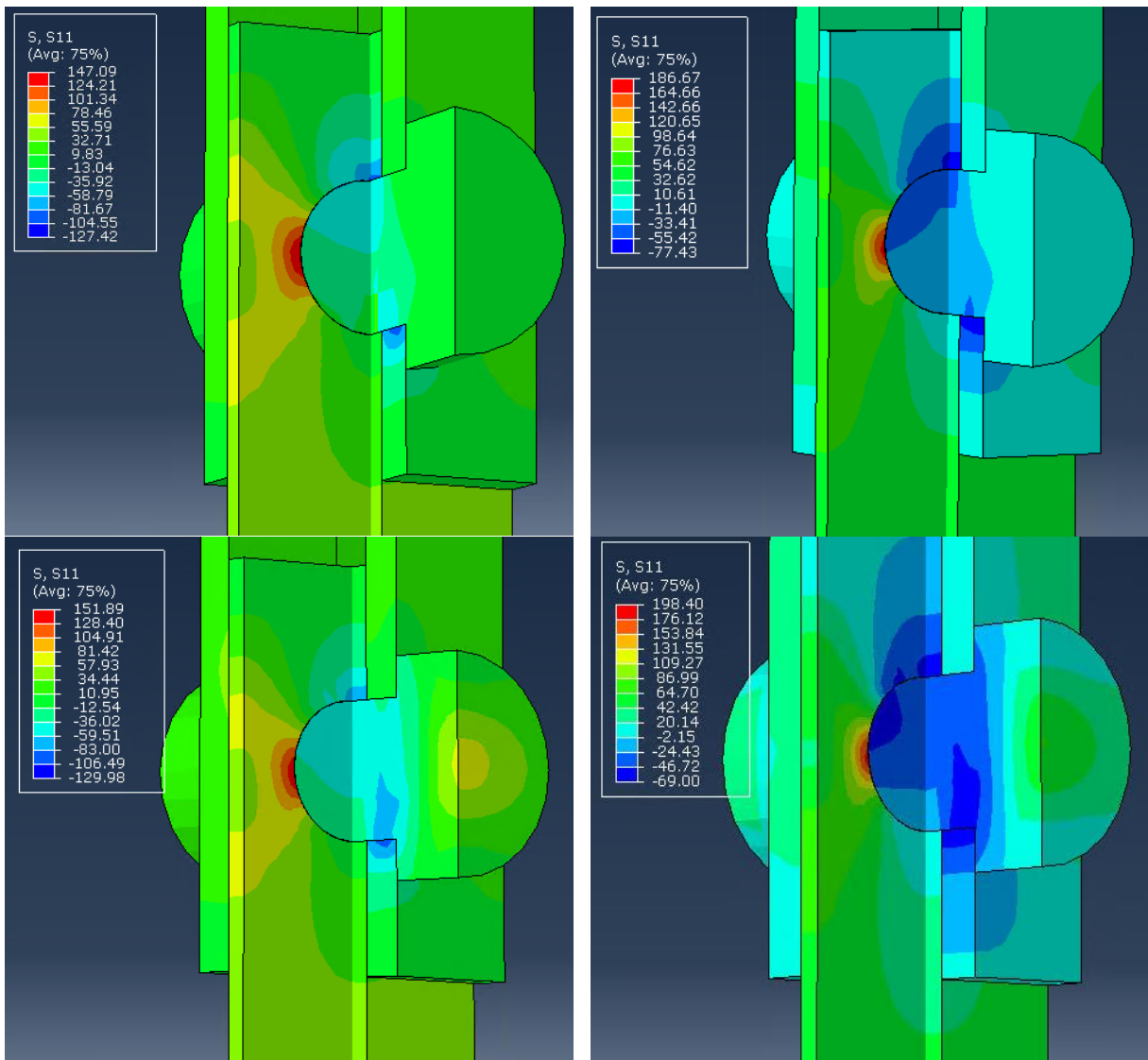|	No Friction / No Prestress	Friction / No Prestress	No Friction / Prestress	Friction / Prestress
σ_{max} [MPa]	147,1	186,7	151,9	198,4
F [kN]	13,9	15,8	14,4	16,6
K_t	1,78	1,99	1,77	2,00
	Difference between reference model and De Jesus:			
σ_{max}	46,20%	45,50%	42,34%	27,28%
F	34,75%	31,04%	31,30%	39,83%
K_t	17,56%	20,96%	16,07%	-20,87%

Figure 62: Stress distribution in ABAQUS/Explicit. Situations with, from left to right, top to bottom, 1) no friction and no prestress, 2) friction and no prestress, 3) prestress and no friction and 4) friction and prestress

As can be seen in Table 21 and Figure 62, the explicit models remain moderately comparable to the original reference models that use linear solid mesh elements, in terms of actual stress distribution, as well as the calculated stress concentrations factors. It should be noted that the stresses in the rivet heads themselves are slightly off compared to the models in ABAQUS/Standard, but this is expected given their change in dimensions and different methods of application of prestressing. However, their actual stress concentrations and forces resulting from the displacement are even further from the expected result, which should line up with De Jesus' model. Parametric studies have been made to approach a more accurate result, such as changing the rivet heads to more accurately represent the experimental models, varying mesh size of the different elements, adjusting the method of imposing displacement, changing parameters in the contact definition and even the method of contact definition itself, but none have yielded results that line up with De Jesus' models. Additionally, shell-based explicit models have shown even less cohesion with the expected results. Without the ability to apply quadratic mesh elements to achieve results close to reality, and no methods to further approach the experimental results without changing the material properties of the model and risking that they no longer match the material properties of the experimental set-up, De Jesus' work has been deemed unusable to assert the accuracy of the bridge joint model.

To ensure the bridge joint model can be modelled with assumptions that are backed by experimental results, another model is constructed. This new reference model is modelled based on the combined work of D'Aniello et al. (2011) and Lundkvist et al. (2023), which have been described in Chapter 0. By attempting to reproduce the results from Lundkvist et al. with a slightly simpler reference model, and comparing the experimental force-displacement curves, the curves generated by Lundkvist et al. and the curves found for the reference model, an assessment can be made on the validity of the reference models. If the reference models line up with the results from Lundkvist et al., their design choices and assumptions used in these reference models can be used to construct the large bridge joint model.

As mentioned, of the 22 specimens considered by D'Aniello et al. (2011), Lundkvist et al. (2023) have modelled nine. In order to illustrate that the models in this thesis correspond with the work of Lundkvist et al., and thus provide comparable results to D'Aniello et al.'s experimental work, two of these nine specimens have been modelled: both are singly-riveted specimens, with either a symmetrical or an asymmetrical plate lay-out.

As ABAQUS/Explicit is used both in the original models by Lundkvist et al. and by the reference models created for this thesis, many of the design choices can be copied directly. It should be noted that neither D'Aniello et al. nor Lundkvist et al. have specified several material properties beyond the plates being of grade S275. Therefore, for both the plates and the rivets, the initial Young's Modulus (E), the Poisson's ratio (v) and the density (ρ) have been assumed to be in line with modern day standards: E = 210 GPa, v = 0,3 and ρ = 7850 kg/m^3. Some adjustments were also made on the plastic behaviour of the model. Where Lundkvist et al. have adopted their elasto-plastic model to define the plasticity of the model, the reference models take the plastic behaviour directly from D'Aniello et al.'s experiments.

Other factors, such as dimensions, boundary conditions, application of prestress and contact interaction remain the same as in Lundkvist et al.'s models.

The mesh does differ between models. Because the bridge joint model will be significantly larger than the reference models, and even the joint sub-model will likely exceed Lundkvist et al.'s model size, different mesh elements have been used. With the large number of straight, symmetric elements in the joint, the model can be adequately captured by using hexahedral elements, rather than the tetrahedral elements adopted by Lundkvist et al., which generally requires fewer mesh elements and is therefore beneficial for computational time. More specifically, the reference models use C3D8R hexahedral mesh elements. Global element size is set to 5 mm, while around the rivet holes the element size is refined to 2 mm. The same global element size of 5 mm is adopted for the rivet mesh. The mesh of the individual elements is displayed in Figure 63 (for the symmetrical specimen). Additionally, the assembly of the different elements can be found in this Figure. Boundary conditions are applied at the edges of the- two outer plates, while the displacement is enforced on the inner plate. For reference, the boundary conditions and displacement on the asymmetrical specimen matches Lundkvist et al.'s model displayed in Figure 53.
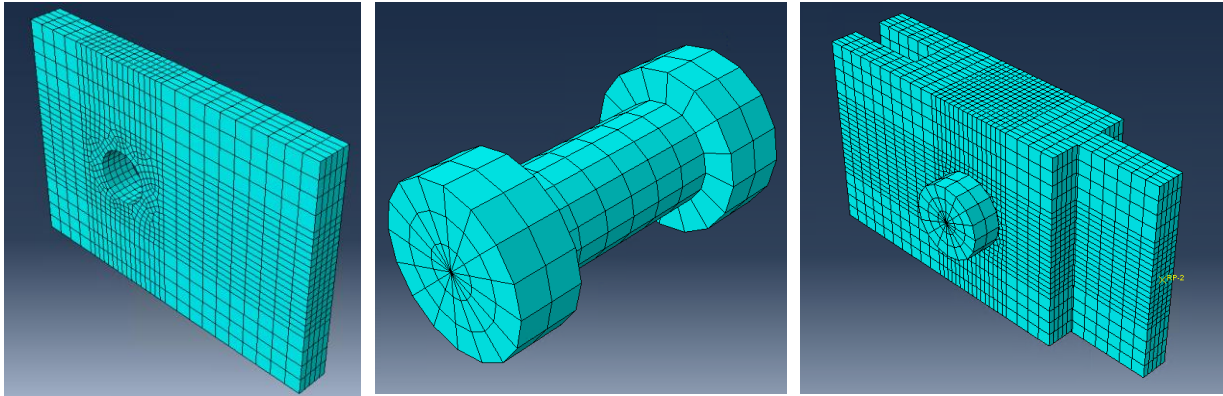
Figure 63: Mesh of plate, rivet and assembly of the symmetric reference model

Given the agreeability of Lundkvist et al.'s models with the experimental results by D'Aniello et al., the F-δ-curves generated by Lundkvist et al.'s are taken to be representative for the experimental curves, and will be used to compare results between experimental data and the reference models. It should be noted that, despite the fact a general range has been given for the prestress applied to the specimen, Lundkvist et al. have not specified precisely what degree of prestressing they have applied to the different models. Therefore, an initial reference model (RM1-1) has been generated without prestress applied. As can be seen in Figure 64, this model underestimates the experimental elastic- and plastic behaviour of the specimen quite significantly, and a new model needs to be generated with some prestress. For this second reference model (RM1-2), the expected average prestress of 100 MPa is applied. This produces significantly better results, though the behaviour of the specimen in its elastic range is not quite captured properly.
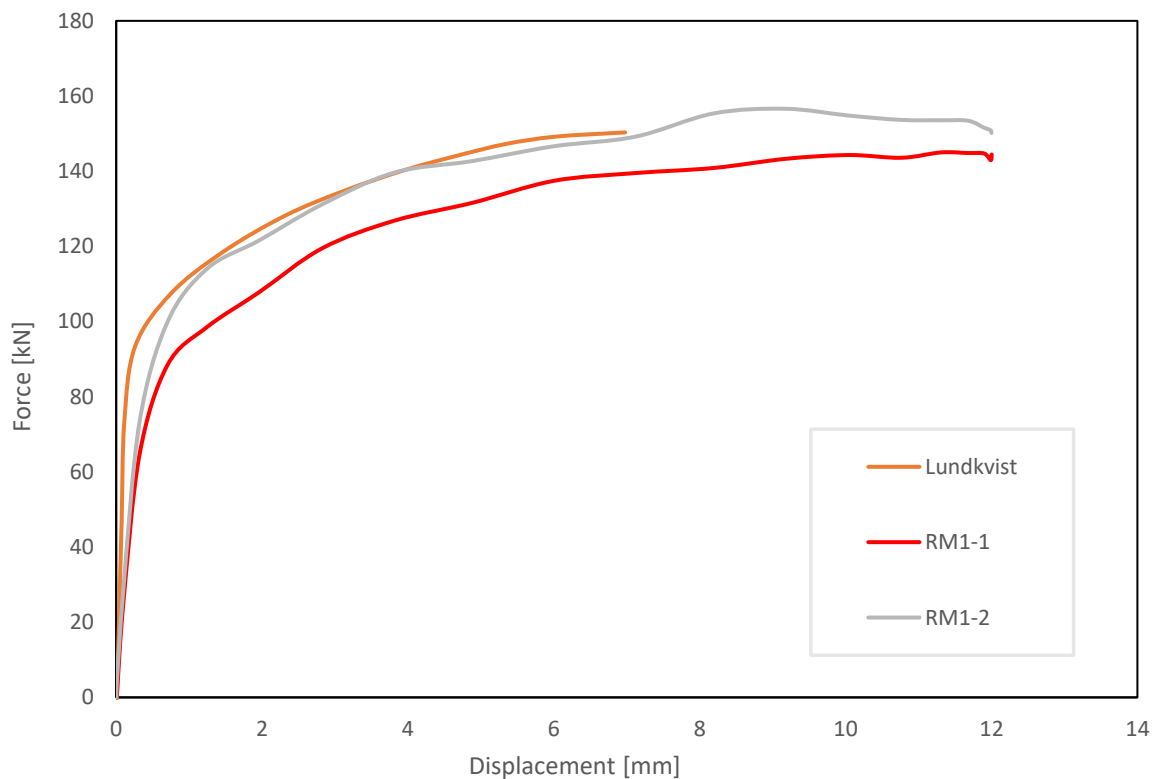

Figure 64: F-δ curves RM1-1 and RM1-2

Further inspection of the model shows the largest stresses occur within the rivet shank, which also lines up with the experimental results and Lundkvist et al.'s models, as they show this specimen exhibits shear failure of the rivet shank. Refining the mesh of the rivet should therefore produce more accurate results. RM1-1 and RM1-2 are rerun with a refined mesh of the rivet (element mesh size of 2,5 mm, as opposed to the 5 mm which was initially adopted). The results of these reruns, RM1-3 and RM1-4 respectively, are displayed in Figure 65. Despite the fact that an unclamped model remains inappropriate to represent the experimental data, RM1-4 shows a very high conformity with the Lundkvist et al.'s models, and, by extension, with the experimental results. A slight increase in applied prestress may slightly improve the reference model curves, but 100 MPa appears to be an adequate assumption.
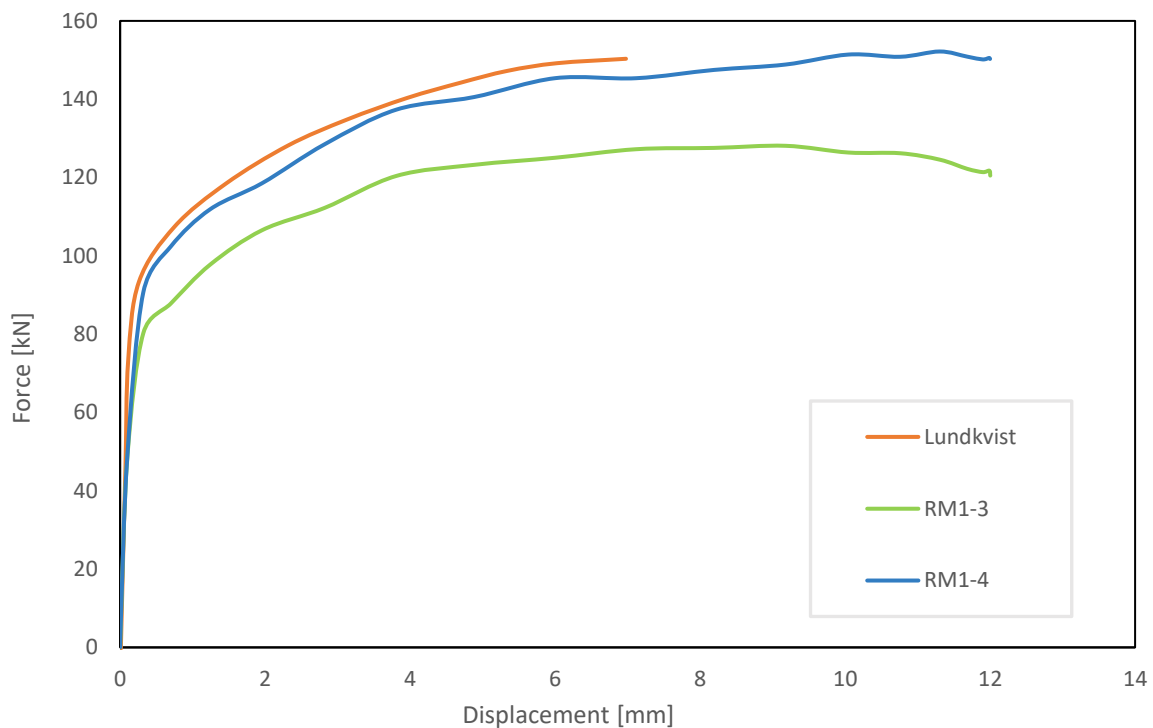

Figure 65: F-δ curves RM1-3 and RM1-4

In addition to solid element-based models, the possibility of utilizing shell element-based models has been investigated. The rivet will remain the same as in RM1-1 to RM1-4, constructed from solid elements, but the plates will consist of shell elements (S4R elements). The mesh element size remains the same as in the original models. Similar to RM1, four models have been constructed, and they follow the same notation as RM1 (with RM2-1 having no prestress and a course rivet mesh, RM-2-2 having prestress, but also a course rivet mesh, etc.).

It can clearly be seen from the force-displacement curves in Figure 66 that shell elements vastly understate the force acting on the specimen when compared to the experimental data, both in the elastic and in the plastic regimen. Therefore, shell elements should not be used to define stress concentrations within any given model.
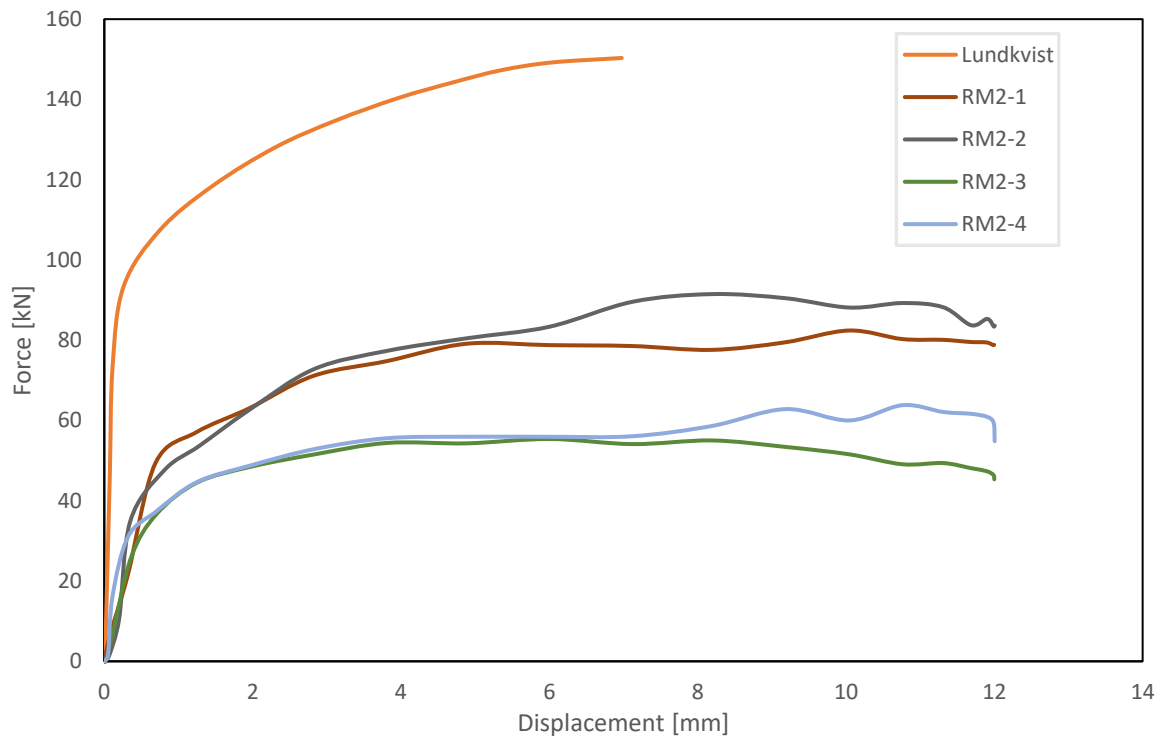
Figure 66: F-δ curves RM2-1, RM2-2, RM2-3 and RM2-4

Finally, the asymmetric specimen has been observed. The modelled specimen is the same specimen as the model by Lundkvist et al. displayed in Figure 53, though with the design choices based on the models from RM1-1 to RM 1-4. It uses the same dimensions (with the exception of the length of the rivet, given that there is one fewer plate), the same boundary and loading conditions, contact interactions and the same mesh. An example of the assembly can be found in Figure 67. Similarly, notation of the different models is maintained for the asymmetric models.
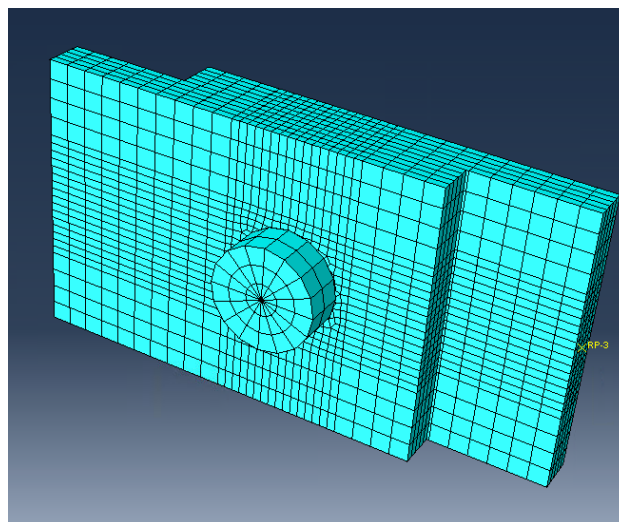

Figure 67: Assembly of the asymmetric reference model

The resulting F-δ curves show a high correspondence between Lundkvist et al.'s models and RM3-4, with RM3-4 slightly overstating the behaviour of the specimen to the behaviour described by Lundkvist et al. This may be caused by an overvaluation of the applied prestress. As previously

mentioned, no precise prestress was mentioned and a prestress of 100 MPa on the rivets is assumed.

Incidentally, RM3-1 also appears to be an acceptable result compared to Lundkvist et al.'s models. However, similar to RM1-1, the critical section in this model is the rivet shank, which suggests that refining the mesh there should provide more accurate results. Because RM3-3, which is the same as RM3-1 with a refined rivet mesh, significantly understates the behaviour of the specimen, while RM3-4, similar to RM1-4 in the symmetric model, does have prestressing applied and closely resembles the experimental results, it is assumed RM3-1's likeness to the experimental results is purely coincidental.
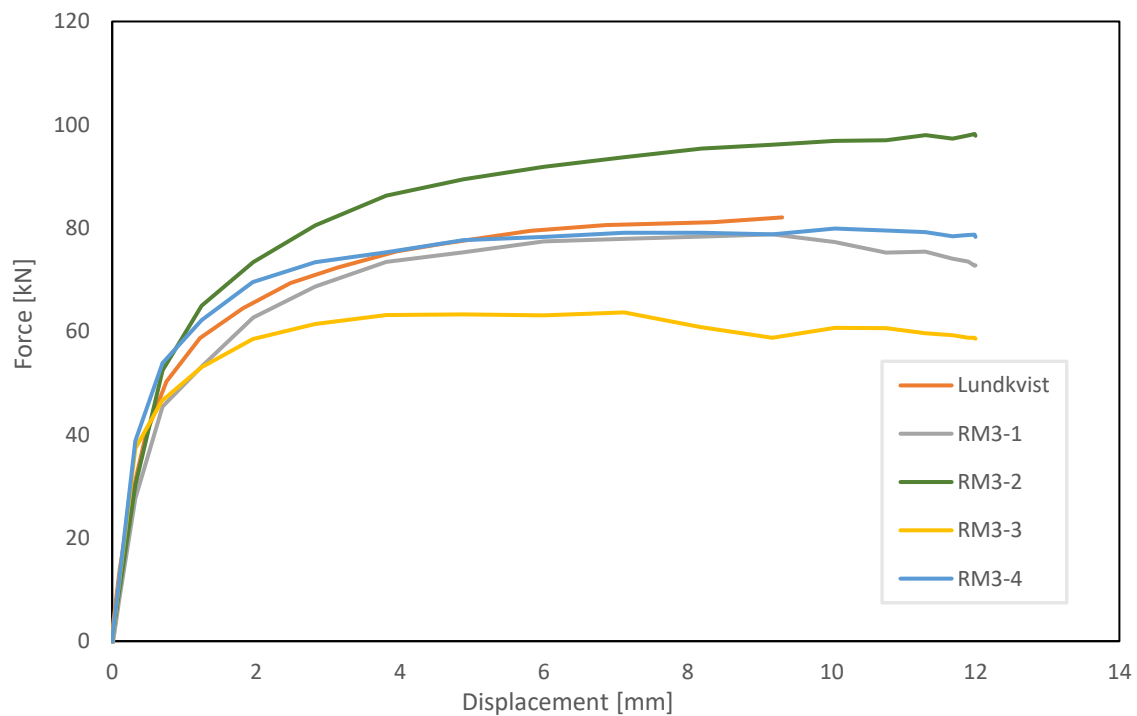

Figure 68: F-δ curves for RM3-1, RM3-2, RM3-3 and RM3-4

Given that the experimental force-displacements graphs of both symmetrical and asymmetrical assemblies can be captured quite accurately with the proposed models, the same principles used to build these models can be applied to a sub-model of the bridge joint model to capture the local behaviour of this joint.

4.2.2. Bridge joint model parameters and input

Through the construction of reference models based on D'Aniello et al.'s (2011) and Lundkvist et al.'s (2023) work, it has been shown that the local behaviour of riveted connections can be captured quite adequately. With this confirmation, the bridge joint model can be constructed. ABAQUS has a standard step-by-step approach to create a model, in which each step is represented by a module. Figure 69 illustrates each of the steps that needs to be performed, including the inputs required to fulfil this step. While several of the inputs are self-explanatory, such as the plate- and rivet dimensions and locations, any inputs that require some additional information will be laid out in this chapter.

A number of models have been built. The first, main model is a rough model of the bridge joint model. In this model, all plates are constructed with shell elements using a coarse mesh, does not

include prestressing, and has as purpose to identify any critical points within the bridge joint. Further models narrow down on these critical points, to identify more clearly the stresses and strains around the critical points, often using sub-modelling. These additional (sub-)models may vary in type of sub-modelling, mesh element size, shell or solid elements, etc. Additionally, several models with prestressing are considered. Further specifics are discussed in Chapter 5.
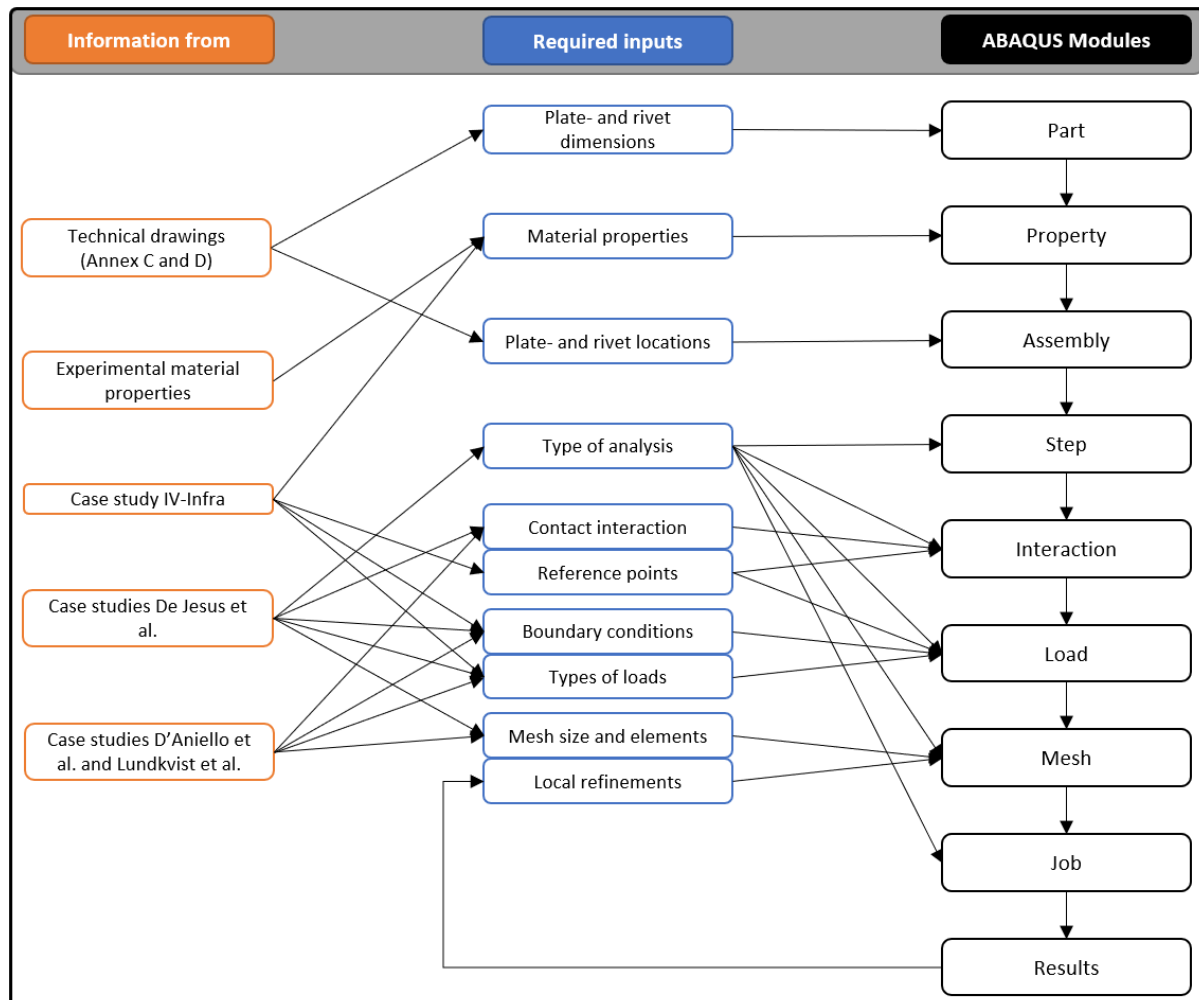

Figure 69: Process of bridge joint model building in ABAQUS

4.2.2.1.   Material properties

According to Chapter 2.3.1.1, the bridge joint is constructed from a mild steel, which roughly corresponds to modern day S235-steel. Standard material properties have been taken and are displayed in Table 22.

Table 22: Material properties joint model

Name	Density ρ [kg/m^3]	Poisson's ratio v [-]	Friction coefficient μ_f [-]
S235	7850	0,3	0,2

From D'Aniello et al.'s experiments and Lundkvist et al.'s models it is evident that the plastic behaviour should be incorporated in the models. The plastic behaviour is defined based on experimental work by Boller & Seeger (1987). It should be noted that the Young's modulus is also taken from this work, rather than the standard value of 210 GPa. Figure 70 illustrates the true stress-strain curve they have found to represent S235 steels. ABAQUS requires this true stress-strain curve for a material in order to model its plastic behaviour. More specifically, it only requires the plastic

region of the true stress-strain curve of the material. Using the values for E, K' and n' and Eq. 7, this curve is reproduced. By applying the 0,2%-proof stress, the yield point is found (which is found at σ = 273 MPa). The plastic region of the curve is then defined by disregarding the section of the curve before the yield point. Transforming the remainder of the curve by plotting the stress versus the plastic strain (essentially setting the yield stress at $\varepsilon_p = 0$, and adjusting the curve accordingly) allows for the plastic region of the true stress-strain curve to be defined and implemented in ABAQUS.
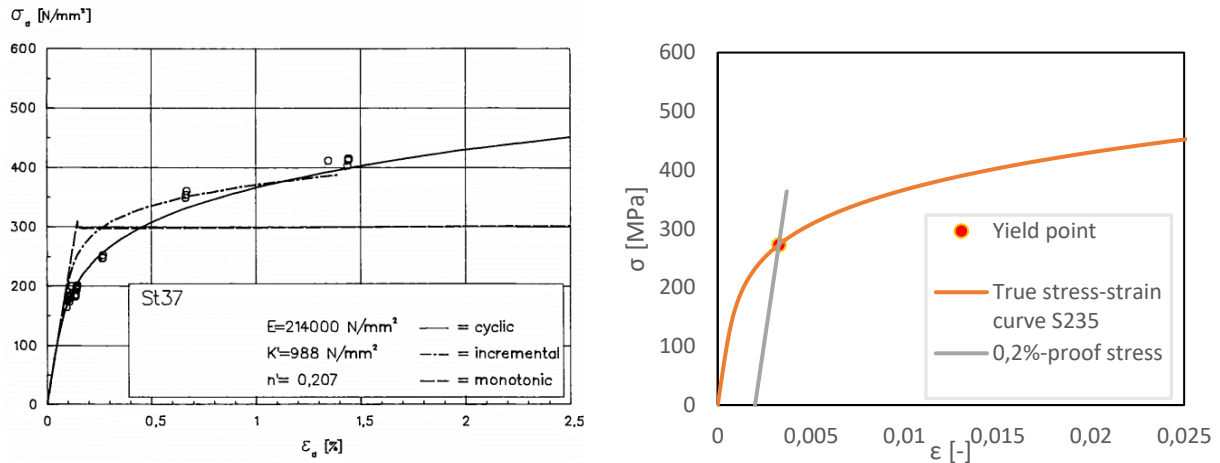

Figure 70: Experimental true stress-strain curve and its corresponding yield point

4.2.2.2. Analysis type

While the implicit ABAQUS/Standard method would normally be able to provide results that line-up with expected experimental results (see Chapter 4.2.1.1), this method has proven to be unfeasible for the bridge joint model, as the large number of contact interactions cause issues with convergence in its calculations. Following the confirmation by Chapter 4.2.1.1 that the use of ABAQUS/Explicit is possible too, this method is adopted for the bridge joint model. This method inherently affects the ways in which the steps (which define when a boundary condition, load or otherwise is applied to the model), contact interactions, loads and mesh elements are defined, but generally ABAQUS automatically adjusts these settings and they do not require additional adjustments by the user.

As mentioned in Chapter 4.1, the bridge joint model involves a large number of contact interactions, and considers the elasto-plastic behaviour of the joint. Therefore, a non-linear dynamic analysis is required. The steps created for such an analysis are inherently related to the type of analysis performed. For this analysis, dynamic explicit steps are used. Normally, the time increments in each of the steps of the analysis is directly dependent on the mesh size. However, to cut down on the amount of time it takes to run the model, the time increment size in each step in this explicit dynamic analysis is set to a minimum of $5 * 10^{-6}$, using the mass scaling function.

4.2.2.3. Contact interaction

With the large number of plates and rivets, it is not feasible to individually identify contact between parts and assign contact pairs accordingly. Therefore, similar to Chapter 4.2.1.1, contact is modelled using the explicit general contact method, which is able to automatically identify contact between different parts. Both tangential and normal contact behaviour are modelled using ABAQUS' recommended values, and with the friction coefficient defined in Table 22.

4.2.2.4. Reference points

Reference points are used to connect the ends of the beams to a singular point, allowing for the easy application of loads or boundary conditions. These points are used at the ends of the horizontal and diagonal beams and connected to all the edges of the plates that make up these beams, at the relevant locations (see Figure 71). The height of the reference points along the beams coincides with the centrelines of the beams as they have been defined in the SCIA model of the joint in Chapter 2.3.1.2. The connection between the reference point and the relevant cross-section is made through ABAQUS' rigid body constraints.
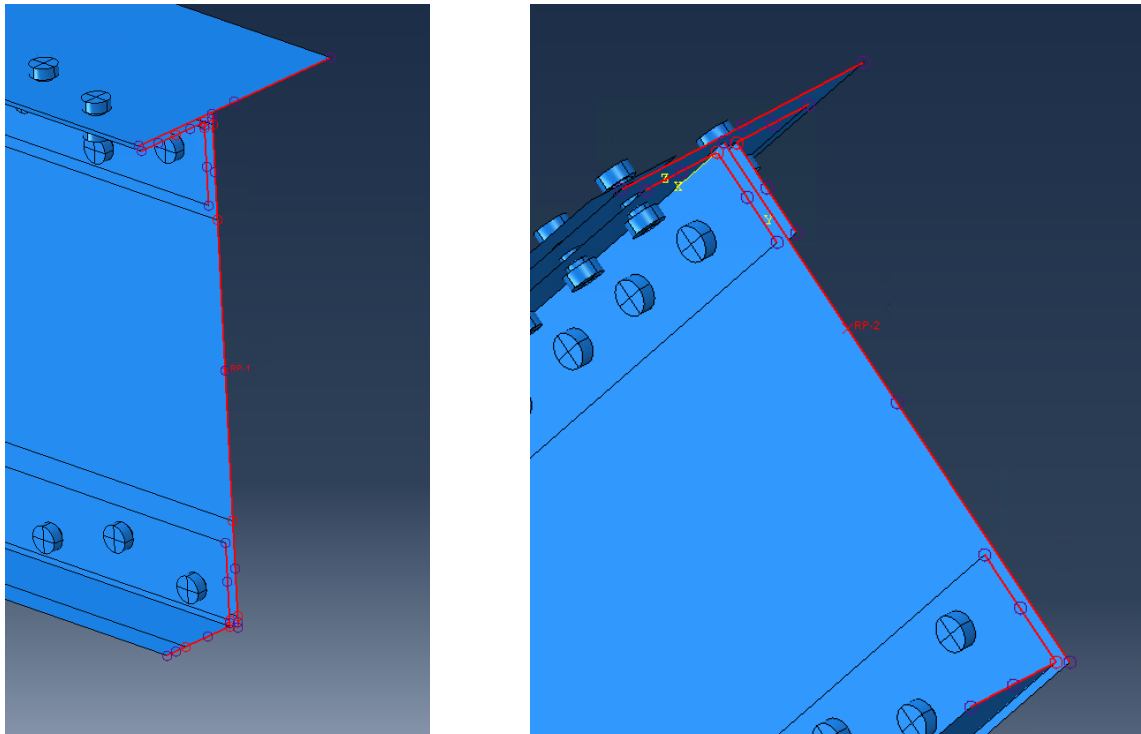

Figure 71: Reference points and connected edge in the horizontal beam (left) and diagonal beam (right)

4.2.2.5. Boundary conditions and types of loads

Boundary conditions are applied in the initial step (which is a step that is automatically created), before any loading is applied. Several boundary conditions can be identified.

Firstly, the model uses a plane of symmetry in the XY-plane. Using this plane of symmetry allows for only half the joint to be modelled, significantly cutting down on the number of elements in the model, as well as the calculation time. This condition puts a Z-symmetry boundary along all edges along the plane of symmetry. The Z-symmetry boundary condition restricts displacement in Z-direction and rotations around the X- and Y-axis.

From Chapter 2.3.1.2, the bottom of the joint is defined as a hinged support. A single pinned boundary condition is applied to the plates at the bottom of the joint. This condition restricts movement in all three directions, though rotations are allowed.
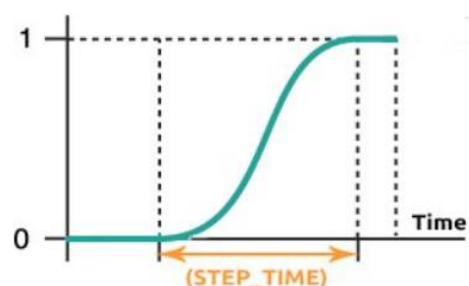

Figure 72: Example of a smooth step

Prestressing of the rivet, if present in the model, is applied directly after the initial step in which the boundary conditions are set. It follows the same principle as used in the reference models of

Chapter 4.2.1.1, applying an axial pressure to all the rivet heads. In ABAQUS/Explicit, a timeframe needs to be defined, which decides how long it will take for the load to be fully applied. The smooth step amplitude definition is used, applying the load from 0 to 100% in a predefined step time in a smooth manner (see Figure 72). For this model, the step time is equal to one second. This amplitude is also used to apply the prestressing. The degree of prestressing is very variable, which is why several models do not include prestressing. If it is present, a clamping stress of 40 MPa is taken, which is close the lower standard deviation of prestressing found by Zhou (1994).

The internal loads on the beams stem from the SCIA model and are modelled as an 'external' load at the shear centre of the cross-sections of the beams, applied directly to the reference points. Based on the presumed truss-like behaviour of the bridge, it can be stated that the internal loads on the main beam and the diagonal beam are inherently related to each other. Thus, only one load needs to be modelled. The other beam can be restrained in axial direction and should, following the force equilibrium, experience the same axial force that SCIA finds. This boundary conditions means no displacements in axial direction, and no rotations around the other axes of the beam. This would normally mean assigning local coordinate systems for the beams that line up with their axial direction, but the local coordinate system for the main beam coincides with the global coordinate system, so no additional coordinate system needs to be defined there. In the main beam an X-symmetry boundary condition can be defined (for which the reference point is used). The axial force applied to the diagonal beam is equal to 1652,39 kN. Rather than the initial step, like the boundary conditions, this axial force is applied in the final step, after the application of the boundary conditions (and possibly the prestressing) has completed.

Finally, as the diagonal is subjected to compression, it is susceptible to buckling. In reality this diagonal has various locations along its length in which out-of-plane buckling is restrained. The plates that accomplish this are not considered in the model. Therefore, in order to still make the diagonal refrain from buckling, an additional boundary condition is applied to all parts that make up the diagonal. This boundary conditions restricts displacement in Z-direction only, preventing the diagonal from buckling.

Figure 73 to Figure 76 show the boundary conditions and loads applied to the model.
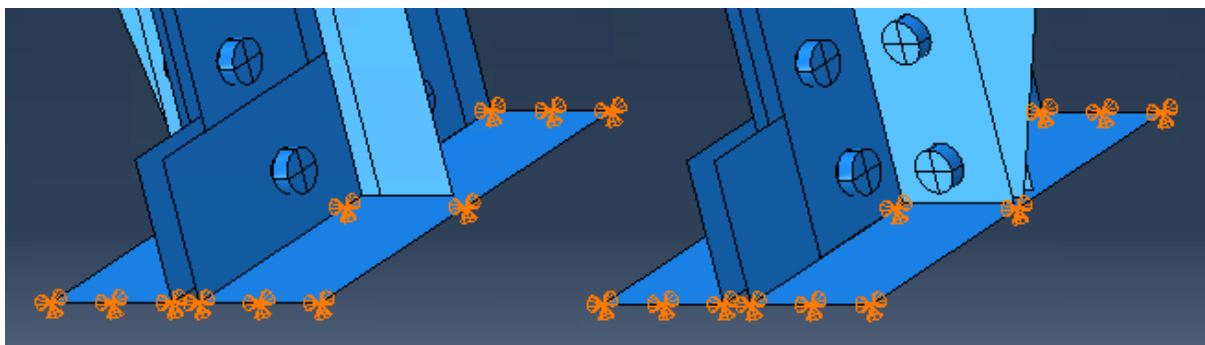

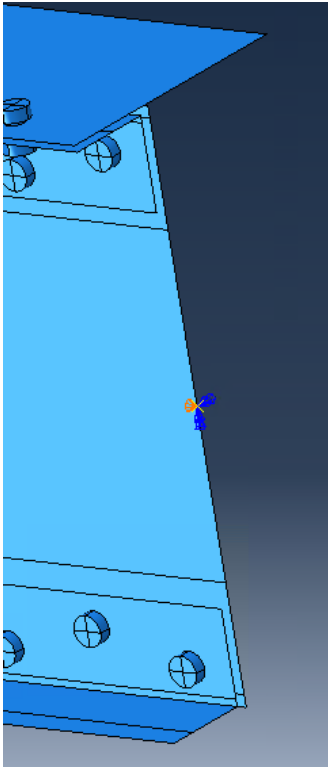*Figure 73: Hinged support boundary condition at bottom of joint*

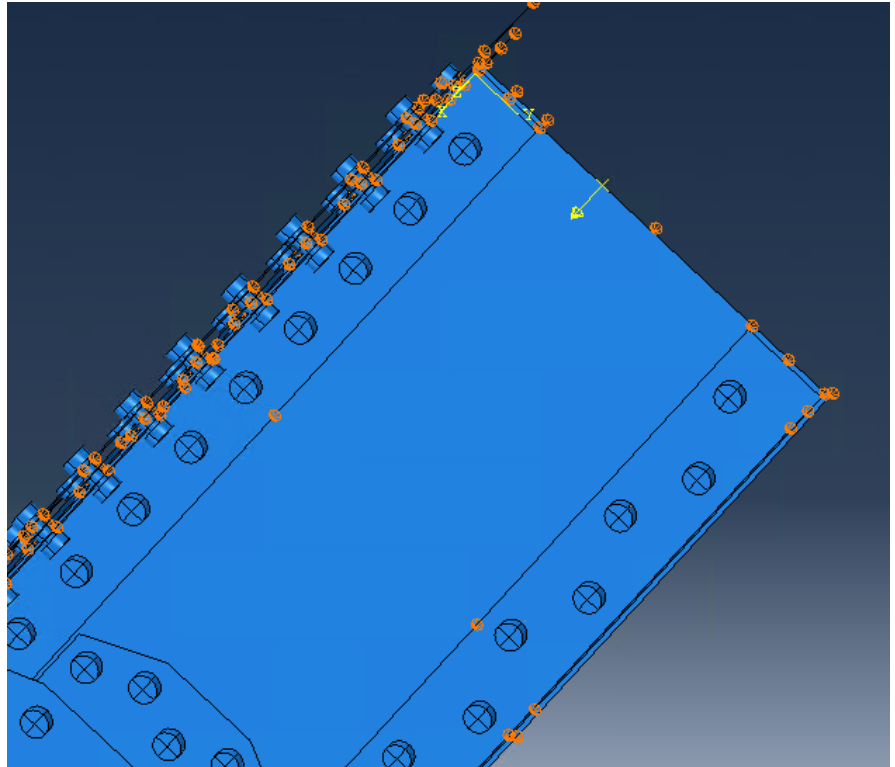*Figure 74: Boundary condition in reference point main beam*

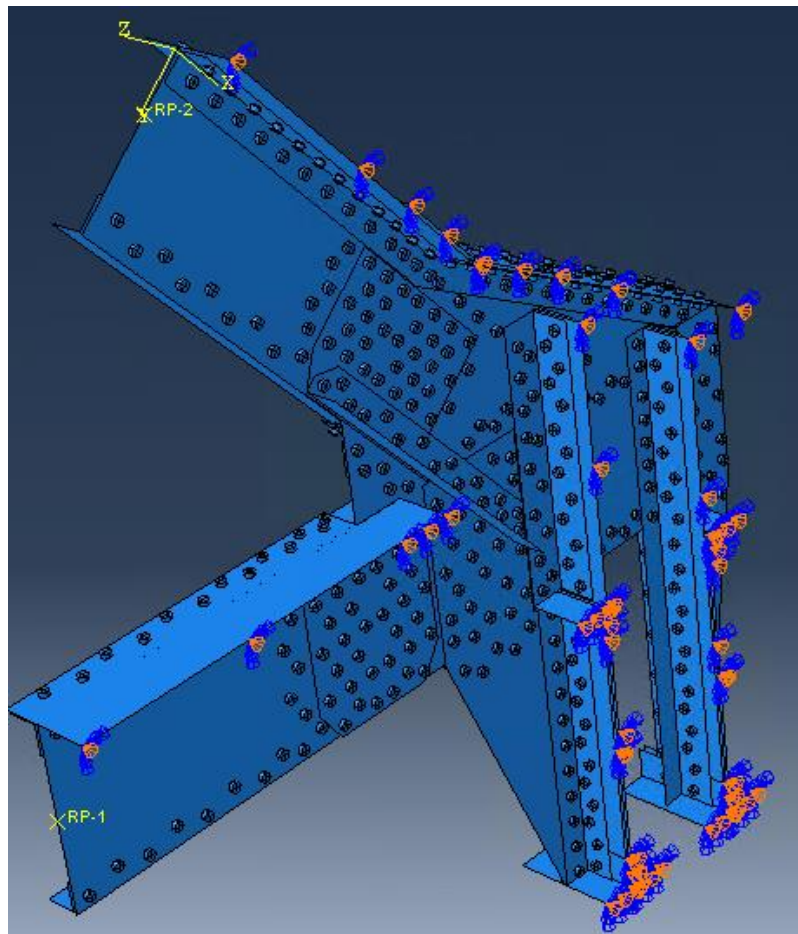*Figure 75: Load in reference point and boundary conditions on diagonal beam*

Figure 76: Symmetry boundary conditions on the complete joint

4.2.2.6.   Mesh size and elements

In general, the plates in the model are meshed using shell elements. These elements are S4R-elements, which are explicit, linear, quadrilateral, 4-noded shell elements with reduced integration. The rivets are meshed with solid elements. The elements for this mesh are C3D8R-elements, which are explicit, linear hexahedral, 8-noded solid elements with reduced integration. The actual mesh element size used in the first model, both on the rivets and on the plates, is very coarse, given the size of the total model, and has a mesh element size of 15 mm on all rivets and plates. The mesh itself is automatically generated by ABAQUS.
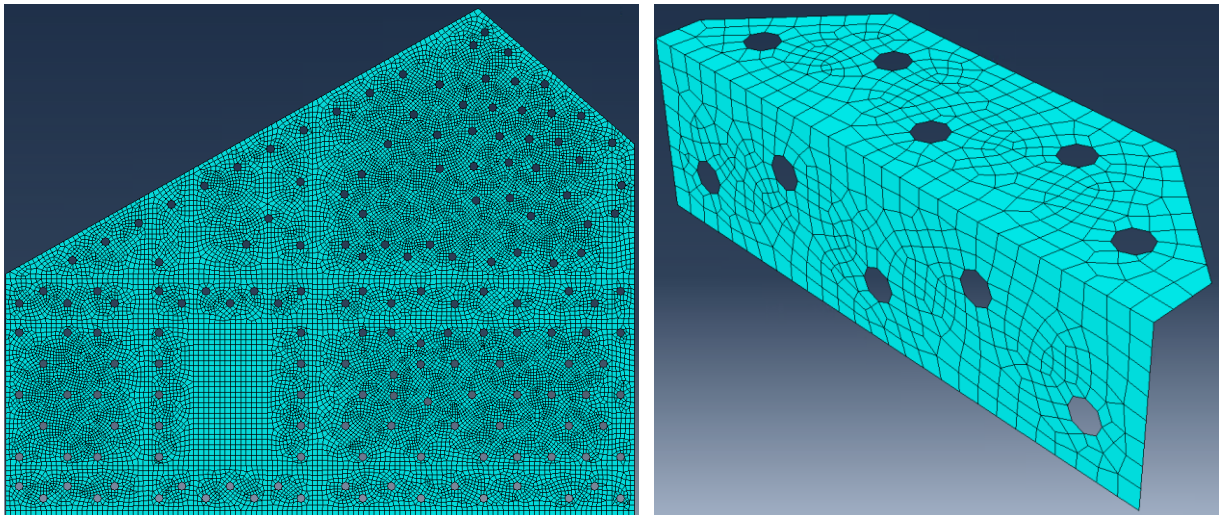

Figure 77: Example of a 15mm mesh on the gusset plate (left) and a small angle plate (right) of the bridge joint model

4.2.2.7.   Sub-models

Upon completion of the analysis of the shell-based bridge joint model, several points of interest within the joint can be identified (which will be discussed in Chapter 5) to be possibly critical to the strength and fatigue resistance. These locations need to be viewed in closer detail. However, as the joint model only uses very coarsely meshed shell-elements, it cannot be used for a detailed analysis. Therefore, sub-models can be constructed for this detailed view. There are two methods that can be adopted to create the sub-models. The first method designs the sub-models separate from the large bridge joint model and takes internal stresses on the large bridge joint as input for its own analysis. The second method incorporates the sub-model directly into the large joint model. By partitioning the bridge joint model around a point of interest, a smaller section can be investigated more clearly. This investigation can be done by either refining the mesh in that partition directly, or cutting out the partition altogether, and replacing it with a separate section, usually constructed with solid elements. Refining the mesh in the partition itself has as benefit that it requires very few additional actions. However, given that the bridge joint model is entirely modelled with shell elements, it may not provide entirely accurate results. Replacing the partition with a solid element-based section may be preferred option, as it generally provides more accurate results.

While the first method would be beneficial to limit calculation times, as the bridge joint model would only need to be run once, the extrapolation of internal stresses in shell elements to the cross-sections of solid element-based models has proven unreliable, resulting in excessive stresses around the edges of the model, which in turn affects the stress distribution throughout the sub-model completely. Therefore, the second method has been adopted in this report.

Mesh element sizes in the refined sub-models, either with shell or solid elements, are set to 2 mm. This matches with the refinement of the mesh adopted in the reference models from Chapter 4.2.1.1. Both shell and solid mesh element types match those mentioned in Chapter 4.2.2.6.

In the case the partitioned section is replaced with a solid-based section, the contact between shell elements and solid elements needs to be established. ABAQUS provides a shell-to-solid coupling constraint, which is used to bind the two cross-sections of the shell part to the connected cross-sections of the solid part. An example of how they are connected is shown in Figure 78, as well as how the solid sub-model is integrated in the large bridge joint model.
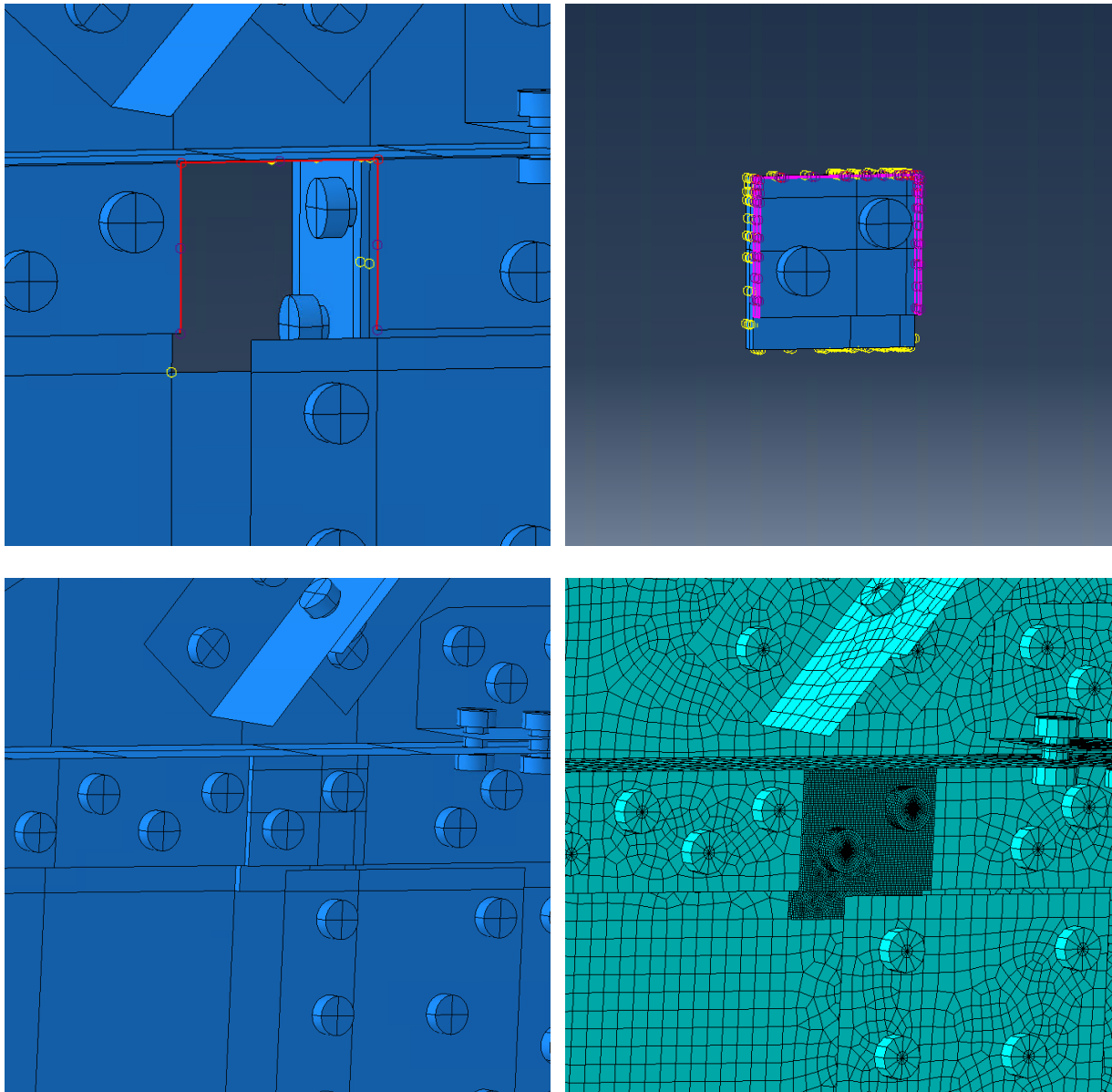
Figure 78: Shell-to-solid connection (top) and the integration of the solid sub-model with the shell-based bridge joint model (bottom)

All plates within the boundaries of the point of interest have been modelled with solid elements, to ensure that contact between the plates themselves and the plates and the rivets can be considered adequately. The sub-models considered are primarily situated in the XY-plane of the model. While some of the plates in the sub-models do have flanges situated in the YZ-plane of the model, as they are originally angle plates, incorporating them into the sub-model would cause issues when

meshing, and would require for the meshing process to be reformatted. Therefore, they have been left out of consideration for the sub-model.

4.2.3. Automatic model generation

As mentioned in the introduction of this chapter, the majority of the models in this report have been constructed automatically, in order to simplify the development of the model and to be able to easily adjust any parameters without having to rebuild the model. All automatically constructed models are based on the initial, shell element-based model. Additional adjustments, such as the construction of the sub-models, or remeshing of the partitioned sections, have been done manually.

ABAQUS' Python-based scripting language as well as Excel was used. This chapter will cover some of the code used to generate the model, following the same order that the ABAQUS modules shown in Figure 69 follow.

In its basis, the script to generate the bridge joint model uses two files. The first file consists of several independent functions, which can be used to manipulate the file ABAQUS uses to generate a model. The second file calls these functions, with the required inputs to create the model of the investigated joint of the John S. Thompsonbridge.

4.2.3.1.   Generation of parts

The start of the model is to create all the individual parts out of which the bridge joint is constructed. Based on the technical drawings from Annex C and Annex D, the dimensions of every single plate within the joint has been manually denoted. The corner points of every single plate, as well as the location of every single bolt hole has been noted down. These locations use [X, Y]-notations based on a plane parallel to the drawings. Flanges of angle plates have their dimensions saved separately.   Furthermore, the thickness of each plate is noted. An example of the plate notation in Excel is shown in Figure 79. For a total of eighty plates, this process is repeated. For all plates combined, 1609 different rivet holes have been identified and noted down.

Name	Thickness	Cornerpoints	Boltlocations	# of rivets
CoverPl_Main_Out	10	[[210,330],[280,225],[280,-225],[210,-330],[-210,-330], [-280,-225],[-280,225],[-210,330]]	[[40,0],[140,0],[240,0],[40,180],[140,180],[240,180],[40,-180],[140,-180],[240,-180],[40,300], [115,265],[190,300], [40,-300],[115,-265],[190,-300],[90,90],[190,90],[90,-90],[190,-90], [-40,0],[-140,0],[-240,0],[-40,180],[-140,180],[-240,180],[-40,-180],[-140,-180],[-240,-180], [-40,300],[-115,265],[-190,300],[-40,-300],[-115,-265],[-190,-300],[-90,90],[-190,90],[-90,-90], [-190,-90]]	38

Figure 79: Example of the plate notation in Excel.

With a simple script, this Excel file can be saved in a dictionary, which can then be referenced within the ABAQUS code.

In order to generate the plates, the 'plates'-function is called, which takes the following inputs:

- The name of the model, which is specified at the very start of the model generation;
- The dictionary with plate geometries taken from Excel;
- The name of the plate that needs to be generated. This name needs to correspond with one of the names within the dictionary;
- The size of the rivet holes. It is assumed in this function that all rivet holes have the same diameter;
- The name of the material the plate is to be made of;
- A list of plate thicknesses. This list is used to keep track of the thicknesses that have already been used to generate shell-based plates;

- A list of parts that need to be modelled using solid elements rather than shell elements. This functionality is built into the 'plates'-function, but is not inherently used, as the base model is constructed with shell elements.

The function subsequently finds the data in the dictionary corresponding to the specified name, checks if the plate is present in the list of parts that require solid mesh elements, and generates the plate as a part in ABAQUS, either as a shell-based or solid-based part.

By looping through every single plate within the dictionary, every plate can be generated in this way. Using the naming convention of the plates this loop can also be used to identify plates that are either part of the kinked plates that connect the diagonal to the large gusset plate, or part of an angle plate, which require some additionally processing. Once both flanges of angle plate have been generated, a new function is called (assemble_Lplate) which is able to combine the individual flanges into a single angled plate. In the same way, a function (assemble_kink) is able to combine the two separate parts of a kinked plate into a single kinked plate. Figure 80 shows the loop used to generate the plates.

```
## Create plates
Lplate_section = []
thiccc = []
kink_list = []

for key in database.keys():
    if 'Kink' in key:
        if (key[-2:] in ['XY', 'XZ', 'YZ']):
            if key[:-3] not in kink_list:
                kink_list.append(key[:-3])
        else:
            kink_list.append(key)
    print('Generating ' + key)
    plates(database, key, 24, model_name, material_name, thiccc, solid_list)
    if (key[-2:] in ['XY', 'XZ', 'YZ']):
        print(key + ' is part of an L-plate')
        if (len(Lplate_section) == 0):
            Lplate_section.append(key)
            print(key + ' has no match in list. Adding to list...')
        else:
            for i in range(len(Lplate_section)):
                if Lplate_section[i][:-3] == key[:-3]:
                    print(key + ' has match in list. Combining ' + key + ' and ' + Lplate_section[i])
                    assemble_Lplate(model_name, key, Lplate_section[i])
                    Lplate_section.remove(Lplate_section[i])
                    break
                if i == (len(Lplate_section) - 1):
                    Lplate_section.append(key)
                    print(key + ' has no match in list. Adding to list...')

## Combine kinked plates
for key in kink_list:
    assemble_kink(model_name, key, database)
time.sleep(1)
```

Figure 80: Loop used to generate plates

Rivets are generated with their own function. The arguments required for this function are:

- The name of the model;
- The name of the material used for the rivets;
- The diameter of the rivet shanks. Again, this function presumes all rivets have the same diameter;

78

- A list of all the shank lengths that are used in the model. These lengths are dependent on the thicknesses of the plates, and the plates that need to be bound together. This list has been assessed manually.

They are always constructed from solid elements. Their heads all have the same dimensions, regardless of shank size, which will be designed based on the recommended dimensions defined by Colette (2014), who states that:

- Head diameter should follow: $1,4 \leq D_{shank} \leq 1,8$;
- Head height should follow: $0,55 \leq D_{shank} \leq 0,75$.

Using the provided diameter and length of the shank, the heads and shank are generated separately and combined into one part after.

4.2.3.2.   Assignment of properties

Both the 'plates'- and the 'rivet'-functions automatically assign the type of material to the plates and rivets respectively. This requires for this material to have been defined prior to this assignment. This material is generated automatically, based on the material properties defined in Chapter 4.2.2.1.

The shell-based parts need to be assigned a cross-section. Given the geometry of the plates, only a material and a thickness are required to generate such a cross-section. The list of thicknesses that is required in the 'plates'-function is used to keep track of the thicknesses that have already been assigned to the shell-based parts, and if a new thickness needs to be assigned, it creates the relevant cross-section for these parts. Solid element-based parts do not need to be assigned a cross-section, so there is no need to keep track of thicknesses of solid-based parts. Because the same material is used for all plates and rivets, the material can automatically be assigned to either the solid parts, or the cross-sections of the shell parts.

4.2.3.3.   Assembly of joint

With all the parts defined, the model can be assembled. This requires for all plates and all rivets to undergo a specific degree of translation and rotation, which is different for all instances. These rotations and translations have first been defined manually, and saved such that the script can automatically assemble all the parts in any subsequent runs. The functions used for this assembly loops through the parts that have been created, and if a part name matches one of the names for which a translation and/or rotation have been defined, loads the part into the assembly and automatically places it in the correct spot. An example of the code used to assemble plates within the joint can be found in Figure 81. In this snippet of code, a part is loaded into the assembly, rotated to ensure the correct orientation, and subsequently translated to its correct position.

```
if 'BottFl_Main' in mdb.models[model_name].parts.keys():
    mdb.models[model_name].rootAssembly.Instance(dependent=ON, name='BottFl_Main-1',
        part=mdb.models[model_name].parts['BottFl_Main'])
    mdb.models[model_name].rootAssembly.rotate(angle=-90.0, axisDirection=(10.0,
        0.0, 0.0), axisPoint=(0.0, 0.0, 0.0), instanceList=('BottFl_Main-1', ))
    mdb.models[model_name].rootAssembly.translate(instanceList=(
        'BottFl_Main-1', ), vector=(0.0, 6.5, 14.5))
```

Figure 81: Script used to load part instance 'BottFl_Main' into the correct location in the assembly

The rivets are placed using a similar method. However, a rivet only needs to be created once for it to be used in multiple instances. Therefore, a separation is made between rivets with different shank sizes. Utilizing ABAQUS' function to copy rivets in a specific pattern, repeat instances are then placed in the correct positions. An example is provided in Figure 82, where two rivets with a shank length of

26 mm are placed withing their corresponding positions on two angle-plates near the bottom flange of the main beam, and copied in a specific pattern to ensure all the rivet holes are filled.

```python
def riv26(model_name, boltloads, clamping_force):
    #AngleBottFl_Main_Left and AngleBottFl_Main_Right
    mdb.models[model_name].rootAssembly.Instance(dependent=ON, name='Rivet_D23_26-1'
        , part=mdb.models[model_name].parts['Rivet_D23_26'])

    mdb.models[model_name].rootAssembly.translate(instanceList=('Rivet_D23_26-1', ),
        vector=(60.0, -50.0, -21.0))
    mdb.models[model_name].rootAssembly.LinearInstancePattern(direction1=(1.0, 0.0,
        0.0), direction2=(0.0, 1.0, 0.0), instanceList=('Rivet_D23_26-1', ),
        number1=2, number2=1, spacing1=120.0, spacing2=180.0)
    mdb.models[model_name].rootAssembly.LinearInstancePattern(direction1=(1.0, 0.0,
        0.0), direction2=(0.0, 1.0, 0.0), instanceList=('Rivet_D23_26-1', ),
        number1=2, number2=1, spacing1=1060.0, spacing2=180.0)
    mdb.models[model_name].rootAssembly.LinearInstancePattern(direction1=(1.0, 0.0,
        0.0), direction2=(0.0, 1.0, 0.0), instanceList=('Rivet_D23_26-1-lin-2-1-1', ),
        number1=3, number2=1, spacing1=166.0, spacing2=180.0)
    mdb.models[model_name].rootAssembly.Instance(dependent=ON, name='Rivet_D23_26-2'
        , part=mdb.models[model_name].parts['Rivet_D23_26'])
    mdb.models[model_name].rootAssembly.translate(instanceList=('Rivet_D23_26-2', ),
        vector=(135.0, -100.0, -21.0))
    mdb.models[model_name].rootAssembly.LinearInstancePattern(direction1=(1.0, 0.0,
        0.0), direction2=(0.0, 1.0, 0.0), instanceList=('Rivet_D23_26-2', ),
        number1=2, number2=1, spacing1=1068.0, spacing2=180.0)
    mdb.models[model_name].rootAssembly.LinearInstancePattern(direction1=(1.0, 0.0,
        0.0), direction2=(0.0, 1.0, 0.0), instanceList=('Rivet_D23_26-2', ),
        number1=2, number2=1, spacing1=1234.0, spacing2=180.0)
```

Figure 82: Script used to insert rivets with shank length of 26 mm into their corresponding positions, utilizing ABAQUS' ability to copy instances in a pattern

Figure 83 illustrates the model of the joint once all plates and rivets have been placed in their correct locations. Additionally, the locations of the reference points are included.

4.2.3.4. Step definition, contact interaction, boundary conditions and load application

The vast majority of actions that need to be performed to create a model, have a corresponding function within ABAQUS' scripting language. Each of these functions require a vast number of parameters, which ABAQUS is able to interpret and apply to the model. Many of these parameters remain untouched. This section will shortly go into the parameters that do require to be touched, for each of the actions.
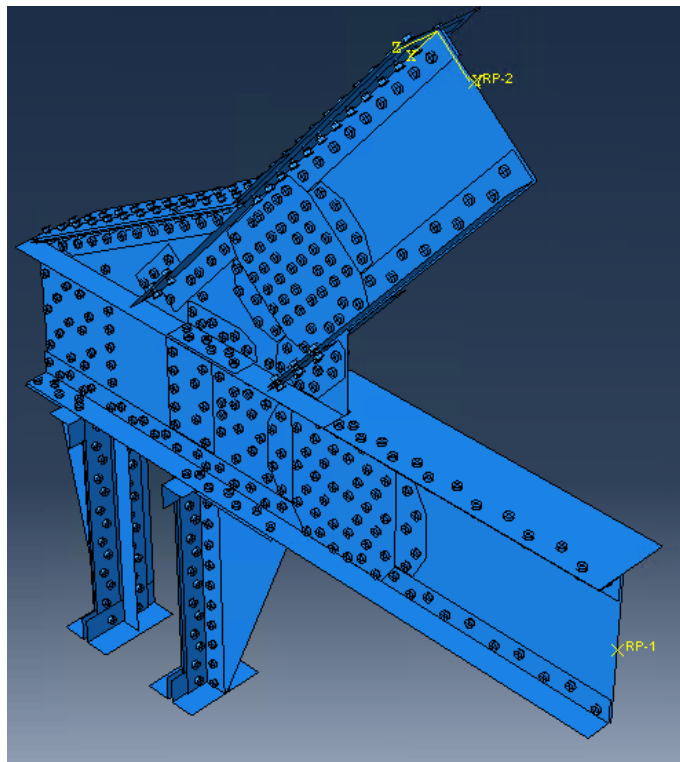

Figure 83: Assembly of the model, with all plates and rivets in their appropriate location

Step definition in ABAQUS/Standard can be performed with a different function that in ABAQUS/Explicit, which is why the type of analysis

needs to be defined first. Once the explicit-step function is called, only the mass scaling needs to be defined, and the smooth step amplitude described in Chapter 4.2.2.5 needs to be implemented. Dependent on the presence of prestressing, either one or two steps are created (beyond the initial step, which is always present), in which the load application can be defined. Boundary conditions and contact interactions are defined in the initial step.

Contact interaction is defined with two functions. The first function defines the type of contact, following the parameters defined by Chapter 4.2.2.3. The second function defines to which elements this contact interaction needs to be applied. The function that is called for this, depends on the type of analysis (implicit or explicit), and if the contact needs to be applied to everything (e.g., 'General contact') or only to individual elements.

Boundary conditions require a similarly simple function, only requiring the type of boundary condition that needs to be applied, and the set of elements to which this condition needs to be applied. The same principle holds for loads. The called function is dependent on the type of load that needs to be defined (e.g., a point load or a pressure). After that, the magnitude of the load and the direction in which it acts are defined. Finally, it requires the time over which said load needs to be applied (which in this case is described by the smooth-step amplitude).

The script used to generate the loads and boundary conditions automatically identifies all edges and faces that should belong to one of the boundary conditions, and groups them in a set. This grouping is done by defining a boundary box (by defining the minimum and maximum value in X-, Y- and Z-direction). Any faces or edges that are completely within this boundary box are added to the set. A simple script then takes this set as input and applies the respective boundary conditions to it.

```python
def create_set_byBoundingBox(model_name, boundaries, setName, elems=False):
    edge_list = []
    surface_list = []
    elem_list = None
    for eachInstance in mdb.models[model_name].rootAssembly.instances.values():
        if elems:
            elem = eachInstance.elements.getByBoundingBox(xMin=boundaries[0],xMax=boundaries[1],
                yMin=boundaries[2],yMax=boundaries[3],zMin=boundaries[4],zMax=boundaries[5])
            if elem_list == None:
                elem_list = elem
            else:
                elem_list += elem
        else:
            if 'Rivet' not in eachInstance.name:
                e = eachInstance.edges.getByBoundingBox(xMin=boundaries[0],xMax=boundaries[1],
                    yMin=boundaries[2],yMax=boundaries[3],zMin=boundaries[4],zMax=boundaries[5])
                for j in range(len(e)):
                    edge_list.append(eachInstance.edges[e[j].index])
                s = eachInstance.faces.getByBoundingBox(xMin=boundaries[0],xMax=boundaries[1],
                    yMin=boundaries[2],yMax=boundaries[3],zMin=boundaries[4],zMax=boundaries[5])
                for i in range(len(s)):
                    surface_list.append(eachInstance.faces[s[i].index])
    if elems:
        if len(elem_list) != 0:
            mdb.models[model_name].rootAssembly.Set(name=setName, elements=elem_list)
        else:
            print('No elements found in bounding box')
    else:
        if len(edge_list) != 0:
            if len(surface_list) != 0:
                mdb.models[model_name].rootAssembly.Set(name=setName, edges=part.EdgeArray(edge_list),
                    faces=part.FaceArray(surface_list))
            else:
                mdb.models[model_name].rootAssembly.Set(name=setName, edges=part.EdgeArray(edge_list))
        else:
            print('No edges or surfaces found in bounding box')
    return
```

Figure 84: Script used to define a set with a boundary box

As can be seen in Figure 84, the function used to create sets is also able to distinguish between (mesh) elements, and faces and edges. For the purpose of load and boundary conditions, only the functionality to group faces and edges is relevant. In these cases, it also ignores rivet-instances, as no boundary conditions are applied to them.

4.2.3.5. Meshing of the model

The process of mesh generation is done automatically by looping through all parts in the model, and calling a function on each of these parts which is used to identify the type of mesh that is required, and subsequently defines this mesh.

```python
def meshing(model_name, part_name, mesh_size=0, solid=False, expl=False):
    if 'Rivet' in part_name:
        try:
            for planename in [XZPLANE, YZPLANE]:
                mdb.models[model_name].parts[part_name].DatumPlaneByPrincipalPlane(offset=0.0,
                    principalPlane=planename)
            names = mdb.models[model_name].parts[part_name].features.keys()
            ids = []
            for j in range(len(names[-2:])):
                ids.append(mdb.models[model_name].parts[part_name].features[names[-2+j]].id)
            for i in range(len(ids)):
                mdb.models[model_name].parts[part_name].PartitionCellByDatumPlane(datumPlane=mdb.models[
                    model_name].parts[part_name].datums[ids[i]], cells=mdb.models[model_name].parts[
                    part_name].cells.getByBoundingBox())
        except:
            pass
    if mesh_size == 0:
        mdb.models[model_name].parts[part_name].seedPart(deviationFactor=0.7,
            minSizeFactor=0.7, size=round(int(part_name[7:9]) / 2))
    else:
        mdb.models[model_name].parts[part_name].seedPart(deviationFactor=0.7,
            minSizeFactor=0.7, size=mesh_size)
    mdb.models[model_name].parts[part_name].setMeshControls(algorithm=
        ADVANCING_FRONT, elemShape=HEX_DOMINATED,
        regions=mdb.models[model_name].parts[part_name].cells.getByBoundingBox(), technique=SWEEP)
    if not expl:
        mdb.models[model_name].parts[part_name].setElementType(elemTypes=(ElemType(
            elemCode=C3D8R, elemLibrary=STANDARD), ElemType(elemCode=C3D6,
            elemLibrary=STANDARD), ElemType(elemCode=C3D4, elemLibrary=STANDARD)),
            regions=mdb.models[model_name].parts[part_name].Set(name='Mesh'+part_name, cells=mdb.models[model_name].parts[
            part_name].cells.getByBoundingBox()))
    else:
        mdb.models[model_name].parts[part_name].setElementType(elemTypes=(ElemType(
            elemCode=C3D8R, elemLibrary=EXPLICIT, secondOrderAccuracy=OFF,
            kinematicSplit=AVERAGE_STRAIN, hourglassControl=DEFAULT,
            distortionControl=DEFAULT), ElemType(elemCode=C3D6, elemLibrary=EXPLICIT),
            ElemType(elemCode=C3D4, elemLibrary=EXPLICIT)),  regions=mdb.models[
            model_name].parts[part_name].Set(name='Mesh'+part_name, cells=mdb.models[model_name].parts[
            part_name].cells.getByBoundingBox()))
    mdb.models[model_name].parts[part_name].generateMesh()
```

Figure 85: Section of the function used to generate meshes. This section identifies and meshes rivet parts.

The inputs for this function are:

- The name of the model;
- The name of the part;
- The mesh element size that needs to be adopted. This element size can either be set to the standard values described above, or be explicitly specified;
- A list of plates that need to be meshed with solid elements rather than shell elements;
- The type of analysis that needs to be run, which in this case is the ABAQUS/Explicit analysis.

The particular section shown in Figure 85 illustrates the process used to generate the mesh on rivets. Using the naming convention, the script identifies whether the part is a plate or a rivet. If it is indeed a rivet, it partitions the rivet into four symmetric sections, assigns an approximate mesh element size, defines the meshing method (e.g. the sweeping method), defines the elements that need to be used, which is dependent on the type of analysis that is to be run, and finally generates the mesh on the rivet.

For the mesh generation on plates, a similar approach is used, though partitioning of the plates is not necessary. Furthermore, a small section of code identifies whether the name of the plate is

present in the list of solid plates, indicating that solid elements need to be used when meshing. If not, shell elements are used.

4.2.3.6. Job creation and running of the model

With the mesh generation completed, a job can be created. This job is used for the analysis of the model. This job can be created manually, but for ease of use a simple is script is used to generate a job automatically. This job uses all standard setting applied by ABAQUS and needs to be run manually.

4.2.3.7. Sub-models

As previously mentioned, there are two methods to create sub-models. The first method designs the sub-models separate from the large joint model, and takes internal stresses on the large joint as input for its own analysis. A script has been written that is able to automatically create these types of sub-models. Part-, material- and assembly definition follow the same principles as the large model does. The sub-model can be generated by defining a point of interest within the assembly (using its X-, Y- and Z-coordinates). All parts in the assembly around this point can be identified with the 'create_set_byBoundingBox'-function displayed in Figure 84 and saved to a list. Using this list, a function is called that that takes all the information on these plates from the Excel-file, and generates them in a new model, with solid elements. Similarly, only the rivets near this point of interest are modelled. The same function used to assemble all parts in the large joint (as described in Chapter 4.2.3.3) is applied to the sub-model, placing all modelled parts into their correct position. From here, the parts are partitioned around the point of interest. All elements of the parts outside of this partition can be removed, which leaves only the point of interest.
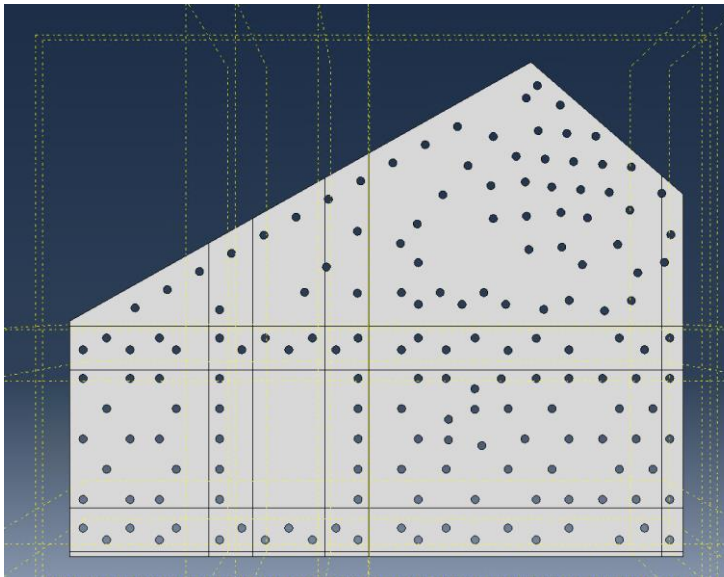
Figure 86: Partition of gusset plate around several points of interest.   Figure 87: Sub-model of a point of interest
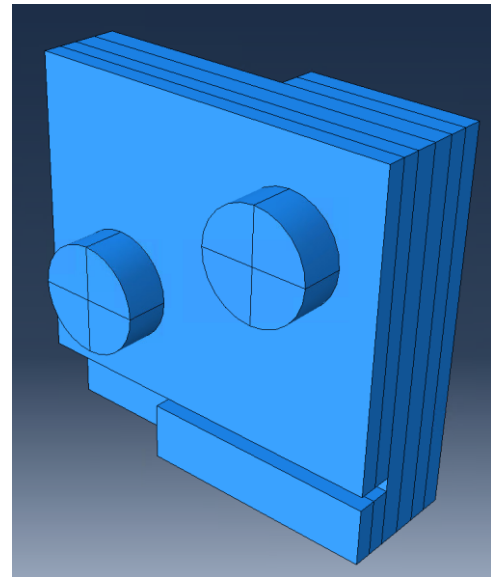
From the results file of the original joint model, the internal stresses present in the main model are found. At the location in the large model, corresponding to where the sub-model would be, these internal stresses are taken and applied onto the edges of the sub-model. As the results are taken from a shell-based model and applied to a solid-based model, the internal stresses are extrapolated by ABAQUS automatically. The sub-model also adopts a more refined mesh compared to the large model, to get a clearer view of the effect of the stresses around the point of interest. This mesh is generated automatically, using the same process as the meshing of the large model. Once the 'loads' are applied and a finer mesh is generated, the sub-model can be run and analysed.

The second method of sub-modelling, and the method that is adopted in this report, starts off the same as when separate sub-models are created. However, rather than initially running the large model and extrapolating the internal stresses to a sub-model, the sub-model is incorporated within the large model. Generation of the large joint model is done automatically, as well as the partitioning around points of interest, but the removal of the shell-element based section (such as in Figure 88) and the creation and placement of its 'replacement' solid-element based section is done manually and is not incorporated into the automatic model generation.
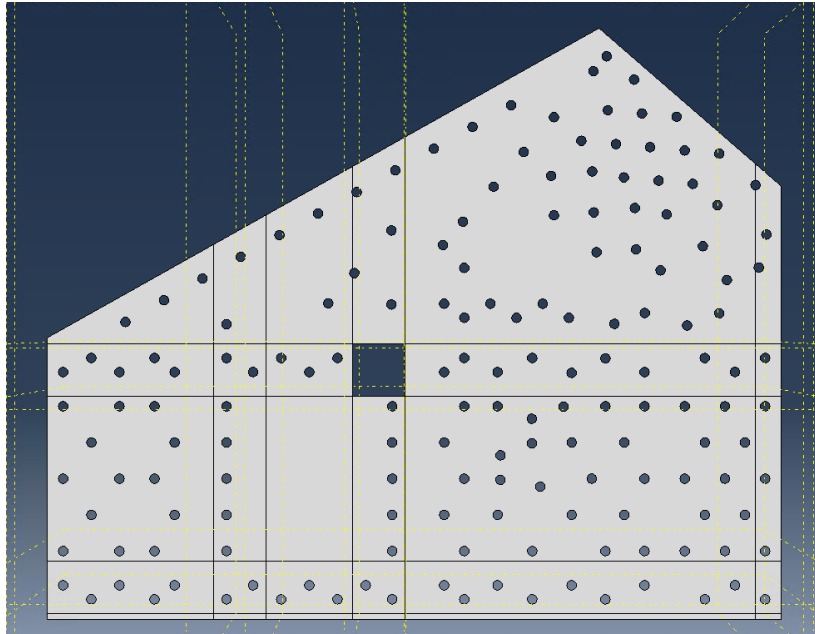

Figure 88: Plate with point of interest removed

5. Results FEA

The first and second sections of this chapter will look into the results from the models described in the previous chapter. The bridge joint model considered in this subchapter 5.1.1 is the base joint model, a model in which all plates are constructed with shell elements, and no prestressing is applied to the rivets. A general insight in the distribution of stresses throughout the joint is provided, and locations that experience excessive stress concentration are identified. The locations with high stress concentrations can be defined as the critical sections for the fatigue response of the joint. One critical section will be chosen to model in more detail (see Chapter 4.2.3.7), and serves as the basis for the sub-model. Subsequently, the internal stresses and strains in the sub-model will be observed. A comparison between the results of the base model and sub-model is made, and any differences are noted.

Chapter 5.2 follows the same principles as outlined in Chapter 5.1, but for a model in which prestressing is applied on the rivets.

After the overview of the results of the different models, results from both the non-prestressed and prestressed models are presented and compared. These results feed directly into Chapter 6, and form the basis for the assessments made in that chapter.

Finally, in the last sub-chapter, a preliminary analytical analysis of the connection is performed. This is intended to show the general distribution of forces in the different members of the connection and will be used as a benchmark to verify the accuracy of the finite element results.

5.1. Results bridge joint model without prestress

In order to identify critical sections in the joint, locations with high stress concentrations need to be observed. Because this is primarily a fatigue-related assessment, compressive stresses can be neglected. For the identification of stress concentrations and subsequent critical locations, the principal stress are considered.

While it may occur in the model that higher stress concentrations are present within rivets than in plates, in the majority of cases the connected members, e.g., plates, are governing in fatigue calculations over the connecting members, e.g., rivets (DiBattista, Adamson, & Kulak, 1998). This is further illustrated by the fact that standalone rivets fall under a very high detail category (see Annex A). Therefore, internal stresses in the rivets are not considered when finding stress concentrations, and critical locations are entirely dependent on the stresses in the plates.

To provide some clarity on which sections of the bridge joint model are referenced with which description, Figure 89 to Figure 92 are provided. The main beam top flange is highlighted in Figure 89. Figure 90 highlights the gusset plate, which forms the connections between the diagonal beam, the main beam, and the angle plates leading to the joint. The diagonal beam top flange is shown in Figure 91. Finally, Figure 92 highlights the most relevant vertical angle plate. It goes down to the support and is thus in part responsible for the transfer of forces from the beams to the support. It is situated on the inside of the joint, on the opposite side of the side shown in the Figure.
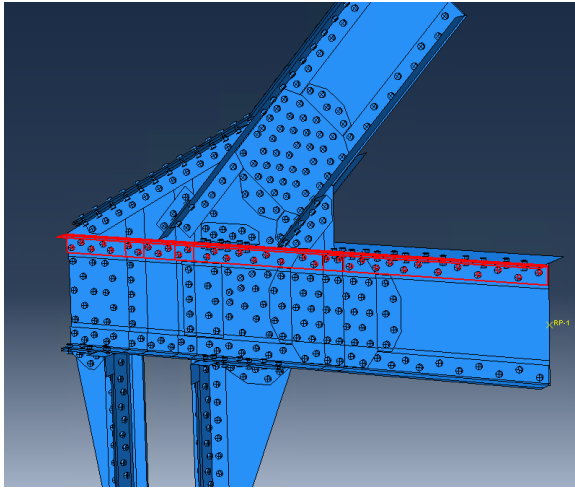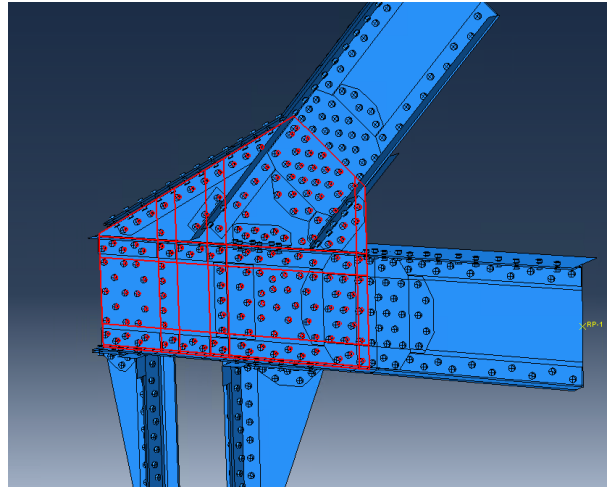
Figure 89: Top flange of the main beam
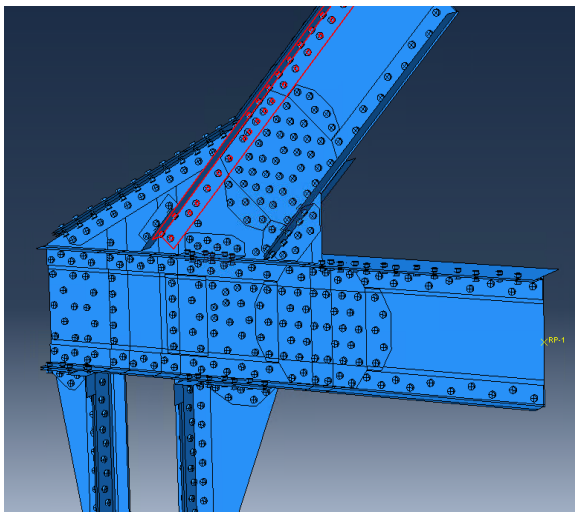

Figure 90: Gusset plate

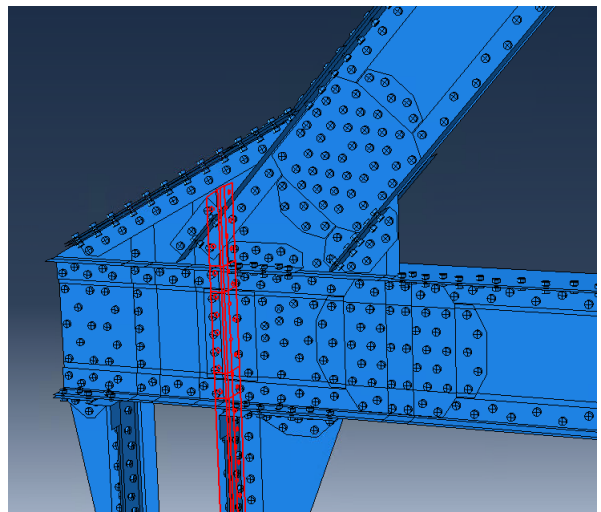*Figure 91: Top flange of the diagonal beam*

Figure 92: Vertical angle plate

5.1.1. Shell model
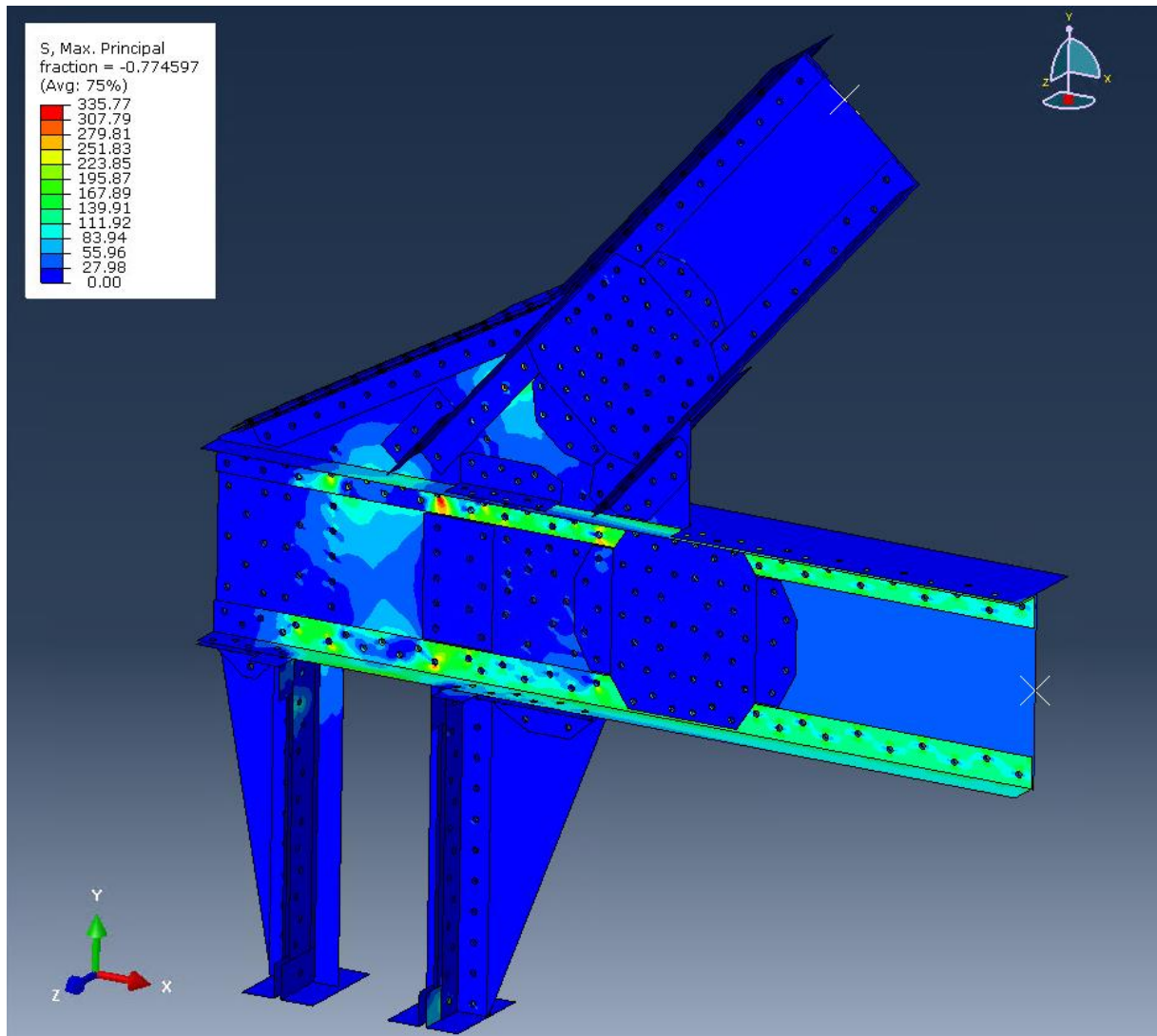
Figure 93: Principal stresses in the non-prestressed joint model. Shell-element based model. Stresses are displayed in MPa.

Figure 93 shows the principal stresses on the joint, as calculated with the shell-element based model. Any stress below 0 MPa (which are compressive stresses) are shown as 0 MPa. This is the reason the diagonal beam exhibits no principal stress in this Figure.

It is quite evident that large parts of the tensile forces in the main beam are taken up by the flanges. This is likely because they form the largest connection between the main beam and gusset plate, and are predominantly responsible for the transfer of tensile forces between them. Similarly, the connection between the beam web and gusset plate, at the location of the cover plates, experiences increased stress concentrations. However, these concentrations are lower than those observed in the flanges, suggesting their contribution to the transfer of forces is relatively limited compared to that of the flanges. In particular, the locations in which the horizontal flanges from the main beam and the vertical angle plates overlap, where forces are directly transferred from the main beam flanges to the vertical angle plates (which in turn are responsible for transferring forces to the support, at the bottom of the joint), experience large stress concentrations around the rivet holes, reaching a peak of approximately 335 MPa, whereas in general the stresses in the flanges hover around 200 MPa. The congregation of forces originating from the diagonal beam and the main beam is the likely reason why the stress concentrations occur here, around the centre of the gusset plate,

within the top flange of the main beam (see Figure 94). This would also explain why the stress concentrations appear to occur under an angle in the top flange of the main beam. As this location experiences the largest stresses, this is the location that will be observed in the sub-model. Aside from the four points shown in Figure 94, where the flanges of the main beam and the vertical angle plates overlap, other points of interested include other locations within the top flange of the main beam, though their maximum stress concentration is slightly lower, reaching stress concentrations of close to 300 MPa; at the connection between the gusset plate and top flange of the diagonal beam, similarly reaching stresses of 250 to 300 MPa, and, to a lesser extent, at the bottom of the model, at the connection to the hinged support. For a full analysis, all of these would likely need to be investigated, but for the purpose of this study, only the critical location marked in Figure 94 is modelled in detail.
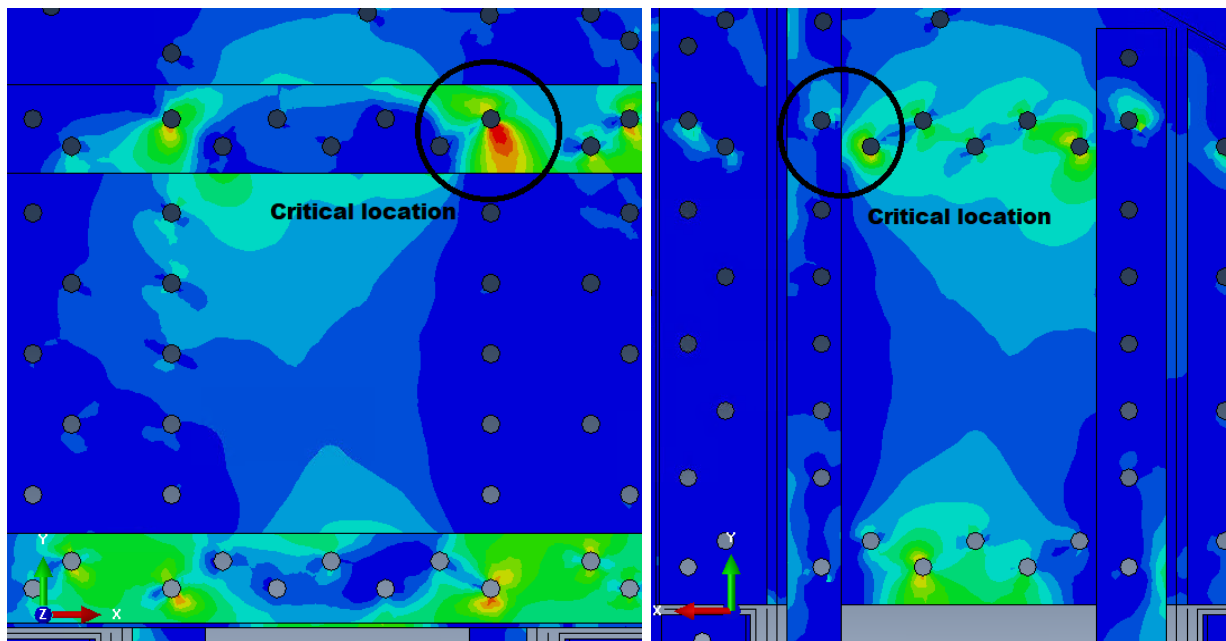
Figure 94: Front and back view of critical locations in the joint. One of the cover plates is removed for clarity.

5.1.2. Solid sub-model

As Chapter 4.2.3.7 describes, there are two methods to incorporate sub-models into the large model. Either a model can be run, and its internal stresses can be applied onto a separate sub-model, as if it were a part of the model as a whole, or the sub-model can be directly incorporated into the large model. For this report, the second method has been adopted, as this method has proven to provide better results.
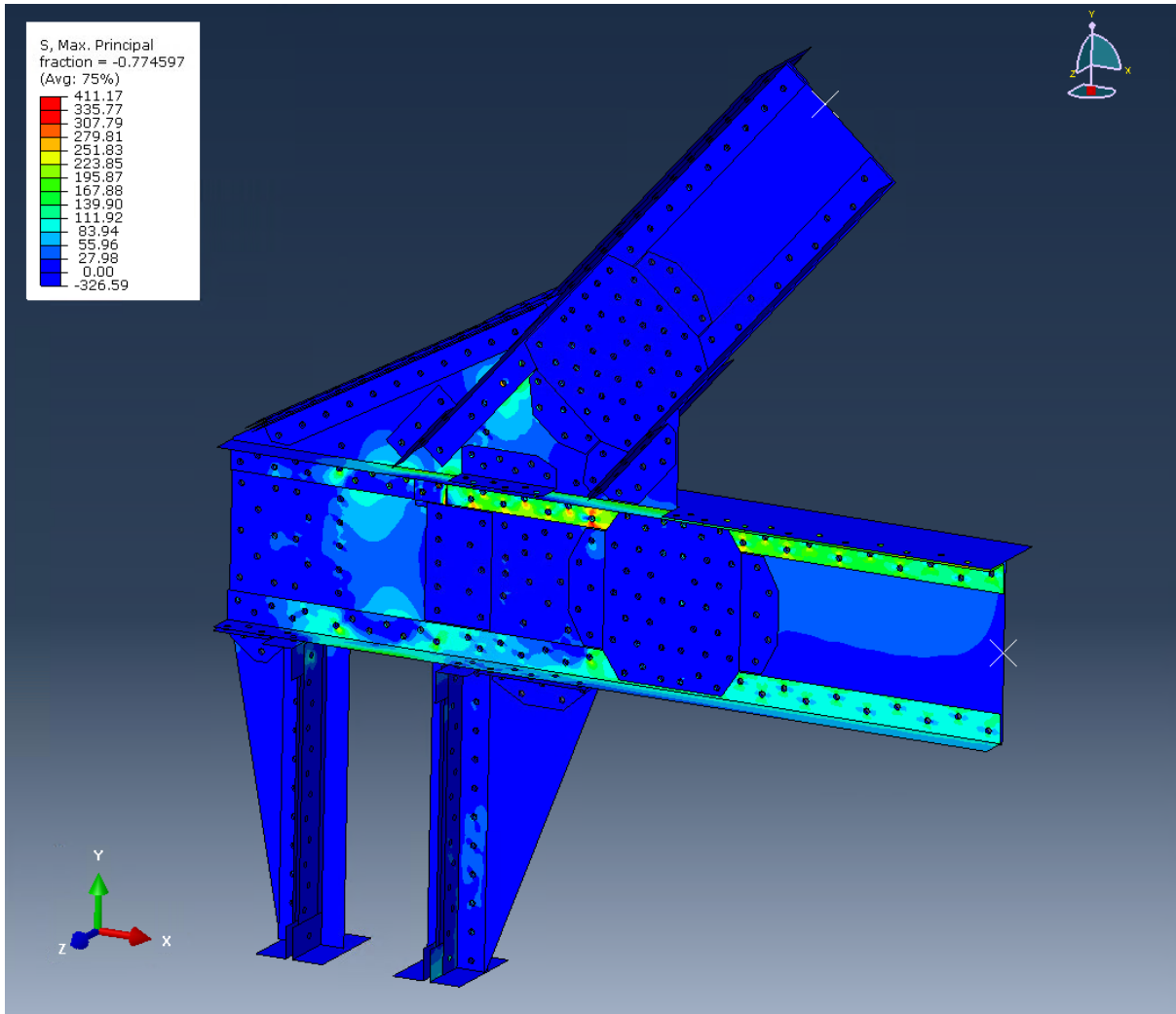
Figure 95: Principal stresses in the non-prestressed joint model. Shell-element based model with solid-based sub-model. Stresses are displayed in MPa.

The following is an adaptation of the previous model, with a solid sub-model included into the critical location. Figure 95 shows the results from this model. The Figure adopts the same scale as the scale adopted in Figure 93, disregarding any increase in stresses beyond the maximum stress in the original, shell-based model, that can be observed in the sub-model for the time being, as it allows for a clearer comparison. The general distribution of forces throughout the joint appears to roughly match the one calculated in the earlier model. However, it appears that incorporating a more detailed sub-model has shifted the transfer of forces more towards the upper flange of the main beam, where the sub-model is located, slightly decreasing the stresses in the bottom flange.

Further investigation of the area around the sub-model shows that while most of the model roughly matches the original shell-based model, the actual stresses within the sub-model do not line up with the stresses around it (Figure 96). This difference can be attributed to the different properties of shells and solids. Where the shell model presumes a uniform stress distribution throughout its thickness, the solids may have different stresses in its inner and outer fibres. This is illustrated by Figure 97, where the backsides of the flanges are shown. On the backside it is evident that the sub-model shows a better match with the expected results originating from the original shell-based model, though it is still relatively different from the original model. It can be noted that there are slightly higher stresses present than found in the original model, reaching a stress concentration of

up to 350 MPa, not only directly around the rivet hole, but also in the flange altogether. The largest stresses still occur around the bottom of the rivet hole, similar to what is found in the shell model. Furthermore, the stresses in the shell elements that surround the sub-model line up much better than they do on the front side.
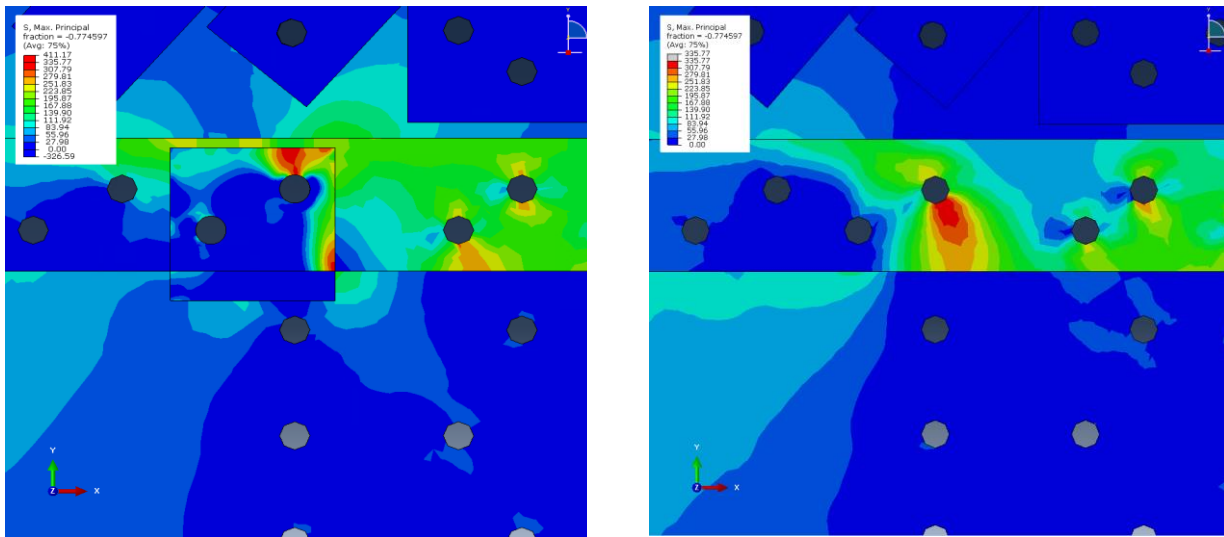
Figure 96: Comparison between local principal stresses on the front side of the joint, between the model with sub-model (left) and the model without (right)
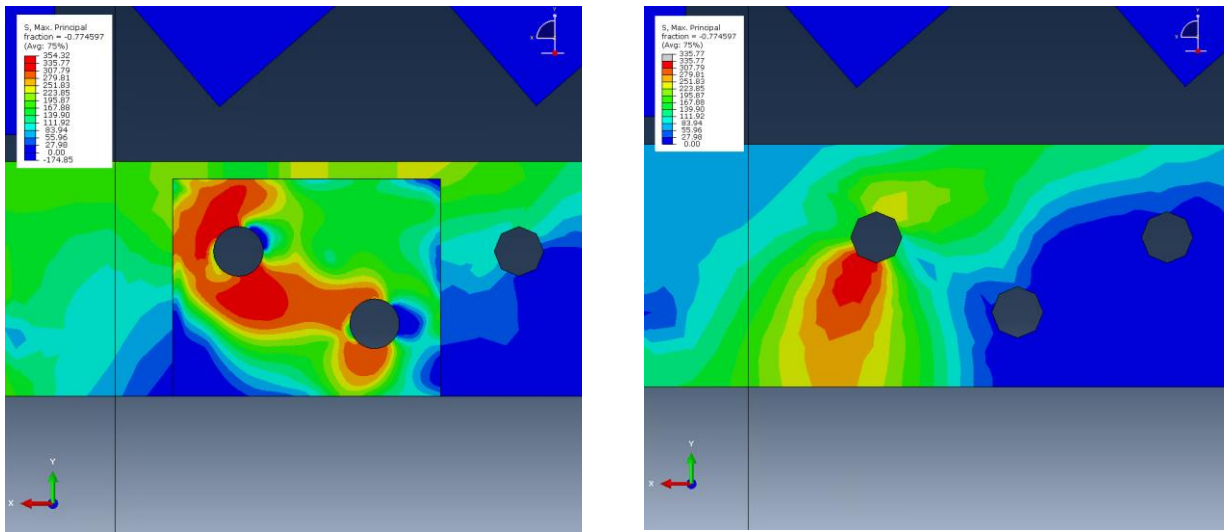
Figure 97: Comparison between local principal stresses on the back side of the main beam flange, between the model with sub-model (left) and the model without (right)

There are some other facts that can be observed. Firstly, the largest stresses no longer occur around the rivet hole. A singularity is present in the corner of the sub-model. While this singularity is not a realistic occurrence in structures in practice, and should therefore not be considered to be the critical location, one should note that the singularity is moderately close to the critical rivet hole. Therefore, this will likely affect the stress distribution in the sub-model, and the singularity may be the reason that the stress distribution in the sub-model differs from the stress distribution in the shell-based model. Secondly, the large discrepancy between the stress distribution on the inner- and outer fibres of the solid sub-model indicate there are internal moments present. These likely originate from the inherent eccentric loading of the model. The transfer of stresses from the main beam and diagonal beam to the support is primarily handled through contact between the flanges of the beams and the rivets. Because the flanges of the beams are not connected symmetrically to the

web of the beams (or the gusset plate), e.g., there are only flanges on the outside of the web and not in the inside, some eccentricity is expected. This is also observed in Lundkvist et al.'s unsymmetric models. Finally, within the sub-models, far larger principal stresses occur in the vertical angle plate than what the shell model has indicated. This may warrant a further investigation of the stresses in this vertical angle plate, but for the purpose of this report, it is not taken into consideration.
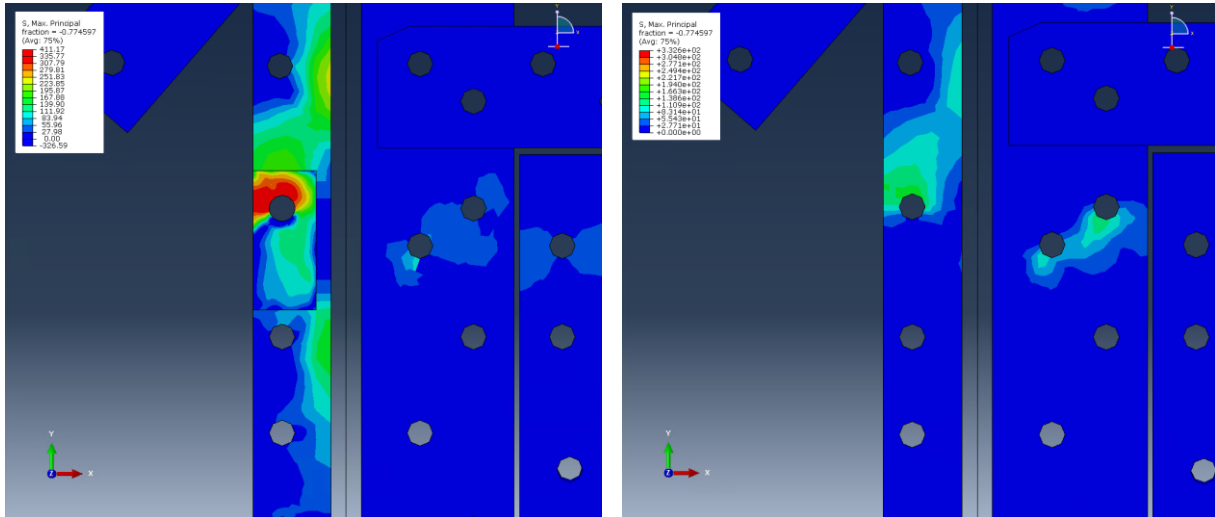
Figure 98: Principal stress distribution in the vertical angle plate with sub-model (left) and without sub-model (right)

5.2. Results bridge joint model with prestress

The results from the prestressed model are illustrated in the same way as the non-prestressed model, utilizing the principal stress to identify critical locations rather than Von Mises stresses. It also uses the same stress scales to present the principal stresses, to facilitate comparing the two models. Additionally, it also presumes that the rivets are not governing for the fatigue resistance.

5.2.1. Shell model
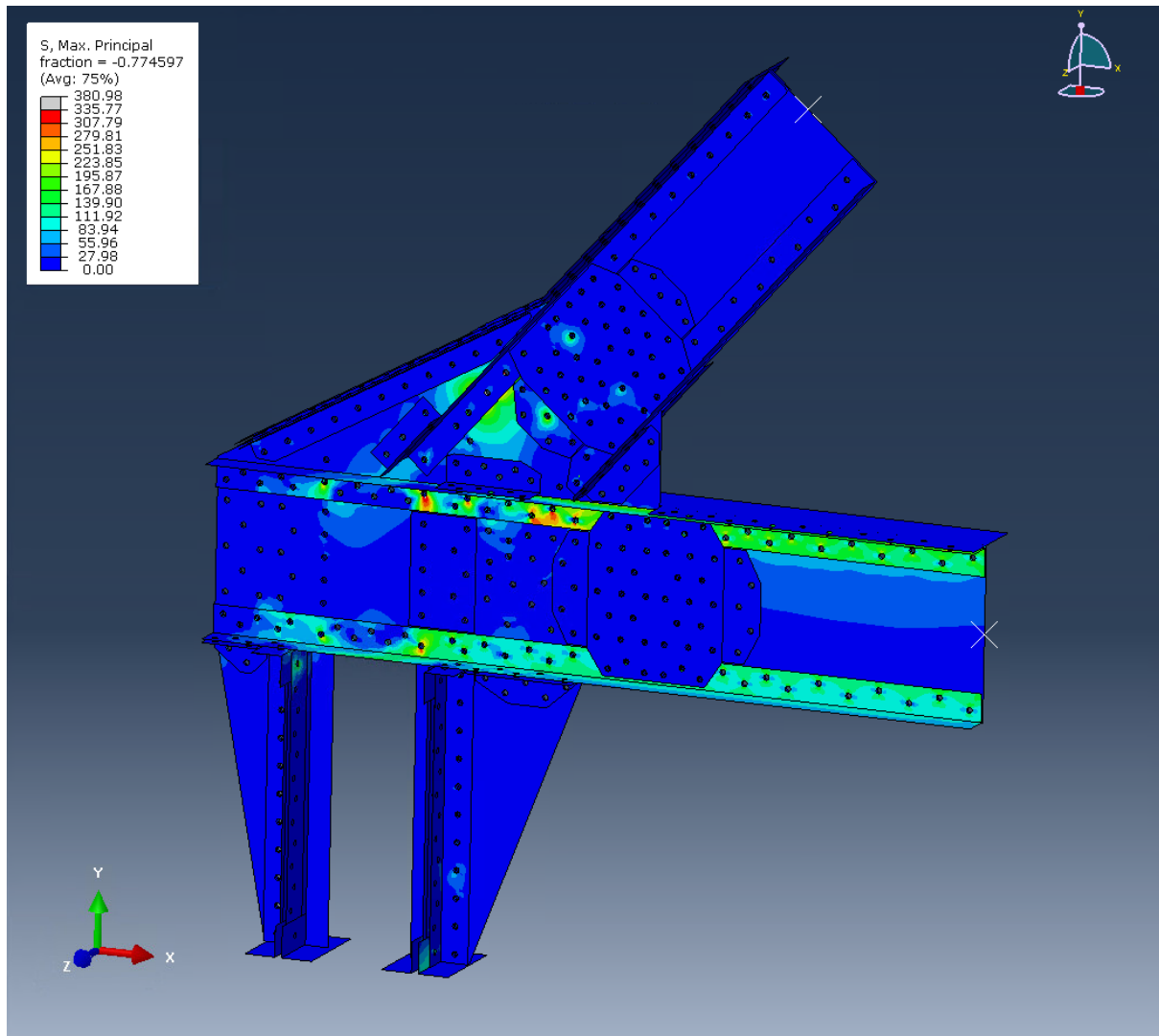
Figure 99: Principal stresses in the prestressed joint model. Shell-element based model. Stresses are displayed in MPa.

The joint model exhibits similar behaviour to the model without prestress. The overall stress distribution appears to be near identical between the two models. Many of the critical locations found in the non-prestressed model are also present in the prestressed model, appearing primarily in the top flange of the main beam and in the gusset plate at the location of the connection to the top flange of the diagonal beam. In particular the stress concentrations in the gusset plate, where the gusset plate is connected to the top flange of the diagonal beam, appear to be more pronounced, reaching a stress concentration of up to 380 MPa, even exceeding the principal stresses that occur in the top flange of the main beam, which lingers around 350 MPa. This further cements that, as previously stated, for a full fatigue analysis all of the critical points should be investigated. While the stresses in the gusset plate near the diagonal top flange are likely governing over those in the main beam top flange, for the purpose of comparing prestressed to non-prestressed models, the focal point of the prestressed sub-model will be the same as in the non-prestressed model, at the location where the top flange of the main beam and the vertical angle plate overlap.

5.2.2. Solid sub-model

Similar to the shell model, the prestressed model with solid sub-model is largely comparable to the non-prestressed model. The biggest differences are the lack of a singularity within the sub-model,

and the increase in principal stresses in the gusset plate at the location of the diagonal beam top flange. Similar to the prestressed shell model, the stresses in the gusset plate slightly exceed those in the sub-model. Apart from these trends, the prestressed and non-prestressed models exhibit mostly the same properties.
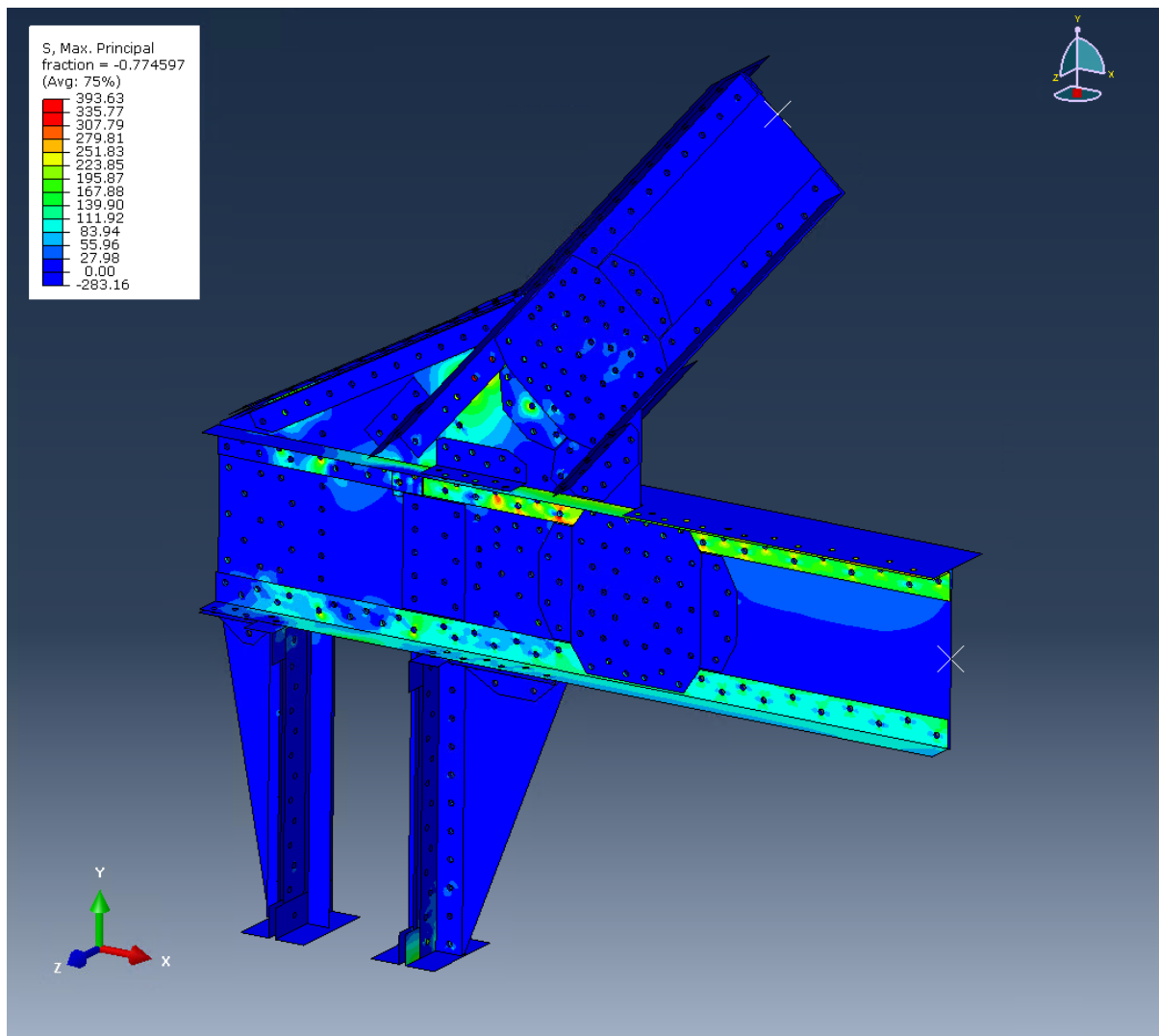
Figure 100: Principal stresses in the prestressed joint model. Shell-element based model with solid-based sub-model. Stresses are displayed in MPa.

The inner- and outer fibres of the main beam top flange are very different (see Figure 101 and Figure 102), where the inner fibres match the stresses in the surrounding shell elements much closer, though the actual distribution of stresses within the sub-model is not really close to the stresses in the same location of the shell model. Interesting to note is that, even though there is no singularity in the prestressed sub-model, the stress distribution in this sub-model remains similar to the stress distribution in the non-prestressed sub-model, indicating that the singularity has a limited effect on the stress distribution in the observed critical section around the rivet hole.

Finally, the observations made on the vertical angle plate within the non-prestressed model hold true for the prestressed model as well, where the vertical angle plate experiences much higher stresses than one would expect following the shell model.
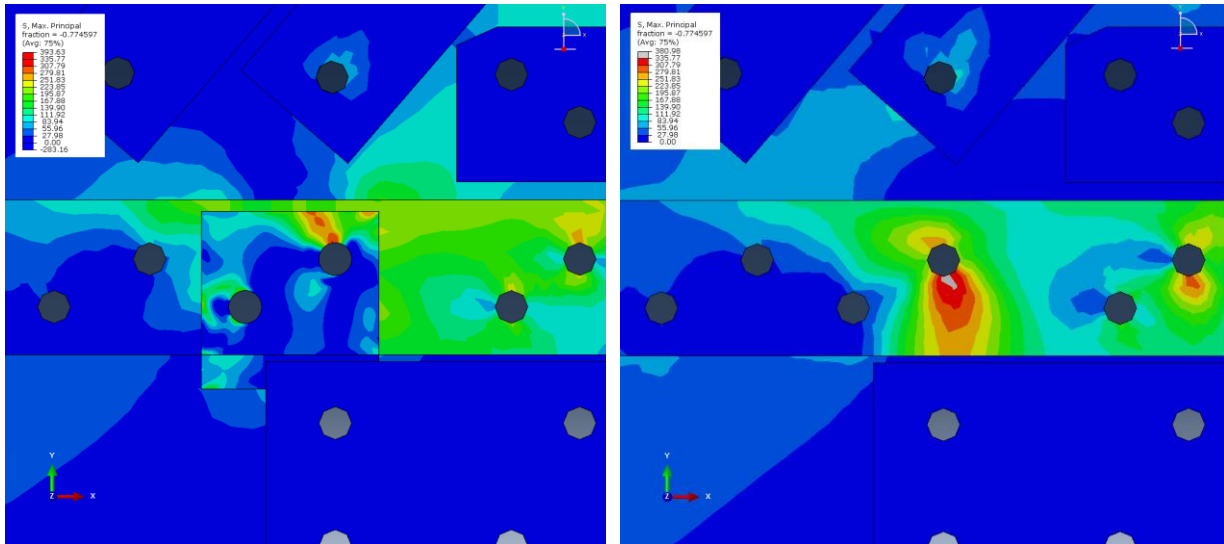
Figure 101: Comparison between local principal stresses on the front side of the joint, between the model with sub-model (left) and the model without (right)
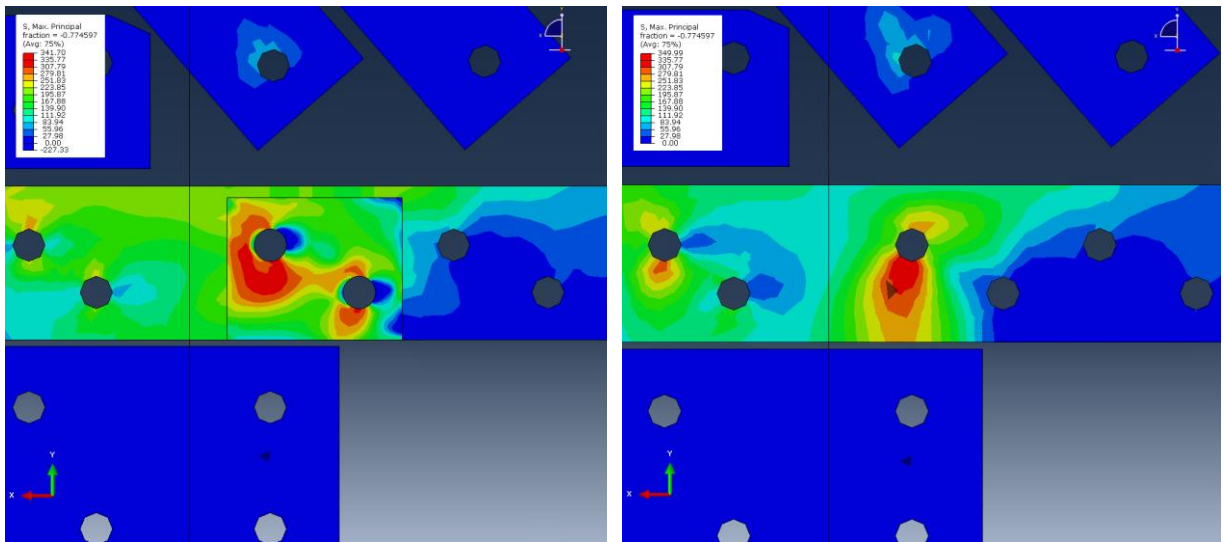
Figure 102: Comparison between local principal stresses on the back side of the main beam flange, between the model with sub-model (left) and the model without (right)

5.3.   Results at critical location prestressed and non-prestressed models

Upon definition of the critical plate, more information can be gathered. Both in the prestressed and in the non-prestressed sub-models, disregarding the singularity in the corner of the non-prestressed sub-model, particularly large stress concentrations occur in the top flange of the main beam and the vertical angle plate leading towards the support, which is why the sub-models have been generated there. However, as the stresses in the vertical angle plate differ significantly between the shell model and solid sub-model, and will require additional investigation, the top flange of the main beam is taken to be the critical plate in the fatigue assessment.

Therefore, for this report, the critical point is taken within the top flange of the main beam. The exact critical point is assumed to be at the location where the principal stresses reach their maximum. Figure 103 shows this location for the non-prestressed model, and is situated on the back side of the flange, on the section connected to the gusset plate. Figure 104 shows this location for the prestressed model. It is located on the inside of one of the rivet holes in the sub-model, at the top.

94
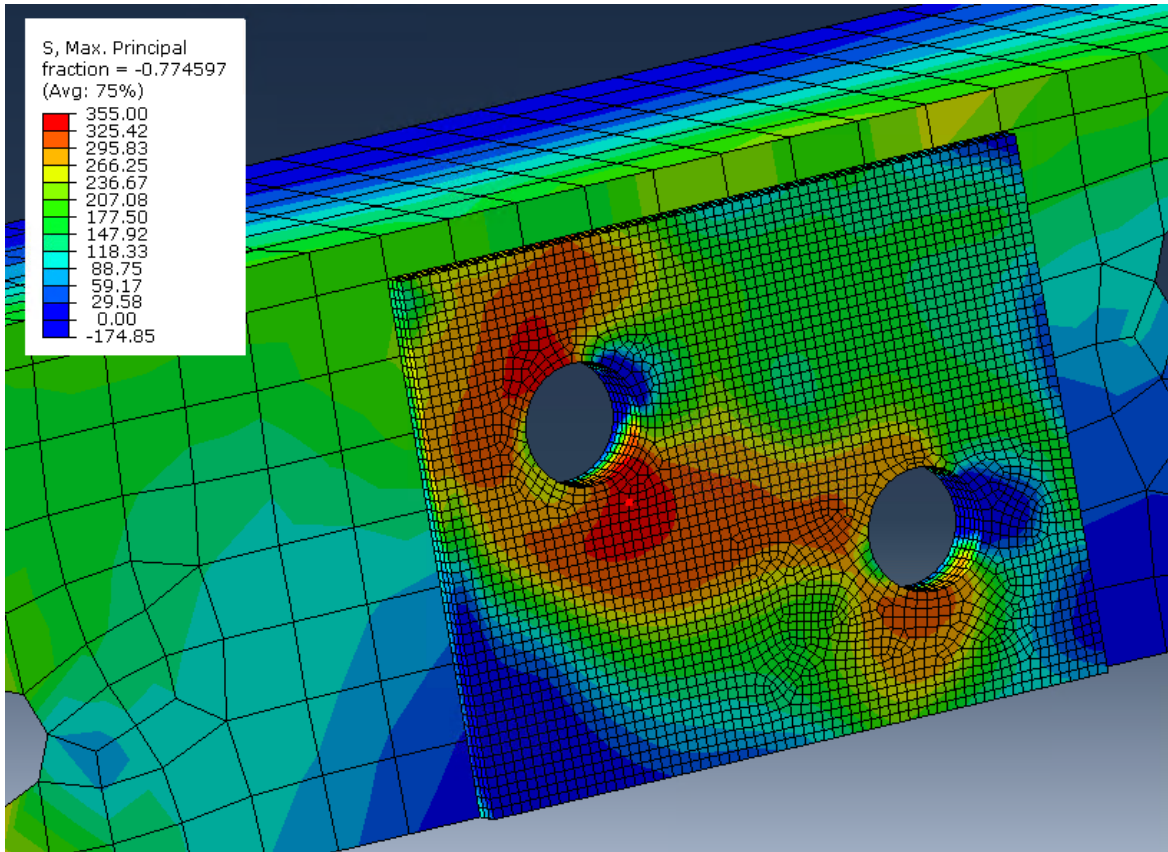
Figure 103: Critical point in non-prestressed joint model
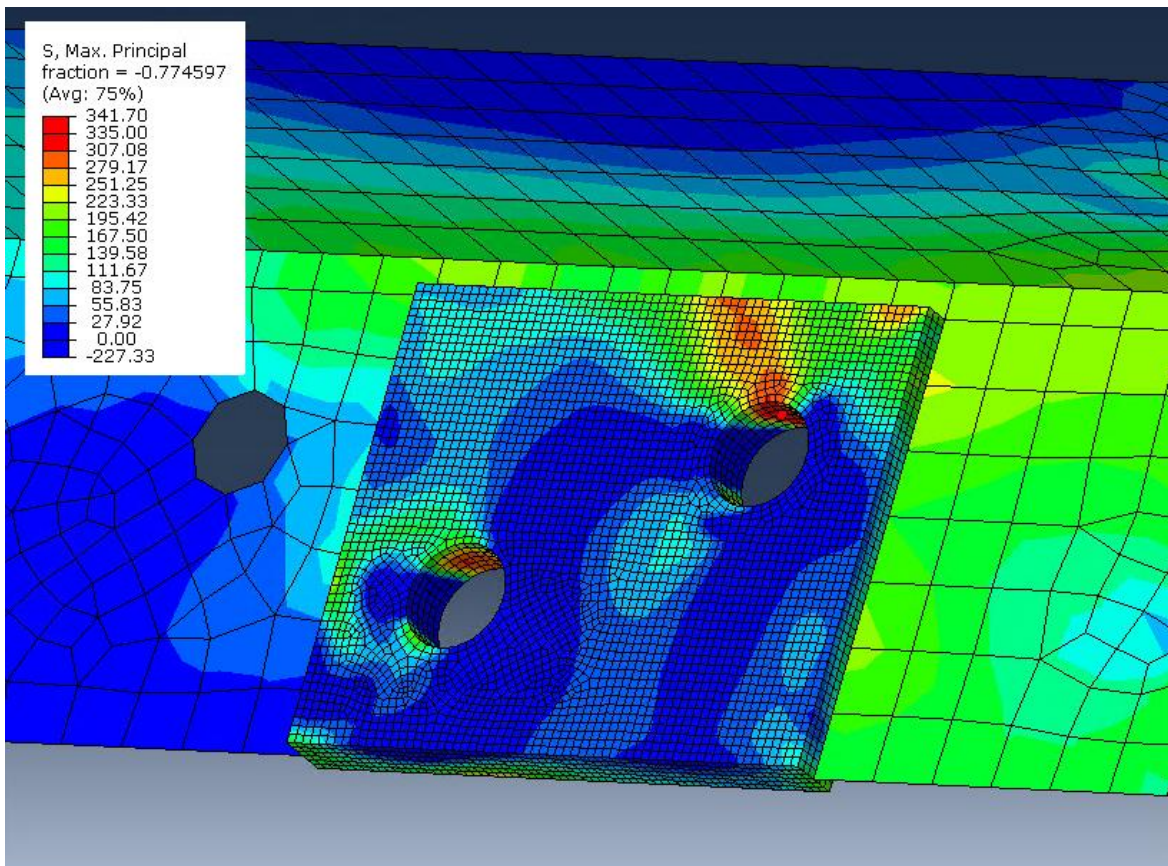
Figure 104: Critical point in prestressed joint model

An advantage of ABAQUS/Explicit is that it allows the user to apply a load over a specific segment over time. With this method, one is able to gather insights in the propagation of stresses and strains proportional to the application of the load. Figure 105 displays the application of the load over the time it takes to apply, at a constantly spaced interval. ABAQUS does not specify a unit for the time over which the force is applied, but rather works with time increments, as shown in the Figures. Figure 106 to Figure 108 display the principal stress, principal strain and shear strain in the critical point resulting from this applied load.

It should be noted that the axial force on the main beam in the prestressed model is slightly larger than zero at the start of the load application, as a result from very small displacements following the previous step, where prestressing has been applied. However, this load is negligible compared to the final load. Similarly, there is small amount of principal stress and strain present before the application of the load, as a direct result of the prestressing of the rivets.
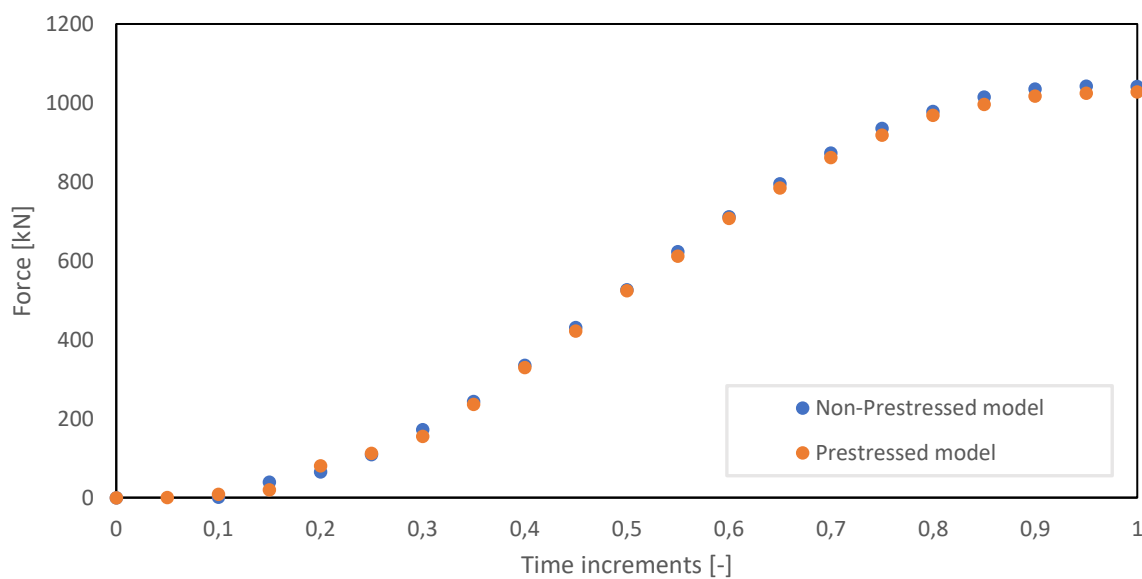
Figure 105: Force applied to the main beam at different analysis time increments
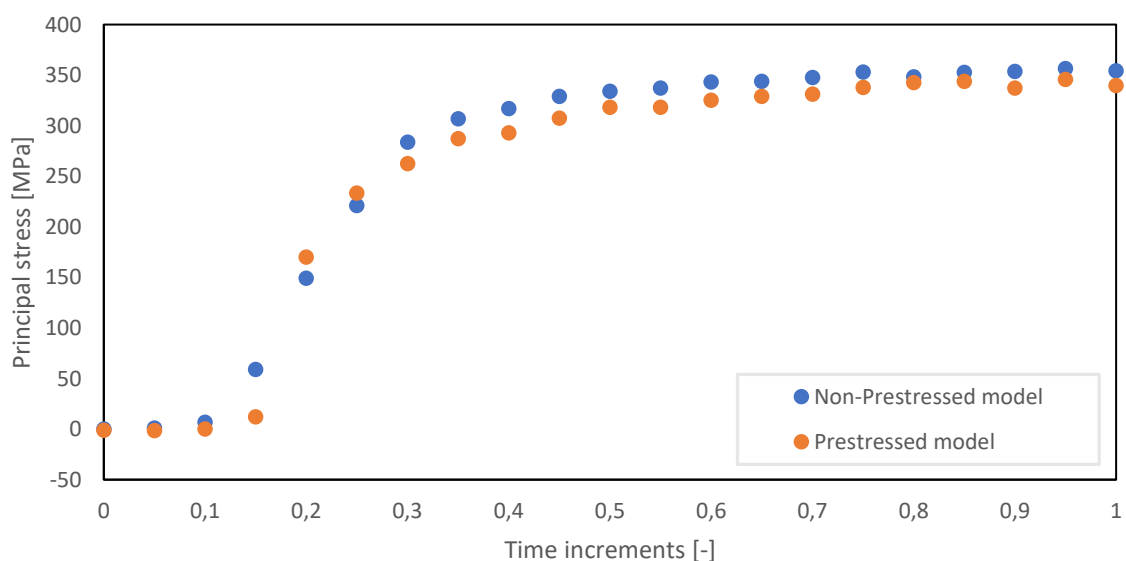
Figure 106: Principal stress in critical location resulting from applied load

96
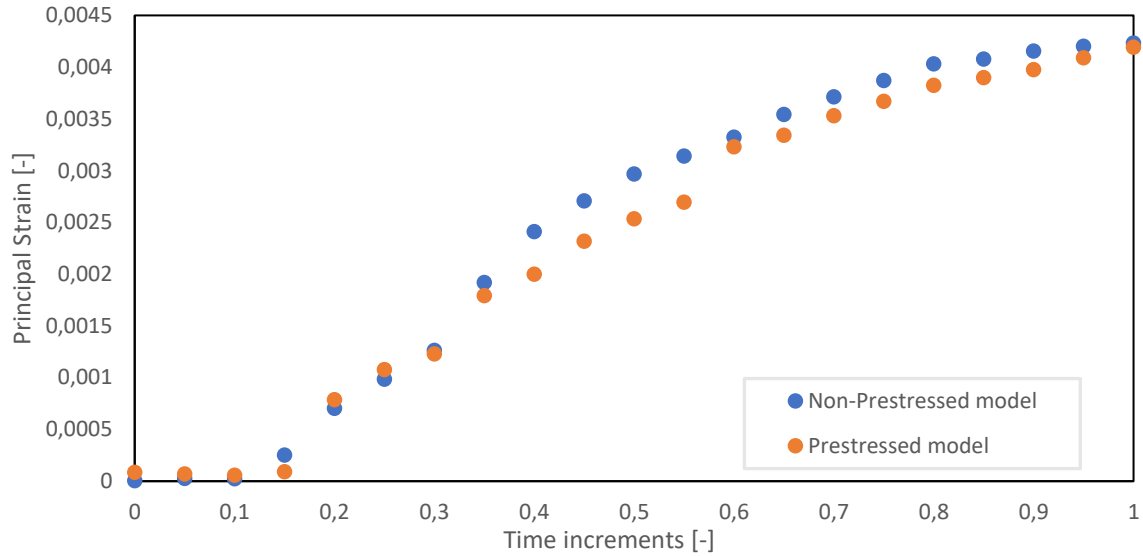
Figure 107: Principal strain in critical location resulting from applied load

Gathering the shear strain requires some additional data manipulation. Using the ε_{11} and ε_{33} field outputs from ABAQUS and applying Eq. 16, the shear strain can be obtained. The resulting shear strain distribution over the time in the critical location can be found in Figure 108.
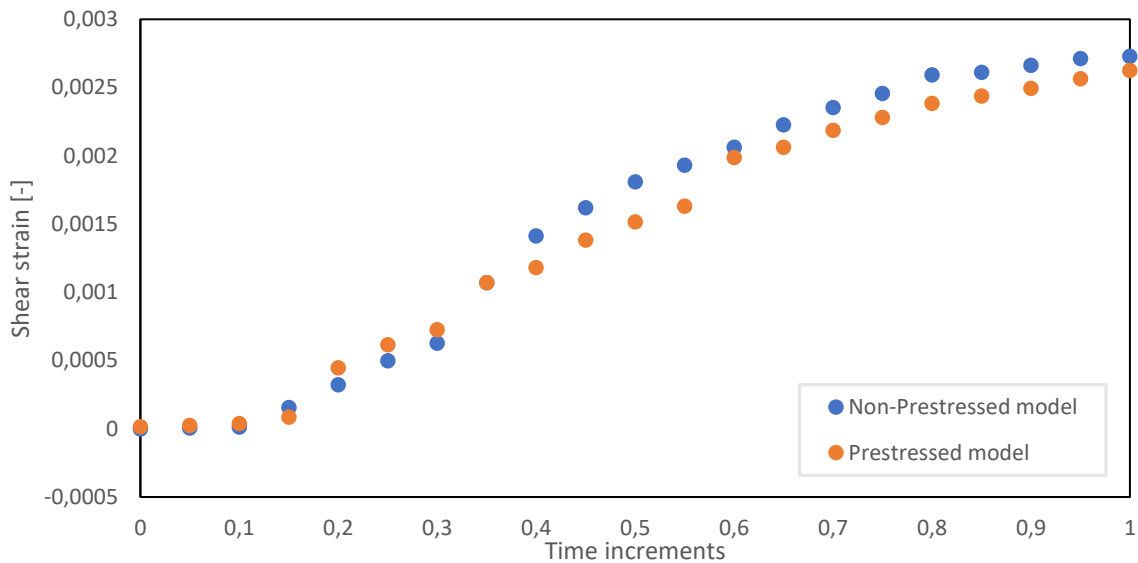
Figure 108: Shear strain in critical location resulting from applied load

It is quite evident that the effect of prestressing on the axial force in the main beam is very limited, resulting in a slightly lower axial force at higher axial loads when compared with the non-prestressed model. Overall, a slight decrease in stresses and strains can be noted in the prestressed cases, which is likely a direct result of the slightly lower axial force, with the exception at lower time increments, where higher axial forces are also present.

It appears that the differences in stresses and strains are slightly more pronounced than the difference in axial force. In combination with the presence of non-zero stresses and strains at an unloaded situation, resulting in smaller stress- and strain ranges, these findings would support the presumptions from the literature that the presence of prestressing does have a positive effect on the fatigue response.

5.4.   Cross validation of output forces

To cross validate the Finite Element, the output of the forces on the horizontal beam as a result from the force on the diagonal beam are compared to a hand calculation, as well as the results originating from the SCIA model described in Chapter 2.3.1.2. In general, the bridge is constructed to act like a simple truss structure. This means the elements of bridge should be primarily loaded axially. A a simple hand calculation can demonstrate the distribution of forces on the bridge joint members one would expect on a truss joint. In addition to a hand calculation, the SCIA model constructed by Iv-Infra can provide an insight in the expected forces on these beams and supports.

The hand calculation relies on a few assumptions. As the bridge is constructed like a truss, it is presumed to experience only axial forces. Any shear forces that may be present are neglected. Similar to the calculation performed by Iv-Infra, transversal forces acting on the joint are not considered. Furthermore, the support at the bottom of the joint is assumed to act as a hinged joint. Finally, frictional forces are neglected. Based on these assumptions and the fact that the forces need to act in equilibrium, the internal axial force in horizontal beam can be calculated with the axial force acting on the diagonal (or vice versa).

The input forces adopted in the hand calculation, and thus with which the bridge joint model is assessed, is taken directly from the SCIA-model created by Iv-Infra. This force is the maximum axial force acting on the diagonal beam of the joint. The maximum axial force is taken because this force generally introduces the largest stresses into the joint and can therefore be used to find

Figure 109: Expected force distribution for hand calculation

critical locations within the joint. Table 23 shows the maximum internal forces in the diagonal at the location of the joint, resulting from the load cases as described in Chapter 2.3.1.1. Load case Z1046 introduces the largest internal normal force, amounting to a compressive force of 3304,77 kN, applied to the shear centre of the cross-section. To account for the symmetry utilized in the ABAQUS model, only half of this force is taken to compare results with, being approximately 1652,39 kN. One can also note that the shear forces are significantly smaller than the axial force, indicating the assumption that they can be neglected appears to be appropriate. The maximum internal forces found in the horizontal beam at the location of the joint are displayed in Table 24. Similar to the diagonal, the axial force far outweighs the other internal forces, further complementing the assumption that the other internal forces can be neglected. The maximum axial force found in the main beam is a tensile force of 1002,96 kN, and corresponds to the same load case in which the maximum axial force in the diagonal is found. Rather than a singular cross-section, like the diagonal, the SCIA model utilizes two separate, symmetrical cross-sections for the main beam, which means the internal forces displayed in Table 24 already display the forces with which the forces from the ABAQUS model can be compared.
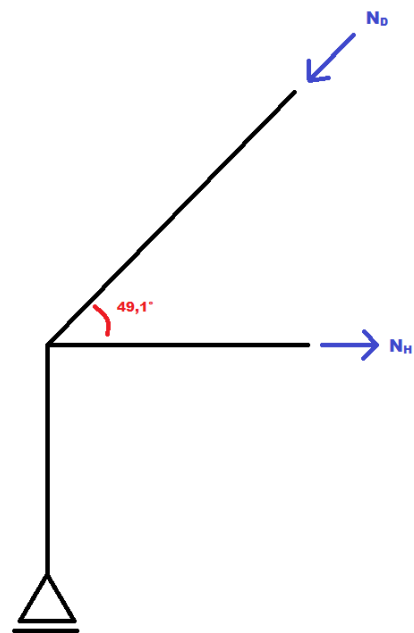
Table 23: Minimum and maximum forces in diagonal beam, taken from SCIA

Load Case	N [kN]	V_y [kN]	V_z [kN]	M_x [kNm]	M_y [kNm]	M_z [kNm]
N2031/1	*-1673,45*	-30,34	3,72	1,34	8,21	86,90
N1045/2	-2304,07	*-35,21*	1,23	1,34	6,10	111,96
Z1046/3	*-3304,77*	34,89	*-7,67*	-1,66	*93,24*	-102,40
Z2017/4	-2525,30	58,60	*6,54*	-2,08	23,74	-199,06
Z1037/5	-2644,81	*76,62*	6,30	*-2,45*	24,40	-281,06
N2033/6	-1831,28	-32,00	4,09	*1,38*	6,39	94,33
N1047/7	-1834,67	10,64	2,34	0,50	*2,01*	-94,93
Z1047/8	-2687,12	78,03	2,32	-2,37	30,25	*-291,36*
N2045/9	-2118,07	-35,13	1,26	1,33	5,65	*112,49*

Table 24: Minimum and maximum forces in horizontal beam, taken from SCIA

Load Case	N [kN]	V_y [kN]	V_z [kN]	M_x [kNm]	M_y [kNm]	M_z [kNm]
Z1046/1	*1002,96*	1,70	35,14	0,02	-23,14	3,83
N1046/2	523,98	*-3,76*	22,75	0,10	-16,02	1,12
Z2021/3	767,62	*2,32*	28,64	-0,04	-36,80	2,54
N4021/4	355,41	-0,13	*17,56*	0,02	-28,75	0,32
Z1037/5	804,99	2,07	*43,05*	*-0,12*	*-60,41*	3,48
N1036/6	513,25	-3,64	21,70	*0,10*	*-13,35*	0,78
N2031/7	*322,35*	-3,13	17,91	0,04	-28,38	*-0,22*
Z1036/8	958,62	1,55	36,77	0,02	-26,56	*4,25*

$$cos(49,1°) = \frac{N_H}{N_D} \rightarrow N_H = N_D * cos(49,1°) = 1652,385 * cos(49,1°) = 1081,88 \, kN \qquad \text{Eq. 31}$$

Applying the maximum axial force on the diagonal, assuming a force equilibrium as displayed in Figure 109, the resulting axial force in the horizontal beam can be calculated with a simple hand calculation (see Eq. 31). The hand calculation shows that the expected force in the main horizontal beam roughly matches the internal axial force calculated by SCIA. The differences can be attributed to the internal moments that SCIA does account for, while the hand calculation does not, resulting in the redistribution of the axial forces between the symmetrical beam sections. With results from both methods, an approximation of the expected internal axial force that should come out of the ABAQUS bridge joint model can be made.

The force distribution onto the bridge joint model can be taken from the model created in Chapter 4.2.2. Applying the same axial force on the diagonal used in the first two methods should generate an axial force in the horizontal main beam within the vicinity of the aforementioned calculated axial forces. According to the ABAQUS model, the axial force acting on the main horizontal beam is a tensile force amounting to 1032,36 kN. From the SCIA model, an expected force of 1002,96 kN has been found. The hand calculation indicates an expected axial force of 1081,88 kN. Since both expected axial forces roughly line up with the axial force calculated by ABAQUS, it can be assumed that the bridge joint model provides accurate results on a 'global' level.

The above comparison was made with the model without prestress. The model with prestress on the rivets experiences a slightly higher axial force in the main beam, at 1037,03 kN, but is still well within the expected range.

6. Fatigue assessment of the bridge joint

In this chapter, the fatigue assessment of the bridge joint is conducted. It is quite clear from Chapter 2.2.2.1 that the nominal stress approach, which is most commonly used in the fatigue assessment of structures, is not applicable for a joint as complex as the joint investigated in this report. Chapter 2.2.2.2 has provided several other methods of fatigue assessment, based on the local strain-life approach. Utilizing the results of the FEA in Chapter 5, several of these proposed analyses will be utilized, in order to generate the ε-N curves for the investigated detail. While a number of different factors have been presented that influence the fatigue resistance of a given connection, this chapter will limit itself to mean stress effects and multiaxiality. The Smith-Watson-Topper's adaptation to the base ε-N curve, which is used to incorporate mean stress effects, based on various values for σ_{max}, is presented. Additionally, the maximum shear strain criterion curve is included to illustrate the effect of multiaxiality. Differences in the curves due to prestressing will be discussed.

Furthermore, the relation between the applied force and the local stresses and strains, a transfer function, will be established. This transfer function will be used to derive the local stresses and strains directly from the applied load.

The final section in this chapter considers a theoretical load case. With this load case, an example on the use of the transfer functions is provided, based on the found strain-life curves. Furthermore, this example allows for the comparison of the different results for the various fatigue assessment methods. In this comparison, a fatigue life prediction based on the Eurocodes is also made, through an assumed simplification of the joint geometry.

6.1. Generation of strain-life curves and transfer functions

6.1.1. Strain-life curves non-prestressed and prestressed model

In order to generate the strain-life curve of the observed critical location, several cyclic material properties are necessary. In their most basic form, which is Eq. 11, the following parameters are required: b, c, σ_f' and ε_f'. Rather than estimate these values using the estimation methods provided in Chapter 2.2.2.2, the experimental results gathered by Boller & Seeger (1987) are taken as normative, as their findings are also used to model the material properties adopted in the FEA model. The values they have found in their research are presented in Table 25. With these values, the base material ε-N curve can be constructed.

Table 25: Cyclic material properties S235

b [-]	c [-]	σ_f' [MPa]	ε_f' [-]
-0,111	-0,569	895,0	0,7051

Both the Smith-Watson-Topper (Eq. 13) and Morrow-Glinka (Eq. 12) equations, which are able to incorporate mean stress effects on the investigated joint, require additional information in the critical location, namely the maximum stress σ_{max} and the mean stress σ_{mean}. Because Smith-Watson-Topper is generally the preferred method of the two, this report focuses only on this approach. To more intuitively incorporate the mean stress into the Smith-Watson-Topper (SWT) equation, one is able to utilize stress ratio R, where R can be used to calculate the mean stress. Knowing the following relations, the SWT equation can easily be rewritten to Eq. 33.

$$R = \frac{\sigma_{min}}{\sigma_{max}} \ and \ \Delta\sigma = \sigma_{max} - \sigma_{min}$$

$$\frac{\Delta\varepsilon}{2}\left(\frac{\Delta\sigma}{1-R}\right) = \frac{(\sigma_f')^2}{E}(2N_f)^{2b} + \sigma_f'\varepsilon_f'(2N_f)^{b+c}$$

Different values for the applied load result in different values for R in the critical location. However, only a single load case is considered in the bridge joint model, which means that not all representative curves for the joint can be presented. Therefore, the SWT-equation has been applied to Boller & Seeger's (1987) experimental data, which is representative for the material used in the FE models, and the results for varying values of R have been presented in Figure 110. It is evident that, as R increases, the material performs better under cyclic loading. For R = -1, it is expected the SWT equation matches the base strain-life (Manson-Coffin) equation (Eq. 11). Furthermore, both SWT for R = -1 and the Manson-Coffin equation should match the experimental results by Boller & Seeger. It is clear that for large strain ranges, this expected equality appears to be abided by, but for smaller strain ranges, a larger degree of conservativeness can be observed.

Differences in material curves between prestressed and non-prestressed models are negligible, as they do not affect the material behaviour, but rather the resulting local stresses and strains. It does mean that, because lower stress- and strain ranges are found in prestressed models over non-prestressed models, an improvement in fatigue performance in prestressed joints can be observed.
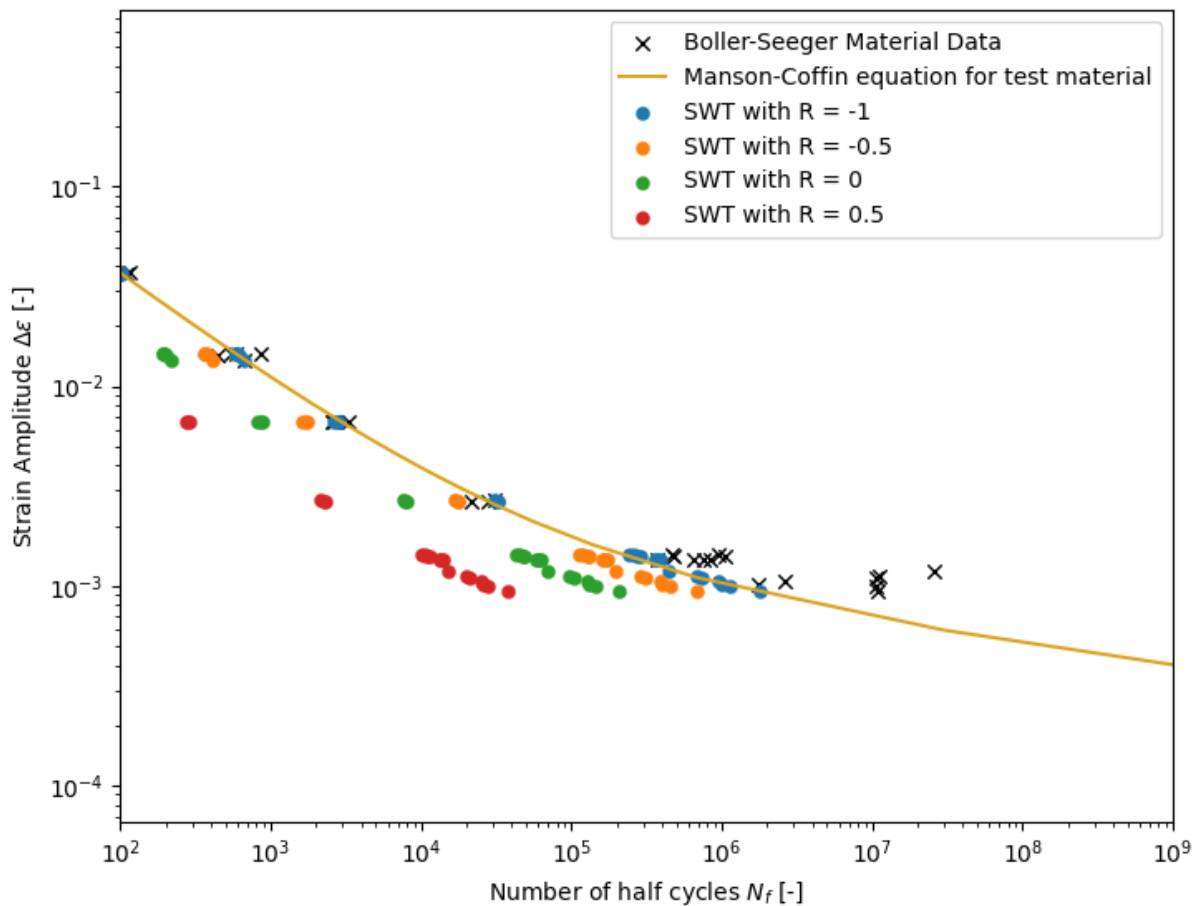
Figure 110: SWT strain-life curves for the critical location from the bridge joint models, using various values for R

Rather than focussing on the mean stress effect, it is possible to include other factors into the fatigue resistance assessment. In particular when assessing a joint as complex as the joint modelled in this report, which is subject to axial loads originating from different directions, it may be crucial to investigate the effect of multiaxial loading on the fatigue resistance. Several formulae for this

consideration are provided in Chapter 2.2.2.2. Figure 111 presents the curve generated through the maximum shear strain criterion (Eq. 18), which is dependent on shear strains rather than strains. Similar to the SWT-curves, there are no differences between the maximum shear strain criterion (MSSC) curve for a prestressed situation or a non-prestressed situation. Differences in fatigue performance are caused by smaller shear strain ranges due to presence of prestressing of the rivets.
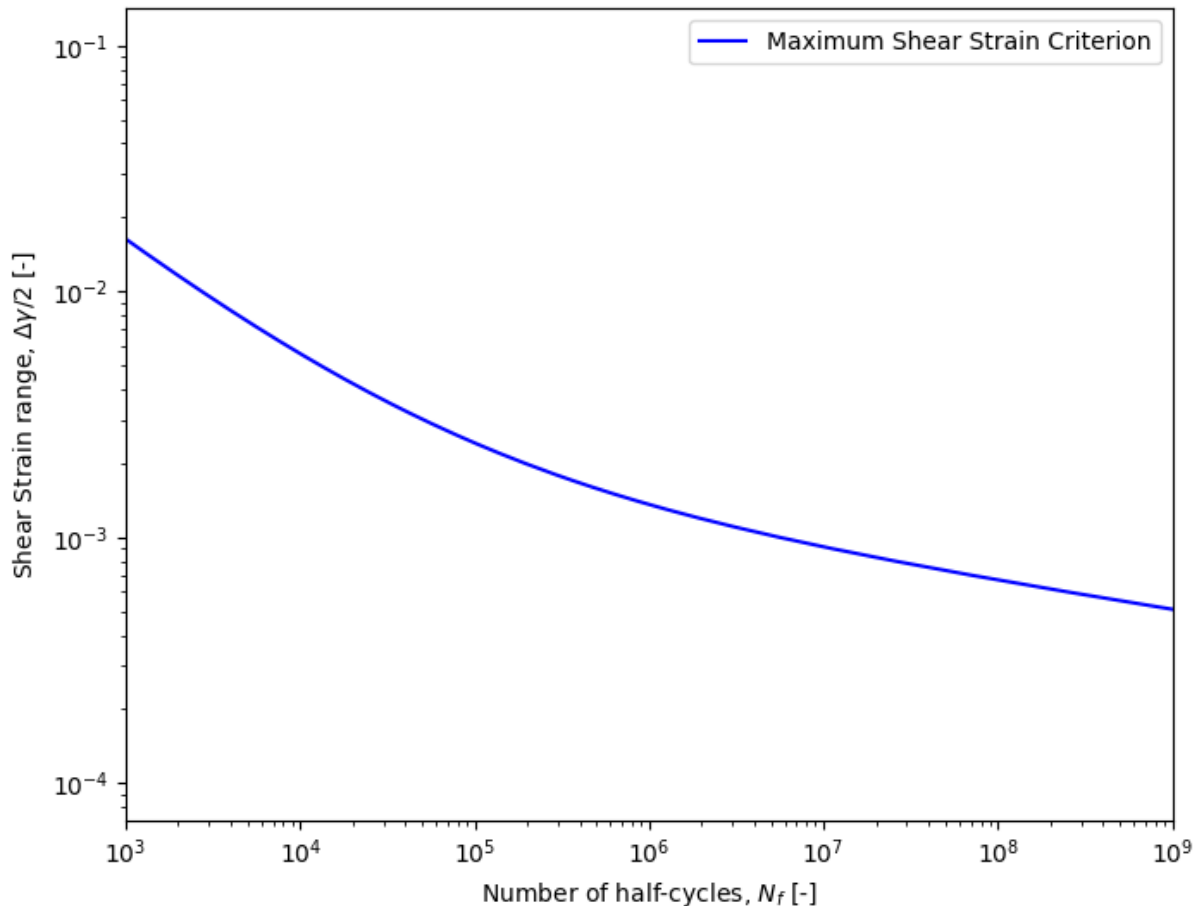
Figure 111: Shear strain-life curve for the critical location from the non-prestressed bridge joint model, using the maximum shear strain criterion method

6.1.2. Transfer functions from forces to estimate local stresses and strains

The aim of the development of transfer functions is to provide a simple mathematical expression to predict the stresses and strains relevant to the fatigue assessment, without the need to run the FE model over and over. This can be particularly useful for variable loading assessment, where these functions can be used to estimate the local stresses and strains at different load levels. Practical examples of the use of transfer functions can be most commonly found in the calculation of off-shore structures, such as Schmidt/Neuper's bolt load model for the calculation of axial bolt forces on pretensioned bolts in (tubular) shell structures (Schmidt & Neuper, 1997).

The derivation of transfer functions relies on the fact that strain ranges are directly related to the actual occurring strains. In the assumption that occurring strains are a direct result of the applied loads, an empirical equation can be drawn up, describing their relationship. This empirical equation can be used calculate strain ranges from the applied loads, which in turn can be used in ε-N curves to estimate the expected number of cycles until failure for a critical location subject to this specific loading configuration.

Transfer functions are derived from the loading in the ABAQUS model. Inherent to the explicit calculation method in ABAQUS is that it applies a load over a specific segment of time. This method of load application, starting at a load of zero, and going up to the maximum load that may occur on the joint (in this case according to the static analysis) in evenly spaced time intervals, can be used to gain the required insight in the relation between the applied load and the stresses and strains at a specific critical location.

For the critical locations in both the non-prestressed and prestressed bridge joint models, the relation between the force acting on the main horizontal beam, and the resulting local stresses, strains and shear strains have been determined. Several types of relations have been considered. Best descriptors for the relation between the applied force and the resulting stress, strain or shear strain are either an exponential function, a 3rd-order polynomial (polynomials of higher order have not been considered as they become too data-dependant and no longer present a realistic representation) or a bilinear function. Investigation of the root mean square error and R^2, which are used to estimate the difference between actual values and predicted values, show that the bilinear fit most closely represents the relation between both the force and strains and the force and shear strains.

The transfer function used to represent the bilinear fit is shown in Eq. 34. In this function, a, b, y_0 and x_0 are constants, and F is the variable, the applied load on the horizontal beam. For each of the established transfer functions, the constants are presented in Table 26.

$$\sigma, \varepsilon \text{ or } \gamma = \begin{cases} aF + y_0 - ax_0 & F < x_0 \\ bF + y_0 - bx_0 & F \geq x_0 \end{cases}$$

Eq. 34

Table 26: Constants used to describe the transfer functions for applied force to strain and shear strain

Model	Dependent factor	Symbol	a	b	x_0	y_0
Non-prestressed	Stress	σ	2,05	6,3 x 10^{-2}	147,43	301,55
Non-prestressed	Strain	ε	7,72 x 10^{-6}	2,44 x 10^{-6}	300,21	2,35 x 10^{-3}
Non-prestressed	Shear strain	γ	4,18 x 10^{-6}	1,76 x 10^{-6}	346,42	1,46 x 10^{-3}
Prestressed	Stress	σ	2,19	7,6 x 10^{-2}	132,56	277,65
Prestressed	Strain	ε	8,32 x 10^{-6}	2,91 x 10^{-6}	187,71	1,60 x 10^{-3}
Prestressed	Shear strain	γ	5,44 x 10^{-6}	1,97 x 10^{-6}	146,28	7,99 x 10^{-3}

It should be noted that by applying a smooth step amplitude over ten equally spaced time increments to create an axial force on the beams, a very limited number of data points (n = 10) is available to establish a relationship between the two factors. Additionally, the data points that are available, are more skewed towards the start and end of the application process. This means that the root mean square error and R^2 are also more heavily influenced by the difference at the start and end of the fit, than they are in the middle of the curve. For both a more accurate (bilinear) fit and approximation of the errors, more data points would be needed, and they would need to be more evenly spread out. However, this comes at the cost of longer modelling times, and as this report primarily aims to illustrate and investigate an advanced method of fatigue calculation, rather than to completely accurately determine the remaining fatigue life of the bridge joint, it has been deemed that a decreased calculation time favours more accurate results.

Figure 112: Relation between axial force, F, and maximum principal stress, σ, in the non-prestressed model

Figure 113: Relation between axial force, F, and maximum principal stress, σ, in the prestressed model

Figure 114: Relation between axial force, F, and strain at maximum principal stress, ε, in the non-prestressed model
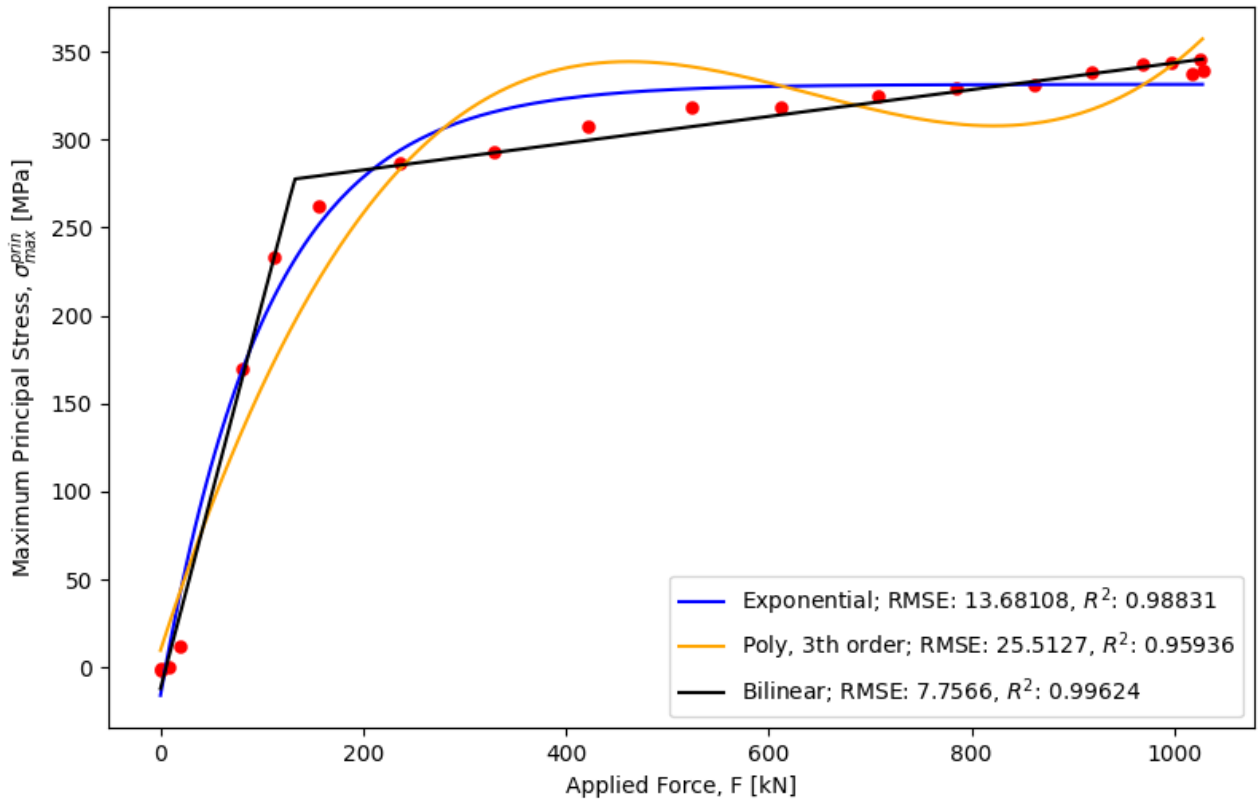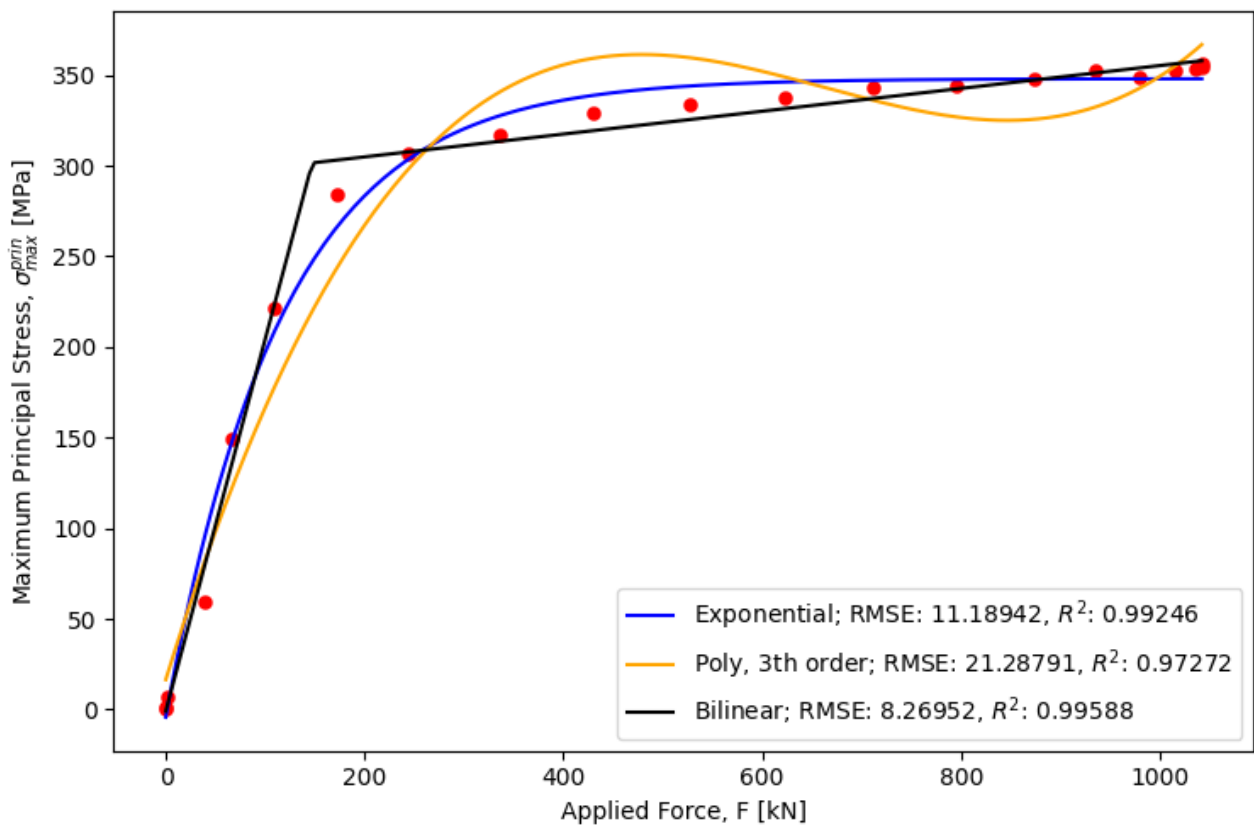

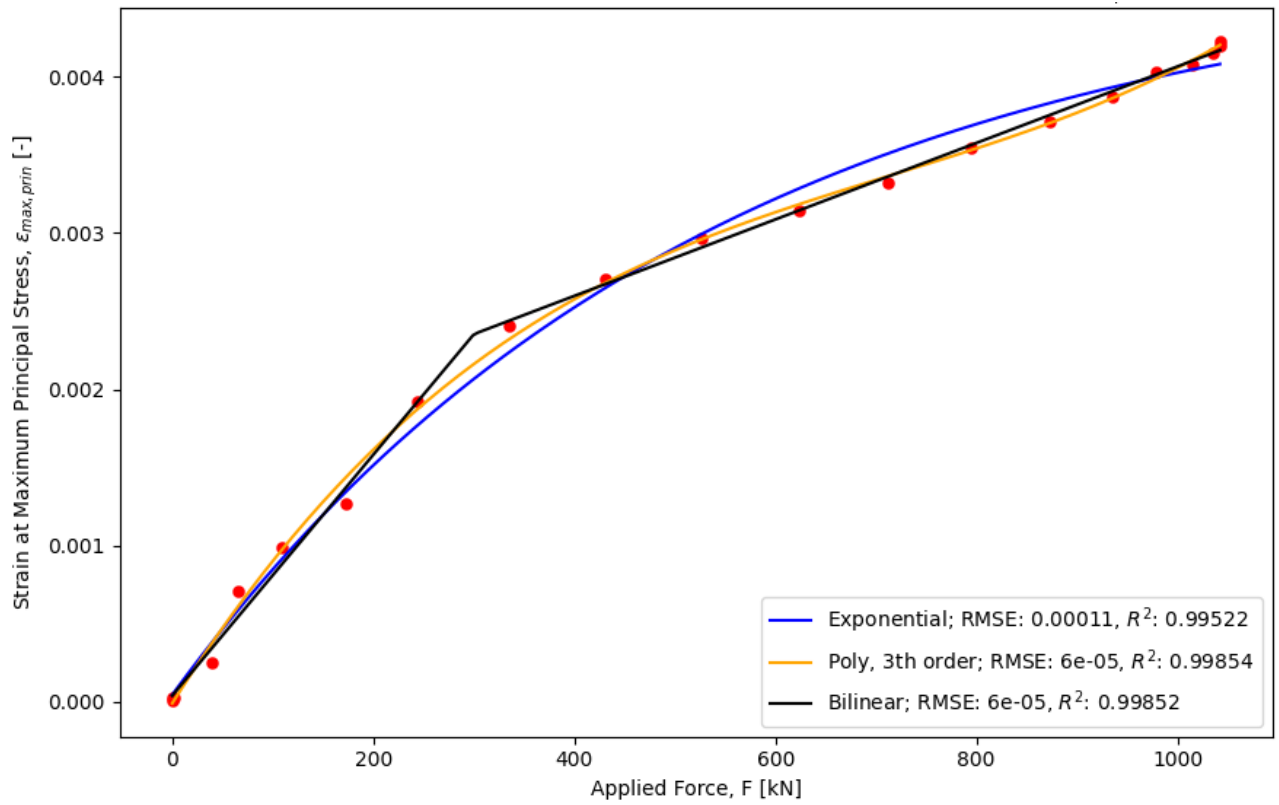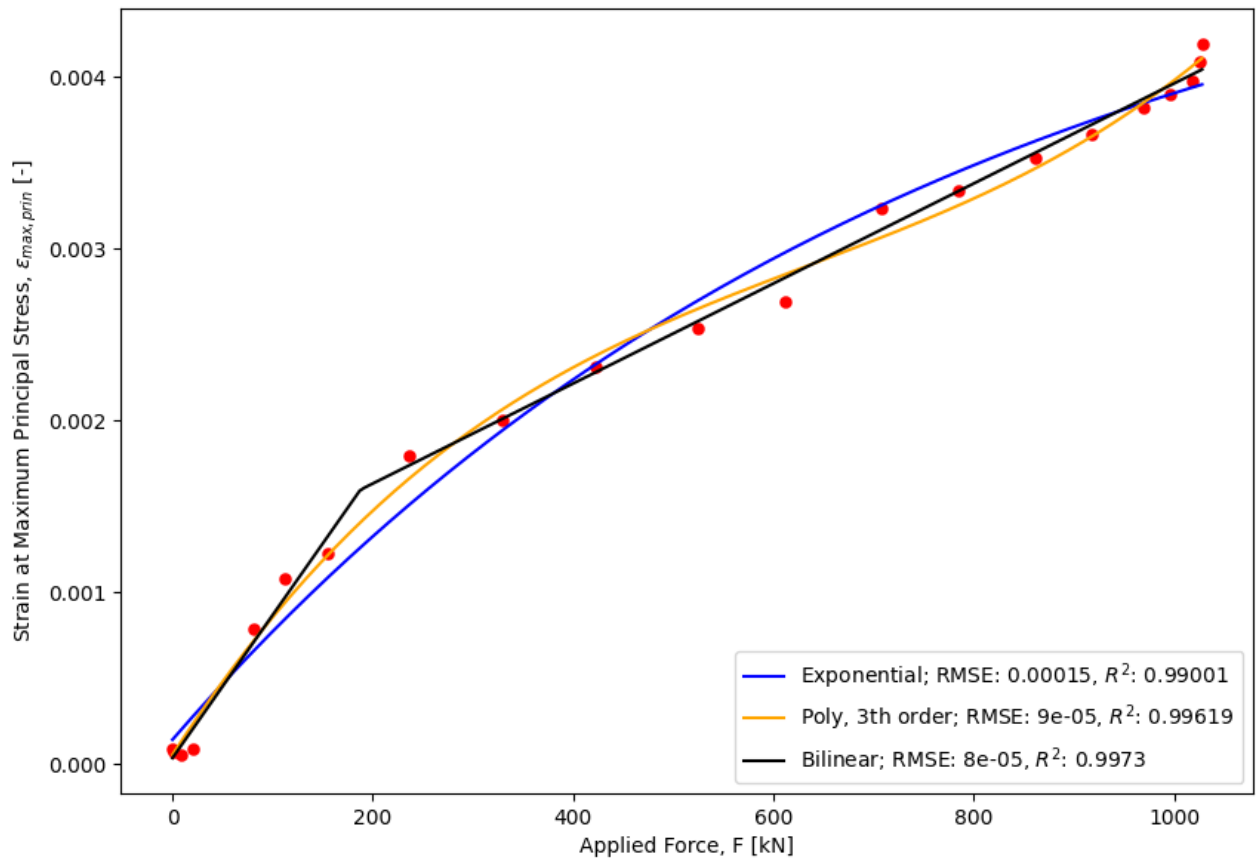*Figure 115: Relation between axial force, F, and strain at maximum principal stress, ε, in the prestressed model*
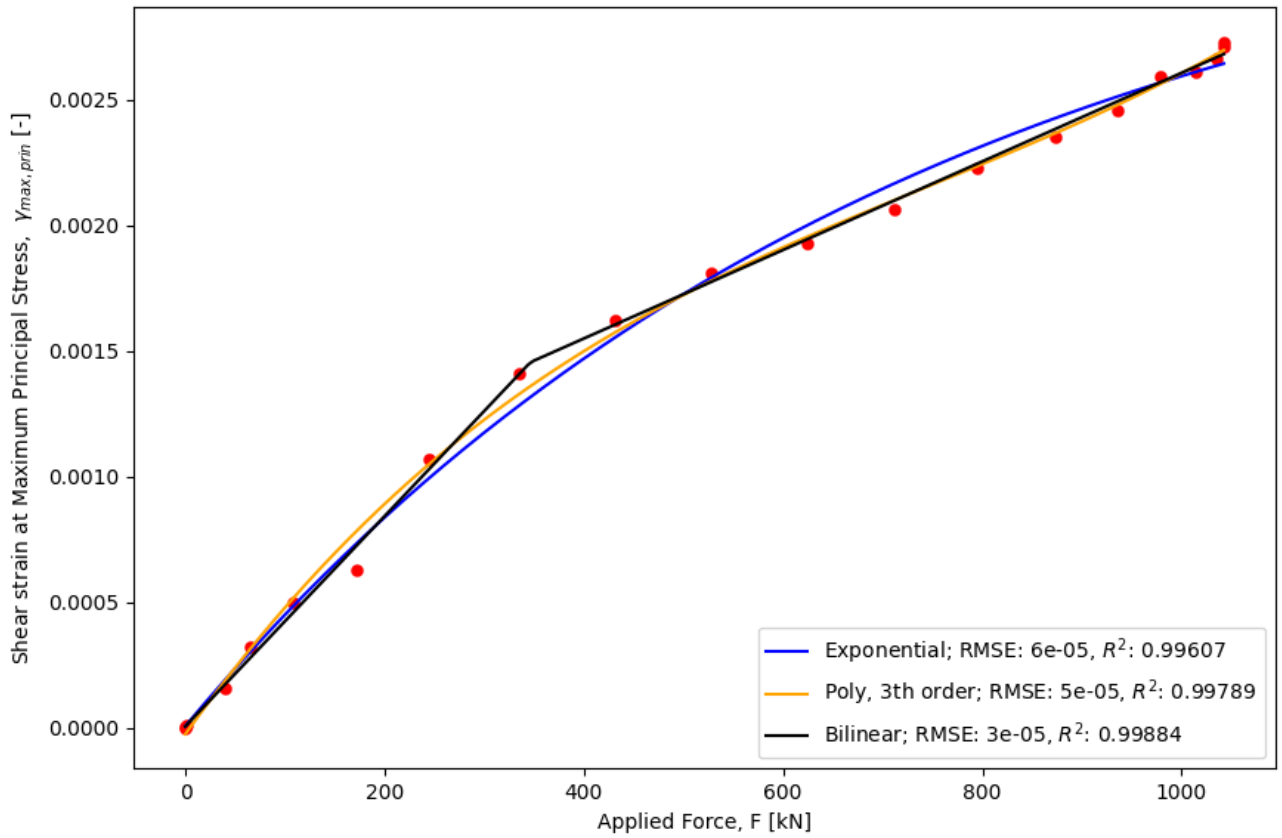
Figure 116: Relation between axial force, F, and shear strain at maximum principal stress, γ, in the non-prestressed model
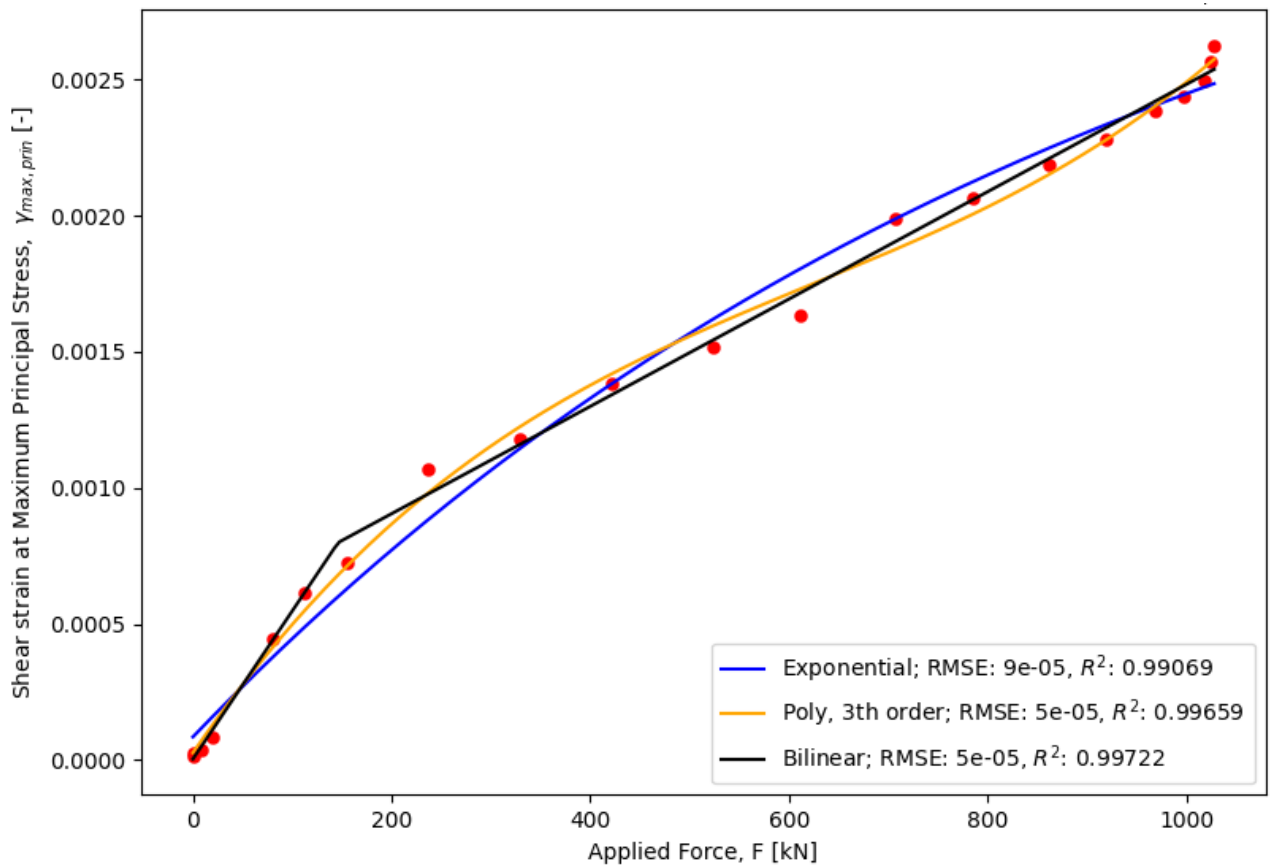
Figure 117: Relation between axial force, F, and shear strain at maximum principal stress, γ, in the prestressed model

6.2. Comparison of Eurocode and strain-life fatigue estimation methods

A common method of investigating the remaining fatigue life of a given connection that is not represented by any of the detail categories, though more commonly adopted in the assessment of welded structures, would be to calculate the stress concentration factor, similar to what is done in De Jesus' (2014) work described in Chapter 2.3.2.1 and 4.2.1.1, and adapt the base material S-N curve accordingly. However, this method relies on the fact that the investigated stress concentration is only as a result from an axial tension load, and that the net cross-sectional area on which this tension acts, can be calculated. Neither of these requirements are true for the critical location investigated in this report, as it is loaded both by the diagonal beam and the main horizontal beam. Furthermore, because the critical location is not subjected solely to axial tension, the cross-sectional area on which it acts cannot be calculated.

However, for the purpose of illustration, a calculation of an effective stress concentration factor and resulting S-N curve is included. This calculation presumes that the force which the critical location is subjected to, is only an axial tensile load, essentially disregarding the effects of the diagonal beam. Also, it presumes that the net cross-section at the critical location can be represented by the net cross-section of the beam on which the axial load acts, namely the main horizontal beam. As the stresses and forces are known from the bridge joint models, and their corresponding transfer function is known, the effective stress concentration factor for a given applied force can be calculated. By definition, the stress concentration factor should be gathered from the elastic stress range, disregarding local plastic deformation. The stress concentration factor is calculated according to Eq. 24. The net cross-sectional area is calculated using the cross-section displayed in Figure 118, and includes seven rivet holes, two of which cross both the web and the flanges. This is the same number of rivets present in the equivalent cross-section in extension of the main beam, at the location of the investigated critical location.
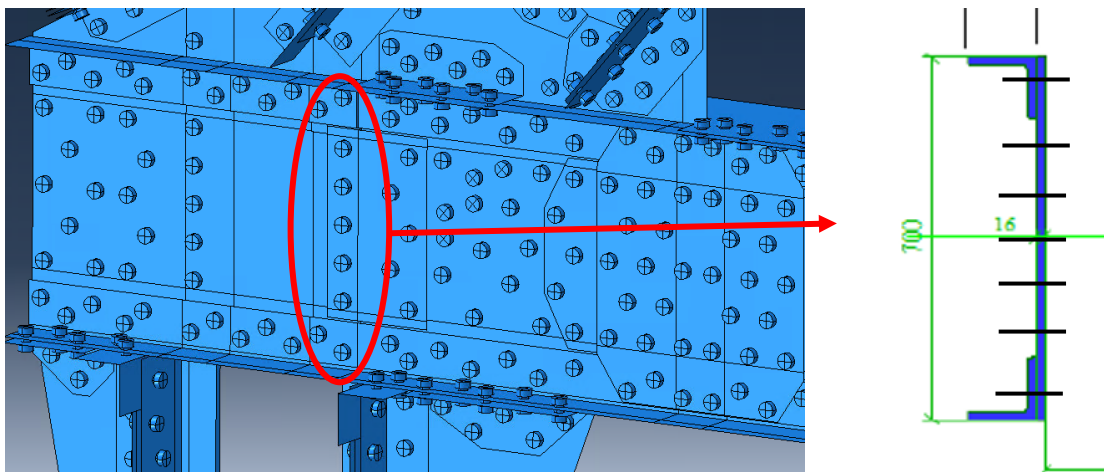
Figure 118: Effective net cross-section for calculation SCF

With an assumed applied load within the elastic stress range, e.g., 100 kN, and using the stress transfer functions to find the corresponding local stress, the effective stress concentration factors become:

$$SCF_{nonprestress} = \frac{\sigma_{prin}}{F/A_{net}} = \frac{204,32}{100 * 10^3/13790} = 28,18 \qquad \text{Eq. 35}$$

$$SCF_{prestress} = \frac{\sigma_{prin}}{F/A_{net}} = \frac{206,34}{100 * 10^3/13790} = 28,45 \qquad \text{Eq. 36}$$

It is evident that the non-prestressed and prestressed models generate almost identical stress concentration factors. Normally, one would expect the stress concentration factor of a prestressed model to be smaller than that of a non-prestressed model. This deviation from the norm can be attributed to the slight inaccuracy of the fits found to describe the load-stress transfer function. An increase in available datapoints with which the transfer function can be generated would increase the accuracy of the transfer functions, and as a result, the SCFs. However, their difference is negligible, and will therefore not be further investigated.

Taking the base material curve (detail category 160), and dividing this detail category by the stress concentration factor, the corresponding S-N curves for the observed critical location within the riveted connection can be gathered (see Eq. 37 and Figure 119). Given the fact that the local stress increases rapidly as the applied forces increases in the elastic stress range, the resulting stress concentration factors are incredibly large. As a result, the expected fatigue performance using this method is extremely poor, being closely equivalent to a detail category 5,6 for both models.

$$\Delta\sigma_R^5 N_R = \left(\frac{160}{SCF}\right)^5 * 2 * 10^\wedge 6 \; for \; N \leq 10^8 \qquad \text{Eq. 37}$$

Inherently, the SCF-method is generally adopted to uninvestigated situations, and the Eurocodes have a tendency to be overly conservative for uninvestigated situations. Therefore, as expected, comparing the SCF-method to Smith-Watson-Toppers equation at R = 0, the SCF-method is significantly more conservative than the SWT-method. Other values of R for the SWT-method are presented in Figure 120. As R increases, a slightly worse performance in the high cycle regimen can be observed. Meanwhile, for low cycle fatigue, better performances are found for higher stress ratios, though to a lesser degree than the difference observed in high cycle fatigue. Because the SCF-method is based on nominal stresses, it should be noted that the nominal stress range is also used in the Figures below, rather than local stresses or strains, which is why a different relation between R and N_f is found than illustrated in Figure 110.
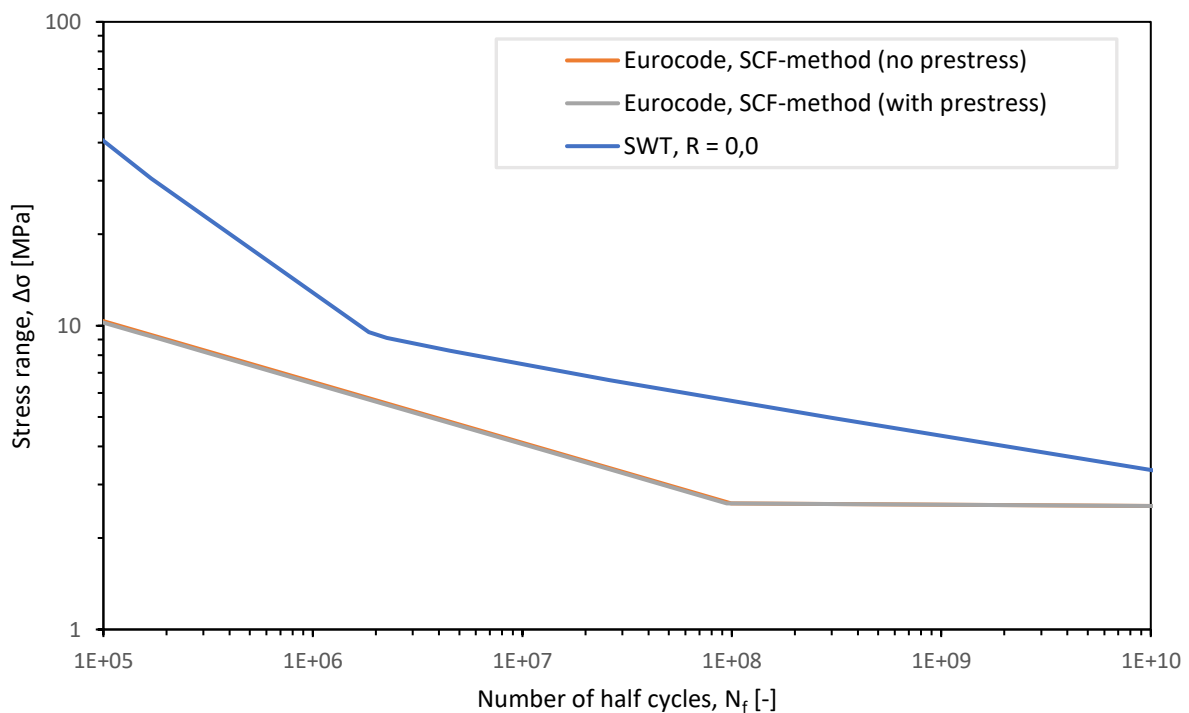
Figure 119: Illustrative S-N curves comparing stress-based fatigue calculation methods to the strain-based SWT-method
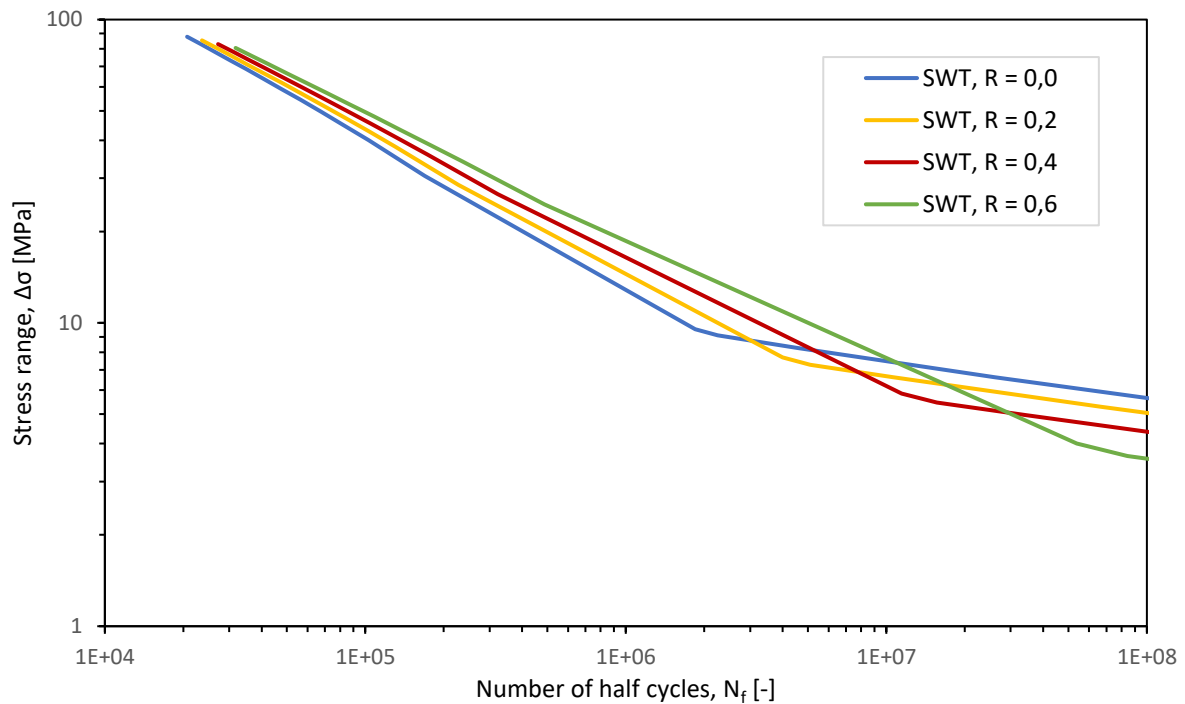
Figure 120: Smith-Watson-Topper curves of the critical detail for different values of R

To compare the investigated strain-life curves to the stress-life curves, a simple example can be taken. By considering a small sub-section of a theoretical loading history of a structure, two arbitrary applied forces (e.g., F_1 = 20 kN and F_2 = 400 kN) can be taken. This singular load range can be used to calculate a singular $\Delta\sigma$, $\Delta\varepsilon$ and $\Delta\gamma$ with the proposed transfer functions. The stress ratio, R, needed for Smith-Watson-Topper is similarly determined with the transfer functions. Using the various methods described in this chapter, the corresponding maximum cycles until failure can then be gathered from the curves. The methods considered in this example are the stress concentration factor method (SCF), Smith-Watson-Topper's strain-life equation (SWT) and the maximum shear strain criterion (MSSC) where SCF uses stresses, SWT uses stresses and strains and MSSC uses shear strains.

Table 27: Number of cycles until failure for a simple force range using various methods

			Non-Prestressed		Prestressed	
			F_1	F_2	F_1	F_2
Applied Force	F	[kN]	20	400	20	400
Nominal stress	σ_{nom}	[MPa]	1,45	29,01	1,45	29,01
Local stress	σ_{loc}	[MPa]	40,14	317,46	31,40	298,00
Local strain	ε_{loc}	[-]	$0,19 \times 10^{-3}$	$2,60 \times 10^{-3}$	$0,20 \times 10^{-3}$	$2,22 \times 10^{-3}$
Local shear strain	γ_{loc}	[-]	$0,09 \times 10^{-3}$	$1,55 \times 10^{-3}$	$0,11 \times 10^{-3}$	$1,30 \times 10^{-3}$
Nominal stress range	$\Delta\sigma_{nom}$	[MPa]	27,56		27,56	
Local stress ratio	R	[-]	0,13		0,11	
Local stress range	$\Delta\sigma_{loc}$	[MPa]	277,31		266,61	
Local strain range	$\Delta\varepsilon_{loc}$	[-]	$2,41 \times 10^{-3}$		$2,01 \times 10^{-3}$	
Local shear strain range	$\Delta\gamma_{loc}$	[-]	$1,46 \times 10^{-3}$		$1,19 \times 10^{-3}$	
Number of half-cycles, SWT-method	N_f	[-]	$1,16 \times 10^{5}$		$2,22 \times 10^{5}$	
Number of half-cycles, MSSC-method	N_f	[-]	$7,16 \times 10^{5}$		$2,03 \times 10^{6}$	

Number of cycles, SCF-method	N	[-]	$7,42 \times 10^2$	$7,08 \times 10^2$
Number of cycles, SWT-method	N	[-]	$2,33 \times 10^5$	$4,43 \times 10^5$
Number of cycles, MSSC-method	N	[-]	$1,43 \times 10^6$	$4,07 \times 10^6$
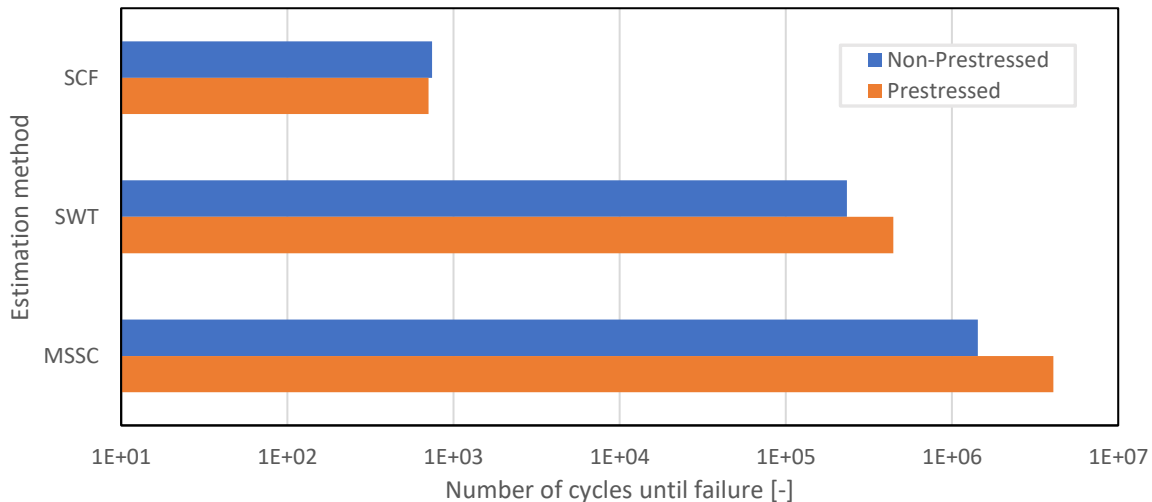
Figure 121: Cycles until failure for the different calculation methods

It is evident that the method employed to find the fatigue cycles until failure for a given stress, strain and shear strain amplitude has a significant influence on the resulting fatigue estimation. The SCF-method, which is prescribed by the Eurocode, shows a significantly smaller estimated cycles until failure than either of the other two methods. This is inherently expected, owing to the fact that the SCF-method is to be used when previously uninvestigated details are assessed. As they are untested, a significant margin of error is expected in the assessment of these details, and the SCF-method needs to be able to account for this large margin of error, while still maintaining safe results. Therefore, the SCF-method has a tendency to provide overly conservative life estimates.

Both SWT and MSSC estimate a significantly larger number of cycles until failure than the SCF-method. Despite this, there still is a large discrepancy between the two methods, as MSSC's estimate is one order of magnitude larger than SWT's estimate. One of the reasons of this, is that the multiaxiality of the joint is limited in the sense that the diagonal and horizontal loads on the critical location are always presumed to be proportional to each other, as internal loads in truss-like structures inherently tend to be. Because the horizontal and diagonal loads remain proportional to each other, the stress distribution around the critical location will likely show minimal deviations from the norm, limiting the influence of multiaxiality on the fatigue resistance of the critical location. Furthermore, as opposed to SWT, most fatigue assessments methods are based on a zero mean stress, e.g., they do not account for mean stress effects. MSSC falls within this category of assessment methods. The axial forces in the truss are expected to maintain in either tension or compression, without switching from one to the other. Hence, the mean stress will always be either larger or smaller than zero, depending on the investigated truss beam. Given that SWT predicts a significantly lower number of cycles until failure than MSSC, it can be concluded that this mean stress effect has a significant influence on the fatigue resistance of the considered critical location. It is clear that it is important to consider the implications of different loading situations and joint

geometries, and using either method may not be able to capture the full fatigue response of the joint. In general, it is expected that the mean stress will always have some effect, whereas multiaxiality may not be relevant for certain connections.

Furthermore, the influence the presence of prestressing has on the fatigue resistance of the critical location is significant. Even a relatively modest prestress of 40 MPa on the rivets results in an expected increase in cycles until failure of a factor two and three for SWT and MSSC respectively. This can be explained by the fact that prestressing introduces small negative principal stresses in the critical location, lowering the mean stress observed in this location. In combination with the tendency of prestressed models to produce higher stresses and strains at lower applied forces, and vice versa, resulting in smaller overall stress or strain ranges than its non-prestressed counterpart, a more optimized resistance to cyclic loading is predicted, resulting in a larger estimated number of cycles until fatigue failure.

It is clear that the assessment of complex, full-scale riveted connections pertaining to fatigue-related issues benefits from the use of local strain-based assessment methods, resulting in significantly less conservatively estimated remaining fatigue lives than the current stress-based approach for unstudied details. While the incorporation of multiaxiality may not need to be considered, dependent on the geometry of the joint and the expected stress- and strain response in critical locations, the inclusion of mean stress effects appears to have a significant influence on the estimated fatigue life of a joint, given the fact that mean stresses are rarely equal to zero, and thus should be taken into consideration.

6.3.　Applicability and complexity of fatigue assessment methods in practice

In order to fully investigate the applicability of the fatigue assessment methods utilized in this thesis, their ease of use needs to be considered. Furthermore, while either method could be used at an engineers discretion, many engineering firms have time constraints to consider when performing an assessment. To account for these issues, the following factors are considered: the complexity of the model used in the analysis, the ease with which results can be gathered, and the complexity of the formulae used to find the number of cycles until failure. Each of the considered methods require a detailed analysis on the internal stresses and strains within critical locations, meaning all methods require a Finite Element model. Creating this is a fairly time-intensive process. If only a single critical location is to be investigated, it may not need to be modelled in as much detail as performed in this report and several simplifications may be adopted, but if all critical locations need to be modelled, this time-intensiveness is especially true. A major advantage of the SCF-method is that only the elastic stress range needs to be considered, whereas the SWT and MSSC-methods both require knowledge on the elasto-plastic behaviour of the joint. Disregarding the plastic response has a significant benefit to the calculation time of the models, compared to models that do include plastic behaviour. While the construction time of the model is dependent on the skill and familiarity of the user with the modelling software, in general, the construction time will significantly exceed the model runtime, assuming a limited number of runs. Therefore, not including plasticity in the model, while significant to model runtime, only presents a relatively modest advantage on the overall assessment time.

On top of model building and its calculation, another factor to consider is the ease with which results can be gathered. The gathering of results from the model with which the SCF-method can be performed is straightforward, utilizing only a single applied load and local stress concentration in the elastic range to calculate the SCF. Both SWT and MSSC use transfer functions to define the relation between local stresses, strains and shear strains and the applied load. Expressing these transfer

functions by a formula requires a multitude of datapoints, and can be calculated either by hand or through any estimation algorithm appropriate for the situation. While this is not necessarily a complex task, it does add to the difficulty with which the methods can be performed. Finally, it should be noted that local stresses and strains are generally easily accessible in modelling software, but gathering local shear strains may require additional data manipulation.

Finally, the complexity of the used formulae is considered. The SCF-method uses adjusted S-N curves to find the number of cycles until failure. This method does not deviate much from the standard, detail category-based approach, and can therefore be considered to be fairly simple to use. The strain-based formulae used in SWT and MSSC are more complex than the standard S-N curves, and require additional material data. The Eurocodes have not adopted predefined values for this material data, meaning the data needs to be gathered either from existing literature, or from an experimental study on the considered material. This adds to the difficulty of the formulae. Finally, SWT's life-cycle assessment is dependent on two variables, namely the local stresses and strains. This means that to use this method, multiple transfer functions need to be drawn up, slightly increasing the time it takes to use the method, as opposed to MSSC's life cycle assessment, which only requires one transfer function to describe the relation between applied force and local shear strain.

It is evident that the SCF-method is the least difficult approach to adopt from the methods discussed in this report, based on the slightly simpler model required, the limited amount of data that needs to be extracted from the model, no need for transfer functions and the use of a simple equation to calculate the number of cycles until failure. However, because model building is a substantial part of the work required to investigate a full-scale joint, and the model itself does not differ much from the models required for the SWT- and MSSC-approaches, the advantage gained by using the SCF-method is relatively limited. This, combined with the fact that the SCF-method has a tendency to predict an overly conservative number of cycles until failure, makes both the SWT- and MSSC-approaches preferred over the SCF-approach.

Both the SWT- and MSSC-method use essentially the same FE model, and require a similar amount of work. While no additional data manipulation is needed for the SWT-approach, making result gathering slightly easier than for the MSSC-approach, the formula used to perform the fatigue assessment is slightly more simple in the MSSC-approach. However, as Chapter 6.2 has indicated, unless one is absolutely certain the level of multiaxiality in the joint is significant, the SWT-approach is a more widely applicable approach, as almost all joints experience some degree of non-zero mean stress. Hence, in general, the SWT-approach is considered to be the preferred method over the MSSC-approach.

7. Conclusions and recommendations

The research questions and objectives stated in the introduction of this report are attempted to be concisely answered in this chapter. A critical review of the scope and methodology is provided, after which the final conclusions are presented. Finally, some recommendations are provided on possible future research that may complement the findings of this report.

7.1. Conclusion

The main objective of this report is to investigate possible approaches to fatigue assessment of complex, full-scale riveted connections in steel bridges, and to consider the complexity of these approaches. To this end, the influencing factors on the fatigue behaviour of riveted connections have been investigated, and an overview of the available methods for fatigue assessment have been presented. A multitude of factors have been determined to be of influence, but the primary aspects that affect the fatigue resistance of a joint are found to be the material properties of the material, the clamping stresses, stress ranges and stress ratios on the joint, and level of multiaxiality. Investigation on the available assessment methods shows a limited degree of incorporation of these essential factors. Guidelines like EN 1993-1-9, the European guideline for fatigue assessment, provide a limited number of detail categories for the fatigue assessment of riveted structures, and additional guidelines like RBK Steel still focus primarily on critical locations in built-up cross-sections of beams rather than critical locations subject to the more complex loading situations in joints. Advanced assessment methods, like local strain-life approaches and fracture mechanics, are able to more completely capture the fatigue response of complex joints, but are not yet adopted in the Eurocodes. Adaptations to the strain-life approach are also able to capture influences like multiaxial loading and mean stress effects. Simultaneous incorporation of multiple factors remains largely uninvestigated. To accurately assess the fatigue in riveted connections, experimental studies or Finite Element (FE) analyses are necessary. As such, in combination with a large variability in the clamping forces on rivets in existing structures, the fatigue assessment of complex riveted joints remains challenging in practice.

To investigate the possibility of fatigue analysis on a riveted joint, a FE model of an existing bridge joint is constructed in ABAQUS, based on the structural analysis of the bridge by Iv-Infra. Bridge joint model assumptions are validated through the assessment and replication of pre-existing experimental studies and corresponding FE models. A shell element-based model is constructed to identify critical locations within the joint, and a solid element-based sub-model of a critical location is created within the shell-based model, to find more accurate results. With the results from the critical location, through the use of transfer functions, a relation between the applied force and local stresses or strains in the critical location is described. These transfer function are empirical formulae that can be utilized to estimate local stresses and strains as a result of a given applied load, reducing the amount of times a detailed FE model needs to be run, significantly cutting down on the total time it takes to perform a fatigue assessment.

A simple fatigue assessment based on a singular load case has been performed, to investigate the results for different fatigue assessment approaches. Smith-Watson-Topper's (SWT) adaptation to the material strain-life (ε-N) curve, to incorporate mean stress effects, and the maximum shear strain criterion (MSSC) method, to incorporate multiaxial loading, have been generated for one of the critical details. Moreover, through a simplification of the geometry, by assuming a simplified cross-section of the joint that matches the cross-section of the beam on which the axial forces act, a stress-life (S-N) curve can be generated. For detail categories not provided by the Eurocode or addendums, the stress concentration factor (SCF) method is prescribed, with which the material S-N

curve can be adjusted. Comparing the stress- and strain-life curves of the various methods, and using a single exemplary force range to find estimated fatigue lives, the following conclusions can be drawn:

- The method used to assess the fatigue is highly influential on the estimated remaining fatigue life. SCF is known to be a very conservative estimation method, as it is used to assess a large variety of details, and this is backed by the results, indicating an estimated fatigue life two or three orders smaller than SWT and MSSC respectively.
- Differences in SWT and MSSC are likely a result from the inherent workings of trusses, where the truss beams will generally remain in either tension or compression, increasing the influence of mean stress effects, and will remain proportional to each other, limiting the effect of multiaxial loading. Users should remain critical on which effects will likely have the highest effect on the estimated fatigue life, and choose estimation methods accordingly.
- While having a limited effect on the S-N and ε-N curves, the presence of prestressing on the rivets has a significant influence on actual local stresses and strains around the critical location resulting from a predefined applied load. For a load case with the same loads, estimated fatigue lives tend to increase by a factor two or more for prestressed situations compared to non-prestressed situations. This is caused by an increased local stress and strain at low applied loads, and decreased local stress and strain at high applied loads, resulting in an overall lower stress range.

On top of their perceived accuracy and conservatism from the example calculation, each of the approaches is also assessed on the applicability in practical calculations, particularly related to ease of use and time intensity. Considering the complexity of the construction of the required models, the difficulty of gathering required results and simplicity of the different formulae used to perform the estimation, a comparison is made between the three methods. Despite the SCF approach being significantly simpler to adopt, the increased accuracy and resulting decreased conservativity perceived in both SWT and MSSC suggests both methods to be preferred over SCF. Between SWT and MSSC, their complexity in model construction, result gathering and simplicity of formulae are very comparable, but given that SWT is in general more widely applicable, being relevant in most joints, SWT would be the overall preferred approach to perform a fatigue assessment of riveted joints.

7.2.   Discussion and limitations

From the literature review it is clear there is a significant number of influential factors responsible for the response to both static and cyclic loads. It is impossible to investigate all factors at the same time. Given the fact that the proposed strategy has been applied to a single riveted connection, factors like the joining typology and riveting patterns, which inherently affect the distribution of stresses throughout the joint, are not within the scope of the report. External factors such as imperfections resulting from human error or the effect of corrosion are similarly left out of this report.

Within the report, very limited load cases are presented; to establish the relation between applied force and local stresses and strains only a single load case is considered. While the purpose is to reduce the amount of time it takes to investigate a detailed Finite Element model, it does result in a low confidence in the established transfer functions, which are based on a small number of data points.

Because the John S. Thompsonbridge is a truss structure, loads on the joint have been simplified to only include axial forces. Inclusion of internal moments and applied shear stresses on the beams of

the joint may cause for significantly different stress- and strain distribution which are not captured by the suggested empirical formulae. Furthermore, investigation of different loading applications could indicate the presence of other, as of yet unidentified critical locations.

It should be noted that the calculations carried out on the fatigue of the joint do not encompass a complete fatigue life assessment, but rather an investigation of the crack initiation phase under a specific load case. For a full fatigue assessment, the fatigue loads prescribed by the Eurocode, and the resulting forces on the bridge joint, would need to be considered, and all identified critical locations would need to be investigated. If a full overview of the cracking phase is required as well, fracture mechanics could be adopted.

In the comparison between the ease of use of the different approaches, it is stated that a substantial part of the fatigue assessment is the construction and calculation of the model of the full-scale joint, limiting the benefit of using slightly simpler calculation methods. While this remains true in most cases, it is reliant on both the size of the joint and the skill of the constructor. If the purpose of the fatigue assessment is only an exploratory investigation, without a complex loading situations, and the joint model is sufficiently simple to create, it may be warranted to use the SCF-approach over the more complex SWT- or MSSC-approaches. Furthermore, additional experimental investigations may provide more details on the accuracy of the suggested approaches in complex joints, suggesting the use of other methods than proposed in this report.

Finally, the proposed fatigue assessment methodology is entirely based on the use of ABAQUS. While an attempt was made to perform the fatigue assessment using other tools, like IDEA Statica (see Annex E), these attempts where unsuccessful. The reason for this is that IDEA Statica has no built-in function to model rivets, meaning a simplified, not completely representative substitute needed to be used. Furthermore, extraction of the specific results required for the adopted fatigue assessment strategy are unobtainable from IDEA Statica. Replication of the work with other Finite Element software packages may provide different results.

7.3. Recommendations for future research

With the obtained results, the following recommendations for future studies are suggested:

- Rather than the single critical location investigated in this report, a full fatigue analysis of the joint may be performed. This would entail the incorporation of multiple critical locations, all with their own force-stress and force-strain transfer functions. Application of actual forces on the joint, derived from a fatigue load analysis, may be applied to perform the complete remaining fatigue life estimation of the joint.
- The method with which the sub-model of the critical detail is constructed has yielded unusual results, likely as a consequence of the extrapolation of internal stresses of a shell element to a solid mesh element-based sub-model. A definitive method to perform shell-to-solid sub-modelling in such complex joints needs to be defined.
- The use of empirical equations to correlate internal stresses and strains to the applied loads needs further investigation. Experiments performed on smaller specimens may increase the confidence in the use of these empirical formulae.
- This report has limited itself to the application of axial loads on the joint. The inclusion of internal moments and shear stresses may affect the ability to express the local stresses and strains in terms of applied loads. Different loading configurations and their effect on the local stresses and strains need to be investigated. Furthermore, different critical locations, unidentified by the current loading situation, may be uncovered.

- The difference in results between the prestressed and non-prestressed models has further highlighted the need for an adequate method with which the clamping stresses on rivets can be estimated. For practical applications, it would be particularly interesting to develop a non-destructive method to identify clamping stresses in riveted connections in practice.
- Procedures to perform a fatigue analysis provided by the Eurocodes have shown to be insufficient for the analysis of complex riveted connections, as they are currently not applicable or require significant simplifications to be used. The development of detail categories that can be applied to connections with more complex geometries would be beneficial. Furthermore, establishing detail categories that differentiate between non-preloaded and preloaded riveted structures would help reduce the conservativeness of fatigue life estimations on riveted connections.

References

Åkesson, B. (2010). *Fatigue Life of Riveted Steel Bridges.* London: Taylor & Francis Group. doi:10.1201/b10429

Al-Bahkali, E. A. (2011). Finite Element Modeling for Thermal Stresses Developed in Riveted and Rivet-Bonded Joints. *International Journal of Engineering and Technology, 11*(6), 86-92.

Baker, K. A., & Kulak, G. L. (1985). Fatigue of Riveted Connections. *Canadian Journal of Civil Engineering, 12*(1), 184-191. doi:10.1139/l85-017

Basquin, O. (1910). The exponential law of endurance tests. *10*, pp. 625-630. American Society for Testing Materials.

Bertolesi, E., Buitrago, M., Adam, J. M., & Calderón, P. A. (2021). Fatigue assessment of steel riveted railway bridges: Full-scale tests and analytical approach. *Journal of Constructural Steel Research, 182*. doi:10.1016/j.jcsr.2021.106664

Boller, C., & Seeger, T. (1987). PART A: Unalloyed steels. In *Materials data for cyclic loading* (pp. 19-22). Elsevier.

Brown, M. W., & Miller, K. J. (1973). A Theory for Fatigue Failure under Multiaxial Stress-Strain Conditions. *Proceedings of the Institution of Mechinical Engineers, 187*(1), 745-755. doi:10.1243/PIME_PROC_1973_187_161_

Brühweiler, E., Smith, I. F., & Hirt, M. A. (1990). Fatigue and fracture of riveted bridge members. *Journal of Structural Engineering, 116*, 198-214. doi:10.1061/(ASCE)0733-9445(1990)116:1(198)

BS 7910:2013+A1:2015. (2015). *Guide to methods for assessing the acceptability of flaws in metallic structures.* London: British Standards Institution.

Cinitha, A., Umesha, P. K., & Nagesh, R. I. (2014). An overview of corrosion and experimental studies on corroded mild steel compression members. *Journal of Civil Engineering, 18*(6), 1735-1744. doi:10.1007/s12205-014-0362-0

Coffin, L. (1954). A Study on the Effects of Cyclic Thermal Stresses on a Ductile Material. *Transaction of the American Society of Mechanical Engineers, 76*(6), 931-949. doi:10.1115/1.4015020

Colette, Q. (2014). *Riveted connections in historical metal structures (1840-1940). Hot-driven rivets: technology, design and experiments.* Doctoral thesis, Vrije Universiteit Brussel.

Correia, J. A., De Jesus, A. M., Calçada, R., Pedrosa, B., Rebelo, C., Simões da Silva, L., & Lesiuk, G. (2017). Statistical Analysis of Fatigue Crack Propagation Data of Materials from Ancient Portuguese metallic bridges. *Frattura ed Integrità Strutturale, 42*, 136-146. doi:10.3221/IGF-ESIS.42.15

Cox, H. L., & Munse, W. H. (1952). *Static Strength of Rivets Subjected to Combined Tension and Shear.* Urbana, Illinois: University of Illinois.

D'Aniello, M., Portioli, F., Fiorino, L., & Landolfo, R. (2011). Experimental investigation on shear behaviour of riveted connections in steel structures. *Engineering Structures, 33*(2), 516-531. doi:10.1016/j.engstruct.2010.11.010

Davis, R. E., Woodruff, G. B., & Davis, H. E. (1940). Tension of Large Riveted Joints. *Transaction of the American Society of Civil Engineers, 105*(1). doi:10.1061/TACEAT.0005216

de Jesus, A. M., da Silva, A. L., & Correia, J. A. (2014, November). Fatigue of riveted and bolted joints made of puddle iron—A numerical approach. *Journal of Constructional Steel Research, 102*, 164-177. doi:10.1016/j.jcsr.2014.06.012

de Jesus, A. M., da Silva, A. L., & Correia, J. A. (2015, January). Fatigue of riveted and bolted joints made of puddle iron—An experimental approach. *Journal of Constructional Steel Research, 104*, 81-90. doi:Journal of Constructional Steel Research

de Jesus, A. M., da Silva, A. L., Figueiredo, M. V., Correia, J. A., Ribeiro, A. S., & Fernandes, A. A. (2011). Strain-life and crack propagation fatigue data from several Portuguese old metallic riveted bridges. *Engineering Failure Analysis, 18*(1), 148-163. doi:10.1016/j.engfailanal.2010.08.016

De Jonge, A. E. (1945). *Riveted joints: a critical review of the literature covering their development, with bibliography and abstracts of the most important articles.* New York: The American Society of Civil Engineers.

DiBattista, J. D., Adamson, D. E., & Kulak, G. L. (1998). Fatigue Strength of Riveted Connections. *Journal of Structural Engineering, 124*(7), 725-853. doi:10.1061/(ASCE)0733-9445(1998)124:7(792)

Dusicka, P., & Lewis, G. (2010). High strength steel bolted connections with filler plates. *Journal of Constructional Steel Research, 66*(1), 75-84. doi:10.1016/j.jcsr.2009.07.017

EN 1993-1-5+C1. (2012). *Eurocode 3: Design of steel structures - Part 1-5: Plated structural elements.* Brussels: CEN.

EN 1993-1-8:2007. (2007). *Eurocode 3: Design of Steel Structures - Part 1-8: Design of Joints.* Brussels: CEN.

EN 1993-1-9+C2:2012. (2012). *Eurocode 3: Design of Steel Structures - Part 1-9: Fatigue.* Brussels: CEN.

Fatigue Theory Reference Manual. (2002). *2*.

Fisher, J. W., Yen, B. T., & Wang, D. (1991). Corrosion and its influence on steel bridge members. *Transportation Research Record*(1290), 211-219.

Frémont, C. (1906). *Etude Expérimentale du Rivetage.* Paris: Société d'encouragement pour l'industrie nationale.

Gallegos Mayorga, L., Sire, S., Correia, J. A., de Jesus, A. M., Valente, I., Rebelo, C., . . . Plu, B. (2016). Design S-N Curves for Old Portuguese and French Riveted Bridges Connection Based on Statistical Analyses. *Procedia Engineering, 160*, 77-84. doi:10.1016/j.proeng.2016.08.865

García, O. M. (2017). *The impact of the connection stiffness on the behaviour of historical steel railway bridges.* MSc Thesis, Czech Technical University.

Garud, Y. (1981). Multiaxial Fatigue: A Survey of the State of the Art. *Journal of Testing and Evaluation, 9*(3), 165-178. doi:10.1520/JTE11553J
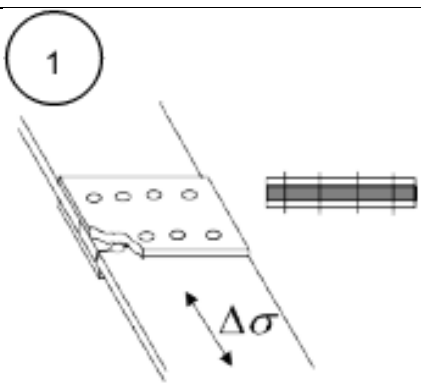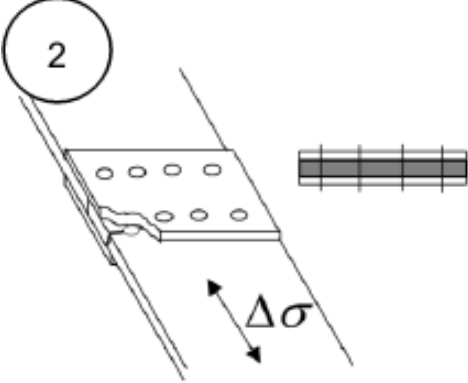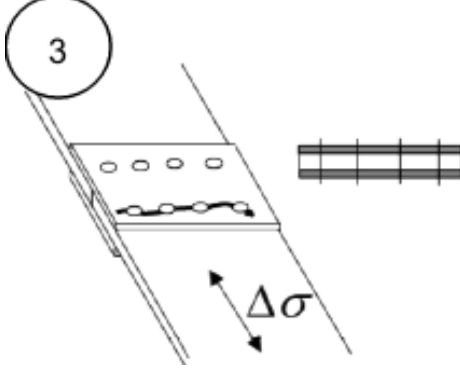
Glinka, G. (2010). The Local Stress-Strain Fatigue Method.

Heinemeyer, C., & Feldmann, M. (2011). The influence of rivet corrosion on the durability of riveted connections. *Steel Construction, 4*(3), 188-192. doi:10.1002/stco.201110026

Hilber, H. M., Hughes, T. J., & Taylor, R. L. (1978). Collocation, Dissipation and `Overshoot' for Time Integration Schemes in Structural Dynamics. *Èarthquake Engineering and Structural Dynamics, 6*(1), 99-117. doi:10.1002/eqe.4290060111

Kandil, F. A., Brown, M. W., & Miller, K. J. (1982). *Biaxial Low Cycle Fatigue Fracture of 316 Stainless Steel at elevated temperatures.* London: The Metals Society.

Kumar, R., & Singh, K. (1995). Inlfuence of stress ratio on fatigue crack growth in mild steel. *Engineering Fracture Mechanics, 50*(3), 377-384. doi:10.1016/0013-7944(95)91547-3

Landolfo, R., Cascini, L., & Portioli, F. (2010). Modeling of metal structure corrosion damage: a state of the art report. *Sustainability, 2*(7), 2163-2175. doi:10.3390/su2072163

Leonetti, D., Maljaars, J., Pasquarelli, G., & Brando, G. (2020). Rivet clamping force of as-built hot-riveted connections in steel bridges. *Journal of Constrcutional Steel Research, 167*. doi:10.1016/j.jcsr.2020.105955

Leslie, T. (2010). Built Like Bridges: Iron, Steel, and Rivets in the Nineteenth-century Skyscraper. *Journal of the Society of Architectural Historians, 69*(2), 234-261. doi:10.1525/jsah.2010.69.2.234

Liang, E. (2021). *23 Different Types of Corrosion: The Definitive Guide*. Retrieved from Yubi Steel: https://www.yubisteel.com/types-of-corrosion/

Lundkvist, A., Barsoum, I., Barsoum, Z., & Kurshid, M. (2023). Geometric and Material Modelling Aspects for Strength Prediction of Riveted Joints. *Metals, 13*(3), 500. doi:10.3390/met13030500

Macho, M., Ryjáček, P., & Campos e Matos, J. (2019). Static and Fatigue Test on Real Steel Bridge Components Deteriorated by Corrosion. *International Journal of Steel Structures, 19*, 110-130. doi:10.1007/s13296-018-0099-6

Maddox, S. J., Gurney, T. R., Mummery, A. M., & Booth, G. S. (1978). *An investigation of the influence of applied stress ratio of fatigrue crack propagation in strctural steels.* Cambridge: The Welding Institute.

Moriyama, H., Takai, T., Yamaguchi, T., & Kozai, S. (2020). Effect of number of additional bolts outside playes on behaviour of frictional type bolted joints with a filler plate. In C. M. Wang, V. Dao, & S. Kitipornchai, *EASEC16. Lecture Notes in Civil Engineering* (pp. 1439-1451). Singapore: Springer. doi:10.1007/978-981-15-8079-6_134

Morrow, J. (1968). *Fatigue Design Handbook.* Society of Automotive Engineering.

Nakai, T., Matsuhita, H., & Yamamoto, N. (2006). Effect of pitting corrosion on the ultimate strength of steel plates subjected to in-plane compression and bending. *Journal of marine science and technology, 11*, 52-64. doi:10.1007/s00773-005-0203-4

Niederwanger, A., Ladinek, M., Lang, R., Timmers, R., & Lener, G. (2019). On the stability and sensitivity of the strain-life approach using the example of mild steel. *Journal of Constructional Steel Research, 153*, 483-494. doi:10.1016/j.jcsr.2018.10.030
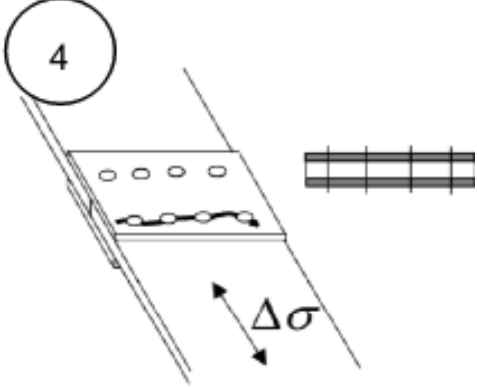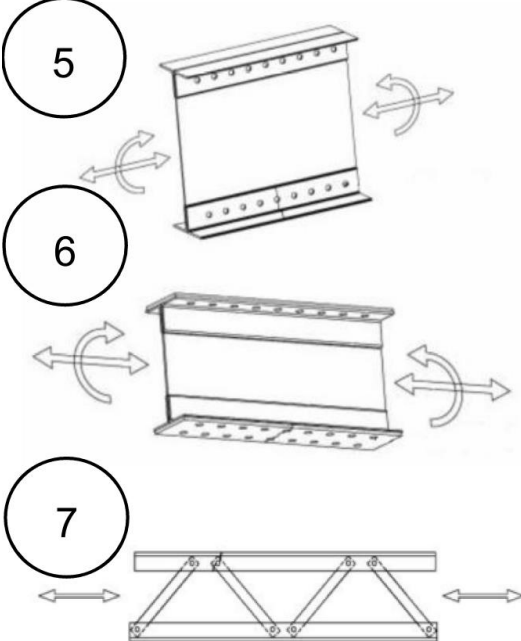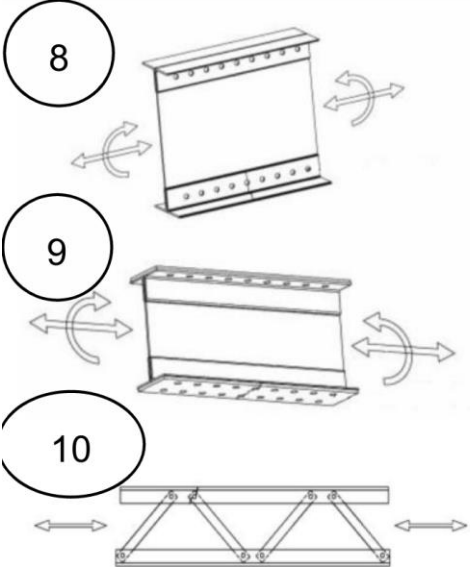
O'Sullivan, M., & Swailes, T. (2009). A Study of Historical Test Data for Better Informed Assessment of Wrought Iron Structures. *International Journal of Architectural Heritage, 3*(4), 260-275. doi:10.1080/15583050902802337

Paris, P., & Erdogan, F. (1963). A Critical Analysis of Crack Propagation Laws. *Journal of Basic Engineering, 85*(4), 528-533. doi:10.1115/1.3656900

Park, J.-H., & Song, J.-H. (1995). Detailed evaluation of methods for estimation of fatigue properties. *International Journal of Fatigue, 17*(5), 365-373. doi:10.1016/0142-1123(95)99737-U

Pazmiño, M. B. (2018). *The Prediction of the Joint Stiffness in Riveted Steel Bridges.* MSc Thesis, Czech Technical Institution.

Pedrosa, B., Correia, J. A., Rebelo, C., Lesiuk, G., de Jesus, A. M., Fernandes, A. A., . . . Veljkovic, M. (2019). Fatigue resistance curves for single and double shear riveted joints from old portuguese metallic bridges. *Engineering Failure Analysis, 96*, 255-273. doi:10.1016/j.engfailanal.2018.10.009

Ramberg, W., & Osgood, W. R. (1943). *Description of stress-strain curves by three parameters.*

Raposo, P., Correia, J. A., Lesiuk, G., Valente, I., de Jesus, A., & Calçada, R. (2017). Mechanical characterization of ancient portuguese riveted bridges steels. *Engineering Structures and Technologies, 9*(4), 214-225. doi:10.3846/2029882X.2017.1414637

RBK Staal. (2017). *Richtlijn Beoordeling Kunstwerken Staal.* Delft: NEN Commissie Bestaande Staalbouw.

Riedel, T., Sieber, L., & Flederer, H. (2021). Influence of rivet clamping stress on fatigue crack growth behaviour. *Eurosteel 2021* (pp. 1145-1152). Sheffield: Ernst & Sohn. doi:10.1002/cepa.1406

Roberge, P. R. (2019). *Handbook of corrosion engineering.* New York, NY: McGraw-Hill Education.

Schenker, L., Salmon, C. G., & Johnston, B. G. (1954). *Structural Steel Connections.* Engineering Research Institute, Department of Civil Engineering. Ann Arbor, Michigan: University of Michigan.

Schmidt, H., & Neuper, M. (1997). Zum elastostatischen tragverhalten exzentrisch gezogener l-stöße mit vorgespannten schrauben. *Der Stahlbau, 3*, 163-168.

Sire, S., Caiza, P. D., Espion, B., & Ragueneau, M. (2020). Contribution to the study of the influence of the stress ratio on the high cycle fatigue behaviour of riveted joints. *Fatigue & Fracture of Engineering Materials and Structures*, 3027-3036. doi:10.1111/ffe.13324

Sire, S., Gallegos Mayorga, L., & Plu, B. (2015). Observation of failure scenarios in riveted assemblies: an innovative. *Procedia Engineering, 114*, 430-436. doi:10.1016/j.proeng.2015.08.089

Smith, K. N., Watson, P., & Topper, T. H. (1970). A stress-strain function for the fatigue of metals. *Journal of Materials, 5*(4), 767-778.

Structural design of steel connections: Theoretical Background. (n.d.). (IDEA Statica) Retrieved from IDEA StatiCa Support Center: https://www.ideastatica.com/support-center/general-theoretical-background

Taras, A., & Greiner, R. (2010). Development and Application of a Fatigue Class Catalogue for Riveted Bridge Components. *Strcutural Engineering International, 20*(1), 91-103. doi:10.2749/101686610791555810

Troschenko, V. T., & Khamaza, L. A. (2010). STRAIN–LIFE CURVES OF STEELS AND METHODS. *Strength of Materials, 42*(6), 647-659. doi:10.1007/s11223-010-9253-x

Twelvetrees, W. N. (1900). *Structural Iron and Steel. A Text Book for Architects, Engineers, Builders, and Science Students.* London - New York: Whittaker & Co.

Vermes, W. J. (2007). Design and Performance of Riveted Bridge Connections. *ISPC Conference.* Akron, Ohio: Jones-Stuckey, Ltd., Inc.

Wilson, W. M., & Thomas, F. P. (1938). *Fatigue tests of riveted joints: a report.* College of Engineering, Engineering Experiment Station. Urbana, IL: University of Illiinois at Urbana Champaign.

Wyly, L., & Scott, M. B. (1956). An investigation of fatigue failures in structural members of ore bridges under service loadings. *American Railway Engineering Association, 57*, 175-297.

You, B.-R., & Lee, S.-B. (1996). A critical review on multiaxial fatigue assessments of metals. *International Journal of Fatigue, 18*(4), 235-244. doi:10.1016/0142-1123(96)00002-3

Zahrai, S. M. (2003). Cyclic strength and ductility of rusted steel members. *Asian Journal of Civil Engineering*, 135-148.

Zhang, X.-Y., Li, S.-X., Liang, R., & Akid, R. (2013). Effect of corrosion pits on fatigue life and crack initiation. *13th International conference on fracture*, (pp. 1-9). Beijing.

Zhou, Y. (1994). *Fatigue strength evaluation of riveted bridge members.* Lehigh University. Bethlehem, PA: UMI.

Annex A.   Detail categories for rivets from RBK Steel/Taras & Greiner

Table 28: Detail categories for riveted connection according to RBK Steel

Detail category	Detail	Description
90 m = 5		Symmetric gusset plated joint, fatigue failure in the middle plate(s). Additional requirements: 7) $\frac{\sigma_{bearing}}{\sigma_{net}} \leq 2$ 8) $f_{ur} \leq 400$ MPa or $f_{ur} > 400$ MPa without additional corrosion-resisting coating.
85 m = 5		Symmetric gusset plated joint, fatigue failure in the middle plate(s). In cases where detail 1 is not applicable.
80 m = 5		Symmetric gusset plate joint, fatigue failure in the cover plate(s). Additional requirements: 9) $\frac{\sigma_{bearing}}{\sigma_{net}} \leq 2$ 10) $f_{ur} \leq 400$ MPa or $f_{ur} > 400$ MPa without additional corrosion-resisting coating.

71 m = 5		Symmetric gusset plate joint, fatigue failure in the cover plate(s). In cases where detail 3 is not applicable.
85 m = 5		Built-up beam, fatigue failure in connection between angle cleats and web, with shear forces per rivet shear plane in SLS smaller than the minimum slip resistance (see Table 29).
		Built-up beam, fatigue failure in connection between angle cleats and flange, with shear forces per rivet shear plane in SLS smaller than the minimum slip resistance (see Table 29).
		Truss connection, with shear forces per rivet shear plane in SLS smaller than the minimum slip resistance (see Table 29).
71 m = 5		Built-up beam, fatigue failure in connection between angle cleats and web, where detail 5 is not applicable.
		Built-up beam, fatigue failure in connection between angle cleats and web, where detail 6 is not applicable.
		Truss connection where detail 7 is not applicable.
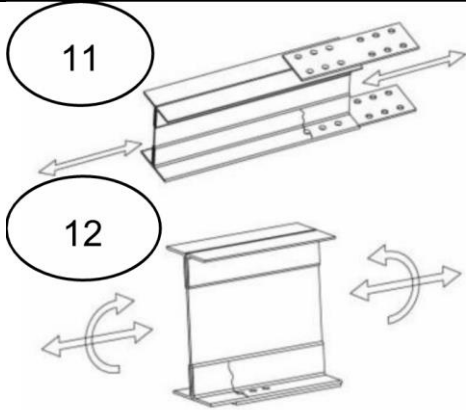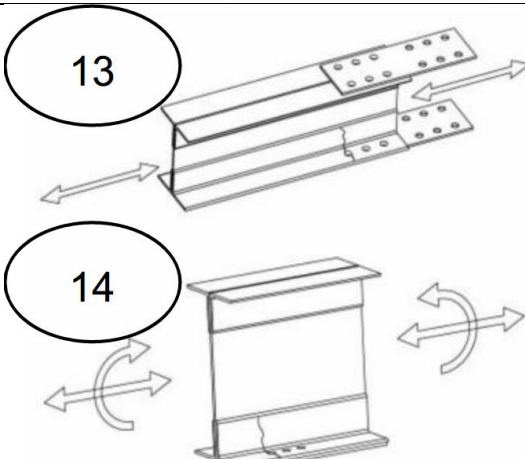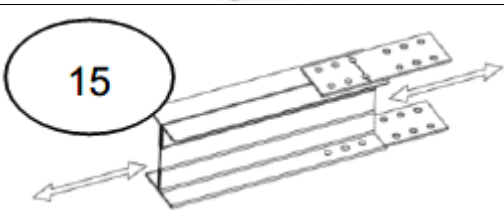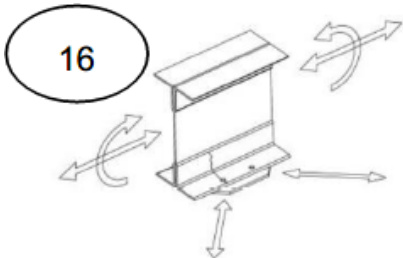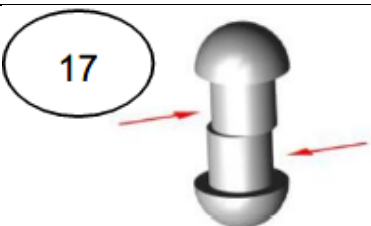
85 m = 5	11 12	Asymmetric gusset plated joint plate between built-up elements, fatigue failure in the flange, with shear forces per rivet shear plane in SLS smaller than the minimum slip resistance (see Table 29).
		Fatigue failure in the first rivet row of a filler plate, with shear forces per rivet shear plane in SLS smaller than the minimum slip resistance (see Table 29).
71 m = 5	13 14	Asymmetric gusset plated joint between built-up elements, fatigue failure in the flange, where detail 11 is not applicable.
		Fatigue failure in the first rivet row of a filler plate, where detail 12 is not applicable.
71 m = 5	15	Asymmetric gusset plated joint between built-up elements, fatigue failure in the gusset plate.
71 m = 5	16	Fatigue failure of the area between transverse connections and the flange of the main beam, with stresses in the flange.
140 m = 5	17	Rivet subjected to shear, with $\Delta\tau$ calculated using ΔF, which is the range of the shear force per rivet per shear plane.

Table 29: Minimum slip resistance per rivet shear plane

Applied riveting technique, and number of rivets (n^2)	Minimum value of the slip resistance per rivet shear plane	
	Iron or steel rivets with $f_{ur} \leq$ 400 MPa	Steel rivets with $f_{ur} >$ 400 MPa
Unknown technique or manual riveting.	12 kN	8 kN
Riveting with pneumatic hammer and n ≤ 15.	12 kN	8 kN
Riveting with pneumatic hammer and n > 15.	15 kN	10 kN

---

[2] Detail categories 5, 6, 8 and 9 have n = 1, categories 7, 10 and 16 have n = the number of rivets between rods/beams and for categories 1-4 and 11-15 n = the number of rivets that apply the forces to the cover/filler plates.

Annex B.   Case Study Koninginnebridge, Fatigue Analysis

Background

The Koninginnebridge is part of the Maasdijk, a road situated within Schiedam, and functions as a connection between the banks on either end of a side channel of the New Meuse. It is a (movable) steel bascule bridge built in 1978. The bridge deck itself spans 10,7 m and has a width of 17 m. When the pivot bar and ballast are considered, the total length of the bridge becomes 15,55 m. The general lay-out of the bridge has gone through a change during 2020, and both situations need to be considered separately.
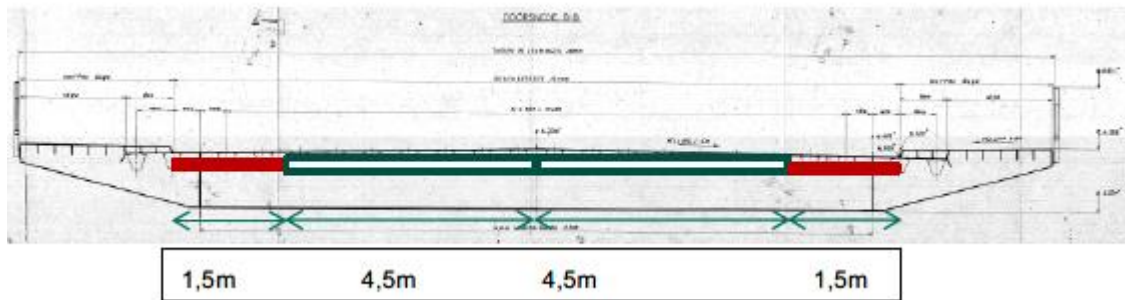
Figure 122: Original bridge lay-out
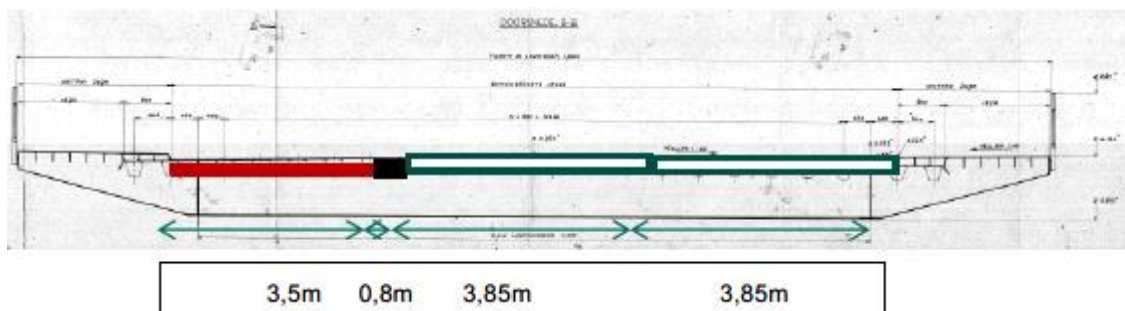
Figure 123: New bridge lay-out

Static and fatigue recalculations of the bridge performed in 2020 to assess the justifiability of performing large maintenance works had raised some concerns on the remaining fatigue strength of the bridge. Therefore, additional calculations have been performed, to verify whether a remaining lifetime of 30 years would be feasible. The main purpose of this case study is to illustrate the process of a standard fatigue assessment, so while both a static and fatigue analysis have been performed, only the fatigue analysis is covered.
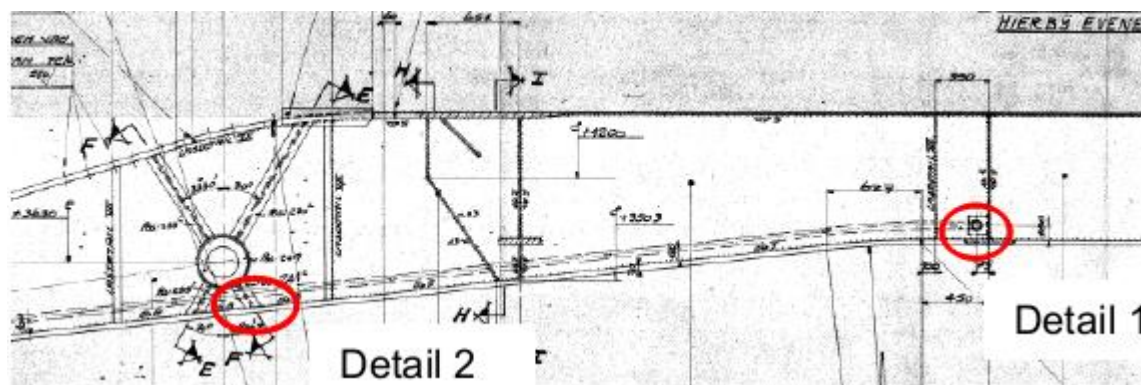
Figure 124: Critical details in the Koninginnebridge

There are a multitude of details that are possibly susceptible to fatigue damage within the bridge deck. By combining knowledge on the determined detail categories and the locations of large stress ranges within the deck, two details have been found to be critical. If upon assessment both details turn out to have a sufficient remaining fatigue capacity, additional details can be considered.

In the calculation only Detail 1 turned out to have an insufficient remaining fatigue life. As such, this report focuses only on Detail 1, though the calculations of both details follow the same principle. Detail 1 is a welded connection between the bottom flange of the main girder and the bottom flange of the first crossbeam, connected perpendicularly. The resulting detail category is category 40.

40		5) Gelast, zonder overgangsronding.

Figure 125: Detail category detail 1

Fatigue loads

In order to find the fatigue loads acting on each of the details, a traffic count needs to be performed. For several days, each truck that passed the bridge per lane has been noted down, in addition to the type of truck, as that affects the loads exerted on the bridge. However, these counts have been performed during the day, under working hours. By incorporating night-, weekend and Covid-19-factors (as this assessment has been done during the Covid-19 pandemic), an appropriate estimate can be made on the actual number of truck passages that occur on the bridge per week. Finally, the weekly number of passages can be extrapolated to find a yearly number. Extrapolating this number to both the past and the future, a fatigue assessment can be done to assess the remaining fatigue
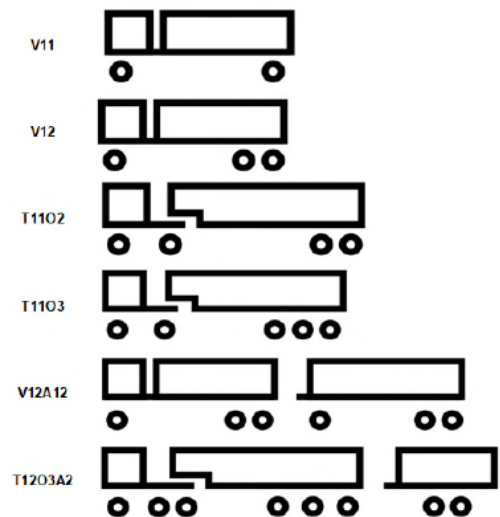
Figure 126: Types of trucks

life. Archive data shows that the total traffic increase tends to correspond to a growth factor of two over a period of 100 years. This yearly growth factor ($2^{1/100} = 1,007$) is assumed to be representative for both the past and future 100 years. Additionally, as a result of a change of infrastructure in the surrounding area, up to 2008, an additional 8 trucks per day are assumed to cross the bridge.

Traffic loads are calculated in accordance with NEN8701, Table A.1, A.2 and A.3. Each table represents the type and percentage of vehicles that can be assumed to cross the bridge for a given situation and time period. Using this data from the tables, the actual loads on the bridge per vehicle type can be determined. The traffic data found during the count corresponds most closely to trucks travelling long distances.

Over the period 2000-2020, traffic loads are assumed to increase by a factor of $100\% + 20\%^{20/100} = 1,04$ per year, while for the period 2021-2050 (which is its intended remaining lifespan) a factor of $100\% + 20\%^{50/100} = 1,10$ is found, all of which is in accordance with NEN8701. Material and dynamic safety factors are taken in accordance with the Eurocodes.

Table 30: NEN8701 – Table A.1 – Truck passages on bridge deck for the period between bridge opening - 1990

Tabel A.1 — Vrachtwagensamenstelling tijdvak opening-1990

type	Vrachtwagens (vrw's) % van totaal aantal vrw's			Assen nr.	afstand (m)	Astype type A, B of C opening-1990	Asbelasting [a] laag (kN) 50% aantal vrw's	middel (kN) 35% aantal vrw's	hoog (kN) 15% aantal vrw's	Vrachtwagenbelasting [a] laag (kN) 50% aantal vrw's	middel (kN) 35% aantal vrw's	hoog (kN) 15% aantal vrw's
	vrw's lange afstand	vrw's middellange afstand	vrw's lokaal verkeer									
1	10,0 %	50,0 %	75,0 %	2	5,20	A	35	55	70	75	125	170
V11						B	40	70	100			
2	10,0 %	10,0 %	10,0 %	3	3,80	A	55	75	90	145	215	315
V12					1,30	B	50	80	125			
						B	40	60	100			
3	25,0 %	15,0 %	5,0 %	4	3,80	A	55	60	70	180	245	350
T1102					6,60	B	55	75	110			
					1,30	B	35	55	85			
						B	35	55	85			
4	50,0 %	20,0 %	5,0 %	5	3,80	A	60	70	80	185	345	475
T1103					5,60	B	50	95	125			
					1,30	B	25	60	90			
					1,30	B	25	60	90			
						B	25	60	90			
5	5,0 %	5,0 %	5,0 %	6	2,80	A	60	70	80	295	460	600
T1203					1,30	B	40	60	90			
					5,60	B	60	90	115			
					1,30	B	45	80	105			
					1,30	B	45	80	105			
						B	45	80	105			
Totaal	100,0 %	100,0 %	100,0 %									

[a] Referentiewaarde geldend voor lange afstand in het jaar 2000, exclusief dynamische effecten en tijdmatige ontwikkeling belasting.

Table 31: NEN8701 – Table A.2 – Truck passages on bridge deck for the period between 1991 - 2011

Tabel A.2 — Vrachtwagensamenstelling tijdvak 1991-2010

type	Vrachtwagens (vrw's) % van totaal aantal vrw's			Assen nr.	afstand (m)	Astype type A, B of C 1991-2010	Asbelasting [a] laag (kN) 50% aantal vrw's	middel (kN) 35% aantal vrw's	hoog (kN) 15% aantal vrw's	Vrachtwagenbelasting [a] laag (kN) 50% aantal vrw's	middel (kN) 35% aantal vrw's	hoog (kN) 15% aantal vrw's
	vrw's lange afstand	vrw's middellange afstand	vrw's lokaal verkeer									
1	10,0 %	50,0 %	75,0 %	2	5,20	A	35	55	70	75	125	170
V11						**B**	40	70	100			
2	10,0 %	10,0 %	10,0 %	3	3,80	A	55	75	90	145	215	315
V12					1,30	B	50	80	125			
						B	40	60	100			
3	25,0 %	15,0 %	5,0 %	4	3,80	A	55	60	70	180	245	350
T1102					6,60	B	55	75	110			
					1,30	C	35	55	85			
						C	35	55	85			
4	50,0 %	20,0 %	5,0 %	5	3,80	A	60	70	80	185	345	475
T1103					5,60	B	50	95	125			
					1,30	C	25	60	90			
					1,30	C	25	60	90			
						C	25	60	90			
5	5,0 %	5,0 %	5,0 %	6	2,80	A	60	70	80	295	460	600
T1203					1,30	B	40	60	90			
					5,60	B	60	90	115			
					1,30	B	45	80	105			
					1,30	B	45	80	105			
						B	45	80	105			
Totaal	100,0 %	100,0 %	100,0 %									

[a] Referentiewaarde geldend voor lange afstand in het jaar 2000, exclusief dynamische effecten en tijdmatige ontwikkeling belasting.

Table 32: NEN8701 – Table A.3 – Truck passages on bridge deck for the period between 2011 - future

Tabel A.3 — Vrachtwagensamenstelling tijdvak 2011-einde referentieperiode

	Vrachtwagens (vrw's) % van totaal aantal vrw's			Assen		Astype	Asbelasting [a]			Vrachtwagenbelasting [a]		
type	vrw's lange afstand	vrw's middellange afstand	vrw's lokaal verkeer	nr.	afstand (m)	type A, B of C 2011 - einde ref.per.	laag (kN) 50 % aantal vrw's	middel (kN) 35 % aantal vrw's	hoog (kN) 15 % aantal vrw's	laag (kN) 50 % aantal vrw's	middel (kN) 35 % aantal vrw's	hoog (kN) 15 % aantal vrw's
1 V11	10,0 %	50,0 %	75,0 %	2	5,20	A	35	55	70	75	125	170
						B	40	70	100			
2 V12	10,0 %	10,0 %	10,0 %	3	3,80	A	55	75	90	145	215	315
					1,30	B	50	80	125			
						C	40	60	100			
3 T1102	20,0 %	15,0 %	5,0 %	4	3,80	A	55	60	70	180	245	350
					6,60	B	55	75	110			
					1,30	C	35	55	85			
						C	35	55	85			
4 T1103	50,0 %	17,5 %	5,0 %	5	3,80	A	60	70	80	185	345	475
					5,60	B	50	95	125			
					1,30	C	25	60	90			
					1,30	C	25	60	90			
						C	25	60	90			
5 V12A12	5,0 %	5,0 %	5,0 %	6	4,20	A	60	75	90	300	450	580
					1,30	B	70	95	125			
					4,20	C	45	70	95			
					3,80	C	45	80	100			
					1,30	C	40	65	85			
						C	40	65	85			
6 T1203A2	5,0 %	2,5 %	0,0 %	8	2,80	A	60	70	80	365	580	770
					1,30	B	40	60	90			
					5,60	B	60	90	115			
					1,30	C	45	80	105			
					1,30	C	45	80	105			
					4,20	C	45	80	105			
					1,30	C	35	60	85			
						C	35	60	85			
Totaal	100,0 %	100,0 %	100,0 %									

[a] Referentiewaarde geldend voor lange afstand in het jaar 2000, exclusief dynamische effecten en tijdmatige ontwikkeling belasting.

In addition to loads resulting from traffic, movement of the bridge introduces loads to the detail as well. Seven states of the bridge have been determined, each exerting a specific stress on the details. These states are:

1) Bridge closed and supported;
2) Bridge closed; support forces no longer present;
3) Bridge barely opened;
4) Bridge fully open;
5) Bridge nearly closed;
6) Bridge closed; support forces not yet present;
7) Bridge closed and supported.

The effect of each of these states, as well as the effect of truck passages are asserted through a model built in SCIA Engineer.

Bridge model

The model is constructed almost entirely of shell elements. The only exception is the main pivot point, which is modelled using a beam element. Connections between the pivot and the tube it is placed in (which is made of shell elements) are through stiff line elements. The remainder of the structure is connected through welds.

Variations of the different states the bridge can be in, are achieved through different supports and support forces. In closed state, the bridge is supported in its pivot point and at the end of the deck. Additionally, the support forces are applied at the 'beginning' of main beams of the bridge (Figure

127), and are applied at an angle of 54,90° compared to the negative z-axis, in order to mimic the real support forces of the bridge introduced in the ballast box.
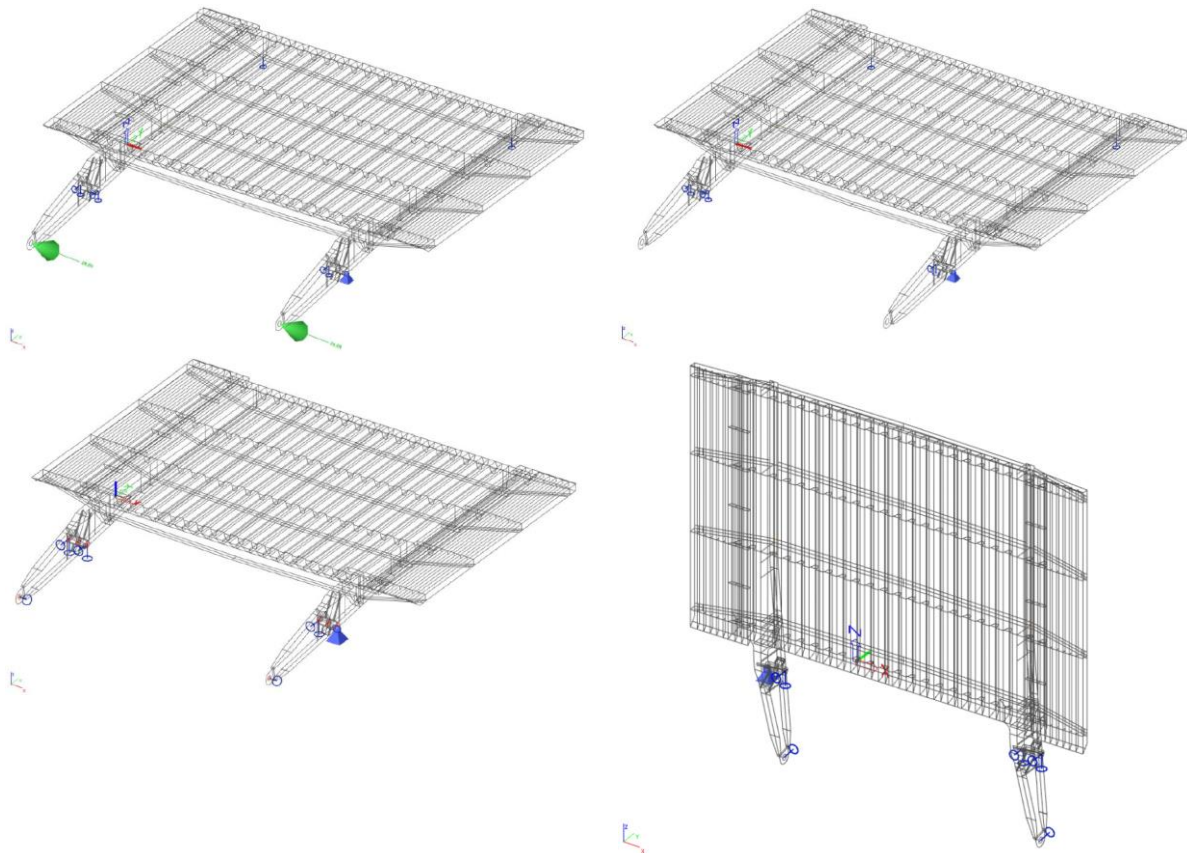

Figure 127: Konninginnebridge in closed (top left), closed but unsupported (top right), barely opened/nearly closed (bottom left) and open (bottom right) state

The model in the following state, closed but unsupported, simply removes the support forces in the main beams of the bridge, while maintaining the actual supports. The barely opened/nearly closed states are modelled the same way. They assume the supports at the end of the deck are no longer present, while a simple support is introduced in the point of application in the ballast box, at the same location and under the same angle as the supporting forces in the closed state.
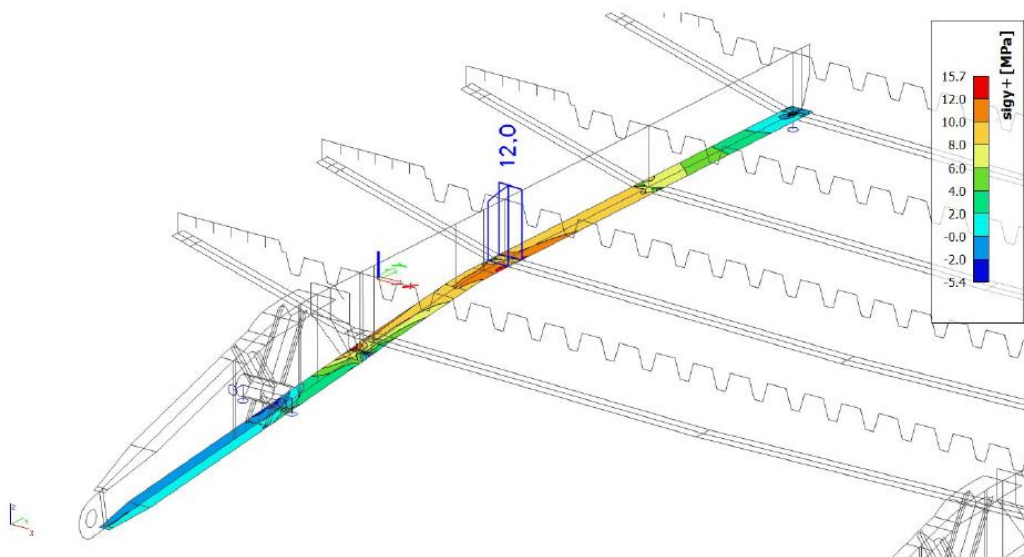

Figure 128: Example of a stress ripple in the critical detail of the bridge, as a result from a V12-truck under medium loading

The loads considered for this model are its self-weight, the loads as a result of the weight of the ballast, and the fatigue traffic loads. Traffic loads are applied centrically to the actual traffic lane. Both the old and the new road layout have been considered. The types of trucks are considered separately. Additionally, low, medium and high loads for each of the truck types have been considered. The governing locations for each of these situations have been found by applying the wheel loads at their relevant location, which allows for the resulting stresses in the critical detail to be found. Subsequently moving up the truck loads by a meter along the length of the bridge deck and rerunning the calculation results in a stress ripple in the bottom flange of the main beam (Figure 128). Assessment of this stress ripple for each of the truck locations can be used to easily find the governing stresses in the critical detail.

Combining the results from the different states of the bridge and the assessment of the traffic fatigue loads a graph can be made displaying the minimum and maximum stresses acting on the critical detail. This in turn can be used to find the stress ranges acting on the critical detail (see Figure 129).
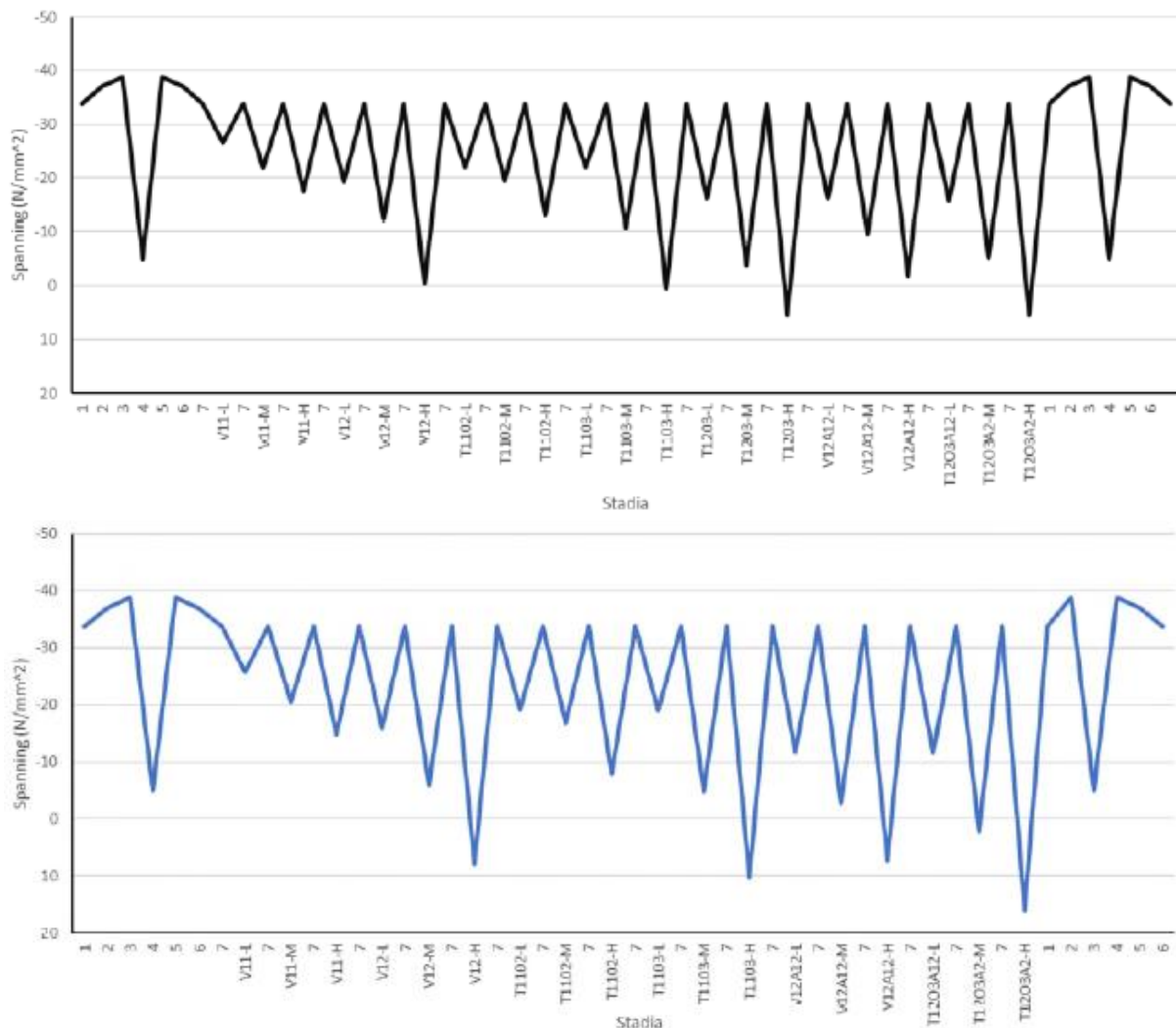

Figure 129: Stresses in critical detail resulting from bridge movements and traffic in the old road lay-out (top) and new road lay-out (bottom)

Joint verification

Once both a traffic count has been performed and the individual effects of different truck loads have been determined, the remaining fatigue life can be determined. This is done based on the damage calculation using Palmgren-Miner's rule. Extrapolating the found traffic data to the entire lifespan of the bridge and accounting for the traffic distribution displayed in Table 30 to Table 32, the total number of passages per truck type can be calculated. Additionally, using the stresses in the detail resulting from the individual truck types and relating that to the S-N curve of the detail category for said detail (which in this case is detail category 40), the maximum total number of passages allowed for a single truck type can be determined. Using Eq. 4, the damage per truck type can then be calculated. By combining the damage numbers for each truck type, the total fatigue damage over the course of the lifetime of the bridge can be calculated. An example for the damage calculation based on the original bridge lay-out, and assuming that failure has large consequences and the bridge is not damage-tolerant, for the period from 1978 to 2020, can be found in Figure 130. Applying this same principle for 2020 to its projected end-of-lifetime, being 2050, the expected total damage can be calculated.

Detailcategorie	40	MPa	
γ_{mf}	1,35	-	Groot gevolg van bezwijken
$\Delta\sigma_C$	29,6	MPa	
$\Delta\sigma_D$	21,8	MPa	
$\Delta\sigma_L$	12,0	MPa	

Huidige wegindeling
Jaar 1978-2020

NEN8701 - Bijlage A	$\Delta\sigma,0$ (MPa)	$\Delta\phi$ (-)	$\Delta\phi$voeg (-)	groeifactor (-)	$\Delta\sigma$ (MPa)	N3 (-)	N5 (-)	Aantal (-)	D3 (-)	D5 (-)	D_{tot} (-)
Combinatie brugbeweging+verkeer	34	1,0	1,0	1,0	34	1347282		7,58E+04	0,06		
V11 - laag	7,20	1,1	1,08	1,04	9			9,89E+04			
V11 - gemiddeld	12,02	1,1	1,08	1,04	15		34788065	6,93E+04		0,00	
V11 - hoog	16,32	1,1	1,08	1,04	20		7546664	2,97E+04		0,00	
V12 - laag	14,50	1,1	1,08	1,04	18		13640651	9,89E+04		0,01	
V12 - gemiddeld	21,80	1,1	1,08	1,04	27	2684609		6,93E+04	0,03		
V12 - hoog	33,40	1,1	1,08	1,04	41	746468		2,97E+04	0,04		
T11O2 - laag	11,80	1,1	1,08	1,04	15		38217746	2,35E+05		0,01	
T11O2 - gemiddeld	14,40	1,1	1,08	1,04	18		14120909	1,65E+05		0,01	
T11O2 - hoog	20,80	1,1	1,08	1,04	26	3090727		7,05E+04	0,02		
T11O3 - laag	11,90	1,1	1,08	1,04	15		36638721	4,95E+05		0,01	
T11O3 - gemiddeld	23,20	1,1	1,08	1,04	29	2227341		3,46E+05	0,16		
T11O3 - hoog	34,40	1,1	1,08	1,04	42	683243		1,48E+05	0,22		
T12O3 - laag	17,70	1,1	1,08	1,04	22		5032790	3,72E+04		0,01	
T12O3 - gemiddeld	30,00	1,1	1,08	1,04	37	1030118		2,60E+04	0,03		
T12O3 - hoog	39,20	1,1	1,08	1,04	48	461735		1,12E+04	0,02		
V12A12 - laag	17,60	1,1	1,08	1,04	22		5177401	1,23E+04		0,00	
V12A12 - gemiddeld	24,40	1,1	1,08	1,04	30	1914613		8,60E+03	0,00		
V12A12 - hoog	32,00	1,1	1,08	1,04	39	848791		3,69E+03	0,00		
T12O3A12 - laag	18,30	1,1	1,08	1,04	23	4538343		1,23E+04	0,00		
T12O3A12 - gemiddeld	28,70	1,1	1,08	1,04	35	1176535		8,60E+03	0,01		
T12O3A12 - hoog	39,20	1,1	1,08	1,04	48	461735		3,69E+03	0,01		
						Σ	2,05E+06		0,59	0,05	**0,65**

Figure 130: An example of the damage calculation for a specific situation and timeframe, in which N3/N5 represent the maximum number of cycles for the given situation, and 'Aantal' denoting the actual number of cycles

Several possible situations have been considered. Situations vary the assumed γ_{MF}, as well as the projected increase in traffic during the remainder of its projected lifespan. Every single situation has resulted in a damage number exceeding 1,0. This means that according to the calculations, in none of the situations the bridge will reach its projected lifespan. The found results are displayed in Table

33. The theoretical end-of-lifetime is the last year for which the damage calculation does not exceed 1,0.

Table 33: Result of fatigue calculation of the Konninginnebridge for various scenarios

Scenario	Assumptions	Damage number	Theoretical end-of-lifetime
0	Initial assumptions	1,98	2029
1	γ_{MF} = 1,15	1,20	2044
2	γ_{MF} = 1,35 and no projected traffic increase	1,85	2029
3	γ_{MF} = 1,15 and no projected traffic increase	1,12	2045

Limitations

The calculation process laid out in this chapter illustrates the standard approach, as defined by the Eurocodes. For this method to have become the standard approach, it has to be extensively studied and tested. The result is an excellent way to assess the fatigue strength and remaining fatigue life of structures.

Its main downside though, is the detail categories. While the categories set a fine baseline for fatigue assessment, there is an infinite number of possible configurations for bolted or riveted joints, and even welded joints have a significant amount of different possible applications. Furthermore, there is a multitude of possible loading situations. The currently accepted detail categories simply do not cover this wide range of possibilities. It is possible to take a known detail category for a given situation, in the assumption that it is the most comparable one for that specific situation, but it does not accurately represent the actual situation, and can only be considered an estimate. It should therefore be taken conservatively, possibly resulting in overly conservative assessments.

Furthermore, the type of influence lines (Figure 128) used in this calculation to find the maximum stresses within the critical detail under different types of loading, cannot be applied to the more complex joints, such as riveted joints, in which the precise load distributions throughout the joint are unknown.
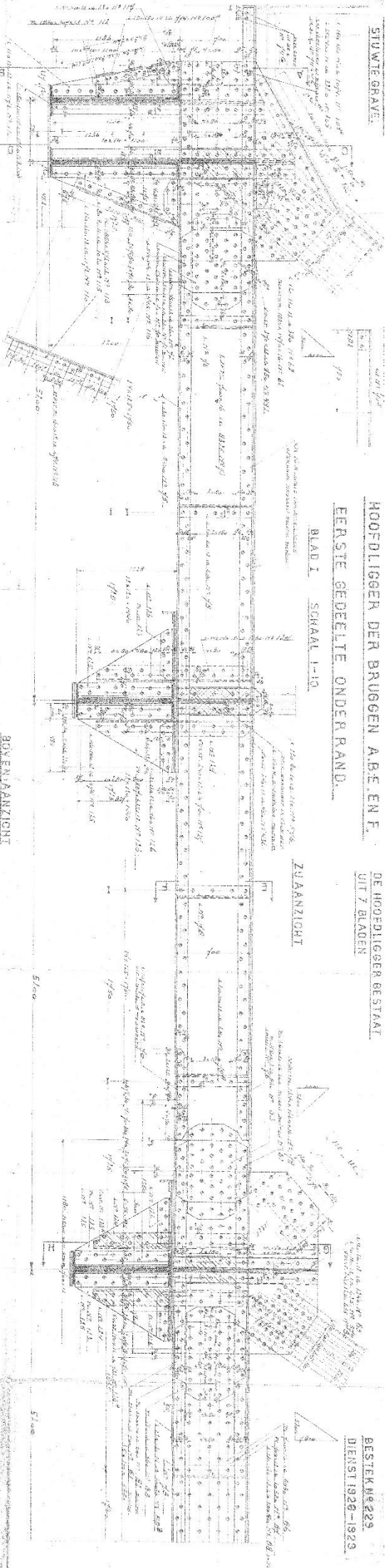
Annex C. Technical drawing Joint, John S. Thompson Bridge, Main beam

HOOFDLIGGER DER BRUGGEN A,B,E EN F.

EERSTE GEDEELTE ONDER RAND.

BLAD I   SCHAAL 1-10

DE HOOFDLIGGER BESTAAT UIT 7 BLADEN
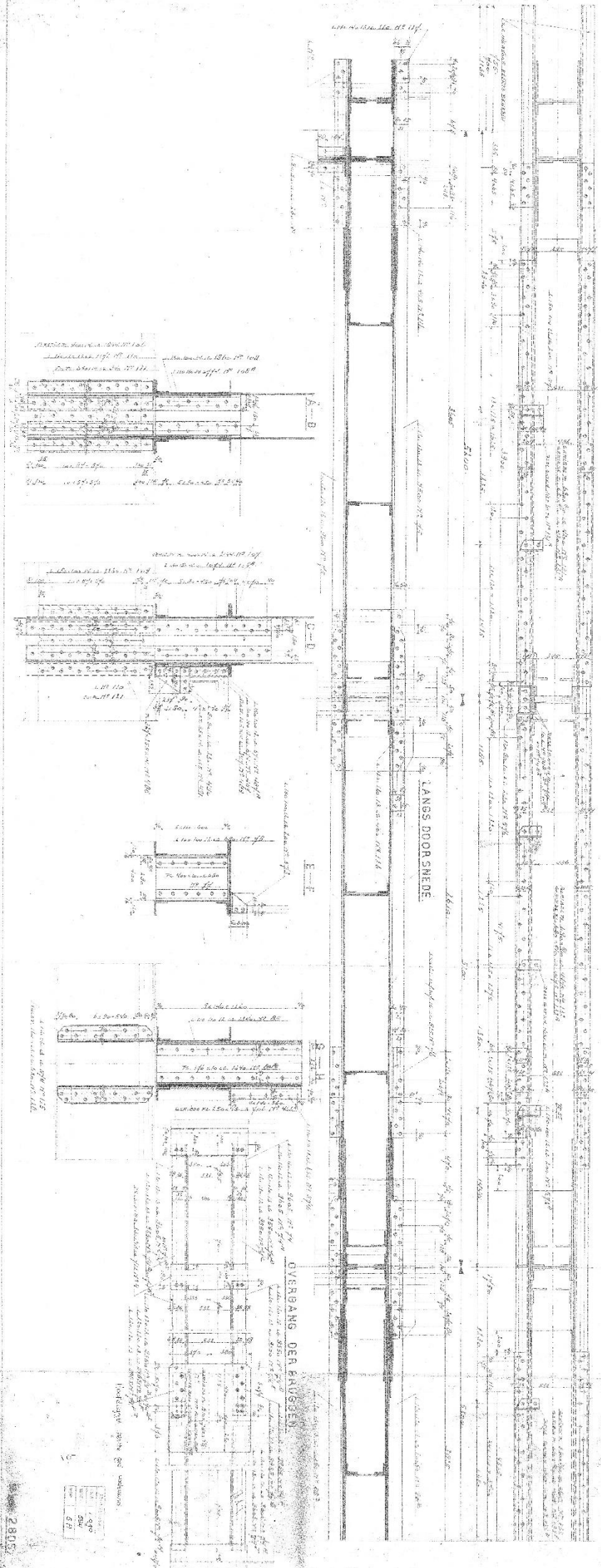
BESTEK No 229

DIENST 1926-1923

A-B

C-D

E-F

BOVENAANZICHT
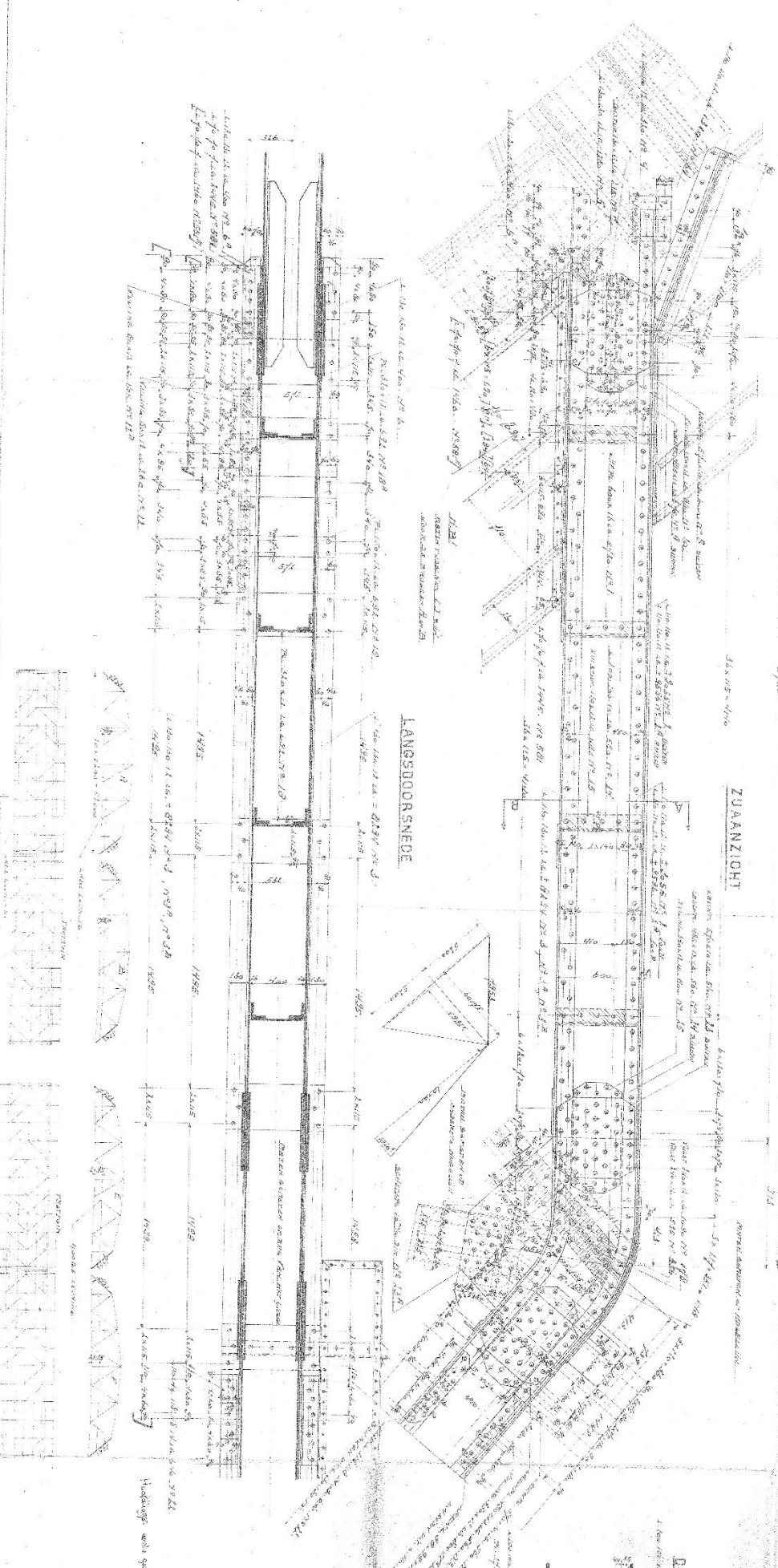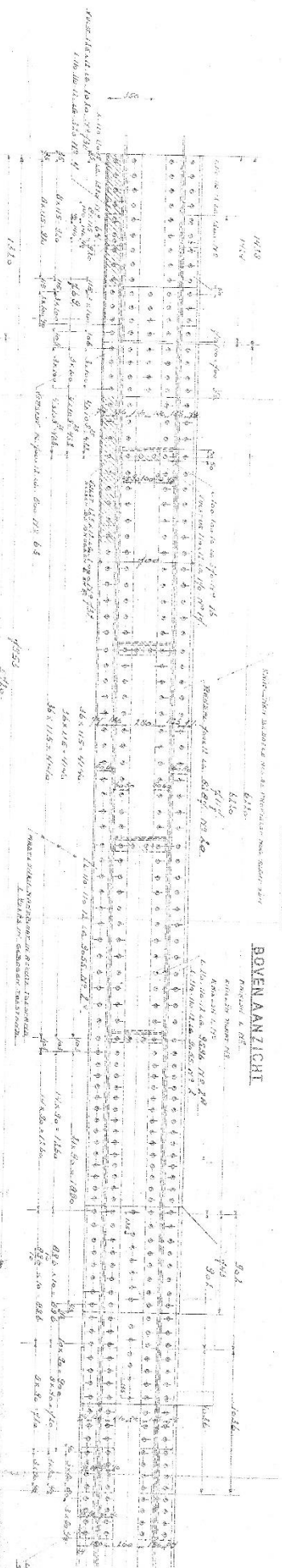
ZIJAANZICHT

LANGS DOORSNEDE

OVERGANG DER BRUGGEN

Annex D. Technical drawing Joint, John S. Thompson Bridge, Diagonal beam

HOOFDLIGGER DER BRUGGEN A.B.E. EN F

EERSTE GEDEELTE BOVENRAND

BLAD III

SCHAAL 1:10

BOVEN AANZICHT

ZIJAANZICHT

LANGSDOORSNEDE

DOORSNEDE A—B

Annex E.   Finite Element Analysis in IDEA Statica

Several Finite Element Software packages can be considered to model a riveted connection. In this chapter, two of these Finite Element Software packages that can be used to model complex riveted connections are characterized, including any assumptions that need to be made in order to appropriately define a model, and any limitations that each program might face. ABAQUS has already been covered. This chapter focuses on the use of IDEA Statica. The use of IDEA Statica, in particular in research, is relatively uncommon, which is why some additional background on the software is provided.

Modelling in IDEA Statica

There are several methods to analyse connections in steel structures. It is not uncommon to model steel joints in specialized finite element software. Additionally, EN 1993-1-8 adopts the Component Method (CM), in which all individual components of a connection will be assessed separately in both strength and stiffness. The active components are assumed to act as representative springs, obtained using their respective formulas, and the components are assembled to find the behaviour of the connection as a whole (Figure 131). This method allows for the simpler connections to be calculated by hand.
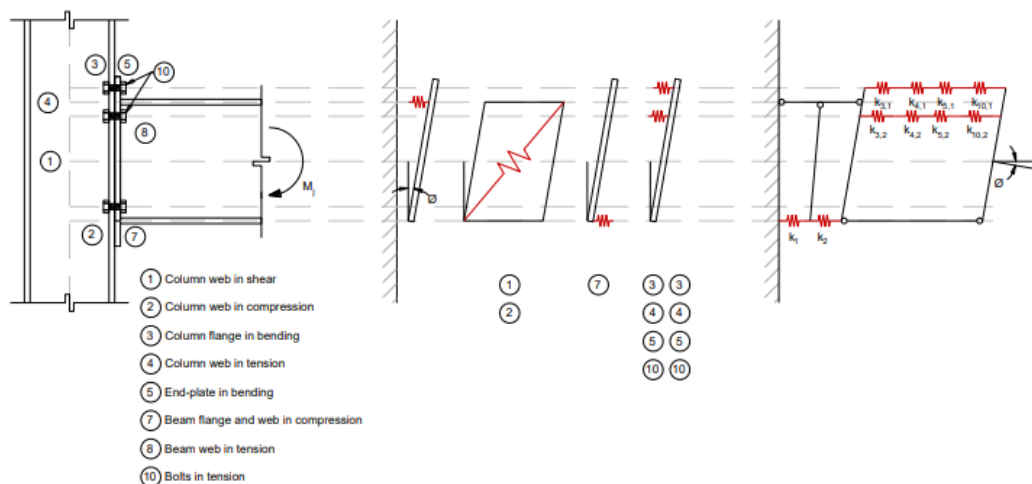

Figure 131: Schematic representation of the Component Method (García, 2017)

Riveted connections provide issues for both methods. While Finite Element Analysis will likely produce accurate results, provided no errors have been made in defining the joint, complicated geometries (and riveted connections are notoriously complex) require a significant number of hours to obtain appropriate results, both in terms of modelling and in terms of calculating. On the other hand, the Component Method is capable of simplifying and calculating the individual stiffnesses of most components, albeit still very time-consuming when done by hand for complex connections such as riveted connections. However, some elements are not described in the available codes and require additional analysis. Furthermore, internal stresses and strains cannot be assessed through the Component Method.

IDEA Statica attempts to tackle some of the problems of either method. The intuitive interface and focus on joints allow for one to drastically cut down on the hours required to model a more complex connections compared to standard Finite Element Software, while still maintaining the verified and useful parts of the individual analyses of the Component Method. Additionally, the facets the Component Method are somewhat lacking at are supplemented excellently by Finite Element Analysis, which is able to model any elements that cannot be described with the Component

Method as well as provide internal stress distributions within elements. The result is a program applicable to a wide variety of joints, while being more approachable and user-friendly than standard Finite Element Software.

This Component Based Finite Element Method (CBFEM) is used in the Connection Evaluation Model of IDEA Statica, which is specialized in 3D modelling in steel joints. Several types of analyses can be performed:

11) **Stress/strain analysis** can be used to find the response of the joint as a result of an applied load;
12) **Stiffness analysis** can be used to find the stiffness of a given member of the connections. For a complete picture, all members need to be analysed separately;
13) **Capacity design** verifies whether the designed connection is able to withstand the design loads imposed on it;
14) **Joint design resistance** is used to find the maximum loads that can be applied on the connection.

Theoretical background

This study will utilize only the stress/strain analysis function of IDEA Statica. Similar to the component method, a joint is divided into individual elements. Each plate-like element is subsequently modelled as a shell element for the Finite Element Analysis, with 4-node quadrangles, each with six degrees of freedom (three translations and three rotations). Materials are assumed to have ideal elastic-plastic properties, with its bi-linear stress-strain diagram as defined in EN 1993-1-5 (2012) (Par. C.6), with a nominal yielding plateau slope following $\tan^{-1}(E/1000)$. IDEA Statica assumes the failure criterion to be based on the Von Mises yield criterion, and the ultimate limit state is assumed at a strain of 5%, as recommended by EN 1993-1-5, Par C.8. The mesh size adopted by IDEA Statica is not as extensive as conventional FEM software. In its default setting, mesh element sizes are limited from 10 mm to 50 mm, though these can be changed in the code setup. Standard cross-sections are built up of eight finite elements along its height, while end plates consist of sixteen. Similarly, this default can be adjusted accordingly in the code setup. Larger mesh sizes result in shorter calculation times, although differences in resistance have been shown of up to 15% for larger mesh sizes compared to smaller ones (Structural design of steel connections: Theoretical Background, n.d.).
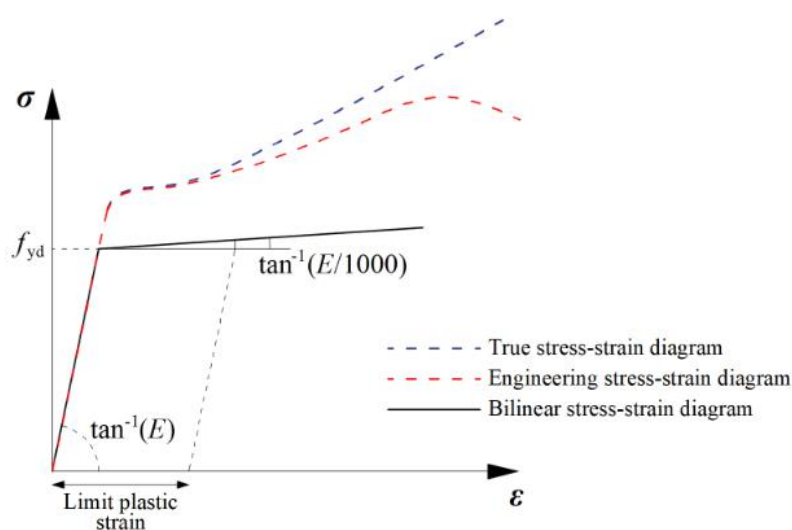

Figure 132: Possible stress-strain diagrams used in FEA

Fasteners such as bolts and welds require a different approach than plates, for which special FEM components have been developed. The tensile-, shear- and bearing behaviour of bolts are modelled with as the component described by dependent nonlinear springs. Tensile behaviour of the bolts relies on four factors: the axial initial stiffness, the design resistance, the initialization of yielding and the deformation capacity. The latter two factors are assumed to occur in the threaded part only. Axial initial stiffness is derived analytically, using the VDI2230 guideline, which corresponds to experimental data. Initiation of yielding occurs at $f_{y,b} * A_t$. Deformation capacity is taken as the combined elastic deformation of the bolt and the plastic deformation of the threaded part of the bolt (see Eq. 38, Eq. 39 and Eq. 40). Compressive forces are transferred from the bolt shank to the plate in the bolt hole. They are modelled using interpolation links between shank nodes and nodes on the edge of the hole. Distribution of forces over the bolts is simulated by the deformation stiffness of the shell elements. Additionally, the distribution of forces may be affected by the interaction between shear and axial forces, and is taken into consideration in the analysis model directly (García, 2017) (Structural design of steel connections: Theoretical Background, n.d.). IDEA Statica does allow for the use of pretensioned bolts, but is does not allow for the user to specify the degree of preloading.

$$\delta_c = \delta_{el} + \delta_{pl}$$

<div align="right">Eq. 38</div>

$$\delta_{el} = F_{t,Rd} * k_{ini}$$

<div align="right">Eq. 39</div>

$$\delta_{pl} = \varepsilon_{pl} * l_t$$

<div align="right">Eq. 40</div>

Here, k_{ini} is the initial deformation stiffness, ε_{pl} the plastic strain limit and l_t the length of the threaded section of the bolt.

Practical background

A model in IDEA Statica consists of members and manufacturing operations. Members are the elements on which loads are applied, while manufacturing operations are all the elements with as purpose to connect the members. Within the model, two types of members can be defined. One member will always be the "bearing member", which can be either continuous or ended, while all other members are "connected members". These will always end in the joint. IDEA Statica assumes continuous members to be supported on both ends, while ended members are supported only on one end. IDEA Statica defines four different types of supports:

Figure 133: Example of a continuous "bearing member" and an ended "connected member"

15) Type N-Vy-Vz-Mx-My-Mz, in which case the member can transfer all six components of internal forces;
16) Type N-Vy-Mz, in which case the member can only transfer forces in the XY-plane;
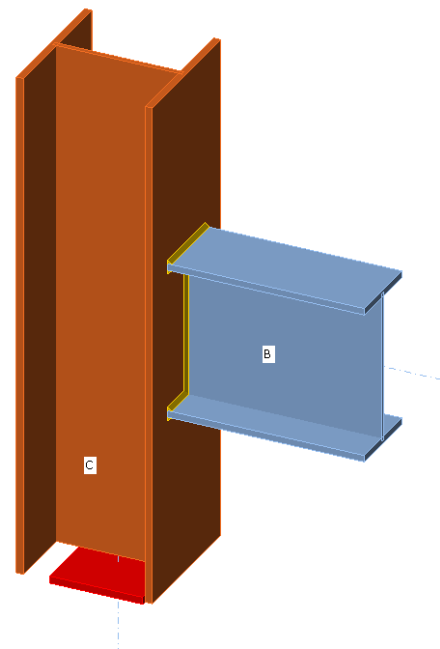17) Type N-Vz-My, in which case the member can only transfer forces in the XZ-plane;

18) Type N-Vy-Vz, in which case the member can only transfer forces and no moments (hinged support).

During analysis, the joint is in a state of equilibrium. When the forces on the individual members are applied, the joint should still be in an equilibrium. By enforcing an equilibrium of the loads in all nodes, the internal load distribution can be found. There are two methods to apply the loads in IDEA Statica. The simplified method assumes the bearing member to be supported, and assumes the supports ensure equilibrium of forces. As a result, this method will only look at the effect of the loads on the connected members. This method does not define applied loads on the bearing member. It should be noted that this method is only relevant for the connection items, and not the joint as a whole. It should only be used if the user is not interested in the interaction between the loads on the bearing and connected members. The advanced method on the other hand, requires an input on both the loads acting on the connected members and loads acting on the bearing member. The sum of these loads should be in equilibrium, and the user is required to ensure that they are. Unbalanced forces may result in inaccurate models. If the loads are in equilibrium, supports are not required to be defined, as their ability to take up specific loads can be enforced. E.g., by ensuring the bottom support of the bearing member has no Mx applied, one has essentially modelled a hinged support in the YZ-plane, despite the fact that a Type N-Vy-Vz-Mx-My-Mz support is used. When a support type other than the first one is chosen, and the designated support still needs to take up forces that it normally cannot, a nonconformity is present. Small nonconformities compared to the applied loads are acceptable, though it might be preferred to design the joint differently when relatively larger nonconformities occur.
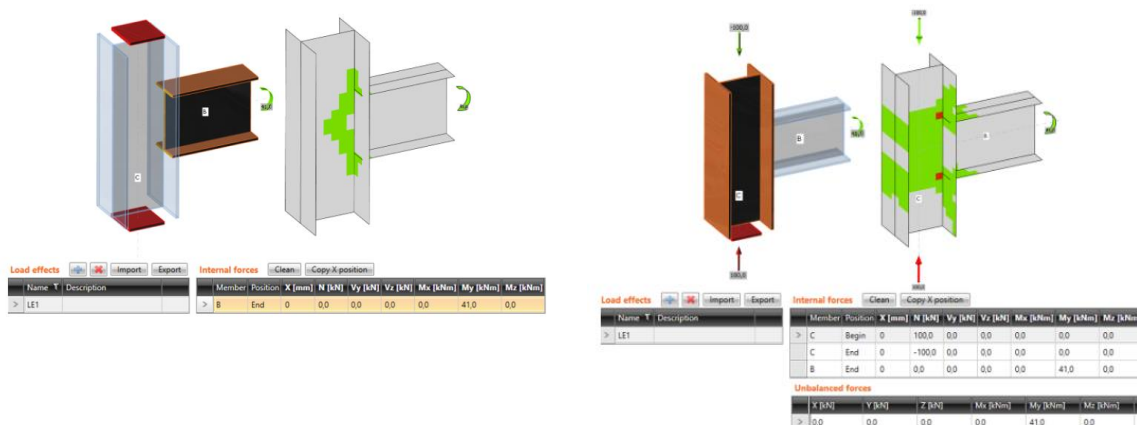

Figure 134: Difference between simplified method (left) and advanced method (right) for applying loads

It should be noted that the applied loads are not actually external forces, even though they may look like it. Rather, they are internal nodal forces, taken from a structural model. As per the law of statics, internal loads should be in equilibrium, which is why this is the basis IDEA Statica works off of. In the same sense, the members are not complete members, but only a section of a complete beam/column, and the supports are not actual supports, but rather simulate the way the members interact with the rest of their beam/column. Displacements are shown by assuming a support in the first end of the bearing member, which resists all deformations, and IDEA Statica relates the displacements to this support. The resulting deformed shape is only a visual representation of the displacements, meant as an aid to assess any unusual behaviour of the joint and for the sake of presentation. The assumed translation-resistant support does not affect the stress distribution or internal forces.

Implementation of materials

IDEA Statica has a vast database on material types, cross-sections and bolt types. However, when assessing older bridges, many of the materials used are not up to date to modern standards. Furthermore, they are no longer being applied in practice and therefore often are not implemented in the standard database. IDEA Statica does allow for the modification or expansion of the material database, based on the input of material properties. Therefore, if the material properties are known, the material can be modelled. In the same way, as long as the properties are known, bolt types different from those in the standard database can be used. In Figure 135, Figure 136 and Figure 137 the material properties used for the model in this thesis are shown, in accordance with Chapter 2.3.1.1. Some additional parameters may be adjusted but are not relevant for this study. Values are taken from RBK Steel (2017), Colette (2014) and, in the case of f_u and f_{ub}, adjusted according to Rijkswaterstaat's specifications.

▼ **General**			▼ **General**			▼ **Properties**	
Name	Mild steel		Name	Rivet		Name	Rivet D24
▼ **Physical properties**			▼ **Physical properties**			Bolt grade	Rivet
m [kg/m3]	7850		m [kg/m3]	7850		▼ **Bolt**	
E [MPa]	210000,0		E [MPa]	210000,0		Diameter [mm]	24
ν	0,3		ν	0,3		Hole for bolt [mm]	24
G [MPa]	80769,2		G [MPa]	80769,2		Head diameter [mm]	36
α [1e-6/K]	12		α [1e-6/K]	12		Head diagonal diameter [mm]	36
λ [W/(m.K)]	50		λ [W/(m.K)]	45		Head height [mm]	16
c [kJ/(kg.K)]	0,49		c [kJ/(kg.K)]	0,49		Gross Cross-section area [mm2]	576
▼ **Properties specific to European standard**			▼ **Properties specific to European standard**			Tensile stress area [mm2]	576
fu [MPa]	360,0		fyb [MPa]	235,0		▼ **Nut**	
fy [MPa]	235,0		fub [MPa]	420,0		Thickness [mm]	16
			Elongation [-]	0,22		▼ **Washer**	
						Thickness [mm]	3
						At the head	
						At the nut	

Figure 135: Material properties mild steel

Figure 136: Material properties rivets

Figure 137: Physical properties rivets

Usually, when constructing a joint, one would take a standard cross-sections from the database. However, riveted structures usually have built-up cross-sections, consisting of several smaller standard plates and L-plates. García (2017) and Pazmiño (2018) have looked at several ways to use IDEA Statica's cross-section editor to construct these built-up cross-sections in order to assess the joint stiffness. Their findings suggest that the custom cross-sections give comparable results to using a multitude of individual elements. The main advantage of using a single, custom cross-section is that the applied loads can be applied to the member as a whole, allowing IDEA Statica to figure out the distribution within each web/flange of the cross-section, rather than having the user define the load on each web/flange individually. Therefore, the members in the model will be constructed using these custom cross-sections.

Limitations

While IDEA Statica is an excellent tool to assess the structural strength of a joint, it is not a perfect solution. As mentioned, IDEA Statica is not designed to model rivets. Changing parameters may be a decent way to approach rivets, some elements are unable to be modelled. Rather than a nut, rivets have an additional head. This head does not have a constant height, which is what is implied at the 'nut'-subsection in Figure 137. Fortunately, this height is only used to find the elongation length, for which the height of a rivet head is still an acceptable measure. The same holds for the head height at the 'bolt'-subsection. Another result of the way rivets are constructed, is the applied clamping forces. Unless a rivet has completely failed, it is under the effect of a pre-tensioning stress. This stress is not governing in structural calculations, which is what IDEA Statica is primarily used for. IDEA Statica does allow for the use of pre-tensioned bolts, but relies on the frictional resistance as a

result of these pre-tensioning stresses of the bolts to provide the structural strength, and once slipping occurs, considers the bolt to have failed. This means it incorrectly assesses the strength of rivets with this method. However, for non-extreme loading situations, the clamping forces have a positive effect on stress concentrations around bolt holes, and in some cases may be sufficient to resist the applied forces as a whole. As a result, it is significant for the fatigue resistance of the joint. The inability to properly apply these clamping forces suggest IDEA Statica may not be appropriate for fatigue calculations.

Another limitation is in cases when the joint is positioned close to a support. IDEA Statica automatically defines a member length in order to ensure that the stresses in members are able to develop realistically and accurately. This automatic length is defined from the latest manufacturing operation, e.g. a bolt, the end of a supporting plate or a hole (see Figure 138), and is normally defined as 1,25 times the largest of the member height or width. This automatic length can be adjusted within the program, but the developers highly recommend leaving it as is. It is impossible to adjust the automatic length for each individual member. As a result, IDEA Statica is unable to model the interaction between a support and a member, without affecting with the modelled stress development in other members. If the internal stresses in the support are not relevant for the model, there is a workaround available. By assuming an oversized member (such that its capacity is definitely

Figure 138: Example of member length definition

sufficient, and yielding is avoided) at the location of the support, and using fictitious, oversized welds to connect the member and the joint, a fictitious support can be created. By enforcing the same boundary conditions on the member that the support would have (e.g., inability to take up specific forces or moments), the support should be modelled in a way that is able to represent the resulting behaviour of the joint correctly.
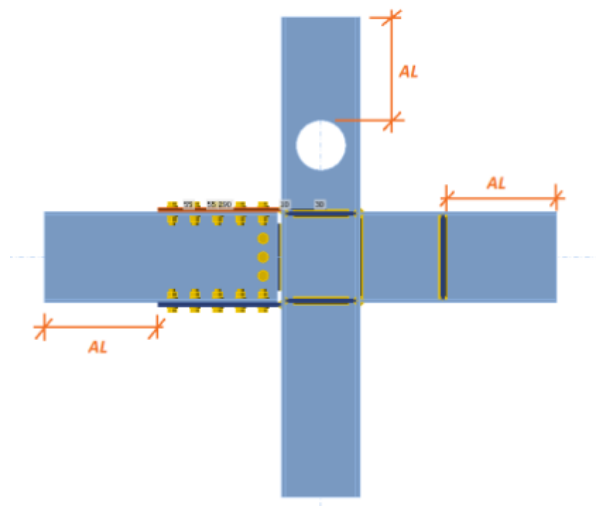
One of the biggest issues is IDEA Statica's ability to export data. Some basic reports involving the geometry and the checks of the most critically loaded sections of the joint are available, but unfortunately a detailed report of all data is not. Additionally, IDEA Statica is unable to quantify the stress or strains at a specific point, only the maximum stress and strain in an element is quantified. Stresses/strains at an arbitrary point can only be taken from a contour plot (which is automatically capped at the maximum stress). While interpolating between the known values and the edges of the contours may be possible to estimate the results, precise values are unavailable. Additionally, the contours have a set threshold. As can be seen in Figure 139, the contours are capped at 235 MPa, the yield strength. If there are stresses present that exceed this maximum yield stress, they are displayed in the same colour as the yield stress, regardless of their actual value, meaning that large internal stresses or singularities cannot be distinguished appropriately from stresses that barely exceed the yield stress. Furthermore, the displayed stresses are Von Mises stresses. These are the only stresses that IDEA Statica has available information on. Stresses in specific directions or for example shear stresses only are not available for display or export.
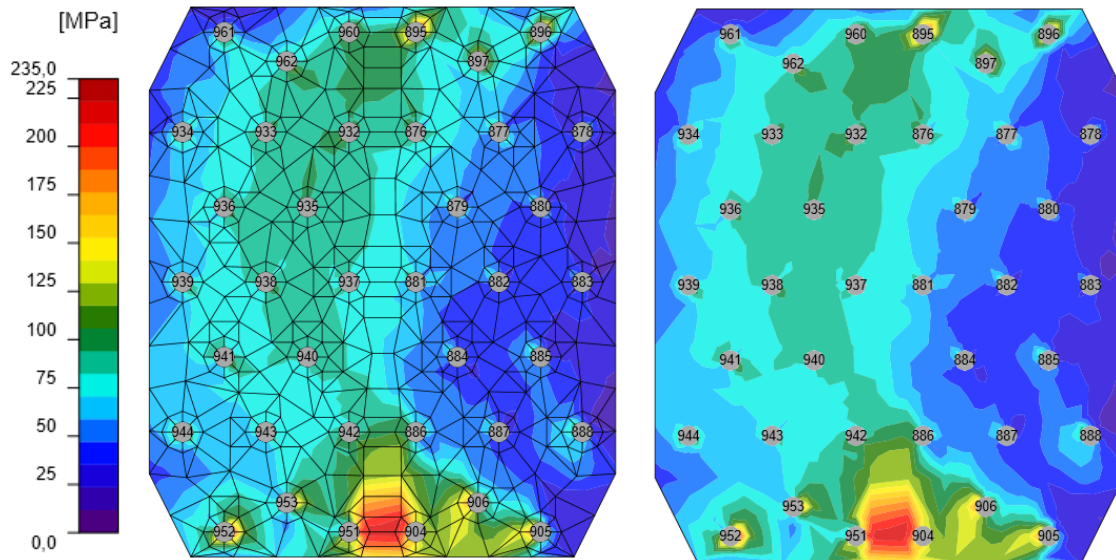
Figure 139: Example of a contour plot by IDEA Statica (with or without grid)

Concluding remarks

IDEA Statica is an excellent tool for the structural calculation of conventional joints. Its user-friendliness allows for a relatively fast assembling of models and its relatively limited complexity results in short calculation times (even complex joints such as in Figure 140, with almost 1500 rivets, takes approximately 30 minutes to calculate, assuming one load case). Furthermore, despite its limitations, using various workarounds, it is possible to moderately accurately approach a complex connection. However, not all limitations can be overcome that way. The inability to define preloading of the bolts means that the fatigue behaviour cannot be appropriately assessed. Finally, the biggest issue is its lack of exportable data. In order to get a grasp on the internal workings of the model, and to account for, for example, multiaxial fatigue, several types of datasets are required, and because IDEA Statica only provides Von Mises stresses, and even that to a very limited degree, the usefulness of IDEA Statica in fatigue assessment appears to be limited. By defining critical sections, interpolating data from contour plots along this section and applying standard detail categories, it may still be possible to do a very simple fatigue assessment, but detailed fatigue calculations appear to be tough to justify. For structural calculations though, the model in IDEA Statica can still be useful.
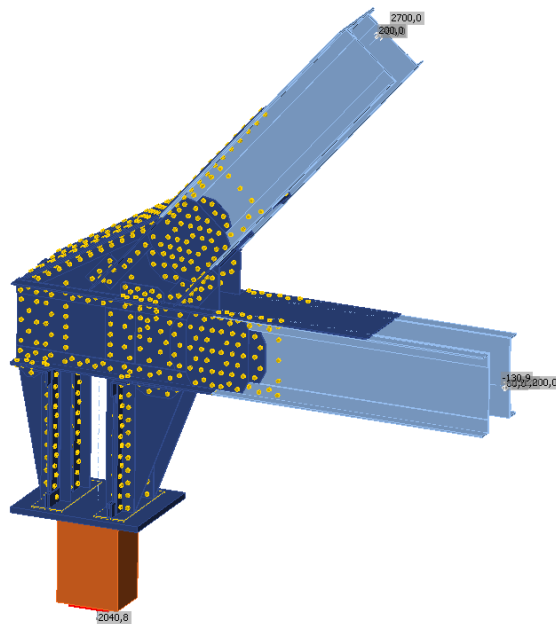

Figure 140: Connection from John S. Thompsonbridge, as constructed in IDEA Statica